

Molecular Exciton Related Phenomena Studied by Two-Photon Photoemission

Dissertation

zur Erlangung des Grades eines
Doktors der Naturwissenschaften (Dr. rer. nat.)

am Fachbereich Physik der Freien Universität Berlin

vorgelegt von

Wibke Bronsch

Berlin 2018

Erstgutachter: Prof. Dr. Martin Weinelt

Zweitgutachterin: Prof. Dr. Katharina J. Franke

Disputationstermin: 06.05.2019

Abstract

The present thesis focusses on exciton dynamics and excitonic coupling in organic thin films on Au(111) surfaces. Two model systems are investigated. Thin α -sexithiophene (6T) films are deposited by molecular beam epitaxy and mixed self-assembled monolayers (SAMs) of azobenzene-functionalized and pure alkanethiols are prepared in a wet-chemical procedure.

6T is a model molecule of an organic semiconductor. The material class of organic semiconductors is used, e.g. in organic light emitting diodes and organic solar cells. A fundamental dynamical process occurring in both devices is the formation and decay of excitons. In the present dissertation exciton population dynamics were studied in dependence of the excitation energy and the film morphology by means of time-resolved two-photon photoemission (2PPE) spectroscopy. Two aspects of the population of excitons in organic semiconductors are addressed, which have been currently under debate: the exciton formation pathway and the dephasing time needed for population after initial excitation. In this work it is shown that a resonant excitation of the lowest optical transition in a 6T aggregate leads to a population of an exciton state within the duration of the exciting fs-laser pulse. Higher excitation energies in the range of the vibrationally broadened absorption band lead to vibronic excitations. Modelling the vibrational relaxation dynamics based on rate-equations it has been shown that the population of the higher vibrational levels of the excited state can be probed through our 2PPE experiments. The excess energy stored in vibrations is dissipated into heat on the femtosecond time-scale. After one picosecond, it cannot be distinguished anymore, whether the system was excited resonantly or with excess energy. The relaxation dynamics of the excitonic state are dominated by an energy transfer into the substrate. Furthermore, I show that the exciton population dynamics is influenced by the film morphology significantly. In amorphous films grown at low temperature, the local environment of the molecules varies stronger in contrast to crystalline films grown at room temperature. This results in a diffusion process in which the excitons hop to energetically more favorable sites within the film and competes with substrate-mediated quenching of the exciton. The downhill migration process is observed to happen on a time-scale of a few picoseconds.

The second investigated sample system are azobenzene-functionalized SAMs. Azobenzene is a model-molecule of a conformational switch. By optical excitation in the ultraviolet and visible spectral range the molecule can be reversibly switched between its *trans* and *cis* configuration. In SAMs the molecules are strongly interacting and therefore excitonic coupling may lead to cooperative switching. In the present work, 2PPE is established as a method to quantitatively measure photoswitching of the SAM via changes of its work function. This allowed monitoring the switching kinetics for various excitation energies across the excitonically broadened absorption band. It is shown that excitonic coupling does not lead to an amplification of the ensemble switching in terms of the number of molecules switchable into the *cis* form or the time needed to establish a new photostationary state. There is no cooperative effect observed, independent of the chromophore density.

Zusammenfassung

Die vorliegende Arbeit beschäftigt sich mit der Untersuchung der Dynamik exzitonischer Anregungen und Kopplungen in dünnen Molekülschichten auf der Au(111)-Oberfläche. Hierbei stehen zwei Modellsysteme im Fokus. Zum einen werden wenige Monolagen dicke, im Vakuum aufgedampfte, α -Sexithiophen (6T)-Filme, sowie zum anderen nasschemisch präparierte selbstorganisierte Monolagen (SAM) aus Gemischen von Azobenzol funktionalisierten und reinen Alkanthiolaten untersucht.

6T ist ein organischer Halbleiter, die in Leuchtdioden und Solarzellen verwendet werden. Für diese Anwendungen spielt sowohl die Erzeugung als auch der Zerfall von Exzitonen eine fundamentale Rolle. In Rahmen dieser Dissertation wird die Populationsdynamik von Exzitonen in Abhängigkeit von der Anregungsenergie und der Filmstruktur mit Hilfe von zeitaufgelöster Zwei-Photonen-Photoelektronenspektroskopie (2PPE) untersucht. Die detaillierte Analyse des Anregungsmechanismus und der zur Population des exzitonischen Zustandes benötigten Dephasierungszeit beleuchtet zwei derzeit strittige Aspekte. Es wird gezeigt, dass eine resonante Anregung des niedrigsten optischen Übergangs in 6T-Aggregaten innerhalb der Laserpulsdauer zu einer Besetzung des Exzitonzustandes führt. Die Verwendung von höheren Anregungsenergien innerhalb der vibrationsverbreiterten Exzitonenbande führt zu vibronischen Übergängen und damit zur Besetzung vibrationsangeregter Zustände. Das Auftreten dieser Zustände in den 2PPE-Daten konnte ich mit Hilfe einer auf Ratengleichungen basierenden Modellierung der Relaxationsdynamik der vibrationsangeregten Zustände zeigen. Die Umwandlung der zusätzlichen Energie in Wärme erfolgt innerhalb weniger Femtosekunden. Nach etwa einer Pikosekunde kann nicht mehr unterschieden werden, ob das System resonant oder mit Überschussenergie angeregt wurde. Der Zerfall des angeregten exzitonischen Zustands ist maßgeblich vom Energietransfer in das Goldsubstrat beeinflusst. Darüber hinaus wird gezeigt, dass die Populationsdynamik der Exzitonen von der Morphologie des Films abhängt. In amorphen Filmen unterscheidet sich die lokale Umgebung der Moleküle stärker, als in kristallinen Filmen. Die Relaxation der Exzitonpopulation wird von einem Diffusionsprozess in energetisch niedriger liegende Energieniveaus begleitet. Der Diffusionsprozess findet auf einer Zeitskala von wenigen Pikosekunden statt.

In Azobenzol-funktionalisierten SAMs, wird die Rolle der exzitonischen Kopplung im Hinblick auf die photoinduzierte Isomerisierung der Chromophore untersucht. Azobenzol lässt sich optisch zwischen seiner *trans*- und *cis*-Form reversibel schalten. Fraglich war, ob die Kopplung zwischen den Molekülen durch kooperative Effekte das Schaltverhalten des Ensembles beeinflusst. Im Rahmen dieser Arbeit wurde die 2PPE als Methode zur quantitativen Bestimmung der Schaltkinetik der SAMs etabliert. Detaillierte Untersuchungen der Austrittsarbeit der Proben in unterschiedlichen photostationären Zuständen zeigen, dass es zu keiner Verstärkung des Schaltprozesses kommt. Weder hängt die Anzahl der in die *cis*-Form schaltbaren Moleküle von der intermolekularen Wechselwirkung der Übergangsdipolmomente ab, noch ändert sich die Schaltgeschwindigkeit zwischen verschiedenen photostationären Zuständen durch die Kopplung. Unabhängig von der Packungsdichte treten keine kooperativen Effekte auf.

Contents

1	Introduction	1
2	Excitons in Organic Layers	3
2.1	Exciton: Definition and Flavors	3
2.1.1	Frenkel Excitons	4
2.1.2	Aggregate Formation and Davydov Theory of Molecular Excitons	7
2.2	Dephasing and Exciton Decay Mechanisms	10
2.3	Exciton Formation in Two Model-Systems	14
2.3.1	The Organic Semiconductor α -Sexithiophene	14
2.3.2	Excitonic Coupling in Azobenzene-Based Alkanethiolate SAMs	18
3	Experimental Methods	23
3.1	Time-Resolved Two-Photon Photoemission Spectroscopy	23
3.1.1	Single-Photon and Two-Photon Photoemission	23
3.1.2	Analysis of Two-Photon-Photoemission Data	25
3.1.3	Two-Photon Photoemission of Molecular Thin Films	30
3.1.4	Experimental Set-ups for Two-Photon Photoemission Spectroscopy	31
3.2	Differential-Reflectance Spectroscopy	43
3.3	Photoelectron Emission Microscopy	45
4	Morphology, Electron and Exciton Dynamics in Thin α-Sexithiophene Films on Au(111)	47
4.1	Sample Preparation and Film Thickness Characterization	48
4.2	The Interplay of Morphology and Electronic Structure in Thin Sexithiophene Films on Au(111)	49
4.2.1	Real-Time Monitoring of Coverage-Dependent Changes in Film Growth and Optical Properties	49
4.2.2	Coverage Dependent Electronic Structure	54
4.3	Exciton Dynamics in Thin Sexithiophene Films	64
4.3.1	Exciton Relaxation Dynamics in α -Sexithiophene Crystallites	64
4.3.2	Vibrational Hot Exciton Relaxation	66
4.3.3	Morphology Induced Changes in the Exciton Dynamics	75
4.4	Summary	79

5	Azobenzene–Functionalized SAMs on Au(111)	81
5.1	Wet–Chemical Preparation of Alkanethiol–Based SAMs	82
5.2	Manipulation of the Sample Work-Function by Light	83
5.2.1	Dipole-Induced Shifts of the Work Function	83
5.2.2	Work-Function Tuning in Bichromatic Experiments	85
5.3	The Role of Aggregation in the Switching Process in Azobenzene-Functionalized SAMs	90
5.3.1	Wavelength-Dependent Work-Function Shifts	90
5.3.2	Wavelength-Dependent Kinetics of the Switching Process	94
5.4	Outlook: Towards Spatial Mapping of the Work-Function Shift	100
5.5	Summary	103
6	Summary	105
	Bibliography	107
	Appendix	123
A	Supplementary Material	123
A.1	Evaporator Design Modification	123
A.2	Electronic Structure of Au(111)	124
A.3	α -Sexithiophene/Au(111)	125
A.3.1	Intensity Loss and Background Correction	125
A.3.2	Electronic Structure	127
A.3.3	Vibrational Relaxation Dynamics	130
A.4	Azobenzene-Based Self-Assembled Monolayers/Au(111)	132
A.4.1	First Order Kinetics	132
A.4.2	Derivation of the Fit Function for Work-Function Changes in Bichromatic Experiments	133
B	List of Acronyms and Abbreviations	136
C	List of Frequently Used Symbols	138
D	List of Publications	140
E	Scientific Contributions and Research Stays	141

1 Chapter 1

1 Introduction

Organic materials open new perspectives in device fabrication in diverse fields of application, since they offer a number of advantages in comparison to their inorganic counterparts. Just some examples: Organic materials have a much higher mechanical flexibility and lower weight than inorganic materials, they are chemically inactive and have lower manufacturing costs. One of the fast developing fields during the last years is the design of modern display technologies based on organic light emitting diodes (OLED). OLEDs are an advancement of LEDs, which became commercially available in the 1960's. The inorganic semiconducting materials used in LEDs are here replaced by organic semiconductors. Flat panel displays, computer monitors or displays of portable devices as mobile phones, tablets or smart watches can be fabricated using OLEDs. In order to exploit the mechanical flexibility offered by organic materials, leading technology companies released a series of patents concerning bendable or foldable displays during the last years. Another fast developing field of application of organic semiconductors during the last decades was the invention of organic solar cells (OSC). Recent research focusses on strategies to improve the efficiency of both types of devices [1–4]. Two main fundamental processes in these technologies are the absorption (OSC) or the emission (OLED) of light. These processes go along with the creation and decay of excitons. Excitons are quasiparticle excitations, consisting of electron-hole pairs dressed by a Coulomb interaction. In the present work, a model system of an organic semiconductor/metal interface, namely α -sexithiophene (α -6T) on Au(111), is studied by two-photon photoemission to investigate the fundamental time scales of the exciton formation and decay processes. The investigation of exciton dynamics in organic semiconductors has been of great interest during the last years [5–9]. However, most studies were focussing on the conversion of singlet into triple excitons, called singlet fission, whereas the singlet exciton formation process is still under discussion. The present thesis addresses this topic and furthermore emphasizes the role of the film morphology on the electronic structure and exciton dynamics.

A second important class of organic materials on which the research focus was drawn within the last years are molecular switches [10–12]. Recently, the pathbreaking character of experiments using molecular switches to build molecular machines working like artificial muscles or nano-cars was underlined by awarding the Nobel Prize in chemistry to Jean-Pierre Sauvage, James Fraser Stoddart, and Bernard Feringa in 2016. The idea behind the use of such molecules in surface science is the modification of surface properties by external stimuli. Therefore, inorganic substrates are coated with organic switches to create a functionalized surface. The second sample system investigated in the present thesis, self-assembled azobenzene-functionalized

alkanethiolates on Au(111), is a model system for this category. Azobenzene is reversibly switchable by light between its *trans* and *cis* conformation. The two conformations have different static dipole moments, which allows for switching the polarity of the surface and hence its hydrophilicity [13]. Also the spatial extension of the molecule changes upon switching. This allows for varying the thickness of the molecular layer by light, an important property for the application in organic field effect transistors [14]. As already mentioned, the absorption of light, which is needed to switch azobenzene molecules optically, comes along with the creation of excitons. Light can only be absorbed, if it has the right polarization with respect to the orientation of the corresponding transition dipole moment (TDM). In well-ordered SAMs, the TDMs of all molecules, which correspond to a specific transition, are aligned. This leads to a coupling between them, which results in a delocalization of the excitation within the molecular layer. In the following, this coupling will be named excitonic coupling. The role of the excitonic coupling in the switching process is currently under discussion and will be investigated in the present work.

Before going into detail about the results obtained in the present thesis, an introduction into the basic terms and theoretical models of molecular excitons will be given in Chapter 2. Exciton based phenomena as excitonic coupling or exciton dynamics have been studied by means of two-photon-photoemission (2PPE) spectroscopy in the model systems of Au(111) surfaces functionalized with thin α -sexithiophene films or azobenzene-based self-assembled monolayers. In order to interpret the 2PPE data a basic knowledge about the morphology and the optical properties of the model systems is necessary, which was gained through photoelectron emission microscopy and differential reflectance spectroscopy. A short introduction into all three techniques is given in Chapter 3. Chapters 4 and 5 focus on the presentation and interpretation of the experimental results obtained for the two model systems. The final part of the thesis, Chapter 6, comprises a summary of the thesis and points to some open research questions, which could be addressed in future works.

2

Chapter 2

Excitons in Organic Layers

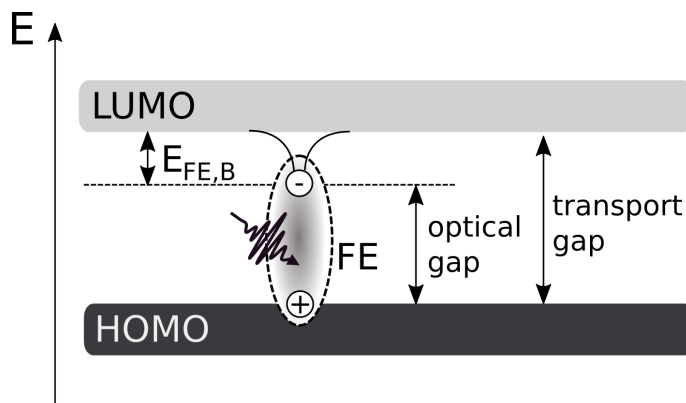
In the present chapter the most important concepts regarding exciton formation in thin organic layers are introduced. Starting from the description of excitons as interacting electron-hole pairs, their spatial extension - or delocalization - depending on the screening of the interaction by the surrounding matter will be discussed to tackle the difference between inorganic and organic semiconductors. Regarding organic semiconductors, different aspects of delocalization will be distinguished, considering a single molecule and a molecular aggregate. Fundamental aspects of intramolecular band formation due to the extension of the electronic wave function over the whole conjugated molecule and the intermolecular band formation due to an excitonic coupling between aggregated molecules will be discussed. In the case of excitonically coupled molecules, the initial excitation is delocalized, but after dephasing the excitation localizes on a single molecule. The coupling of the electronic exciton to nuclei coordinates will be discussed as an origin for dephasing. Considering the relaxation dynamics of the exciton population, hopping models as the exciton transfer between adjacent molecules via Förster transfer will be introduced in the second section of this chapter. Finally, in the last section, the two model systems chosen for experiments, thin α -sexithiophene films and azobenzene-functionalized alkanethiolate self-assembled monolayers on Au(111), are introduced, focussing mainly on the aspects of exciton formation and excitonic coupling.

2.1 Exciton: Definition and Flavors

The exciton theory is a basic concept in the context of optical properties of semiconducting and insulating materials. It essentially describes the difference between the electronic or "transport" gap and the optical gap of a material. The transport gap is the energy gap between material's valence and conduction bands. To measure this gap, ultraviolet photoelectron spectroscopy (UPS) and inverse photoelectron spectroscopy (IPES) can be used. In contrast, the optical gap is the energy a photon needs to be absorbed by the material. The optically excited electron and its hole form a Coulomb-coupled pair, which is called exciton. Due to the attractive Coulomb force between the two particles, the energy of the quasiparticle is lower than the energy of the non-coupled particles. This difference in energy is called exciton binding energy E_B . Figure 2.1 schematically illustrates the difference between the optical and the transport gap.

As pointed out by Kasha in the 60ies [16], the term exciton is very widely used. Hence, it is important to discriminate between different contexts. Since this work deals with organic

Fig. 2.1: Schematic illustration of the concept of transport and optical gaps. In order to combine the one- and two particle states in one picture the HOMO is fixed as the reference level (cf. Ref. [15]). The binding energy $E_{FE,B}$ of the Frenkel exciton (FE) is given as the difference between the transport gap and the optical gap.



materials, the theoretical introduction will not be focussed on the Wannier-Mott exciton limit [17], which is relevant for inorganic semiconductors, but on molecular excitons in the frame of Davydov theory of molecular crystals and aggregates (Frenkel excitons) [18]. The difference between these different flavors will be described in the next sections.

2.1.1 Frenkel Excitons

Excitons are grouped into different categories according to their spatial extensions. The so called Mott-Wannier exciton is an exciton in inorganic semiconductors. Such excitons are delocalized over a certain lattice area, which means that their electron-hole distances, i.e. exciton radii r , extend over several lattice sites ($r > a$). On the contrary, in a Frenkel exciton [19], both charges, electron and hole, are on the same molecule, which represents one lattice site in the molecular crystal ($r < a$). Between the two limits, a third exciton flavor, the charge transfer exciton, can be defined. In this case electron and hole are sitting on adjacent lattice sites ($r = a$). All three flavors are schematically depicted in Fig. 2.2.

Considering a single molecule, the electronic gap (or transport gap) is the energy difference between a singly-ionized molecule having one hole in the highest occupied molecular orbital (HOMO) and the singly negatively charged molecule, having an additional electron in the lowest unoccupied molecular orbital (LUMO). In contrast, the optical gap is the energy needed for an intramolecular excitation, where the electron is optically excited from the HOMO into a state where the electron and the hole it created in the HOMO are still interacting via Coulomb interaction (excitonic state). Note that excitons are created as well through excitations from lower occupied towards higher unoccupied states, since excitons are created whenever light is absorbed by a molecule in a molecular crystal.

From the point of view chosen so far to introduce the different exciton flavors, which focusses on the spatial distance between electron and hole, the Mott-Wannier exciton could be also defined as "delocalized" and the Frenkel exciton as "localized". However, the term "delocalized" is often used in literature in combination with Frenkel excitons. This will be clear when considering two further contexts.

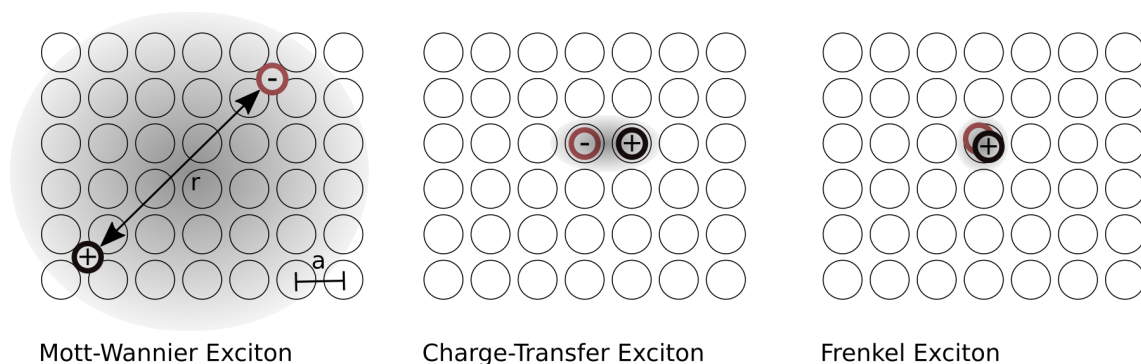


Fig. 2.2: Exciton flavors defined through their spatial distribution in the lattice. In the case of Mott-Wannier excitons, the electron-hole pair is delocalized over several lattice sites ($r > a$), whereas in Frenkel excitons both particles are localized at one lattice site ($r < a$). In the intermediate case of a charge-transfer exciton, electron and hole occupy adjacent lattice sites ($r = a$).

The first context considers the delocalization with respect to the dimensions of the molecule. Here, the degree of delocalization distinguishes between an exciton localized at a specific part of the molecule and an exciton spread over the entire molecule. The latter happens in so-called π -conjugated systems. A classical example is a benzene ring, where the p-orbitals of the six carbon atoms forming the ring overlap and build π -orbitals. In this way, the system has 6 π electrons occupying orbitals that spread over the whole ring and the remaining single bonds are bridged. In molecules consisting of chains of such rings, the conjugation extends over the whole molecule. When considering the limit of an infinitely long molecule, it becomes clear that, in analogy to an inorganic material, the HOMO and the LUMO can be considered as valence band and conduction band respectively. In the following, the term "organic semiconductor" will be used to describe π -conjugated systems. An exciton created in an organic semiconductor is delocalized over the whole molecule. Typical optical band gaps in organic semiconductors are in the order of a few eV [20]. Hence, light in the visible or ultraviolet range is needed to excite an exciton. The main technique used in this work is two-photon photoemission (2PPE), where a first laser pulse is employed to excite the exciton and a second pulse to probe the excited state. Details about the technique and the experimental set-up are given in Sec. 3.1.

The second context in which the Frenkel exciton can be considered as delocalized concerns excitonic coupling between the molecules sitting in the molecular crystal and forming an aggregate. In aggregates, an exciton band formation is observed. This means that it cannot be assessed which molecule hosts the Frenkel exciton created by an optical excitation of the aggregate. The excitation is delocalized over the aggregate. Aggregate formation will be explained in detail in Sec. 2.1.2.

Dielectric Model

As mentioned at the beginning of this section, the simplest way to understand an exciton is to consider it as an electron-hole pair coupled by a Coulomb interaction. This two-particle

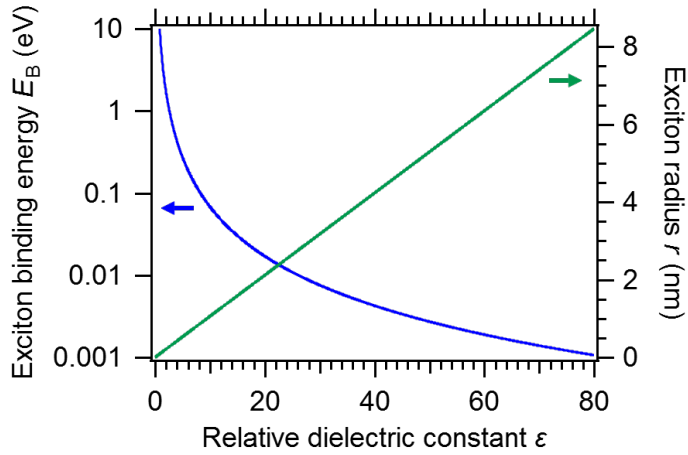


Fig. 2.3: Exciton radius and exciton binding energy as a function of the dielectric constant. Low dielectric constants, as in the case of organic semiconductors, lead to small exciton radii and high exciton binding energies.

system, dealing with a negative and a positive charge, can hence be considered in analogy to the hydrogen atom system, yet considering the relative dielectric constant ϵ of the medium in which the exciton is located. The corresponding Coulomb potential experienced by an electron at the distance r from the hole is hence given by

$$V_C = \frac{e^2}{4\pi\epsilon_0 \epsilon r}, \quad (2.1)$$

where e is the elementary charge and ϵ_0 is the dielectric constant of vacuum. Solving the Schrödinger equation for this system gives the exciton binding energy (exciton Rydberg energy) E_B and the exciton radius r_{ex} as a function of the Rydberg energy R_∞ and Bohr radius a_0 of the hydrogen atom:

$$E_B = \frac{\mu}{m_e} \frac{1}{\epsilon^2} R_\infty \quad (2.2)$$

and

$$r_{\text{ex}} = \frac{m_e}{\mu} \epsilon a_0, \quad (2.3)$$

with the reduced mass μ of the electron-hole pair and the mass of an electron m_e . Figure 2.3 shows the exciton binding energy and the exciton radius as a function of ϵ . Depending on the material, electrons and holes may have different masses; in this case it is assumed, that both electron and hole have electron mass. This graphic enables us to qualitatively understand at a glance the difference between an inorganic and an organic semiconductor. Inorganic materials have high dielectric constants. Therefore excitons formed in such materials have large radii and low binding energies. On the contrary, organic materials have low dielectric constants. Hence an exciton formed in an organic semiconductor is more localized and more energy is needed to separate the charges. Since the dielectric constant is a macroscopic quantity, the model is expected to fit better for the description of Mott-Wannier excitons in inorganic semiconductors. However, Knupfer *et al.* [21] showed that this model is still a good estimate for the exciton binding energies when considering molecules.

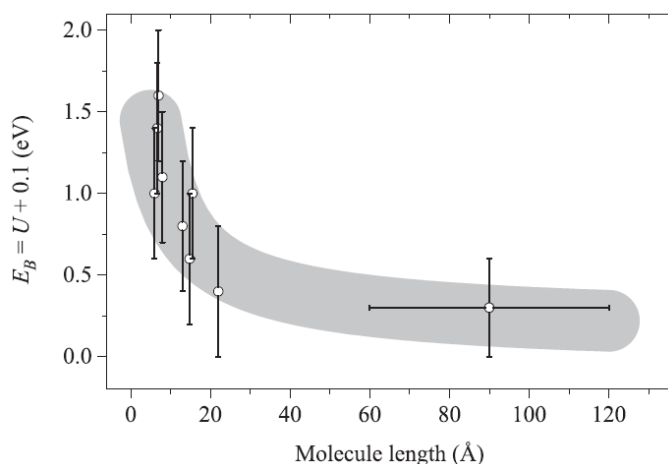


Fig. 2.4: [Figure taken from Ref. [21]] Exciton binding energy as a function of the molecule length. White circles represent experimental results. The gray shaded area shows the result of a simulation of the binding energy modeling the conjugated molecule as a prolate ellipsoid and assuming the Coulomb-potential being the dominant term in the binding energy.

The exciton binding energy in a molecular crystal is the difference between E_{ex} , i.e. the energy of a bound electron-hole pair (exciton) sitting on one molecular unit, and $E_{\text{e,h}}$, the energy of the same two charges when they are independent and uncorrelated and are located on two different lattice sites [21]:

$$E_{\text{B}} = E_{\text{e,h}} - E_{\text{ex}}. \quad (2.4)$$

The binding energy has to be overcome to separate the charges. As Knupfer showed in 2003, the Coulomb potential U is the dominant quantity entering the exciton binding energy in an organic semiconductor. Based on quantum-chemical calculations in the literature, he concluded that the binding energy can be approximated by $E_{\text{B}} \sim U + 0.1\text{eV}$. Knupfer proved this approximation by calculating the Coulomb potential U by modeling the conjugated molecules as prolate ellipsoids and comparing his results for E_{B} with experimental studies performed on oligomers and polymeres (cf. Fig. 2.4). The gray shaded area in Fig. 2.4 represents the results of his simulation for the binding energy as a function of the length of the molecule, while the markers give literature values from experiments. In the present work the organic semiconductor α -sexithiophene will be used, which has a total length of 21.9Å [22]. According to the simulations of Knupfer, the exciton binding energy of this molecule is expected to be in the range of 0.4 to 0.8 eV. Experimental studies hint that the actual value is at the lower end of this range [20, 23].

2.1.2 Aggregate Formation and Davydov Theory of Molecular Excitons

So far, the attention was focussed on the single molecule in which the exciton is created, neglecting that it is part of a molecular lattice. Organic molecules build molecular crystals due to van der Waals interactions. Crystal formation leads to a shift of the absorption bands D_{n} compared to the free molecule due to the change in the environment [24].

The theory of molecular excitons, developed by Davydov [25, 26], applies the concept of Frenkel excitons to molecular crystals or aggregates with more than one molecule per unit cell.

Excitons are closely related to optical transitions. An optical transition is characterized by the corresponding transition dipole moment \vec{p}_t . Its orientation indicates the polarization of the light needed to create an exciton, whereas the square of its absolute value $|\vec{p}_t|^2$ determines the probability that the light is absorbed.

When considering a molecule surrounded by other molecules, the dipole moments interact with each other, which influences the systems potential energy landscape. Hence, the geometrical arrangement of the transition dipole moments of the individual molecules in the molecular matrix must be accounted for.

Excitonic Coupling - Aggregate Formation

The coupling of the transition dipole moments of individual molecules is called excitonic coupling and can lead to an additional shift of the absorption bands. Depending on whether the energetic shift of the absorption line is to lower energies (or longer wavelength, hence red shifted) or higher energies (shorter wavelength, hence blue shifted), one distinguishes between J- and H-aggregates. The nomenclature "J-aggregate" stems from Jelley, who first discovered a red-shift of the absorption band due to dye-formation in solution in 1936 [27], whereas the term "H-aggregates" comes from the arising hypsochromic shift. In a J-aggregate, the transition dipole moments of the individual molecules are oriented in a head-to-tail way, whereas in H-aggregates they have a side-by-side alignment. Since the wavelength of the exciting light is much larger than the dimensions of the molecules, only the in-phase arrangements of the transition dipole moments result in an exciton state, which can be excited by an optical dipole transition [28]. This results in a lowering of the excitation energy in the case of J-aggregates and an increase for H-aggregates, as schematically visualized in Fig. 2.5. The left side of the figure shows energy diagrams for dimer formation with a parallel or head-to-tail arrangement of their transition dipoles. The rectangles represent the individual molecules and the arrows the orientation of the transition dipole moments. The excited state splits for the dimer in two bands, due to the in-phase and the out-of-phase combination of the dipoles. The dashed lines are used to point out that the out-of-phase alternative is forbidden for an optical transition.

The right side of the figure extends this concept to a linear molecular polymer, assuming that it consists of N identical molecular units. The excited state splits in N discrete excited states due to the dipole-dipole interaction of the transition dipole moments, but again only the in-phase arrangement is allowed, as indicated by the solid line and the transition arrow. In the case of the head-to-tail arrangement, the in-phase combination is again the lowest in energy. The exciton wave-function has here no excitation node. The higher the number of excitation nodes, the higher the energy of the excited state, as indicated by the vector diagrams below the energy-level diagrams. Exciton nodes are marked by vertical lines between transition dipole moments pointing in opposite directions. If equal amounts of dipole moments point to opposite directions, the absolute value of the total dipole moment becomes zero. Those states have no oscillator strength, which means that they are not excitable by light.

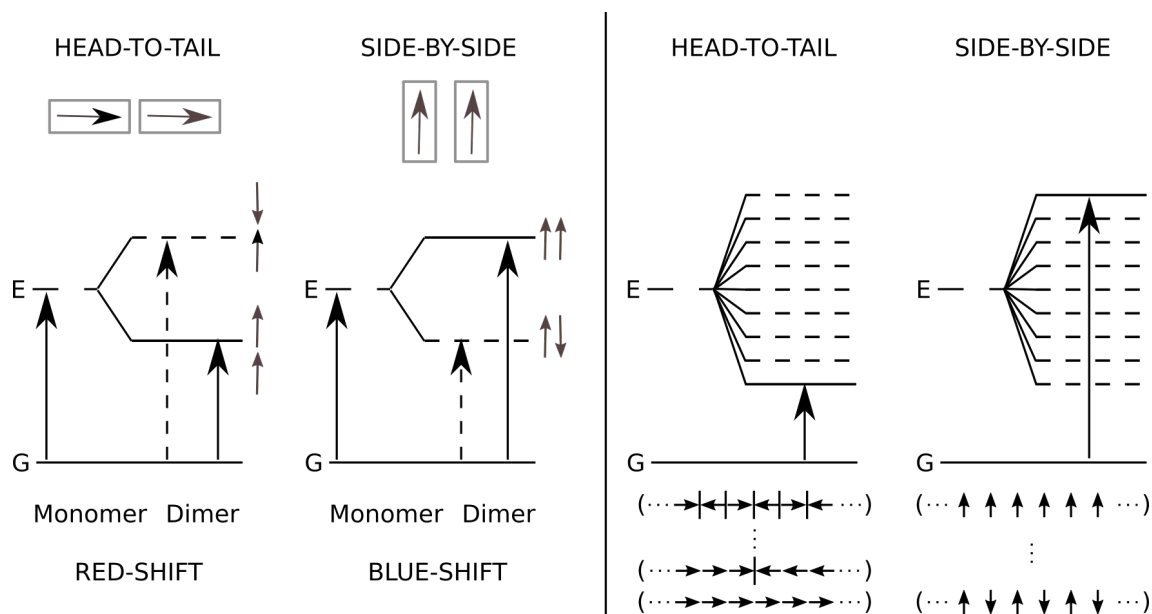


Fig. 2.5: [Figure adapted from Ref. [28, 29]] Energy-level diagrams for exciton band structure in molecular dimers (left) and linear molecular polymers (right) with head-to-tail and side-by-side arrangements of the transition dipole moments. The small arrows represent the orientation of the single molecule transition dipole moments. Energy levels drawn with solid lines correspond to in-phase oscillations of the interacting dipoles (exciton wave function has no nodes), whereas the exciton wave functions corresponding to the dashed lines do have nodes, since the interaction dipoles are oscillating out of phase. In the latter case the eigenstate has a non-vanishing wave vector k and therefore an excitation via an optical dipole transition is not possible. Large solid and dashed arrows mark allowed ($k = 0$) and forbidden ($k \neq 0$) transitions, respectively.

The side-by-side arrangement can be discussed in an analog way. The only difference is that here the in-phase arrangement of the dipole moments is the energetically highest and the highest number of nodes is reached in the lowest state.

The cases discussed above always assume only one molecule per unit cell. In the case of two or more molecules per unit cell, their dipole moments do not align. Figure 2.6 exemplarily shows the case of two molecules per unit cell, where both transition dipole moments are tilted by 45° . In this case the dipole moment of a molecule has to oscillate in phase with all molecules at the similar site in the unit cell to be optically excitable. In this way two states are getting oscillator strength, either with a total dipole moment parallel to the chain or perpendicular to it. The energetic difference between these states is called Davydov splitting. In general, there are as many allowed exciton transitions as molecules per unit cell.

Considering further the example of two molecules per unit cell in a 1D molecular chain, the change in the energy levels of the excited states E_n of a molecule in the molecular crystal in comparison to the states of a single molecule E_n^0 can be described as follows:

$$E_n = E_n^0 + D_n \pm U_n. \quad (2.5)$$

U_n is an energy shift due to an excitonic coupling.¹ The Davydov splitting is given by $2U_n$. In

¹Note that, when changing from 1D to 3D molecular arrangements, the energies of the lower and higher

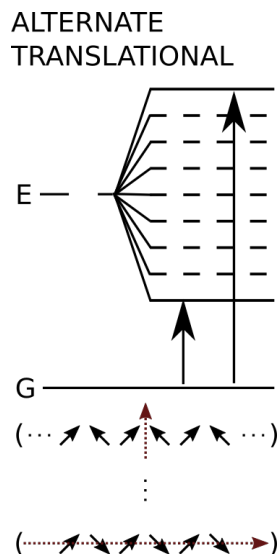


Fig. 2.6: [Figure adapted from Ref. [28, 29]] Exemplary excitonic coupling in the case of two molecules per unit cell whose transition dipole moments are canted by 45° from the vertical and are either mirrored on the vertical or on the horizontal plane with respect to each other. The dashed arrows mark the resulting total dipole moments of a 1D chain.

the simplest model, U_n is determined by the strength of the dipole-dipole interaction and thus proportional to \overline{p}_t^2/R^3 , where R is the distance between the molecules.

2.2 Dephasing and Exciton Decay Mechanisms

In the previous section excitonic coupling between molecules within a molecular crystal was discussed. In this case, the absorption of a photon leads to a coherent excitation of the excitonically coupled molecules. One key aspect of this thesis is the study of population and relaxation dynamics of excitons in organic layers by means of time-resolved two-photon photoemission. To populate the excitonic states dephasing is necessary. One mechanism leading to dephasing is the coupling of the electronically excited state to the nuclei coordinates.

Including vibrations, weak and strong coupling of the molecules due to dipole-dipole interactions can be distinguished in optical spectroscopy. When strong coupling occurs, the intramolecular electronic and vibrational wave functions of the molecule are separable, which is not the case for weak coupling [28, 30]. Hence, in case of weak coupling, the molecules are only little affected by their environment and can vibrate for many periods before the excitation energy is transferred to another molecule. The electronic states interact with the vibrational motion of the nuclei. A combined electronic and vibrational excitation is called vibronic excitation. On the contrary, in the strong coupling case the excitation is transferred faster from one molecule to another than the duration of a vibration period. Hence, the electronic states do not interact with the nuclei vibrations.

In weakly coupled systems, each vibronic sublevel shows a Davydov splitting. The magnitude of this energetic splitting scales quadratically with the transition dipole moment. In the case of vibronic transitions the vibrational overlap integral $S_{\nu\nu'}$ between the ground state and the

Davydov component do not have to be symmetric with respect to $E_n^0 + D_n$.

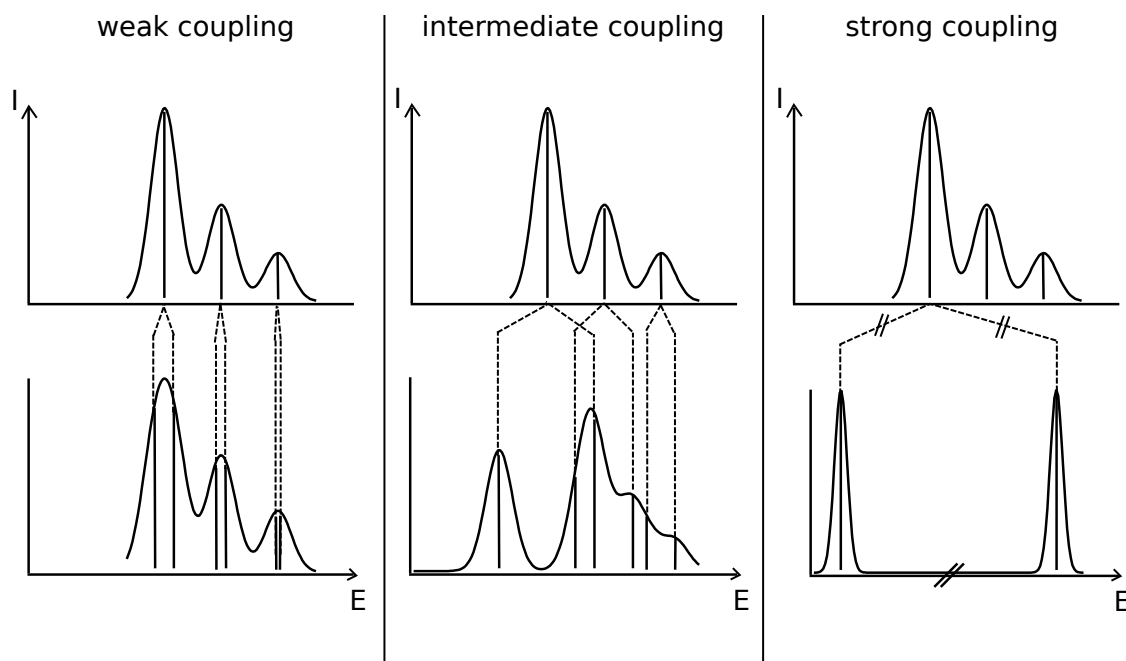


Fig. 2.7: Schematic illustration of the influence of the coupling strength in a molecular crystal with two molecules per unit cell (bottom row) on the spectral shape of an absorption band with respect to the monomer band (top row). In the case of weak coupling (left) the Davydov splitting of the vibronic levels is small, leading only to a small broadening of the peaks. For intermediate coupling (middle) the splitted states clearly separate, cross and overlap energetically with other sublevels. In the strong coupling case (right) no vibrational substructure is excited and only the Davydov splitted electronic level appears.

excited state enters the transition dipole moment leading to different energetic splittings for the vibrational sublevels. An indication for the coupling strength can be found in absorption and emission spectra of a molecular crystal. In order to illustrate the effect of excitonic coupling on the shape of absorbance spectra, Fig. 2.7 shows schematically the absorbance of a molecular crystal with two molecules per unit cell compared to the corresponding spectrum of a monomer. In the case of weak coupling, the rather small splitting of the vibronic sublevels leads only to a broadening of the peaks. If the coupling gets stronger, the splitting of each sub-level increases. Each level appears twice, the splittings cross and overlap, so that the spectral shape changes completely. If the coupling gets so strong that no vibrations are excited, only two sharp lines appear with a separation equal to $2U_n$.

Simpson and Petterson [30] defined criteria for strong and weak coupling depending on the exciton band width U and the total Franck-Condon band width $\Delta\epsilon$ of the considered molecular electronic transition. Strong coupling occurs in systems in which $\frac{2U}{\Delta\epsilon} \gg 1$ holds, whereas for the weak coupling case $\frac{2U}{\Delta\epsilon} \ll 1$ applies.

A third intermolecular exciton transfer category is the so called Förster vibrational-relaxation resonance transfer mechanism. In a Förster transfer, energy can be transferred radiationless from one molecule to another via a dipole/induced-dipole interaction, if the emission spectrum

of the excited molecule overlaps with the absorption spectrum of the acceptor molecule. In contrast to Simpson's concept, Förster considered the individual vibronic band width $\Delta\epsilon'$ in his model. According to Kasha [28], the following expressions for the excitation transfer rates k (number of exciton transfers per second) in the different coupling categories can be found:

$$\begin{array}{lll} \text{Strong-coupling} & \text{Weak-coupling} & \text{Förster transfer} \\ k \sim \left(\frac{f}{r^3}\Theta(\theta)\right), & k \sim \left(\frac{f}{r^3}\Theta(\theta)\right) \sum_{\nu,\nu'} g_{\nu}^* g_{\nu'} S_{\nu\nu'}^2, & k \sim \left(\frac{f}{r^3}\Theta(\theta)\right)^2 \frac{\sum_{\nu,\nu'} g_{\nu}^* g_{\nu'} S_{\nu\nu'}^4}{\Delta\epsilon'}. \end{array}$$

The parameters used in these expressions are the oscillator strength f of the electronic transition, the distance r between the interacting molecules and a geometric function $\Theta(\theta)$ including the angular dependence of the dipole-dipole interaction. Whereas in the strong-coupling case the oscillator strength is integrated over the whole electronic band, in the weak coupling case the overlap of the vibrational sub-levels is considered. Hence, the expression used for strong-coupling excitons is multiplied with the sum over the vibrational levels of the ground state ν and of the excited state ν' , the populations of the excited state $g_{\nu'}^*$ and the ground state g_{ν} and the vibronic overlap integrals $S_{\nu\nu'}$. At large distances the Förster transfer can dominate in comparison to the weak coupling case [28]. The expected orders of magnitude for the transfer rates in the different coupling categories are $k > 10^{12} \text{s}^{-1}$ for the strong coupling, $k \sim 10^{12} \text{s}^{-1}$ for the weak coupling and $k < 10^{11} \text{s}^{-1}$ for Förster transfer [28].

In an energy transfer process, the exciton moves through the sample. Hence, its energy is transferred from one lattice site to another. As depicted in Fig. 2.8, there are two different processes for energy transfer: migration and fusion. In a migration process, one exciton is transferred from one excited molecule to a previously non-excited one, whereas in a fusion process the exciton is transferred to another excited molecule, leading to a fusion of the two excitons and the creation of a higher excited state. Exciton fusion is hence strongly related to exciton annihilation.

Exciton transfer rates k are given by the spectral overlap of the emission from the excited

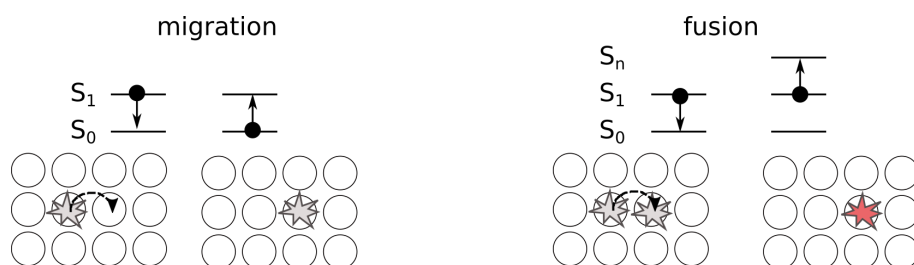


Fig. 2.8: Schematic illustration of exciton migration (left) and exciton fusion (right) processes in a molecular lattice. In a migration process the excitation is transferred to a molecule in the ground state, whereas in a fusion process to another excited molecule, leading to a decrease in the number of excited molecules.

state and the absorption in the ground state, or in the case of fusion, the absorption of the excited state. Exciton migration dynamics strongly depend on the coupling strength between the molecules. The stronger the interaction, the faster the energy transfer among the molecules. Hence, the strong coupling case applies to delocalized excitons, which means that there are collective excitations. Band shifts and band splittings are observed in this case, as discussed above. On the contrary, weak coupling applies to localized excitations. In this case, the energetic states of the coupled molecules are closer to those of the single molecule. In the case of thin molecular films, in the vicinity of the substrate, the exciton energy can also be transferred to the substrate creating an electron-hole pair there. In the case of a metal substrate like gold the interaction between electron and hole is screened on an attosecond timescale. Subsequently the independent charge carriers decay towards the Fermi level on a fs timescale.

Within the molecular film the amount of excited molecules can decrease via exciton annihilation. This may happen via either an intramolecular decay of the exciton or exciton-exciton annihilation in a fusion process. In the second case an exciton hops onto a molecular site with another exciton, which leads to the formation of a very short-lived higher-excited state. As a matter of fact, this process annihilates one exciton [31].

A third process which can reduce the Frenkel exciton density within the film are charge transfer processes. In a charge transfer process electron and hole separate from each other. The charge transfer exciton is a pre-stage, as both charges are still coupled to each other. Charge transfer excitons play an important role in molecular films or layers with different molecules, where one type serves as donor molecule and the other type as acceptor, or at organic/inorganic donor/acceptor interfaces [32, 33].

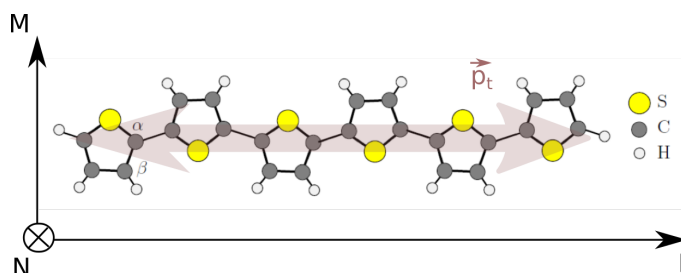
2.3 Exciton Formation in Two Model-Systems

The present section applies the theoretical concepts exposed above to the two model systems, which are experimentally investigated in this thesis. The model systems belong to two material classes which were extensively studied during the last decades in the context of device fabrication: organic semiconductors and molecular switches. Since in this work thin films are studied on Au(111) surfaces, a particular focus is drawn to the self-assembly on such surfaces.

2.3.1 The Organic Semiconductor α -Sexithiophene

Organic semiconductors play a crucial role in devices like organic solar cells or light-emitting diodes [34–39]. Oligothiophenes represent good model systems to study basic properties of this material class. In this work, α -sexithiophene (6T) is chosen to study exciton formation and relaxation dynamics. 6T consists of six thiophene units. One thiophene unit contains four carbon atoms and one sulfur atom, as depicted in Fig. 2.9. In α -sexithiophene, the connection of the rings is located at the α -carbons, which are the ones next to the sulfur atom. In single

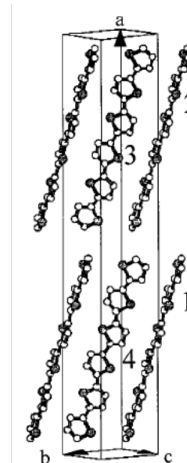
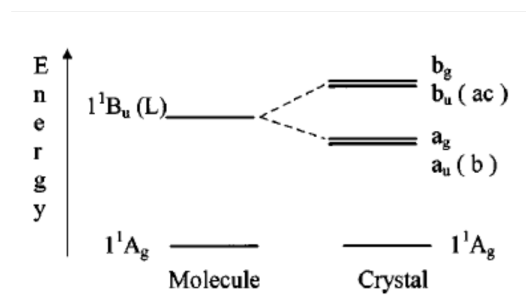
Fig. 2.9: 2D projection of a ball-and-stick model of an α -sexithiophene molecule including the orientation of the transition dipole moment p_t with respect to the molecular axes L, M and N. The three different atoms (Carbon, Sulfur and Hydrogen) are shown with circles of different size and color, as shown in the legend at the right.



crystals, 6T has a quasi-planar all-*trans* configuration [40], meaning that adjacent thiophene units have opposite orientation in M direction (short molecular axis, cf. Fig. 2.9). In this configuration, the molecular point group of 6T is C_{2h} and hence its electronic levels transform according to the irreducible representation of this point group [41]. The Frenkel exciton, which will be discussed in Ch. 4, is the lowest singlet (S_1) excited state in a 6T molecule. The corresponding transition dipole moment \vec{p}_t is oriented parallel to the long molecular axis L [41–43], as depicted in Fig. 2.9. The irreducible representation of the lowest singlet excited level is 1B_u . In the crystalline phase the 6T molecules form a monoclinic unit cell of the space group $P2_1/n$ [40]. Figure 2.10 shows at the right the four molecules per unit cell in their herringbone arrangement. The interaction of the transition dipole moments of the single molecules leads to a Davydov splitting in four different states a_g , a_u and b_g , b_u [44, 45], as indicated in the energy-level diagram in Fig. 2.10, but only a_u and b_u are accessible by one-photon spectroscopy [44]. Muccini *et al.* [44] report that the a_u component is found to be negligibly weak and completely polarized along the b crystal axis (cf. Fig. 2.10). In contrast the b_u is polarized in the ac crystal plane.

Absorption and emission studies on 6T single crystals and thin films showed that the 1B_u transition couples to vibrational modes, especially the ring-breathing mode with ≈ 180 meV [42,

Fig. 2.10: [Figures taken from Ref. [44]] Energy-level diagram regarding the ground state (1^1A_g) and the first excited state of a single 6T molecule and in a 6T crystal with the unit cell shown at the left. The quasi-planar 6T molecules arrange in a herringbone structure with four molecules per unit cell (labeled with numbers 1 to 4). This leads to a Davydov splitting of the first excited state (1^1B_u) into four states, namely $b_{g/u}$ and $a_{g/u}$. Whereas in a single molecule the S_1 transition dipole moment points along the L axis of the molecule, in a crystal the transition dipole moments are oriented along the b axis and in the ac plane of the crystal.



45–48]. Hence, a series of vibronic replica of the a_u and b_u states is observed. The magnitude of the Davydov splitting has been under debate for many years. The values are ranging from 0.2 eV [49] to 1.1 eV [47, 50].

Aggregation in Thin Films on Au(111)

When 6T attaches to surfaces, it does not directly grow in its crystalline growth mode, since its growth is strongly influenced by the bonding to the surface. In this work, thin 6T films grown on Au(111) are studied. As scanning tunneling microscopy (STM) measurements showed, the first monolayer of 6T absorbs with the long molecular axis (L-axis) parallel to the surface [51]. This is shown in Fig. 2.11a. The molecules arrange in a side-by-side fashion, which hints towards H-aggregation. To figure out how strong the interaction between the molecules is, one has to compare the absorption spectrum of the thin film with that of the single molecule. Since the 6T molecule is very flexible, it has to be embedded into a molecular matrix to measure the absorption spectrum of a planar 6T molecule. This was done by Horowitz *et al.*. They investigated 6T embedded in a polyethylene matrix by means of photoluminescence. The absorbance (excitation) and emission spectrum are shown in Fig. 2.11b. The spectra show the 180 meV vibrational progression which was already mentioned before. The lowest vibrational level is detected at 2.5 eV in the absorption spectrum. Absorption and emission spectra overlap, which would allow for Förster transfer between single 6T molecules.

In the master thesis of Malte Wansleben [52], we showed that the S_1 absorption band of a one monolayer thick film of 6T on Au(111) has its maximum around 2.4 eV (cf. Fig. 2.12). This is slightly red-shifted with respect to the single molecule spectrum observed by Horowitz *et al.*, which could stem from the change of the environment when the 6T molecule is part of a 6T molecular crystal in comparison to the single 6T molecule studied in a polyethylene

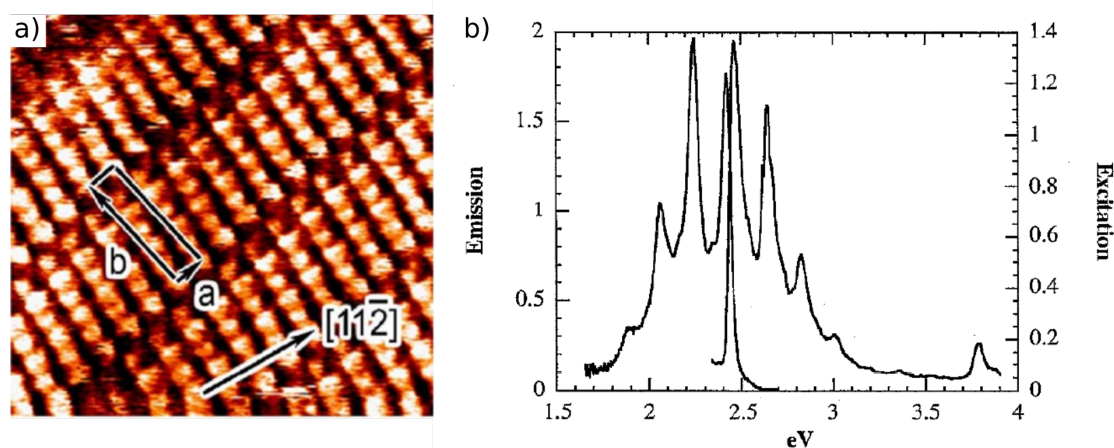


Fig. 2.11: **(a)** [Figure taken from Ref. [51]] Room temperature monolayer arrangement of 6T molecules on Au(111) studied by scanning tunneling microscopy with submolecular resolution ($10 \times 10 \text{ nm}^2$, -0.18 V , 0.6 nA). The structure can be described by an oblique unit cell with a single molecule basis. **(b)** [Figure taken from Ref. [50]] 6T molecules embedded in a polyethylene matrix. The left curve shows the photoluminescence emission spectrum for excitation at 450 nm and the right curve the photoluminescence excitation spectrum for emission at 550 nm . The measurements are performed at 10 K .

matrix. A further difference between the absorbance of a 6T molecule in the monolayer film on Au(111) and the single molecule is the absence of the vibrational substructure in the case of the monolayer. This can be explained by a strong coupling of the molecules to the substrate which quenches vibrations of the molecules.

A common strategy to measure the absorption bands on isolated molecule is to measure the molecule in solution. However, this is not possible in the case of 6T since the molecule does not keep its planar geometry in solution, but the individual thiophene rings within the molecule twist against each other, which shortens the conjugation length [53, 54].

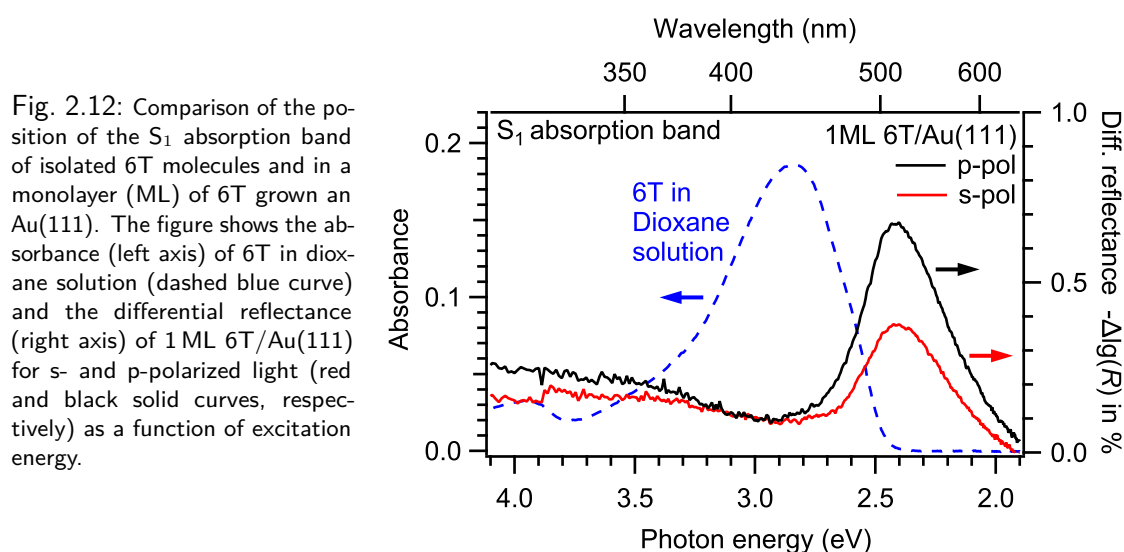
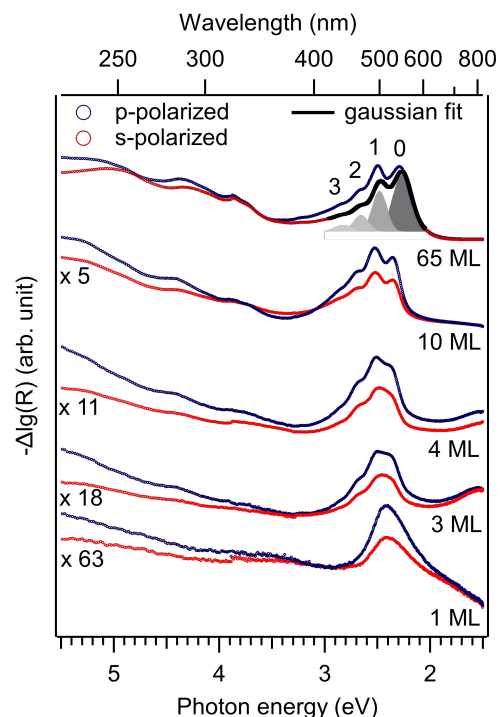


Fig. 2.12: Comparison of the position of the S_1 absorption band of isolated 6T molecules and in a monolayer (ML) of 6T grown on Au(111). The figure shows the absorbance (left axis) of 6T in dioxane solution (dashed blue curve) and the differential reflectance (right axis) of 1 ML 6T/Au(111) for s- and p-polarized light (red and black solid curves, respectively) as a function of excitation energy.

Fig. 2.13: [Figure adapted from Ref. [52]] Coverage dependent negative differential reflectance ($-\Delta\lg(R)$) of s- and p-polarized light (red and blue curves respectively) of thin 6T films on Au(111) as a function of the photon energy of the exciting light. Since the $\Delta\lg(R)$ only contains the reflectance of the molecular film (the reflectance of the gold substrate is subtracted), for reasons of comparability the signal obtained for film thicknesses of a few monolayers is multiplied with the factors written at the left side of the graphs. The S_1 absorption band of 6T/Au(111) is observed around 2.5 eV. Whereas 1 ML coverage shows a structureless broad band, 3 ML thick films already show a substructure, that evolves with increasing coverage and can be clearly seen in 65 ML films as a vibrational progression with 180 meV splitting (vibrational levels are numbered with 0 to 3). The band-bottom shifts slightly to lower energies with increasing coverage. The polarization contrast is low, confirming an orientation of the molecules parallel to the surface plane.



The optical gap of the non-coupled non-planar molecule was studied in dioxane solution as previously done by other groups [42, 53]. The dashed blue curve in Fig. 2.12 shows the absorbance measured for 6T in the dioxane solution. The S_1 absorption band is centered at ≈ 2.9 eV, which is significantly blue-shifted with respect to the single 6T molecule measured in a polyethylene matrix.

To estimate the absorbance of a thin 6T film grown on non-transparent substrates such as Au(111), the reflectance of the film is studied. Since the change in reflectance due to the adsorption of thin films is small, Fig. 2.12 shows the difference signal to a clean Au(111) surface. Here and in the following the y-axis gives the negative differential reflectance (DR) signal, which in first order approximation mimics the absorbance of a thin film. The response of the monolayer (ML) 6T on Au(111) to s- and p-polarized light agrees with the flat-lying arrangement of the molecules determined by STM.

Coverage dependent differential reflectance spectroscopy (DRS) shows that the absorption band remains energetically stable even for higher coverages, but a vibrational substructure appears in the band (cf. Fig. 2.13). 10 ML films already show a vibrational substructure in the S_1 absorption band, which strongly reminds of 6T single crystal studies. As the exemplary fit for a 65 ML film shows, the spectrum can be described by four equidistant gaussians with decreasing intensity. The separation of the individual gaussians is 180 meV, which can be assigned to the ring-breathing mode. The same behavior was observed in reflectance difference spectroscopy at 6T films grown on Cu(110)-(2 \times 1)O [49]. The authors claimed that 6T crystallites form on top of a two monolayer wetting layer. Such a growth mode was observed by the group of Thorsten Wagner in Linz through photoelectron emission microscopy (PEEM) measurements

on 6T films grown on Ag(110) [55, 56]. In a collaboration with Thorsten Wagner the growth of 6T on Au(111) was studied in real time by means of PEEM. As discussed in Ch. 4, we observed the formation of a two monolayer thick wetting layer in the case of 6T/Au(111) as well, but there are significant differences in the size of the crystallites formed on top of this layer in comparison to the silver surface. A detailed study of the development of the optical properties by monitoring the DRS signal during the growth process is reported in Ch. 4.

2.3.2 Excitonic Coupling in Azobenzene-Based Alkanethiolate Self-Assembled Monolayers

The second model-system is a gold surface functionalized with the molecular switch azobenzene. As in the case of the sexitiophene films described above, azobenzene-functionalized alkanethiolate SAMs tend to form H-aggregates considering the transition dipole moments of the S_2 transition [57–59]. The main question regarding these studies was, whether the excitonic coupling between the molecules opens an additional channel which allows for switching. Therefore, I will first shortly introduce azobenzene and its switching mechanism as well as the terms and concepts relevant for optically induced switching.

The Conformational Switch Azobenzene

The conformational switch azobenzene was discovered by Mitscherlich in 1834 [60]. It consists of two phenyl rings that are connected via a dinitrogen bridge, as it is shown in Fig. 2.14. In the ground state azobenzene is found in the *trans* configuration, where the two phenyl rings are on opposite sides with respect to the nitrogen double bond. The *cis* form of azobenzene (cf. Fig. 2.14), where the phenyl rings are on the same side with respect to the dinitrogen bridge, was discovered by G. S. Hartley hundred years later during a solubility study [61]. The *cis* state is metastable, which results in thermal back-switching to the *trans* state. Azobenzene is photochromic. Under exposure to UV-light it changes from the *trans* to the *cis* state. Blue light illumination accelerates the back-switching process with respect to the thermal back-isomerization.

In the present work a derivate of azobenzene was used, where the chromophore is attached via an oxygen atom to an alkyl chain with a length of eleven carbon atoms, as shown at the bottom of Fig. 2.14. In the following this derivate is called Az11. The black curve in Fig. 2.15 shows the absorbance of Az11 dissolved in methanol in the pristine pure *trans* case. The relevant intramolecular transitions in the context of this work are the S_1 and S_2 transition. The signature of the S_1 transition ($n\pi^*$ -transition, where an electron is excited from the HOMO) is rather weak in the pristine case. For a pure *trans*-azobenzene this transition is forbidden due to the inversion symmetry of the molecule. This symmetry is broken in the case of Az11.

The dominant transition is the S_2 transition, which is a $\pi\pi^*$ -transition, where an electron is excited from the HOMO-1 to the LUMO. The absorbance of the molecule changes drastically,

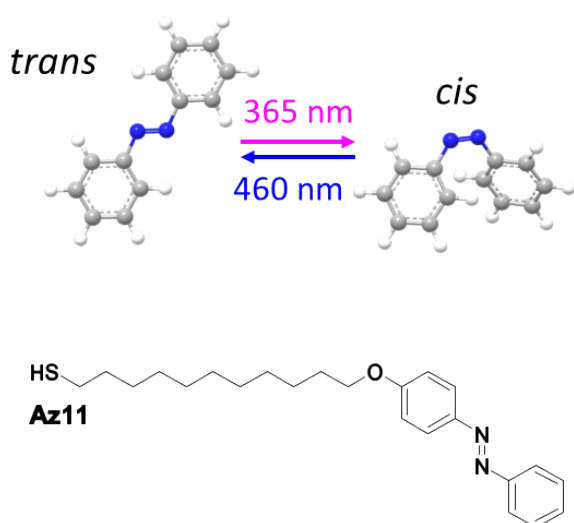


Fig. 2.14: **Top:** Ball-and-stick models of an azobenzene molecule in its *trans* and *cis* configuration. Gray balls symbolize carbon, white ones hydrogen and blue ones nitrogen atoms. The switching between the two isomers can be triggered optically. UV light of e.g. 365 nm (S_2 transition) mainly induces *trans-cis*-isomerization, whereas blue light of e.g. 460 nm (S_1 transition) mainly triggers the back-isomerization to the *trans* ground state. **Bottom:** Structural formula of the azobenzene derivate Az11, 11-(4-(phenyldiazenyl)phenoxy)undecane-1-thiol, which is used in this work.

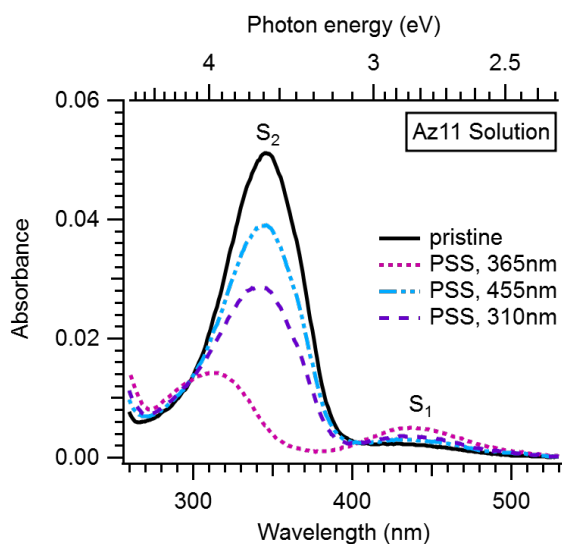


Fig. 2.15: Absorbance of Az11 in $\approx 1.8 \cdot 10^{-6}$ M methanolic solution in the pristine case and in the photostationary state (PSS) under illumination with light at a wavelength of 310 nm, 365 nm and 455 nm.

when it is switched to its *cis* form. To measure the absorbance of the *cis* isomer, the solution is illuminated with 365 nm light during the measurement (cf. dotted magenta line in Fig. 2.15, Ref. [57, 62]). 365 nm light excites in the lower energetic part of the S_2 -band and thereby mainly triggers *trans-cis* isomerization. The S_2 absorption band of the *cis* isomer is shifted to higher energies (lower wavelengths) with respect to the *trans* form and the maximal absorbance is reduced to one third. In contrast, the S_1 band is more intense. Hence, light in this energy range is mainly absorbed by *cis* molecules and therefore triggers mainly the *cis-trans* back-switching. The blue dashed double-dotted curve in Fig. 2.15 shows exemplarily the spectrum for illumination with 455 nm. The spectral shape is closer to the pristine case than to the *cis* spectrum. However, the pure *trans* sample cannot be reproduced under illumination. The reason for the non-complete back-switching can be found in the fact that both isomers absorb photons of this wavelengths. The optically induced switching process can be described with rate equations. Assuming that the total amount of present molecules N can be divided into

2.3. EXCITON FORMATION IN TWO MODEL-SYSTEMS

two reservoirs, containing respectively a certain number N_t of *trans* molecules and N_c of *cis* molecules, we can define switching rates r_{tc} and r_{ct} for *trans-cis*- and *cis-trans*-isomerization. The change in the amount of *cis* molecules per time unit under illumination is hence the number of *trans* molecules switching into the *cis* form minus those switching back from *cis* to *trans* :

$$\dot{N}_c = r_{tc}N_t - r_{ct}N_c = r_{tc}N - (r_{tc} + r_{ct})N_c. \quad (2.6)$$

After a certain illumination time, the average number of *cis* molecules in the ensemble does not change any longer, even though single molecules keep on switching back and forth. The so called photostationary state (PSS) is reached and \dot{N}_c becomes zero:

$$\dot{N}_c \stackrel{\text{PSS}}{=} 0. \quad (2.7)$$

Hence, the *cis* fraction χ_c of molecules in a PSS depends only on the rates for the two isomerization directions:

$$\chi_c = \frac{N_c}{N} = \frac{r_{tc}}{r_{tc} + r_{ct}}. \quad (2.8)$$

Note that, when calculating χ_c , it has to be considered that $r_{ct} = r_{ct}^{\text{opt}} + r_{ct}^{\text{therm}}$ is not only optically induced, but includes a thermal back-switching rate as well.

The optical rates depend on the photon flux j and the isomerization cross-section σ_{isom} of the illuminating light ($r_{ct} = j \cdot \sigma_{\text{isom,ct}}$). The isomerization cross-section is related to the probability of inducing switching. The higher the isomerization cross-section, the higher the switching probability. The isomerization cross-section depends on the absorption cross-section σ_{abs} , which is a measure of the fraction of incident photons that is absorbed, and on the isomerization quantum yield ϕ_{isom} , which is the probability that an absorbed photon triggers the isomerization ($\sigma_{\text{isom}} = \sigma_{\text{abs}} \cdot \Phi_{\text{isom}}$). To understand the difference between the absorption and the isomerization cross-section, it is necessary to have a look at the potential energy landscape for the isomerization process. As calculated by Conti *et al.* [63], the dominant pathway in the isomerization of azobenzene is the torsion around the NN double bond. Figure 2.16 shows a simplified diagram of the potential energy surfaces of the ground state S_0 and the first excited state S_1 for the torsion angle ξ as reaction coordinate according to the calculations done by Conti. A *trans* molecule excited with UV light from the ground state to the second excited state moves to the S_1 potential energy surface, from where it can relax back to the S_0 potential energy surface. If it completes the torsion or rotates back into the *trans* form is statistically described by the isomerization quantum yields. A similar process can happen to a *cis* molecule that is excited to the first or second excited states.

Excitonic Coupling in Alkanethiolate-Based Self-Assembled Monolayers

For surface functionalization with the molecular switch azobenzene, it is necessary to lift the NN double bond from the surface to preserve its switching ability. One well-established

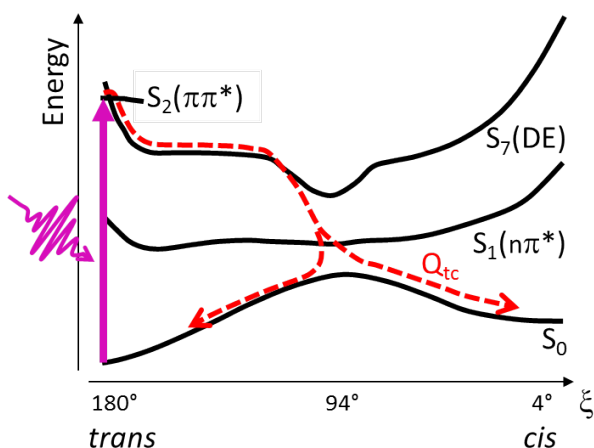


Fig. 2.16: Simplified diagram of the potential energy surfaces of azobenzene along the torsion coordinate ξ representing the CNNC angle, discussed by Conti *et al.* [63]. The global minimum of the S_0 ground state is reached for the *trans* configuration. After exciting a *trans* molecule from the ground state to the S_2 potential energy surface with UV light, the relaxation path to the ground state (red dashed curve) goes through the S_7 and the S_1 potential energy surfaces. If the CNNC angle reaches 94° , the excited molecule could either twist back and reach the S_0 ground state at the *trans* side of the potential barrier or twist further to the *cis* side. The probability for the latter is given by the isomerization quantum yield Q_{tc} .

method to do this is to use an azobenzene derivate like Az11, which was described before. The end of the chain without chromophore is then linked via a sulfur atom to the gold surface. The attachment to the surface reduces the orientational degrees of freedom of the molecules. The average orientation of the chromophores in a close-packed Az6 SAM was determined by near-edge x-ray absorption fine structure (NEXAFS) measurements [64] and yielded a tilt of the chromophore C1-C4 axis of $\vartheta = 30^\circ$ from the surface normal. Calculations by McNellis [64] showed that the transition dipole moment (TDM) of the S_2 transition is rather parallel to the molecular axis (axis connecting the centers of the two benzene rings, cf. Fig. 2.17). The TDM of neighboring molecules will hence couple in a side-by-side fashion and form an H-aggregate, which can be proven by DRS measurements. The uppermost solid black curve in Fig. 2.18

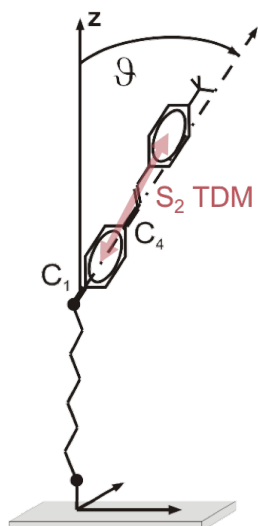


Fig. 2.17: Orientation of the azobenzene chromophore in an Az6 close-packed SAM. The tilt angle of the $C_1 - C_4$ axis of the lower phenyl ring from the surface normal was determined by NEXAFS [64] to be $\vartheta \approx 30^\circ$ in a closed packed SAM. The S_2 transition dipole moment (TDM) was calculated to be oriented parallel to the connection line between the centers of the two benzene rings.

shows the DRS signal of a pristine close-packed Az11 SAM on a 300 nm thick Au(111) film on a mica substrate. We focus on photon energies in the interval between 3 and 4.5 eV, where the S_2 band is located. The S_2 band is split in two parts, one remaining in the same region as the S_2 band for non-coupled Az11 molecules in solution and a second, more intense part,

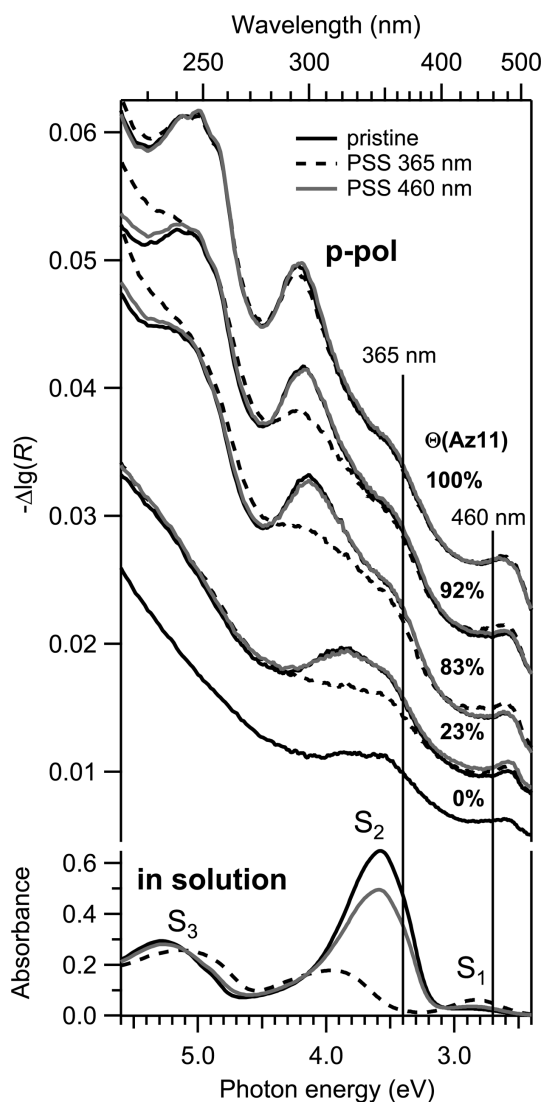


Fig. 2.18: [Figure taken from Ref. [57]] Negative differential reflectance data observed for p-polarized light illuminating mixed Az11 and C12 SAMs/Au(111) with different Az11 concentrations $\Theta(\text{Az11})$ (given at the right side above the corresponding curves) in comparison to single molecule absorbance in solution as a function of the photon energy (bottom). Samples containing Az11 are measured in the pristine case (solid black curves) as well as under 365 and 460 nm illumination (dashed black and solid gray curves respectively). The given photon energy range covers the range of the S_1 to S_3 absorption bands of the azobenzene monomer in methanol solution. In the pristine (*trans*) case the S_2 band shows highest absorbance. In solution the PSS reached under 365 nm illumination can be considered as the all-*cis* case ($\chi_c = 97 \pm 3\%$). Here the S_2 band is shifted to higher energies and has lower absorbance. The amplitude of the S_2 band at 380 nm can be seen as a measure for the fractions of *trans* molecules. The DR signal shows a broadening and a shift of the maximum of the *trans* S_2 band with increasing Az11 density due to excitonic coupling between the molecules. For a pure 100% Az11-SAM, the DR signal under 365 nm illumination is close to the pristine case. A reduction of the Az11 coverage to 92% is already sufficient to allow for switching.

which is shifted to higher energies (excitonic S_2 band), as expected for H-aggregate formation. The energetic shift is about 0.5 eV. The dashed lines in Fig. 2.18 are the DRS results under 365 nm illumination. For the close-packed Az11 SAM there is almost no change with respect to the pristine all-*trans* case. The switching is prevented by steric hindrance [64–66]. To allow switching, the chromophore density has to be reduced. This is done by producing mixed SAMs of Az11 and C12 (1-Dodecanethiol) [57]. As shown in Fig. 2.18, already a small reduction in the packing density of Az11 to 92% is enough to induce significant differences between the pristine case and the case under 365 nm illumination. When reducing the Az11 coverage besides the steric hindrance, the excitonic coupling is reduced as well, which results in smaller shifts of the excitonic S_2 band with respect to the monomer band known from solution. In addition, due to the lower packing density, the average tilt angle of the C1-C4 axis with respect to the surface normal increases to 45° in the case of 15% Az11 coverage [57], while the tilt of the C11 linker chain remains 30° .

3 Chapter 3

Experimental Methods

In order to gain the necessary insight in the systems under study, a combination of different techniques was used in this thesis. The main part of the experiments was performed using time-resolved two-photon-photoemission spectroscopy (tr-2PPE), described in Sec. 3.1. In order to apply this pump-probe technique, it is necessary to know which photon energies are needed. As described before, the photon energies needed to drive specific optical transitions can be determined by absorption or, in the case of a thin film grown on an intransparent substrate, by differential-reflectance spectroscopy (DRS), outlined in Sec. 3.2. To gain information about the multilayer film structure and growth mode of multilayer films, photoelectron emission microscopy (PEEM) was performed, illustrated in Sec. 3.3. This allows us to assign the electronic structure measured with 2PPE to different phases in the multilayer growth. The experiments performed with the two latter methods were done in collaboration with Thorsten Wagner at the Johannes-Kepler university in Linz (Austria).

3.1 Time-Resolved Two-Photon Photoemission Spectroscopy

Time-resolved two-photon photoemission is a pump-probe technique based on the photoelectric effect. Here, two photons are needed to induce photoemission. The first photon, the pump photon, excites the object of investigation from its ground state into an excited state. The second photon, the probe photon, leads to emission of an electron. To study the population and relaxation dynamics of the excited state, the second photon is sent to the sample with a variable time delay with respect to the first one. This is realized by a laser system generating ultrashort laser pulses. To perform the time-resolved measurements, the pump and the probe photon have to originate from different pulses which are sent to the sample with a respective time delay. The present section contains an introduction to the methodology of photoemission (Sec. 3.1.1) and the experimental set-up needed to realize tr-2PPE measurements (Sec. 3.1.4).

3.1.1 Single-Photon and Two-Photon Photoemission

The principle of photoemission was first explained by A. Einstein [67]. He described the photoelectric effect, where a photon absorbed by a sample induces the emission of an electron, if the photon energy $h\nu$ is higher than the work function $\Phi = E_{\text{vac}} - E_{\text{F}}$ of the sample, which is determined by the difference in energy of the vacuum level E_{vac} and the Fermi level E_{F} .

of the sample. To use this effect for the analysis of the band structure of solid surfaces, a monochromatic beam of photons is sent to a sample to create photoelectrons. The kinetic energy of the photoelectrons E_{kin} allows to determine the binding energy E_b of the state from where the electron is emitted through the relation

$$E_{\text{kin}} = h\nu - \Phi - E_b. \quad (3.1)$$

Here, the binding energy E_b is referred to the Fermi level ($E_b = E_F - E$).¹ If the photon energy is higher than the work function, excitation by a single photon is sufficient to induce photoemission, as shown in the left energy diagram in Fig. 3.1. In this case the process is called *direct* or *single-photon* photoemission.

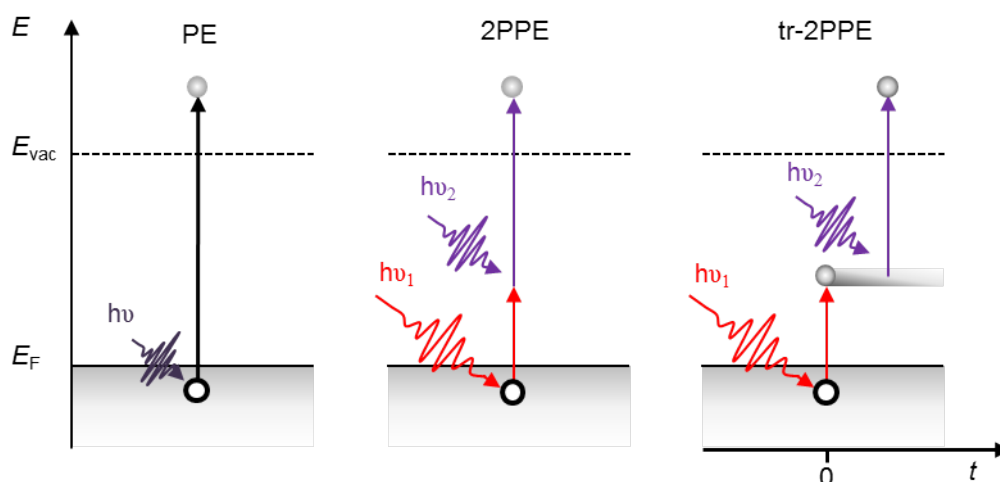


Fig. 3.1: Schematic illustration of the principle of single-photon photoemission (PE, left), 2PPE (middle) and tr-2PPE (right). In single-photon photoemission an incident photon has enough energy $h\nu$ to lift an excited electron above the vacuum level of the sample, whereas in 2PPE excitation of the same electron with two photons is necessary to induce photoemission. The relaxation dynamics of an excited state created by the absorption of the first photon can be studied by introducing a time delay between the first and the second photon in tr-2PPE.

In contrast to single-photon photoemission (PE), in two-photon photoemission (2PPE) the energy of the photons sent to the sample is not high enough to induce direct photoemission. As shown in the middle part of Fig. 3.1, a second photon transferring its energy to the electron excited with the first one is needed to induce photoemission. 2PPE can be performed by simultaneous illumination with photons of different color (bichromatic 2PPE) or with both photons having the same energy (monochromatic 2PPE). Since the probability for a 2PPE process goes with the square of the probability of a single excitation process, the excitation density needed in a 2PPE measurement is much higher than in single photon photoemission. The necessary excitation densities can be obtained by ultrashort laser pulses, as described

¹It is also common in photoemission to define the binding energy as the energetic distance of a state to the vacuum level. The difference of values of the binding energies in the two definitions is given by the material's work function.

in Sec. 3.1.4. In contrast to single-photon PE, which enables to investigate only occupied states, 2PPE allows for studying the unoccupied band structure of the sample through resonant excitation from the occupied states into the unoccupied states, which are then probed by the second incoming photon. Introducing a delay between the two photons, the evolution of the population density of the unoccupied band structure after excitation can be studied, as schematically shown in the right part of Fig. 3.1. This technique is called time-resolved two-photon photoemission.

3.1.2 Analysis of Two-Photon-Photoemission Data

Figure 3.2 gives an example of a static 2PPE spectrum. The investigable spectral range is delimited by the sample work-function and the Fermi edge. The sample work-function defines the low-energy cut-off of the spectrum. The high energy cut-off, the Fermi edge, results from electrons excited from the Fermi level. It is hence given by the sum of the two photon energies. Between those two limits, spectral features appear, which may have three different

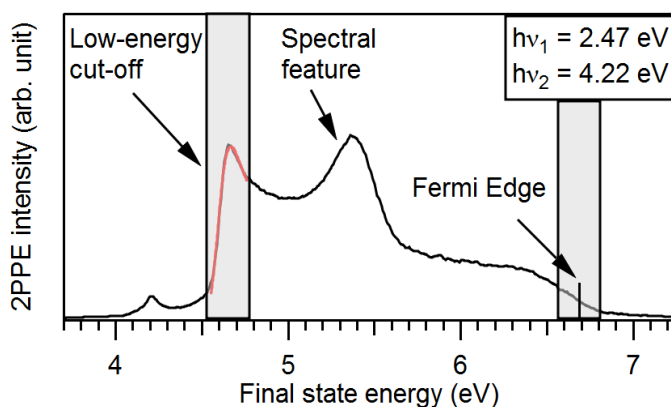


Fig. 3.2: Example spectrum of a static 2PPE measurement. The measured 2PPE intensity is plotted as a function of the final state energy of the detected electrons. The spectra show a low energy cut-off at a final state energy corresponding to the sample work-function. The high-energy cut-off is given by the Fermi level. Spectral features detected between these two cut-offs correspond to projections of unoccupied states below the vacuum level, the projection of occupied states with binding energies $E_b \leq -(h\nu_1 + h\nu_2 - \Phi)$, or to final states.

origins: they are projections of occupied energy levels (initial states) with binding energies up to $E_b = -(h(\nu_1 + \nu_2) - \Phi)$, projections of unoccupied energy levels (intermediate states) below the vacuum level, or final states that are resonantly excited in the two-photon process.

Low-Energy Cut-Off

The low energy cut-off in the 2PPE spectra is defined by the sample work-function.² To extract the value of the work function from the spectra, the low energy cut-off is mathematically

²Note that the kinetic energy of the emitted electrons is measured with respect to the vacuum level of the analyzer. If the work function of the sample is lower than the one of the analyzer, it is necessary to apply a bias voltage to the sample to lift the Fermi level of the sample by more than the work-function difference in order to detect the low energy cut-off.

described by a step function followed by an exponential decay representing the secondary electron background:

$$I(E) = \begin{cases} A \cdot e^{-\frac{\Phi-E}{d}} & \text{for } E \geq \Phi \\ 0 & \text{for } E < \Phi \end{cases}, \quad (3.2)$$

where A is the amplitude and d the decay constant of the secondary electron background. Secondary electrons are those electrons which lose energy due to inelastic scattering processes, as electron-phonon or electron-electron scattering, on their way to leave the sample. Actually, in an experiment, the cut-off is broadened due to the finite spectrometer resolution. Therefore, in the fit function the step function is convolved with a gaussian:

$$I(E) = A' \cdot e^{\frac{1}{2}\left(\frac{\sigma}{d}\right)^2 + \frac{(\Phi-E)}{d}} \cdot \text{erfc}\left(\frac{\sigma}{\sqrt{2} \cdot d} + \frac{(\Phi-E)}{\sqrt{2} \cdot \sigma}\right), \quad (3.3)$$

where σ is the width of the cut-off and hence the energy resolution of the electron detection system.

Assignment of Spectral Features

As mentioned before, a spectral feature observed in a 2PPE experiment may result from an initial, an intermediate or a final state of the sample. To understand this, we first concentrate on a monochromatic 2PPE experiment, where pump and probe photon come from the same laser beam. Figure 3.3a schematically shows the principle of two-photon photoemission from a defined initial state E_i . The pump photon excites an electron from the occupied initial state into a virtual intermediate state. This state has no lifetime. Hence, the second photon needs to probe this state instantaneously after the pumping step. This process is similar to single photon photoemission with a photon of twice the energy used in the 2PPE process. The kinetic energy of the emitted electron will hence be

$$E_f = E_i + 2 \cdot h\nu. \quad (3.4)$$

Performing the same experiment with another photon energy $E_2 = h\nu_2$, which is e.g. higher as the first one E_1 , will result in a final state energy two times the difference of the two photon energies higher than in the first experiment.

Considering the emission of an electron from an intermediate state, the pump photon will excite an electron from the available occupied states into an unoccupied state and the second photon will emit the electron from this state. As long as the photon energy of the incident light is large enough to populate the intermediate state, a final state at the energy:

$$E_f = E_{\text{int}} + h\nu \quad (3.5)$$

is reached. Since the energy of the unoccupied, intermediate state is fixed, only the photon

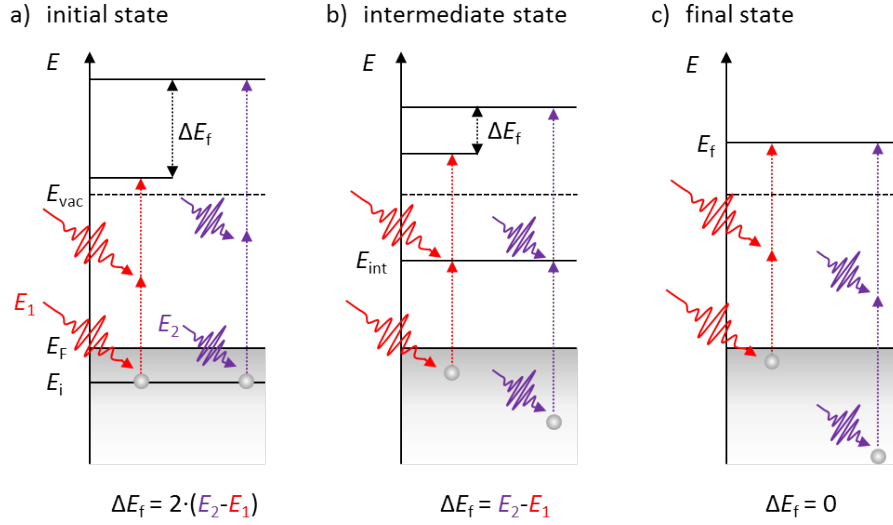


Fig. 3.3: States detectable by 2PPE at the example of monochromatic 2PPE. (a) Initial state: An electron is excited from an occupied state into a virtual intermediate state, from where it is directly emitted by the second photon. When changing the photon energy to E_2 , the final state energy of the electron E_f changes with two times the difference in photon energy with respect to the previous photon energy E_1 , i.e., $\Delta E_f = 2 \cdot (E_2 - E_1)$. (b) Intermediate state: An electron is excited into an unoccupied energy level of the sample. In this case, the change in the final state energy of the emitted electron is equal to the difference in photon energy with respect to the previous photon energy E_1 , i.e., $\Delta E_f = E_2 - E_1$. (c) In the case of a final state, the energetic position of the corresponding peak in the spectrum will not change when changing the photon energy, i.e., $\Delta E_f = 0$.

energy of the probe photon changes the final state energy at which the electron will be detected. Final states appear at the same energy independent of the photon energy of the incident light, as shown in Fig. 3.3c.

Analyzing Population and Relaxation Dynamics

Considering a three-level system consisting of an occupied state, which is the initial state $|i\rangle$ of the excitation process, an unoccupied intermediate state $|n\rangle$, where the electron can be excited to and from where it is excited to a final state $|f\rangle$ of the photoemission process with a second photon, the electrical fields of the pulses will lead to a coherent overlap of these eigenstates. In the wave function formalism, the resulting state is given by a linear combination of the eigenstates:

$$|\psi\rangle = \sum_k A_k(t) |k\rangle, \quad (3.6)$$

with $k \in \{i, n, f\}$ and population amplitudes $A_k(t)$. The laser induced coupling between eigenstates of the system is called polarization of the transition between the involved states. The population of the intermediate state is only reached due to quasi-elastic scattering processes, which induce dephasing and hence lift the coherence with the incoming light. A common approach to describe the population dynamics in time-resolved 2PPE data is to use the optical Bloch equations, given by a set of differential equations based on the density matrix formalism

[68–71]. The matrix elements $\rho_{kl} = \langle k | \rho | l \rangle$ of the density operator ρ

$$\rho = \sum_j p_j |\psi_j\rangle \langle \psi_j| \quad (3.7)$$

give the probability p_j of the system to be in the state $|\psi_j\rangle$. The diagonal elements of the density matrix ρ_{kk} thereby give the population probability of a state k , whereas the off-diagonal elements $\rho_{kl} = \rho_{kl}^*$ ($\hat{\rho}$ is self-adjoint) describe the polarization of the transition between $|k\rangle$ and $|l\rangle$. The temporal evolution of the density operator in the context of the three-level system can be described by the Liouville-von Neumann equation [69, 70]:

$$\dot{\rho}_{kl} = \frac{1}{i\hbar} [\hat{H}_0 + \hat{V}, \hat{\rho}]_{kl} - \Gamma_{kl} \rho_{kl} \quad (3.8)$$

including the Hamiltonian of the unperturbed three-level system \hat{H}_0 , the interaction with the electric field of the pulses \hat{V} , the density operator $\hat{\rho}$ and the damping matrix elements Γ_{kl} . The damping matrix in this formalism includes spontaneous decay rates of the population of the involved states Γ_k , which define the lifetimes $\tau_k = \hbar/\Gamma_k$ of these states, as well as pure dephasing rates Γ_{kl}^* due to quasi-elastic scattering processes that do not influence the population. The damping matrix is phenomenologically introduced and is restricted to an exponential behavior of the decay and dephasing processes.

Assuming that the pump pulse with an envelope of its electric field $\mathcal{E}_1(t)$ mediates only transitions from the initial state to the intermediate state and the probe pulse $\mathcal{E}_2(t')$ from the intermediate state to the final state, one can define \hat{V} as:

$$\hat{V} = |i\rangle p_1 \langle n| + |n\rangle p_2 \langle f| \quad (3.9)$$

with

$$p_1 := \mathcal{E}_1(t) \langle i | \mu_{in} | n \rangle \quad \text{and} \quad p_2 := \mathcal{E}_2(t - T_d) \langle n | \mu_{nf} | f \rangle,$$

neglecting higher order corrections. The coupling strength between the two states is described by the dipole operator μ and the time delay of the second pulse with respect to the first one is T_d .

Applying the rotating wave approximation, considering finite detunings $\Delta_1 = \hbar\omega_1 - (E_n - E_i)$ and $\Delta_2 = \hbar\omega_2 - (E_f - E_n)$ of the pulse energies with respect to the energy levels E_k involved in the optical transitions (i.e. off-resonant excitations) and using $\rho_{in}^{(1)} := e^{i\omega_1 t} \rho_{in}$, $\rho_{nf}^{(2)} := e^{i\omega_2 t} \rho_{nf}$ and $\rho_{if}^{(3)} := e^{i(\omega_1 + \omega_2)t} \rho_{if}$, one finally obtains the optical Bloch equations [70]:

$$\begin{aligned} \dot{\rho}_{ii} &= +\frac{1}{\hbar} \text{Im} \left(p_1^* \rho_{in}^{(1)} \right) \\ \dot{\rho}_{nn} &= -\frac{1}{\hbar} \text{Im} \left(p_1^* \rho_{in}^{(1)} \right) + \frac{1}{\hbar} \text{Im} \left(p_2^* \rho_{nf}^{(2)} \right) - \Gamma_{nn} \rho_{nn} \\ \dot{\rho}_{ff} &= -\frac{1}{\hbar} \text{Im} \left(p_2^* \rho_{nf}^{(2)} \right) \end{aligned} \quad (3.10)$$

$$\begin{aligned}
 \dot{\rho}_{in}^{(1)} &= -\frac{i}{\hbar}\Delta_1\rho_{in}^{(1)} - \frac{i}{2\hbar}p_2^*\rho_{if}^{(3)} + \frac{i}{2\hbar}p_1(\rho_{nn} - \rho_{ii}) - \Gamma_{in}\rho_{in}^{(1)} \\
 \dot{\rho}_{nf}^{(2)} &= -\frac{i}{\hbar}\Delta_2\rho_{nf}^{(2)} + \frac{i}{2\hbar}p_1^*\rho_{if}^{(3)} + \frac{i}{2\hbar}p_2(\rho_{ff} - \rho_{nn}) - \Gamma_{nf}\rho_{nf}^{(2)} \\
 \dot{\rho}_{if}^{(3)} &= -\frac{i}{\hbar}(\Delta_1 + \Delta_2)\rho_{if}^{(3)} + \frac{i}{2\hbar}p_1\rho_{nf}^{(2)} - \frac{i}{2\hbar}p_2\rho_{in}^{(1)} - \Gamma_{if}\rho_{if}^{(3)}.
 \end{aligned}$$

The optical Bloch equations allow for simulating energy and time-resolved 2PPE data.

In the case of non-resonant excitations or dephasing times much smaller than the pulse duration, a simplification of the optical Bloch equations to a rate equation system allows for deriving a simple equation to describe the 2PPE intensity I_{2PPE} as a function of pump-probe delay [72]:

$$I_{2PPE}(\tau) \propto \int_{-\infty}^{\infty} I_{XC}(t-t')\Theta(t')e^{-\Gamma(t')}dt', \quad (3.11)$$

where I_{XC} is given by the intensity cross-correlation of the two laser pulses, $\Theta(t')$ is a Heaviside step function and Γ is the decay rate. This model is limited by the cross-correlation of the two laser pulses. Processes which are faster than the pulse width of the laser pulses can be identified by a shift of the maximum of the 2PPE intensity with respect to t_0 [68].

In the present work, the cross-correlation of the two laser pulses was determined by evaluating the Shockley surface state (SSS) of a clean Au(111) surface [73] at the beginning and at the end of each measuring day. Figure 3.4a shows an exemplary time-resolved 2PPE measurement on a clean Au(111) surface. In the shown case, photon energies of $h\nu_1=2.47$ eV and $h\nu_2=4.26$ eV were used, which results in a projection of the occupied surface state in the final state range of 6.25 eV to 6.45 eV. The transient of the 2PPE intensity as a function of pump-probe delay integrated over this energy range is plotted using orange markers in Fig. 3.4b. The single pulses have a gaussian pulse shape, which leads to a gaussian profile of the convolution of both intensities with a full width at half maximum (FWHM) $\text{FWHM}_{XC} = \sqrt{(\text{FWHM}_{\mathcal{E}_1})^2 + (\text{FWHM}_{\mathcal{E}_2})^2}$. A gaussian fit to the data is shown by the black curve. The fit yields $\text{FWHM} = (86 \pm 1)$ fs in the case of this example measurement. In the experiments presented in this thesis different wavelength combinations were used, resulting in a variety of cross-correlations with FWHM down to 60 fs in the most compressed cases. With I_{XC} being a gaussian function, Eq. 3.11 has the same functional form as Eq. 3.3, which was introduced to fit the low energy cut-offs of the spectra.

When investigating the population decay of excitons in thin films of organic materials, it is often not possible to fit the data with a single exponential decay, but a multi-exponential decay behavior is observed [7, 74–76], due to diffusion processes and different decay rates depending on the distance of the molecule hosting the exciton to the substrate, as it will be discussed in Sec. 4.3.

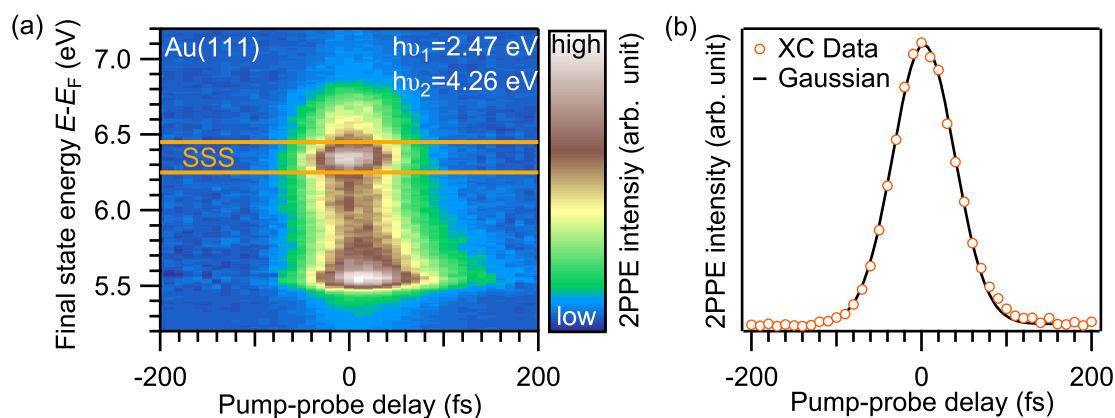


Fig. 3.4: (a) Correlated 2PPE signal of a Au(111) single crystal surface measured with photon energies $h\nu_1=2.47$ eV and $h\nu_2=4.26$ eV as a function of final state energy $E - E_F$ and pump probe delay. In the final state range of 6.25 to 6.45 eV, the final state projection of the Shockley surface state (SSS) is detected. (b) Integrated 2PPE intensity in the range of the Shockley surface state (6.25 eV to 6.45 eV) as a function of pump-probe delay to determine the cross correlation of the two laser pulses.

3.1.3 Two-Photon Photoemission of Molecular Thin Films

As described before, in 2PPE experiments photon energies in the range of a few eV are transferred into kinetic energies of valence electrons of the investigated sample. The information depth is limited by the inelastic mean free path (IMFP) of the electrons. The IMFP of the electrons depends strongly on their kinetic energy [77]. In the case of kinetic energies up to 5 eV, which are relevant in this work, electrons from at least a few layers below the vacuum interface are expected to escape from the sample. Theoretical studies of the IMFP of organic materials suggest values in the same order of magnitude as for inorganic materials [78]. As long as the film thickness is in the order of the escape depth, electrons excited within the molecular film as well as in the underlying substrate can escape the sample. In this way it is possible to detect states corresponding to the electronic structure of the organic film and of the substrate simultaneously.

Furthermore, interactions between the substrate and the organic film have to be considered. Charge and energy transfer between both might serve as population or relaxation channels. Figure 3.5 shows possible population channels for unoccupied molecular orbitals (right) and excitonic states (left). Unoccupied molecular orbitals may be populated due to charge transfer from the substrate into the molecules. Here, the primary excitation takes place in the substrate and not in the molecules. Excitonic states within the organic film are excited through intramolecular (Frenkel exciton) or intermolecular excitations (Charge Transfer Excitons). Electrons are excited from the occupied molecular orbitals into the excitonic states.

Whereas a hole created in an occupied state or an electron populating a previously unoccupied state can be described as single-particle states, excitons have to be considered as two-particle states. Xiaoyang Zhu discussed the problems arising from referring both, single-particle and two-particle states, to a common energy scale [15]. Let us consider e.g. the ionization potential

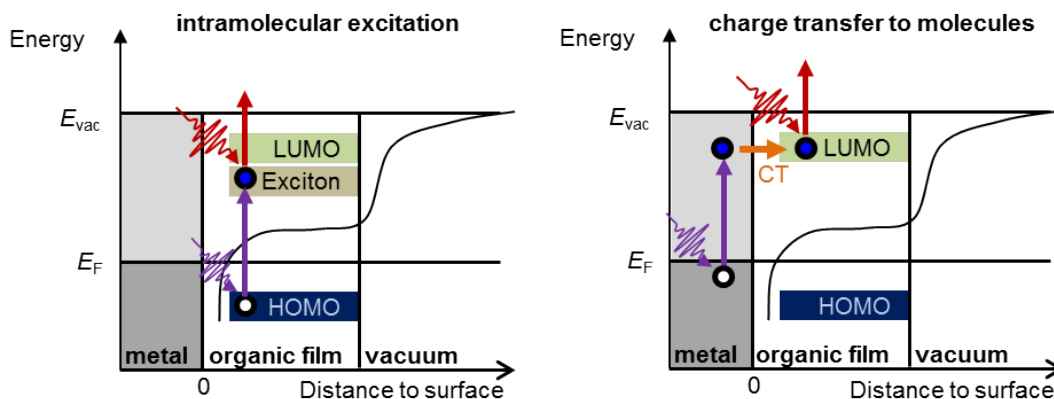


Fig. 3.5: Optical excitation channels of electronic states of an organic thin film on a metal substrate. The excitation of electrons within the substrate may lead to the population of unoccupied molecular states via charge transfer (right), whereas intramolecular excitations lead to exciton formation (left).

of a HOMO and the one of an exciton, created via an excitation from the HOMO level. The initial state for the excitation of an electron from the HOMO level is the ground state of a neutral molecule, whereas the final state is a hole in the HOMO and an electron at rest at the local vacuum level. In the case of an exciton, the initial state for the emission of the electron from the excitonic state is a hole in the HOMO. The common state of both cases is hence the final state with a hole in the HOMO and an electron at rest at the local vacuum level, whereas the initial states of the two excitations are different. The reference energy would hence be the ionization potential of the conventional HOMO level with respect to the local vacuum level. The problem in the application of this model is that in 2PPE not the local, but the global vacuum level is measured, which is not an appropriate reference energy for a common energy scale.

If not stated differently, the reference energy given in the 2PPE spectra shown in this work is the Fermi level of the Au substrate, even though this might not be the most proper reference for the excitonic states compared to the transport levels of the molecules.

3.1.4 Experimental Set-ups for Two-Photon Photoemission Spectroscopy

The experimental set-up for static and time-resolved 2PPE experiments combines a laser system for the generation of ultrashort light pulses with two ultra-high vacuum systems, which can be used alternately for the analysis of samples in a clean and stable environment. A schematic illustration of the complete set-up is shown in Fig. 3.6. A part by part description of the components of the laser set-up and the UHV systems is given in the following two paragraphs.

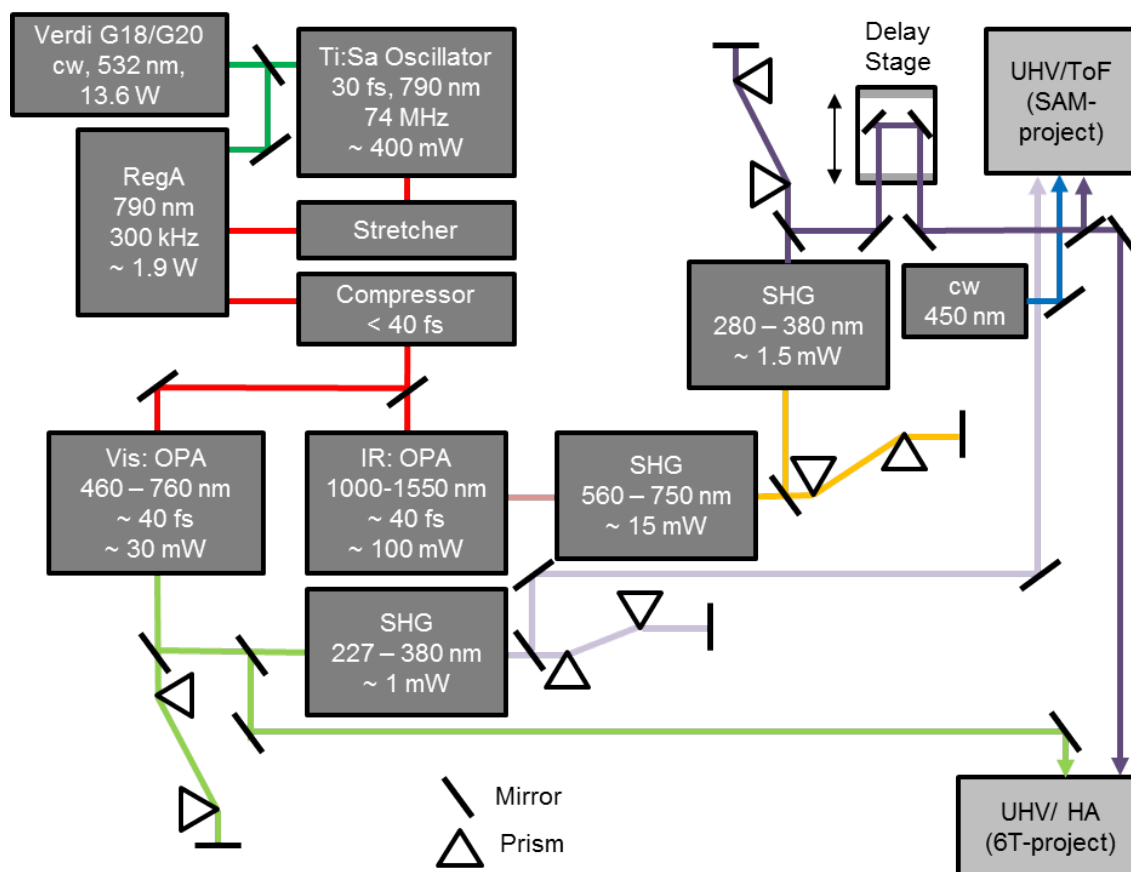


Fig. 3.6: Experimental set-up for the 2PPE experiments comprising an amplified Ti:Sapphire-laser system and two different UHV chambers which can be used alternatively. A homebuilt Ti:Sa oscillator is pumped with a continuous wave (cw) pump laser (Verdi G18/20) operating at 532 nm. Within the oscillator, fs light pulses of 790 nm are generated. For amplification, those pulses are stretched and sent into a regenerative amplifier (RegA). The amplified pulses are then recompressed and guided into optical parametrical amplifiers (OPAs). The OPAs allow for generation of photons in a broad wavelength range. To reach the UV range, second harmonic generation (SHG) with those pulses is necessary. To preserve the shortness of the pulses, prism compressors are added after each wavelength change. In tr-2PPE experiments, one of the two used laser beams has to pass a delay stage, as shown here through the UV beam in the upper part of the figure. The beam paths sketched here refer to those utilized in this thesis. In the experiments performed in the SAM-project, in addition to the fs-laser system, a cw laser working at 450 nm was sent to the investigated samples. Some parameters, concerning power, wavelength or compression are given to characterize the optical components. A more detailed description is given in the main text.

Amplified Ti:Sapphire-Laser System

An amplified Ti:Sapphire-laser system including optical parametrical amplification (OPA) and second harmonic generation (SHG) enables us to produce femtosecond laser pulses and vary their wavelength in the ranges from 230–760 nm and 1000–1550 nm. This allows for system specific wavelength selection for resonant and off-resonant excitation.

As shown in the scheme of the set-up in Fig. 3.6, an optically pumped semiconductor laser (Coherent, Verdi G18/G20) working at 532 ± 2 nm is used to pump a homebuilt oscillator set-up for pulse generation at 790 nm. The pump laser is thereby set to an output power of

13.6 W, of which 30% are used to pump the oscillator and 70% to pump the Ti:Sapphire crystal of a regenerative amplifier (Coherent, RegA 9050). The amplified pulses are then sent into OPAs and SHG units to be able to generate short pulses with a variety of different central wavelengths [79–81]. In the following, some details about the different steps of pulse generation and modification needed to create the desired output will be given without making claim of completeness. For a more general overview or details about ultra short laser pulses see Refs. [82, 83].

Pulse Generation: Pulse generation takes place in the oscillator part of the set-up. A short pulse can be described by a wave package, created by the interference of monochromatic waves in a given frequency range $\Delta\nu$. The initial pulse in the oscillator set-up is created via a short modification of the resonator lengths, by a fast movement of one of the end mirrors. In this way a time-dependent phase shift of the resonator modes is caused, leading to the formation of a wave package. To create a short and stable pulse, the frequency components contributing to the wave package need to have a well defined phase relationship, which is achieved by so called modelocking techniques. The oscillator set-up used here is a self-modelocked Ti:Sapphire laser. The first successful generation of laser pulses with a pulse duration of a few tenths of fs with this technique was accomplished by Spencer *et al.* [84].

Ti:Sapphire is a non-linear material with a linear dependence of its refractive index n on the intensity $I(t)$ of incident light [82] due to the optical Kerr effect: $n(\omega, I) = n_0(\omega) + n_2 \cdot I(t)$. Here, $n_0(\omega)$ is the material refractive index in the absence of light and n_2 the Kerr coefficient. The linear dispersion described by $n_0(\omega)$ leads to a spatial splitting of the contributing frequencies, whereas the non-linear contribution to the refractive index leads to a spectral broadening due to an intensity dependent frequency shift of the waves interfering in the pulse. To understand this effect a plane wave

$$E(t, x) = e^{i\phi} = E_0 e^{i(\omega_0 t - kx)} \quad (3.12)$$

with $k = \omega_0/c \cdot n(t)$ can be considered as a simple example [85]. Since the instantaneous frequency is the time derivative of the phase:

$$\omega(t) = \frac{\partial}{\partial t} \phi(t) = \omega_0 - \frac{\omega_0}{c} \frac{\partial n(t)}{\partial t} x, \quad (3.13)$$

the frequency variation is given by

$$\delta\omega(t) = \omega(t) - \omega_0 = -\frac{\omega_0 n_2}{c} \frac{\partial I(t)}{\partial t} x. \quad (3.14)$$

In the case of a positive value of n_2 , which applies for Ti:Sapphire, low frequencies are added in the leading edge of the pulse envelope and high frequencies at the tailing edge in every phase-modulation process. The temporal dispersion of the pulse is called chirp. Since the phase modulation is caused by the pulse itself when passing through the nonlinear material,

the process is called self-phase modulation.

Furthermore, due to the gaussian intensity distribution of a laser beam across its profile, significant changes in the refractive index of the Ti:Sapphire crystal are induced spatially across the crystal when the beam passes through. The modulation of the refractive index operates as a lens and hence leads to a self-focussing of the beam. The self-modelocking process described here is called Kerr lens modelocking.

To compensate the temporal chirp of the pulse due to the modulation process, the oscillator set-up contains specially coated mirrors to recompress the pulse in every round trip. The output pulses of the oscillator reach a pulse duration < 30 fs, but pulse energies of only a few nJ.

Regenerative Amplification: In order to drive optical parametric amplification for wavelength selection, pulse energies in the order of μJ are necessary. To reach such high pulse energies, the oscillator pulses are amplified through the technique of regenerative amplification [86]. The RegA set-up contains another Ti:Sapphire crystal, which is pumped by the Verdi 532 nm laser. To realize a high population inversion, the quality factor Q of the laser cavity is reduced by an acousto-optic modulator³. Every $\approx 3.33 \mu\text{s}$, Q is enhanced and simultaneously a pulse coming from the oscillator (seed pulse) is injected by a second acousto-optic modulator, called cavity dumper. The seed pulse is then amplified usually within 28 round trips in the cavity. The output pulses are generated with a repetition rate of 300 kHz and a pulse energy of $\approx 6 \mu\text{J}$. After each pulse ejection, Q is reduced again so that the population inversion within the Ti:Sapphire crystal can be regenerated.

As shown in Fig. 3.6, the oscillator pulse is first stretched, before it enters the RegA. Otherwise the amplification of the maximal intensity within the pulse would exceed the damage threshold of the Ti:Sapphire crystal. Consequently, the pulse has to be recompressed after amplification in the RegA. In the stretcher the pulse passes four times a grating compressor and a concave mirror. The grating compressor spatially disperses the different wavelengths within the pulse and the concave mirror recollimates the beam. When the pulse passes the stretcher it gets a positive chirp. Chirps induced in the stretcher and the RegA are later compensated in the compressor part.

Optical Parametric Amplification and Second Harmonic Generation:⁴ The compressed 790 nm beam is split and used to pump two optical parametric amplifiers, one with a visible output (Coherent, OPA 9450), called Vis-OPA, and one with an output wavelength in the infrared range (Coherent, OPA 9850), called IR-OPA. The output signal of the Vis-OPA is tunable in the range from 460 nm to 760 nm, whereas the IR-OPA can generate output pulses in the wavelength range from 1000 nm to 1550 nm. Some experiments shown in the present

³The working principle of an acousto-optic modulator is the generation of an optical grid by sound waves in a solid transparent material. In this way, incoming light is bent and frequency shifted [87].

⁴A more detailed description of the fundamental processes discussed here can be found in Refs. [83, 88, 89].

work are performed with both photon energies in the UV range. In this case, second harmonic generation (SHG) was performed once with the Vis-OPA output and twice with the output of the IR-OPA.

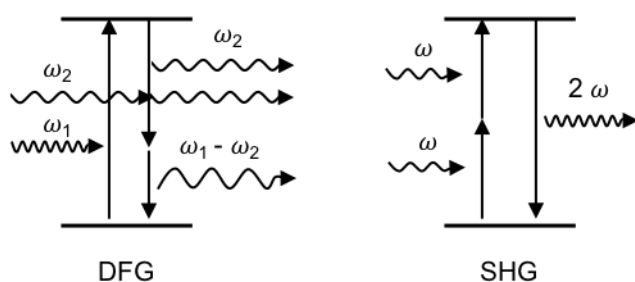


Fig. 3.7: Photon pictures of the nonlinear processes of difference-frequency generation (DFG, left) and second harmonic generation (SHG, right).

Optical parametric amplification is based on the physical concept of difference-frequency generation (DFG) in non-linear materials. Here, two beams with different frequencies overlap within the non-linear material. In the photon picture shown in Fig. 3.7, photons of the first beam with frequency ω_1 drive a virtual excitation and the photons from the second beam with frequency ω_2 induce stimulated emission, while additional photons with a frequency corresponding to the difference in frequency of the two incoming ones, $\omega_1 - \omega_2$, have to be emitted to fulfill energy conservation. The two beams needed to perform DFG are generated by splitting the 790 nm beam in two paths. In one of the paths the beam is focussed to a sapphire crystal. Sapphire is a non-linear material, hence a chirped pulse with a broad spectral range is created through the Kerr effect. Here, so many new frequencies are generated that a white light continuum is created. This chirped white light pulse is then focussed to another non-linear crystal, namely a barium boron oxide (BBO) crystal. Within the BBO crystal, the white light pulse overlaps with the other path of the original 790 nm beam to induce DFG. In the case of the IR-OPA, the 790 nm beam is used directly, whereas in the Vis-OPA frequency doubling is needed to reach the desired output frequencies. Frequency doubling, or SHG, takes place in a BBO-crystal as well. In the photon picture, two photons with frequency ω add up their energies to drive a virtual excitation, which results in the spontaneous emission of a photon with the frequency 2ω (cf. Fig. 3.7). To transfer energy from the fundamental wave into the second harmonic, their phase velocities have to match in the propagation direction. So called phase matching can be achieved by tilting the optical axis of the BBO-crystal with respect to the incoming light. The phase matching angle has to be adjusted for the specific wavelength of the incoming light. The wavelength of the amplified pulse is set by the delay between the chirped white light pulses and 790 nm pulses (or 395 nm pulses in the case of the Vis-OPA). To recompress the pulses after the wavelength tuning processes, prism compressors are installed after OPA and SHG units in the set-up.

Continuous Wave Laser: To perform the experiments described in Ch. 5, additionally to the pulsed laser beams, a continuous wave (cw) laser (Oxxius, 450 nm) was focussed onto the sample to induce photoswitching without inducing photoemission. The cw laser works at a

maximal output power of 70 mW.

Determination of Beam Parameters: In a photoemission experiment, the pulsed or continuous laser beams described above have to be focussed onto a sample placed in a UHV chamber. To this aim, a small bread board is attached to the chamber and decoupled from the laser table containing the optical set-up described so far.

Figure 3.8 shows the basic elements needed to focus the beam into the chamber and to characterize its properties. To characterize the beam entering the chamber, its power P , its central wavelength λ (and hence photon energy E_{ph}) and the area A the beam illuminates at the sample have to be measured to determine the photon flux density j :

$$j = \frac{P}{E_{\text{ph}}} \cdot \frac{1}{A}. \quad (3.15)$$

To calculate the photon density per pulse one has to divide j by the repetition rate of the laser system, which in the present case amounts to 300 kHz.

A movable power meter (Melles Griot 13PEM001) is used to detect the average power per second, which is usually in the range of few mW. It has to be taken into account that some percent of the detected power gets lost through the reflectance at the mirrors and the transmission through the entrance window of the chamber. As window material, UV fused silica has been chosen, because it allows transmission in a broad range of wavelengths, especially in the UV range. Knowing the energy of the incoming photons, the number of impinging photons per second can be calculated. When removing the power meter from the beam path, the beam can be directed to a spectrometer (Avantes, Avaspec 2048) to detect the central wavelength and the spectral width of the beam. Example measurements for an output beam of the Vis-OPA and the two times frequency doubled output of the IR-OPA are given in Fig. 3.8b and c, respectively. The measured central wavelength is converted to the corresponding photon energy via:

$$E_{\text{ph}} = h\nu = \frac{h \cdot c}{\lambda} \approx \frac{1240 \text{ eV} \cdot \text{nm}}{\lambda}. \quad (3.16)$$

The spectral width (FWHM of the spectral amplitude distribution) is inversely proportional to the pulse duration [90].

After measuring the spectrum, the mirror directing the beam towards the spectrometer is removed, so that the beam passes through a plane mirror and a focussing mirror through the entrance window of the chamber. If not stated differently, the incoming beam is p-polarized, i.e., its electric field is polarized parallel to the plane of incidence. To determine the sample area covered by the beam, a modified⁵ CCD camera (DMK 21AU04) is positioned at the same distance from the focussing mirror as the mirror has to the sample, but outside of the chamber.

⁵In order to allow for detection of light in the UV range, the protective glass in front of the CCD-chip is removed from the camera.

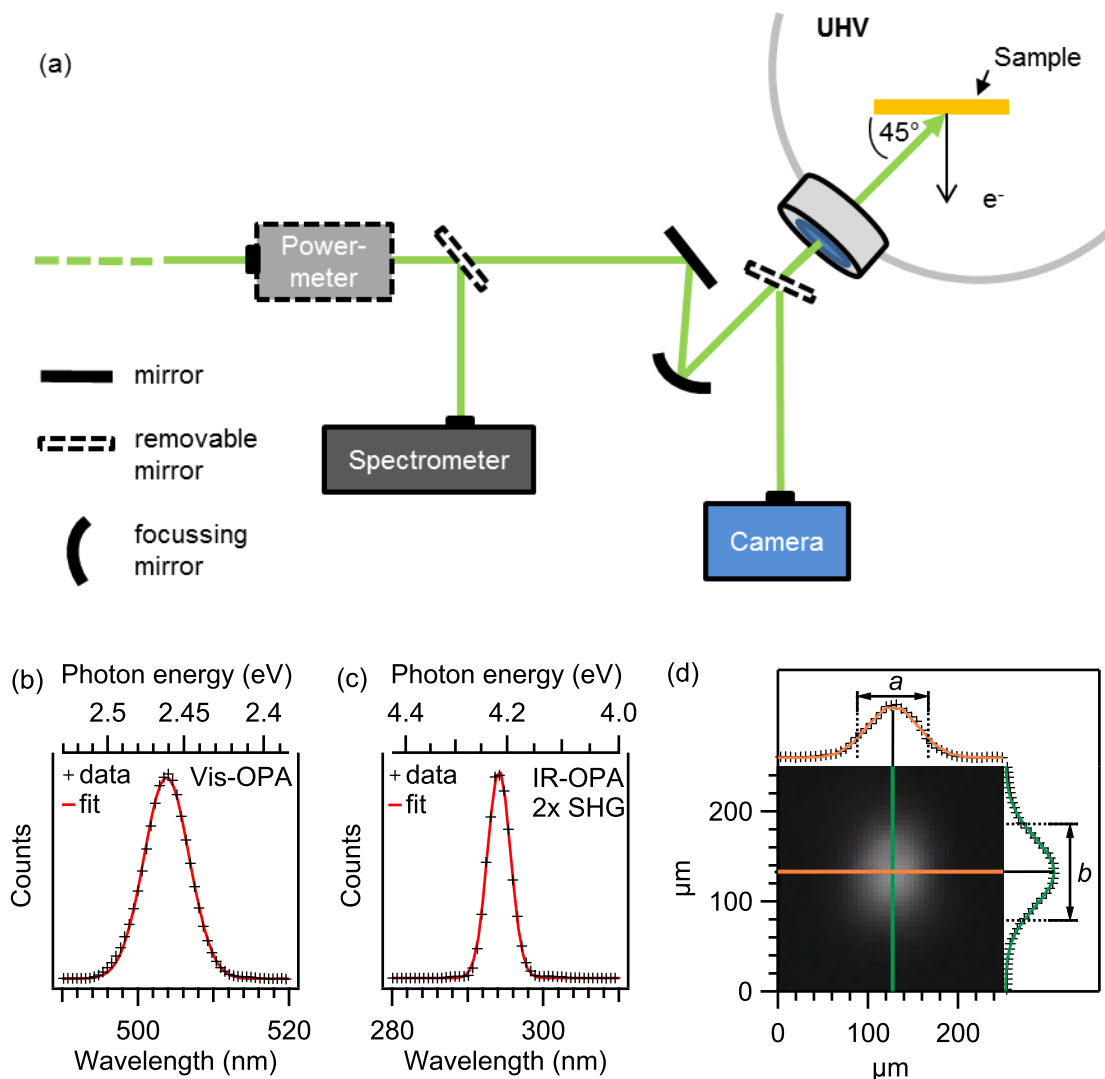


Fig. 3.8: (a) Sketch of the set-up used to characterize the pulsed laser beams and to focus them onto the sample placed in a UHV chamber. A movable power meter allows for measuring the average beam power. Adding a removable mirror into the beam path, the beam can be sent to a spectrometer to determine its spectral profile. The spatial profile is measured by a CCD camera placed at the same distance to a focussing mirror as the mirror has to the sample surface. To lead the beam to the camera, a removable mirror is placed just before the entrance window into the UHV chamber. When the beam is entering the chamber, it hits the sample surface under an angle of 45° . (b) Example spectrum of the output generated by the Vis-OPA. (c) Example spectrum of a UV pulse, generated by the IR-OPA followed by two SHG units. (d) Example of a spot profile measurement with the camera. Line profiles for a horizontal (top) and a vertical (right) cross-section through the center of the imaged beam are used to determine its widths a and b at $1/e$ of the maximal intensity in both dimensions. The intensity distributions can be described with single gaussian functions.

Therefore, another additional mirror must be put into the beam path, as shown in Fig. 3.8a. An example image taken by the camera is shown in Fig. 3.8d. Line profiles in horizontal and vertical direction through the center of the spot allow to fit the diameter of the 2D projection of the beam profile. Usually, the projection is not completely circular, but elliptic. Therefore, the horizontal and the vertical line profiles are fitted with gaussian curves and their width at $1/e$ of the intensity in the maximum are used as the semiaxis a and b of an elliptic area. Since the

beams are hitting the sample with an angle of 45° , the lateral dimension has to be multiplied by $(\cos 45^\circ)^{-1} = \sqrt{2}$. The sample area illuminated by the laser beam is hence calculated by $A = \sqrt{2} \cdot \pi \cdot a \cdot b$.

In tr-2PPE experiments, two laser beams enter the chamber with a small angle of maximal 2° with respect to each other. The beams have to overlap spatially and temporally at the sample position. For this purpose, a $100 \mu\text{m}$ pinhole and a photo diode can be placed at the position of the chip in the camera. Since the beam diameters exceed $100 \mu\text{m}$, the beams will at least partially overlap if both are centered to the pin hole. The optimization of the spatial overlap is performed via adjusting maximal count rates resulting from the correlated signal in the temporal overlap. The delay between the pulses from the two beams can be reduced down to 100 ps by reading out a fast photo diode (ThorLabs DET10A/M) with an oscilloscope. As a trigger for the photo diode, a second diode is used, which is placed in the first part of the set-up before the OPAs. The exact overlap is then determined by measuring the dependence of 2PPE signal on the pump-probe delay at a suitable sample for the chosen wavelengths combination.

Ultra-high Vacuum Apparatuses

Photoemission experiments have to be performed in ultra high vacuum chambers in order to minimize the contamination of the surface of the investigated sample with gas molecules. Since the two different sample systems investigated in this work have different needs in terms of preparation and measuring conditions, two different UHV set-ups were used.

6T project: Thin 6T films on Au(111) required in situ preparations. Those are performed in a set-up with two separable vacuum chambers – preparation and analyzer chamber – to prevent contaminations with organic molecules of the spectrometer due to molecule evaporation. The set-up was originally designed and constructed by Christian Eickhoff [91]. Samples can be transferred in the preparation chamber with a transfer rod and placed on a manipulator, which can be moved in 3 dimensions and rotated around its axis. The base pressure in both chambers was below $3 \cdot 10^{-11}$ mbar. A homebuilt evaporator for organic molecules designed by Daniel Brete [92] was installed in the preparation chamber. In contrast to the original design, the evaporator possesses two separate crucibles, each tilted by 3.5° with respect to the normal of the base plate, so that the molecular beams meet in the 100 mm distant sample plane. To reduce the contamination of the vacuum chamber with organic molecules, a 11.7 cm long shield with an opening slit of 1 cm in diameter was constructed and fixed to the base plate to surround both of the crucibles. The modified evaporator design is shown and described in detail in appendix A.1. To measure the flux of the evaporated organic molecules, a quartz micro balance was mounted on a tilt stage, so that its sensor can be moved to the sample position. Furthermore, the preparation part is equipped with a low energy electron diffraction (LEED) optic, which was used to proof the quality of the Au(111) surfaces by checking regularly for the herringbone surface reconstruction. To clean the gold single crystal surfaces, a sputter gun and

an argon gas line are connected to the chamber. The argon is dosed via a leak valve. During sputtering, a constant argon flow of $\approx 10^{-6}$ mbar is used. Sputtering was performed in a normal incidence geometry. For subsequent annealing of the sample surface, the sample slot at the manipulator is equipped with an oven for heating via electron bombardement. Heating and cooling rates are automatically controlled with a PID temperature controller (Eurotherm), which regulates the filament current. Furthermore, a mass spectrometer (Pfeiffer, PrismaPlus QMG 220) is installed at the chamber, which is used to perform thermal desorption spectroscopy for investigating the surface coverage with the 6T molecules.

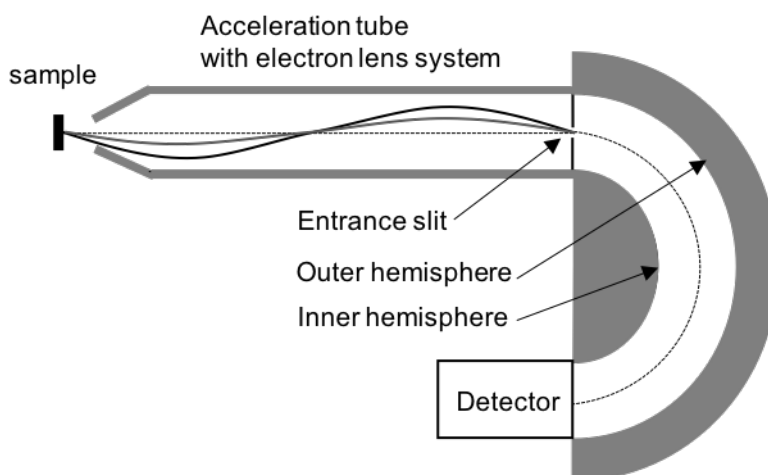


Fig. 3.9: Schematic illustration of a hemispherical analyzer based spectrometer. Electrons emitted from the sample pass through a lens system to undergo an acceleration towards the entrance slit. Only electrons with a kinetic energy in a defined energy window are able to pass through the hemispherical part from the entrance slit to the detector.

To perform the photoemission experiments, the sample is moved on the manipulator to the analysis chamber, where the laser beam can enter the chamber as shown in Fig. 3.8a. The analysis chamber is equipped with a photoelectron spectrometer (Phoibos 100, SPECS). The spectrometer contains a hemispherical analyzer and a 2D-CCD detector. A schematic representation of the spectrometer is shown in Fig. 3.9. Electrons emitted from the sample first have to pass through a lens system, that accelerates them towards the entrance slit to a specific pass energy E_{pass} . With this kinetic energy they pass through the entrance slit of the hemispherical analyzer. The analyzer contains an inner and an outer hemisphere, which are operated with a difference in their potential energies defined by the pass energy. Only electrons reaching $E_{\text{pass}} \pm 10\%$ at the entrance slit will have a trajectory ending in the detection area. All other electrons will be deflected towards the inner or outer hemisphere. The central kinetic energy of electrons being able to pass the hemispherical analyzer is termed E_{kin} . The concept of electron detection used in the Phoibos spectrometer allows to distinguish electrons in the energy range of $E_{\text{kin}} \pm 0.1 \cdot E_{\text{pass}}$ and hence allows to detect the whole spectrum in this range at once. The detector contains a stack of two multi-channel plates (MCPs) for signal amplification. The number of incoming electrons is increased by eight orders of magnitude. Those electrons are then accelerated to a phosphor screen. The emitted photons from the phosphor screen are imaged by a CCD camera with the help of an optical lens system. Camera and optics are mounted outside of the vacuum chamber. Besides distinguishing between different kinetic energies of the electrons, the analyzer also separates the electrons by their emission angles,

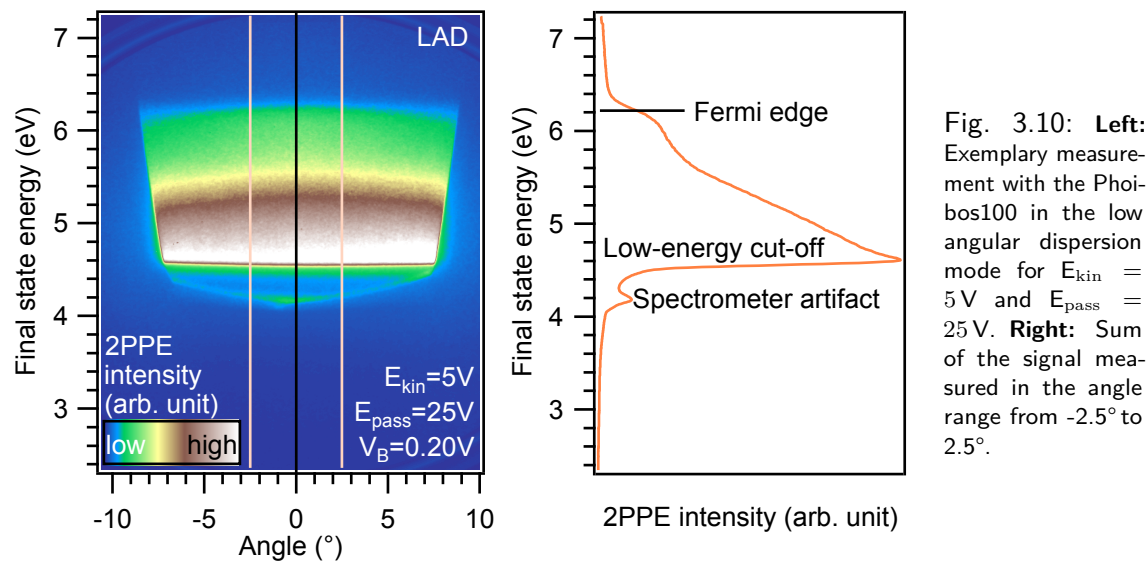


Fig. 3.10: **Left:** Exemplary measurement with the Phoibos100 in the low angular dispersion mode for $E_{kin} = 5V$ and $E_{pass} = 25V$. **Right:** Sum of the signal measured in the angle range from -2.5° to 2.5° .

thus allowing for angle resolved spectroscopy.

To minimize influences of external magnetic fields, a μ -metal shielding is installed, which surrounds the lens system of the spectrometer as well as the part of the analysis chamber where the sample has to be placed to face the spectrometer. To bring the entrance part of the spectrometer closer to the sample, the original set-up was modified by mounting a micro-tip at the spectrometer front. The distance between sample and spectrometer entrance was ≈ 4 mm during the experiments.

The most frequent used parameters for the measurements performed on the 6T films were $E_{kin} = 5V$ and $E_{pass} = 25V$ in the low angular dispersion (LAD) mode, which allows to detect emission angles in the range of $\pm 7.5^\circ$ around normal emission. Figure 3.10 shows an exemplary dataset acquired with this setting. In the left part of the figure, the horizontal axis shows the detection angle and the vertical axis the final state energy. In the given setting, for energies below 4.5 eV, the spectrometer starts to fail in correct imaging of the arriving electrons. Therefore, it is necessary to apply a bias voltage to the sample when the sample work-function is 4.5 eV or lower. The complete angle range is correctly imaged up to 6.6 eV. In the range from -2.5° to 2.5° , electrons can be detected up to 7.2 eV. Angle integrated spectra presented in this thesis will consider only this small angle range. The integrated spectrum determined from the angle resolved dataset is shown in the right part of Fig. 3.10. Below the low energy cut-off, an artifact appears due to the incorrect imaging of some electrons, so that the signal does not abruptly go to zero.

SAM project The *ex situ* prepared azobenzene-based self-assembled monolayers on Au(111) are investigated in a second ultrahigh vacuum chamber, which is equipped with a time-of-flight spectrometer (Themis 1000, SPECS). The Themis spectrometer was developed to enable angle-resolved detection of photoelectrons. Therefore, the usual drift tube is replaced by a lens

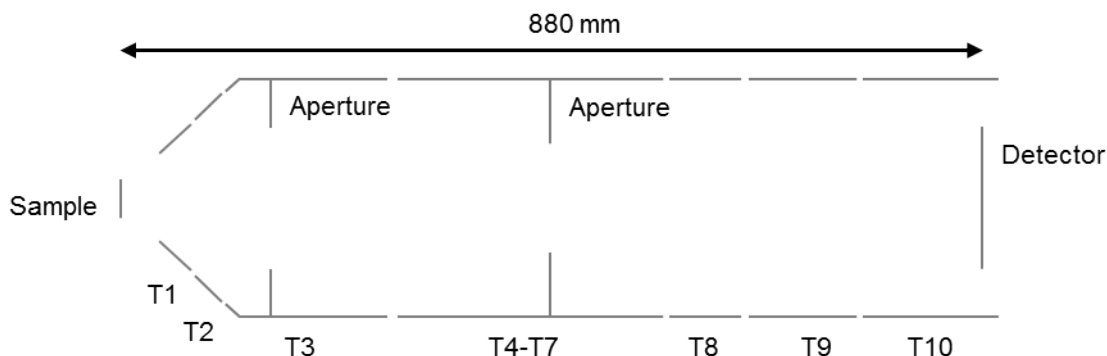


Fig. 3.11: [Adapted from Ref. [93]] Schematic illustration of the longitudinal section of an angle-resolved time-of-flight spectrometer. All lens elements that can be individually changed are sketched as separate elements. The lenses T4 to T7 are always at the same potential. The pin hole in lens element T3 can be used to manually change the acceptance angle of the spectrometer and to catch stray field electrons.

system, which contains in total ten conical and cylindrical lens tubes, as shown in Fig. 3.11. The lens system allows for electron detection resolved in energy and in a two-dimensional k -space or real-space. To assign the right energies and angles to the detected electrons, the trajectories of the electrons have to be simulated in the specific measuring modes to define conversion matrices. As in the set-up described before, a μ -metal shielding surrounds the lens system of the spectrometer and the sample to reduce influences due to external magnetic fields. As in the case of the hemispherical analyzer, the electrons are accelerated within the lens system to E_{pass} . The Themis spectrometer contains a 3D delay line detector (Surface Concept, DLD 3636). A detailed description of the Themis spectrometer and the calculations of the transformation matrices can be found in the PhD thesis of Thomas Kunze [93], who developed the spectrometer in cooperation with SPECS GmbH. The spectrometer can be operated in different modes. In the present work, the drift mode and the wide angle mode (WAM) were used for experiments. In the drift mode, the lens system operates as a normal drift tube. Hence, only electrons in a small solid emission angle of $4\pi \cdot d/(2L)$ are detected. Here, d is the diameter of the MCPs and L the length of the drift tube. In contrast, the WAM accepts emission angles in the range of $\pm 15^\circ$ around normal emission. In the present work, only energy-resolved spectra are shown, since no dispersive states are discussed in the SAM-project. The WAM was used only to achieve better statistics. The data presented in Ch. 5 are summed over the whole range in k -space.

The vacuum chamber, in which the spectrometer is mounted, has a base pressure in the range of 10^{-11} mbar. Between the experiments, the samples are stored in a garage in the transfer part, which is separated from the main chamber by a valve. The base pressure in this part was in the upper 10^{-10} mbar range. Besides the slot for movable sample plates, a Cu(111) crystal is mounted on the manipulator. The Shockley surface state of the clean copper surface is used to determine the cross correlation of the two pulses in the time-resolved measurements to determine the time resolution. The copper crystal is cleaned by Ar^+ ion bombardment and subsequent annealing up to 773 K via direct current heating. The crystal temperature is thereby

3.1. TIME-RESOLVED TWO-PHOTON PHOTOEMISSION SPECTROSCOPY

manually controlled using a pyrometer. The quality of the copper surface can be checked with a LEED optic, which is mounted in the chamber. As in the case of the other UHV-system, the laser beam enters the chamber via a UV fused-silica window and hits the sample with an angle of incidence of 45° .

3.2 Differential-Reflectance Spectroscopy

Differential-reflectance spectroscopy (DRS) is an optical spectroscopy technique. Since the optical properties of molecular ensembles depend sensitively on their structural arrangement, optical spectroscopy yields information not only about optical interactions, but also about the structure of the sample [94]. Optical spectroscopy methods rely on the wavelength dependency of investigated material's absorbance. This means, that the intensity loss of light passing through a sample is studied as a function of its photon energy E . If the sample is transparent, its absorbance can be studied by comparing the intensity of the transmitted light I to the intensity of the incident light I_0 in normal incidence. The absorbance A is thereby defined as the negative decadic logarithm

$$A \equiv -\lg(T) \quad (3.17)$$

of the transmittance $T \equiv I/I_0$ of a material. In case of thin films down to monolayer or even sub-monolayer thickness grown on non-transparent substrates (e.g. metal substrates), differential reflectance spectroscopy is a suitable method to gain information about the absorption bands of the adsorbate [94–97]. In this technique, not the transmitted light, but the reflected light is measured to detect the absorption bands of the investigated thin film. To distinguish the optical properties of the thin film with thickness d from those of the substrate, it is necessary to study the change in reflectance with and without the adsorbate $\Delta R(E, d) = R(E, d) - R(E, 0)$ normalized by the reflectance of the clean substrate $R(E, 0)$ [95]:

$$\text{DRS} \equiv \frac{\Delta R(E, d)}{R} := \frac{R(E, d) - R(E, 0)}{R(E, 0)}. \quad (3.18)$$

The reflectance itself is defined analogously to the transmittance as the ratio of the intensity of the reflected light to that of the incident light. In analogy to the definition of the absorbance given in Eq. 3.17, DRS spectra are plotted as the negative differential reflectance

$$-\Delta \lg(R) = -[\lg(R(E, d)) - \lg(R(E, 0))]. \quad (3.19)$$

It is important to notice that the DRS signal does not only originate from adsorbate's absorbance, but is influenced as well by changes in the optical constants of the underlying surface due to the adsorbed film. For this purpose, Nitsche *et al.* [98] developed a numerical algorithm to extract both real and imaginary part of the complex dielectric constant of the film using the Kramers-Kronig transformation. To apply this method, it is necessary that the spectrum covers an entire molecular absorption band, so that the signal tends to zero at both ends of the spectrum, which is often not the case. Nevertheless, DRS measurements allow for determination of the position of the absorption bands in an organic thin film, even though it is not possible to directly read off absolute values of the absorbance.

In the present thesis, besides the identification of the spectral range of the S_1 absorption bands of the investigated materials, DRS was used to link changes in the optical properties of an

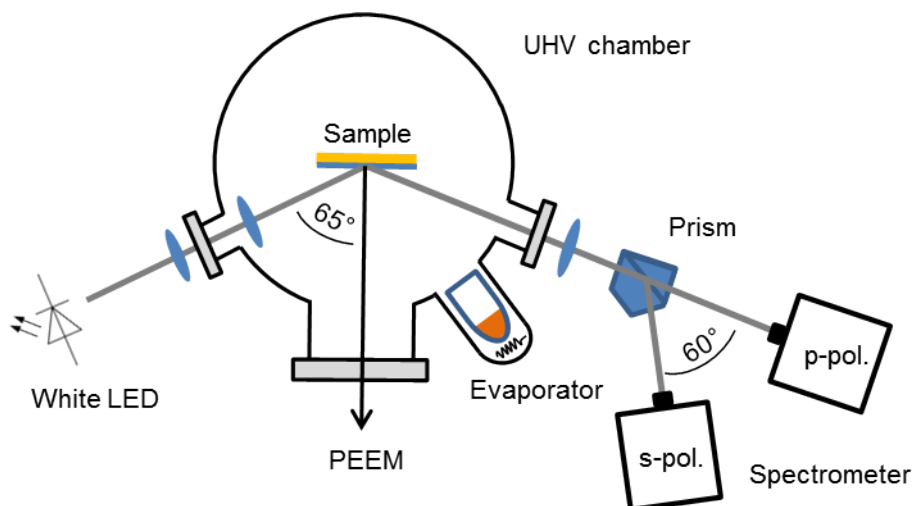


Fig. 3.12: [Adapted from Ref. [99]] DRS setup for monitoring changes in the optical properties of films of organic semiconductors during the growth processes. The collimated beam of a white light LED hits the sample, which is placed in a UHV chamber, with an angle of 65° with respect to the surface normal. The reflected beam is split and sent to two spectrometers to measure the s- and p-polarized components of the reflected light separately. An evaporator attached to the UHV chamber is used to deposit molecules to the sample surface during the acquisition of DRS data. DRS and photoelectron emission microscopy measurements described in Sec. 3.3, can be performed simultaneously. Therefore, the sample surface faces the microscope in the setup.

organic thin film to changes in the film morphology and its electronic structure.

The DRS experiments which are presented in Ch. 4 were performed during a research stay in the group of Thorsten Wagner at the Johannes-Kepler Universität in Linz in April 2016. The set-up in Linz allows real-time monitoring of the reflected light of the sample during the growth process of a molecular film by in situ vapor deposition. A detailed description of the set-up, which is sketched in Fig. 3.12, is given in Ref. [99]. A white light LED placed at a viewport of the vacuum chamber is used to illuminate the sample in a broad wavelength range. The collimated LED beam hits the sample with an angle of 65° with respect to the surface normal. The reflected beam at the surface can leave the UHV chamber through another viewport. Behind the viewport, the beam is split by a polarizing prism in its s- and p-polarized components, allowing for determining the orientation of the adsorbate's optical transition dipole moments. Both components are measured separately by two spectrometers (Ocean Optics, STS-VIS) of the same type. Before starting the vapor deposition, the spectrum of the bare surface of the substrate is measured as a base line, which is subtracted from every spectrum taken during deposition to extract the optical properties of the film.

3.3 Photoelectron Emission Microscopy

Concerning photoelectrons, so far the focus was on the spectroscopic investigation of a sample, but photoexcited electrons can be used as well for real-space imaging of the sample surface. The corresponding technique is called photoelectron emission microscopy (PEEM). In this thesis PEEM experiments are used to detect the growth mode of α -6T on Au(111) surfaces (cf. Sec. 4.2.1) as well as to image photo-induced work-function changes in azobenzene-based self-assembled monolayers on Au(111) (cf. Sec. 5.4). In the following, a short introduction into this technique will be given, concentrating on the details that are relevant for this thesis. A broader overview about PEEM can be found e.g. in Ref. [100] and [101].

Nowadays, most PEEMs comprise an electron lens system which allow for two operation modes: real-space imaging and reciprocal space imaging. In the present work, PEEM setups were used only for real-space imaging of the samples. As an example of a PEEM set-up, Fig. 3.13 shows a sketch of the basic parts of the Focus IS-PEEM used for measuring the growth mode of 6T/Au(111). A sample is placed inside a vacuum chamber in front of the PEEM instrument at a distance of a few millimeters. The beam of an external light source is focussed onto the sample to excite photoelectrons, which are accelerated to the opening of the PEEM with a high voltage. In the PEEM experiments presented in Sec. 4.2.1 and 5.4, photoelectrons are produced via sample excitation with the light emitted from Xe and Hg lamps, respectively. In general, other light sources as lasers or synchrotron radiation can be used as well to perform PEEM experiments. The objective lens, also called extractor, is the main part of the PEEM, allowing for magnified real imaging. It is followed by an aperture to catch stray electrons and an octupole stigmator to correct for axial astigmatism. The two projection lenses allow for further magnification. The PEEM is furthermore equipped with an energy filter comprising the entrance lens and the grids behind to perform spectroscopy. In this thesis, the energy filter was switched off to operate the PEEM in the standard non-filtered mode. To achieve a spatially resolved detection of the electrons, a stack of a MCP and a phosphor screen is used. The screen is imaged by a camera for data acquisition.

Counting the electrons as a function of the region of the surface from where they are emitted, PEEM is sensitive to local work-function variations at the sample surface. A homogeneous signal over the whole image indicates that no significant work function variations can be observed in the probed area. This is expected for flat single crystal surfaces and surfaces uniformly covered with e.g. organic films. Films growing in a layer-by-layer fashion show small PEEM contrasts as long as a layer is incomplete, whereas the often observed Stranski-Krastanow growth mode (wetting layer formation and crystallization on top) shows usually high work-function variations between the crystallized islands and the substrate or wetting layer [55]. Besides changes in the work function, differences in the density of states for different materials in the sample result in different PEEM contrasts. For example, in the case of a molecular layer on a metal substrate, electrons can be emitted directly from the molecules, if the photon energy of the light source exceeds the ionization potential of the molecules. As a consequence, different light sources

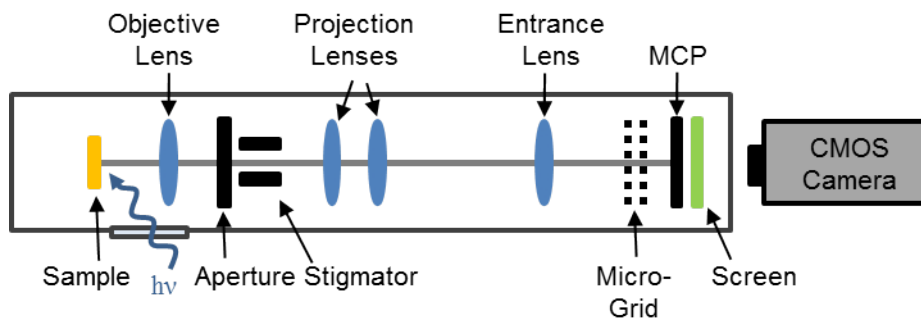


Fig. 3.13: [Adapted from the FOCUS IS-PEEM data sheet.] Schematic image of the FOCUS IS-PEEM used at the JKU Linz. Photoelectrons emitted from the sample pass through an array of electron lenses: an objective lens for real space imaging, an aperture and a stigmator to catch stray electrons and correct for astigmatism, a pair of projection lenses for further magnification and an energy filter to allow for spectroscopy before they hit a multichannel plate followed by a phosphor screen. A CMOS camera takes images from the screen.

working with different photon energies result in different contrasts in the images [56].

Set-up at the JKU Linz: The PEEM data of α -6T films presented in Sec. 4.2 are recorded with the set-up used by the group of Thorsten Wagner at the Johannes Kepler university (JKU) in Linz. Here, the microscope (Focus, IS-PEEM) is attached to a UHV chamber with a base pressure of $5 \cdot 10^{-10}$ mbar. The UHV system includes an evaporator for organic materials that is attached in a way to direct the molecular beam to the sample stage of the microscope. In this way, PEEM images can be recorded during the film deposition. The images are acquired with a sCMOS camera, which limits the lateral resolution to ≈ 150 nm by its pixel resolution. PEEM images are detected with a frame rate of 1 frame per second, which allows for real-time monitoring of changes in the PEEM contrast during the deposition. The photoelectrons are excited by a super quiet Xe lamp (Hamamatsu). The lamp has a rather continuous spectrum with a maximum photon energy of 7.75 eV, which is high enough to excite photoelectrons from the bare Au(111) surface ($\phi_{\text{Au}(111)} = 5.4$ eV) and after functionalization with α -6T molecules.

Set-up at the FU Berlin: The PEEM data recorded for the self-assembled monolayers presented in Sec. 5.4 are performed with a prototype of the METIS 1000 spectrometer by SPECS, which is a time-of-flight PEEM originally designed by Gerd Schönhense [102]. The microscope is equipped with a 3D (k_x, k_y, t)-resolving delay-line detector to allow for spatially resolved spectroscopic investigations of the sample [103]. The UHV set-up containing the momentum microscope was operated at a base pressure in the upper 10^{-10} mbar range. In this thesis, the spectrometer was used in the standard non-energy-filtered mode. A Hg lamp was used as light source to induce photoemission.

4 Morphology, Electron and Exciton Dynamics in Thin α -Sexithiophene Films on Au(111)

Organic semiconductors play a crucial role in modern device fabrication, since their mechanical flexibility and low production costs allow for new designs including bending or large size surfaces. Usually organic films are part of a layered system, as in the case of an organic solar cell or an organic light emitting diode [34–37]. To establish the functionality of those devices, it is necessary to create excitons in the organic films and to find the right level alignments at the interfaces of the different layers to allow for charge transfer. It has been under debate, whether a resonant excitation and instantaneous population of the S_1 Frenkel exciton (FE) in the model molecule α -sexithiophene (6T) is possible or whether excess energy is needed to first populate a higher excited state and to relax from there into the FE [7].

Based on the comprehensive discussion of the relation of film morphology and electronic structure presented in Sec. 4.2, it will be shown that the population and relaxation dynamics of the Frenkel exciton strongly depend on the film morphology (Sec. 4.3). At room temperature the 6T molecules form crystallites on top of a two layers thick wetting layer. It will be shown that the creation of FEs with longer lifetimes than a few femtoseconds is only possible in the crystallites and that instantaneous population is observed for resonant excitation as well as excitation with excess energy.

Parts of the physical contents presented in Sec. 4.2 are published in W. Bronsch *et al.*, *Interplay between morphology and electronic structure of α -sexithiophene films on Au(111)*, Journal of Physical Chemistry C **123**, 7931-7939 (2019).

4.1 Sample Preparation and Film Thickness Characterization

All 6T films were prepared on Au(111) single crystals. The crystal surface was treated by argon ion bombardment (sputtering) and subsequent annealing to 873 K. Within each cleaning cycle, the crystal was sputtered for 10 min at a sputtering current of 5–8 μA . The target temperature was hold for 10 min. Heating and cooling rates were set to 1 K/s. Below 470 K the cooling rate was even lower than 1 K/s. For film preparation at room temperature (RT) the sample was first equilibrated with the air conditioned laboratory environment, which was set to 296 K. To grow films at lower temperatures, the cryostat of the manipulator holding the gold sample was cooled with a constant flow of liquid nitrogen. Film deposition was started when the sample temperature was not changing anymore. In this case the sample temperature was ≈ 120 K.

The molecular powder was evaporated by a homebuilt evaporator originally designed by Daniel Brete [92]. The crucible filled with the molecules was heated to 533 K for evaporation. A quartz micro balance positioned in a geometry similar to the gold crystal was used to monitor the flux of the molecules before and after the actual film preparation to control the amount of molecules sent to the surface. To determine the actual surface coverage, temperature programmed desorption (TPD) spectroscopy was performed while removing the molecules from the surface via thermal desorption. As discussed in the PhD thesis of Kristof Zielke [104], TPD measurements show different desorption energies for the multilayer and the second layer, while the monolayer does not desorb. The average surface coverages given in this thesis are based on the assumption that the packing density of the molecules does not significantly change from the monolayer to higher layers.

4.2 The Interplay of Morphology and Electronic Structure in Thin Sexithiophene Films on Au(111)

On several metal substrates, 6T molecules show a well-ordered flat-lying arrangement in the monolayer range [51, 105–111]. However, this growth mode is not expected to be conserved in thicker layers. Growth studies of 6T on silver surfaces show the formation of crystallites on top of a two layers thick wetting layer [55, 56, 112–115]. The size of the crystallites thereby strongly depends on the surface orientation and the deposition temperature. In contrast to scanning tunneling spectroscopy, which is able to detect the electronic structure of single molecules but only in a narrow energy range around the Fermi level, photoemission measurements investigate the electronic structure of the sample over an area with a diameter of a few hundred μm . To interpret the electronic structure and dynamics correctly, it is therefore necessary to know the morphology of the organic film.

4.2.1 Real-Time Monitoring of Coverage-Dependent Changes in Film Growth and Optical Properties

All data presented in this section have been recorded during a research stay in the group of Dr. Thorsten Wagner at the Johannes Kepler Universität in Linz. A combined study of PEEM and DRS measurements allows to detect changes in the morphology and the optical properties of the film at the same time.

Real-Time Photoemission Electron Microscopy

The PEEM set-up described in Sec. 3.3 allows for imaging during film deposition and hence monitoring changes in the PEEM contrast in real time. The PEEM data presented here were analyzed by Thorsten Wagner. We recorded a series of PEEM images during the deposition of 6T onto a Au(111) surface. The gold single crystal was held at room temperature during the deposition. Figure 4.1 shows a selection of PEEM images for coverages of 0.6, 1.2, 1.7, 2.3, 4 and 9 ML obtained during the deposition. Up to 4 ML the electron yield changes almost homogeneously across the whole image with increasing coverage. For coverages higher than 4 ML, small bright spots appear on top of the grayish wetting layer (WL) in the PEEM images, as can be seen in the image with an average coverage of 9 ML. Such spots are equally distributed over the probed area and are interpreted as 3D crystallites. The average size of the crystallites can be determined from the PEEM images. In contrast to the growth of 6T on single crystal silver surfaces at room temperature or elevated temperature [55, 56, 112–114], we observe comparatively small 6T crystallites on Au(111) with diameters in the order of 1 μm . To determine the surface area covered with these small-sized crystallites in comparison to the surface area covered by the wetting layer only, histograms, giving the frequency of the occurrence of a specific local electron yield (LEY), can be generated and analyzed for

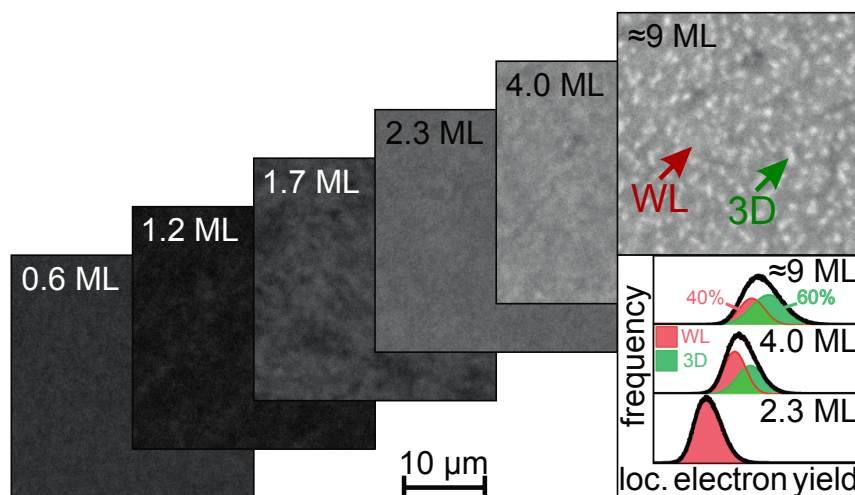


Fig. 4.1: PEEM images for average sample coverages of 0.6, 1.2, 1.7, 2.3, 4 and 9 ML 6T molecules on a Au(111) surface at room temperature. Each image shows a $30\ \mu\text{m} \times 30\ \mu\text{m}$ large cut of the probed area. The inset below the 9 ML image shows the histograms of the images taken at coverages of 2.3, 4 and 9 ML, plotting the frequency of the occurrence of each measured local electron yield (LEY). While the histogram taken at a nominal coverage of 2.3 ML can be described by a single gaussian distribution, the histograms taken at 4 and 9 ML are fractioned in a contribution of the wetting layer (red) and the 3D crystallites (green). In the case of the 9 ML film 60% of the surface are covered by crystallites.

each PEEM image. Figure 4.1 shows such histograms for the PEEM images with a nominal coverage of 2.3, 4 and 9 ML. While the histogram taken at 2.3 ML can be described by a single gaussian distribution, the distribution of LEY for 4 and 9 ML must be fitted with the sum of two gaussian distributions, one for the wetting layer and one for the crystallites. Comparing the portions of the two gaussians in the case of 4 ML nominal, one can conclude that the crystallites cover $\theta_{3D} = (45 \pm 2)\%$ of the surface, whereas $\theta_{WL} = (55 \pm 2)\%$ of the surface are covered only by the wetting layer. In contrast, in the case of 9 ML nominal coverage, we determine $\theta_{3D} = (60 \pm 2)\%$ and $\theta_{WL} = (40 \pm 2)\%$. The comparable sizes of the sample areas covered with the WL and the 3D crystallites lead to the conclusion that 2PPE experiments on sample coverages higher than two layers should show contributions from the electronic structures of wetting layer and crystallites.

To determine the thickness of the wetting layer, the histograms of the LEY are plotted in Fig. 4.2 as a function of the deposition time. The histograms are represented by the green shadowed curve, plotted against the left axis. The deposition time is plotted on the top axis of the figure. To interpret the histograms, the average electron yield Y_e is plotted as a dark green curve in the same figure. Furthermore, the right axis gives the normalized standard deviation (NSD) $\sigma/\sqrt{Y_e}$, shown as a function of the deposition time by the red curve. The standard deviation σ is normalized with the square root of the mean electron yield, since the electron detection system, consisting of a stack of MCPs and a camera, follows Poisson statistics. Following the evolution of the mean electron yield, it shows a local minimum after ≈ 220 s deposition. This minimum is attributed to the closure of the first layer (cf. bottom axis). The NSD reaches a plateau when half of the monolayer is filled. Later it reaches a minimum some

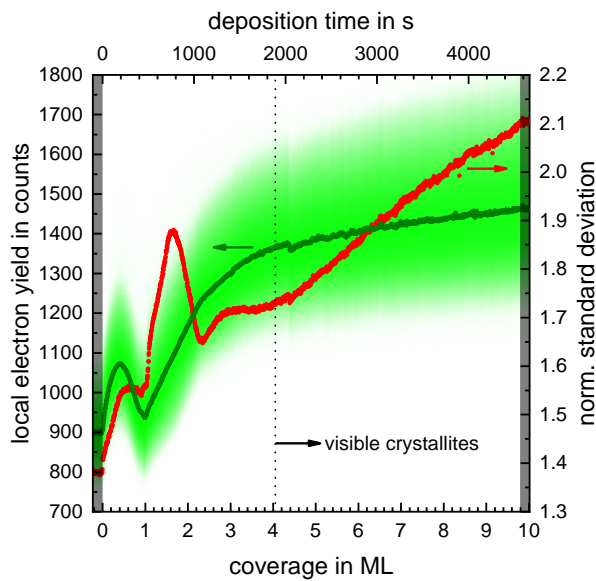


Fig. 4.2: LEY (green shadowed area), mean electron yield Y_e (green curve) and NSD for the mean electron yield (red) as a function of deposition time (top axis) and the corresponding coverage (bottom axis) measured during the deposition of 6T molecules on a Au(111) surface at room temperature. The gray areas at the left and right edges of the graph mark that the shutter of the evaporator was closed at those times.

seconds before the minimum in the Y_e is reached. This indicates that the filling of the second layer already starts before the first one is completely closed. Continuing the deposition, Y_e increases almost linearly, while the NSD reaches a local maximum at about 1.7 ML. This means that the gaussian distribution of the LEY broadens up to this coverage, indicating an increasing inhomogeneity in the LEY. Afterwards the gaussian peak narrows again, i.e., the NSD decreases, while the absolute value in the LEY further increases, as it was shown in the histograms in Fig. 4.1. We interpret this observation as the formation of small islands within the second layer whose lateral extent is just below the resolution limit of the PEEM for the given measuring conditions (ca. 150 nm). This causes speckles in the PEEM images, but no sharp contrast boundaries, since the intensity measured in one pixel of the camera is given by the weighted average of the monolayer emission and the emission from the island in the second layer. As soon as more than one half of the sample is covered with the second layer, the layer starts to close and the PEEM images become more uniform again, which causes a narrowing of the gaussian distribution. The second local minimum of the NSD is hence interpreted as the closing of the second layer. This is reached for a nominal coverage of 2.3 ML, which indicates that the packing density of two closed layers is higher than that of the monolayer. However, since the coverage determination of the 2PPE experiments bases on the coverage determined for one monolayer, all coverages are given as a multiple of the monolayer coverage to get comparable values. Afterward the second minimum in the NSD curve the Gaussian peak starts to broaden again. Hence, the NDS increases again and reaches a plateau from 2.8 to 4 ML. For coverages higher than 4 ML, bright features with sharp borders start to appear in the PEEM images and the distribution of the LEY becomes asymmetric, which causes an increase in the NDS. Those sharply edged bright features are interpreted to be 3D crystallites formed by 6T molecules on top of the wetting layer. Since there is no indication in the data that a third layer closes, we conclude that the wetting layer consists of two layers. The onset of the crystallization is

hence expected to take place in the coverage interval from 2.3 to 4 ML. Based on previous experimental works performed by Thorsten Wagner on the growth of 6T on silver surfaces, we can assume that the pre-stage of the formation of the crystallites is a 2D gas of molecules moving freely on top of the wetting layer [56, 112–114]. It is expected that nucleation first sets in at defect sites of the surface and later on homogeneous nuclei.

Since we assume the wetting layer to be two layers thick and have a nominal coverage of 2.3 ML, we can calculate the average height of the crystallites from their portion on the surface. For an average coverage of 9 ML, we determined a portion in surface coverage of 60%. This translates into an average height of 12 ML above the wetting layer. The thickness of the wetting layer is far below the escape depth of the electrons excited in the 2PPE experiments shown in the following, which means that electrons from 6T molecules in the crystallites and the wetting layer, as well as from the substrate can be probed.

Real-Time Differential-Reflectance Spectroscopy

Simultaneously to the PEEM images, DRS data have been recorded during the deposition of the 6T molecules onto the Au(111) surface (cf. set-up shown in Fig. 3.12). Figure 4.3a shows the negative differential reflectance as a function of deposition time (bottom axis) and photon energy (left axis) for p-polarized light. The top axis shows the translation of the deposition time to an average film thickness according to the PEEM data discussed in the previous part of this subsection. Before starting the deposition of the 6T molecules, some spectra of the clean gold surface were recorded to determine the base line, which is subtracted in the DR spectra. A selection of DR spectra from the map is presented in Fig. 4.3b. The films with a nominal coverage of 1, 2.3, 4, 6 and 10 ML are highlighted by different colors. As described in Sec. 2.3.1 for DR measurements of 6T/Au(111) under ambient conditions, we observe the S_1 absorption band in the range of photon energies from 2 eV to 3 eV. For photon energies higher than 3 eV, the DR signal changes its sign. Such an effect may appear in DRS on the higher energetic side of a strong absorption line as described by Wakamatsu *et al.* [116]. Focussing first on the DR spectrum of an average coverage of 8 ML (blue curve in Fig. 4.3b), we observe the same splitting of the S_1 absorption band in a series of sub-peaks as discussed in Sec. 2.3.1. The lowest sub-peak appears at a photon energy of (2.33 ± 0.02) eV. The second peak, which is the most intense, is observed at (2.54 ± 0.02) eV. At least two more peaks are observable in the higher energetic shoulder of the second peak.

To learn more about the origin of the substructure in the S_1 absorption band and the relation between the optical properties of the thin film and its phase of growth, the focus is now drawn to average thicknesses up to 4 ML, which covers the regime of the wetting layer and the beginning of crystallite formation. Figure 4.4a shows a zoom into the map presented in Fig. 4.3a for coverages up to 4 ML. For a coverage of 0.5 ML the DR signal becomes large enough to be clearly distinguishable from the baseline. The maximum of the S_1 band appears at (2.43 ± 0.02) eV and shifts then gradually upwards up to (2.51 ± 0.02) eV until the first layer

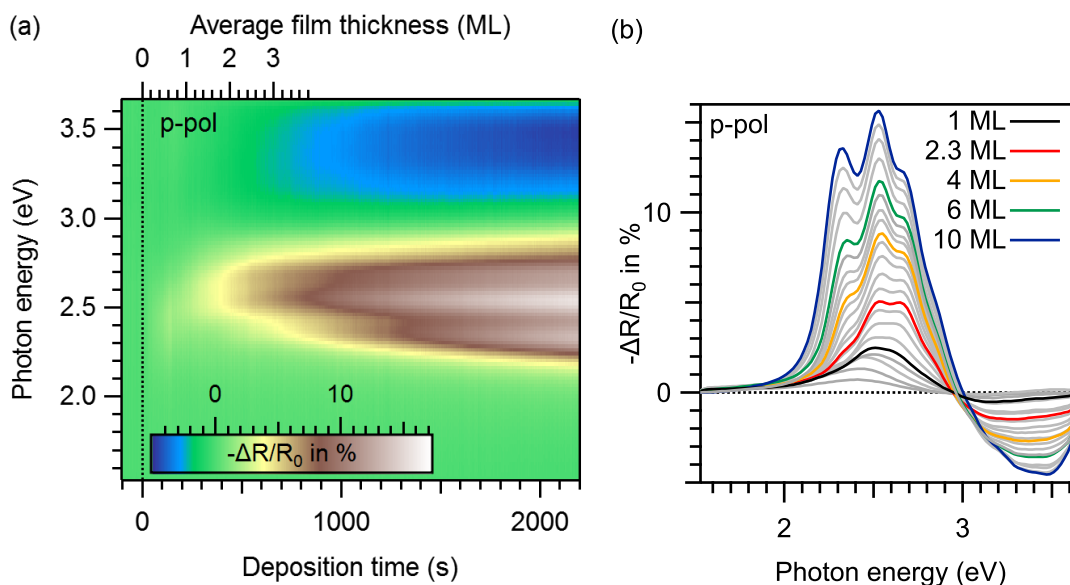


Fig. 4.3: **(a)** Map of the negative DR signal of thin 6T films on Au(111) as a function of the deposition time and the photon energy for p-polarized light. The top-axis shows the average film thickness derived from the deposition time according to the PEEM data. **(b)** Series of DR spectra from the map shown in (a). The average coverages of 1, 2.3, 4, 6 and 10 ML are highlighted by different colors.

closes, as it is shown in Fig. 4.4b in the series of spectra taken from the map. The DR spectrum of the monolayer according to the coverage calibration obtained by PEEM is highlighted in black. The spectrum shows already a broadening of the higher energetic shoulder of the peak, leading to a double-peak structure which appears when the second layer grows. From these data, one would guess that the first layer is already completed earlier, namely just before the peak broadens towards higher energies. The difference between PEEM and DRS might be an indication that the second layer already starts to grow before the first one is completely closed. Note that the DRS is more sensitive to such an effect than PEEM. The DR spectrum of the completed second layer (red curve) then shows an onset of two more peaks, one at each side of the band. For coverages higher than 2.3 ML, the peak at 2.3 eV becomes more and more intense. Furthermore, the peak at 2.5 eV gets more and more emphasized in comparison to the peak at 2.7 eV. This effect may at least partially result from the increase of the 2.3 eV peak, since the peaks at 2.3 eV and 2.5 eV overlap to a certain degree. At a coverage of 4 ML the DR spectrum contains already the same substructure as observed for higher coverages, but with different ratios of the peak amplitudes.

Sun *et al.* [49] observed the first two peaks at similar energies on 6T/Cu(110)-(2x1)O surfaces by means of reflectance difference spectroscopy and assigned them to the two Davydov components a_u and b_u , which leads to a Davydov splitting in the order of 200 meV. The higher peaks are assigned to a row of rather equidistant sub-peaks originating from the excitation of the C=C stretching mode with an energy of 180 meV. Since the peak at 2.3 eV observed in the DRS measurements presented in this work appears delayed with respect to the one at 2.5 eV and the ratio of the intensities of the two peaks changes with increasing coverage, I go along with

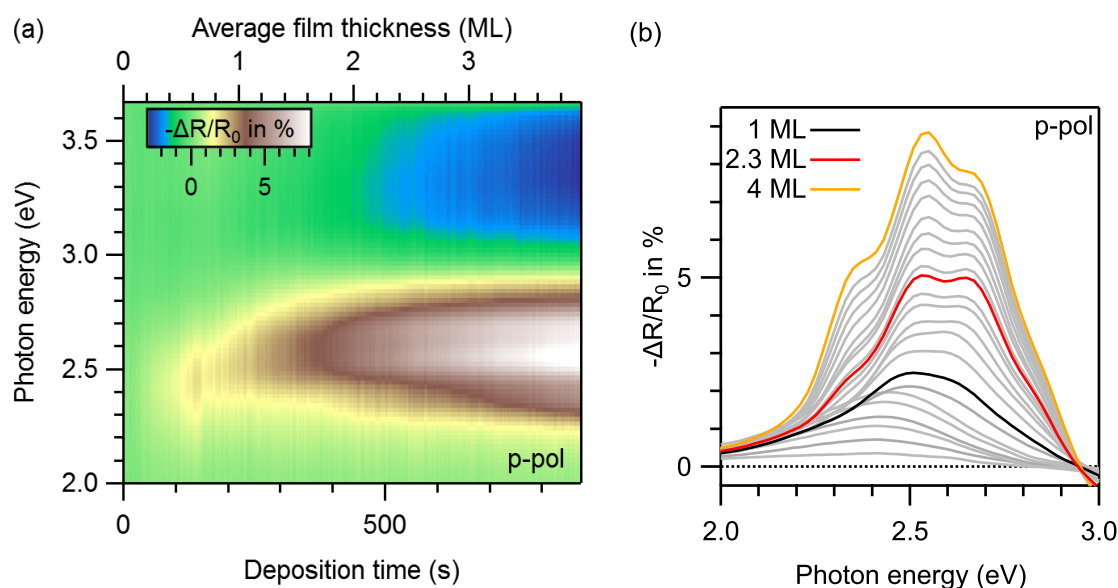


Fig. 4.4: (a) Zoom in the map shown in Fig. 4.3 for average film thicknesses up to 4 ML. (b) Series of DR spectra from the map shown in (a). The average coverages of 1, 2.3 and 4 ML are highlighted by different colors.

Sun *et al.* and assign the origin of this 2.3 eV peak to the a_u and the peak at 2.5 eV to the b_u Davydov component. In this case the form of the absorption spectrum can be described by a weak to intermediate coupling strength in an H-aggregate according to the theoretical considerations of Simpson and Peterson [30] and Spano [117].

4.2.2 Coverage Dependent Electronic Structure

To investigate the electronic structure of 6T/Au(111), a series of monochromatic and bichromatic 2PPE experiments were performed at 6T film thicknesses of 1, 2, 3 and 10 ML. As described in Sec. 3.1.2, photon energy dependent changes in the detected final state energies are monitored to distinguish between initial, intermediate and final states.

When working with thin organic layers, care has to be taken that the chosen measurement conditions do not damage the investigated samples. STM measurements on monolayer thick films of 6T grown on Ag(001) and Au(001) showed heat and light induced polymerization [111]. All measurements presented in this section are performed at room temperature, which is far below 450 K, where Sander *et al.* observed heat induced polymerization on non-reconstructed Au(001) surfaces. Furthermore, they observed a strong dependence of the heat induced polymerization on the reactivity of the surface. Reconstructed and hence less reactive Au(001) surfaces showed a 120 K higher threshold temperature. Light induced polymerization on Ag(001) was observed to be dependent on the photon energy and the photon flux. Although no damage was observed by IR light at 1.7 eV, UV light at 3.5 and 3.8 eV caused a fluence dependent decrease in the photoemission intensity in PEEM measurements. Sander *et al.* concluded that a single photon process triggers the polymerization. Additionally to the data presented, the

authors stated that a similar drop in the photoemission signal was observed for photon energies of 3.0, 3.9 and 4.2 eV.

The photon energies used in this work range from visible to UV light (2.14 – 4.25 eV), which covers the range of photon energies for which light induced polymerization was observed on Ag(001). The Au(111) surface is the least reactive gold surface. Therefore we expect even lower polymerization rates than on Ag(001). In the present experiments photon fluxes in the order of 10^4 to 10^6 photons per $\text{nm}^{-2}\text{s}^{-1}$ were used. Assuming polymerization rates determined for Ag(001), the 6T-derived photoemission signals should completely vanish within the first 10 to 100 seconds. On the contrary, the light-induced decrease we observe on Au(111) amounts in most cases to 5 to 10% within 80 minutes. In some cases the loss reached up to 30% of the original signal. The effect was observed independently of the detected final state energy in the range of the molecular electronic structure, which made us confident that the detected signal stems from intact molecules. Furthermore, the coverage dependence of the intensity loss described by Sander *et al.* was not observed. It has to be noted that slight losses in the laser power during the measurement result in the same effect. Since the time-resolved measurements presented in this work are measured with a series of non-equidistant pump-probe delays, it is necessary to correct the measurement time-dependent intensity loss. The procedure applied to the data is described in appendix A.3.1.

2D Wetting Layer

PEEM experiments presented in Sec. 4.2.1 allowed the conclusion that 6T forms a two layers thick wetting layer on top of the Au(111) surface. Scanning tunneling microscopy measurements showed that the 6T molecules in a monolayer thick film are lying flat on the Au(111) surface [51]. This layer is strongly bonded to the surface, as it was shown by the fact that molecules in this layer do not thermally desorb (cf. TPD experiments presented in Ref. [104, 118]). In contrast, the second layer is bonded less strongly and the onset of thermal desorption is observed at ≈ 455 K, which is about ≈ 15 K higher than the onset of the multilayer desorption. The different desorption behavior of the monolayer and the second layer raises the question, whether the wetting layer possesses a uniform electronic structure or whether the electronic structure of the second layer already resembles the one of the crystallites. To answer this question, the focus is first drawn to the clarification of the electronic structure of the monolayer.

Figure 4.5a shows the evolution of the final state energies of the detected photoelectrons from a monolayer film prepared and measured at room temperature for different monochromatic 2PPE measurements with photon energies ranging from 2.32 to 4.20 eV. The bottommost spectrum, detected for excitation with 2.32 eV photons, shows the signal resulting only from three-photon photoemission, since the sample work-function is higher than two times the photon energy. All other spectra are dominated by the two-photon photoemission signal. For 3.11 eV excitation, a pronounced peak can be observed close to the Fermi edge. Increasing the photon energy further to 3.36 eV, the shape of the secondary edge still suggests a peak close to the edge. At

4.2. THE INTERPLAY OF MORPHOLOGY AND ELECTRONIC STRUCTURE IN THIN SEXITHIOPHENE FILMS ON Au(111)

final state energies above 6 eV, two additional smaller peaks can be distinguished from the background. The spectra taken for 3.86 eV and 4.20 eV excitation show a prominent peak close to the Fermi edge and a series of further peaks.

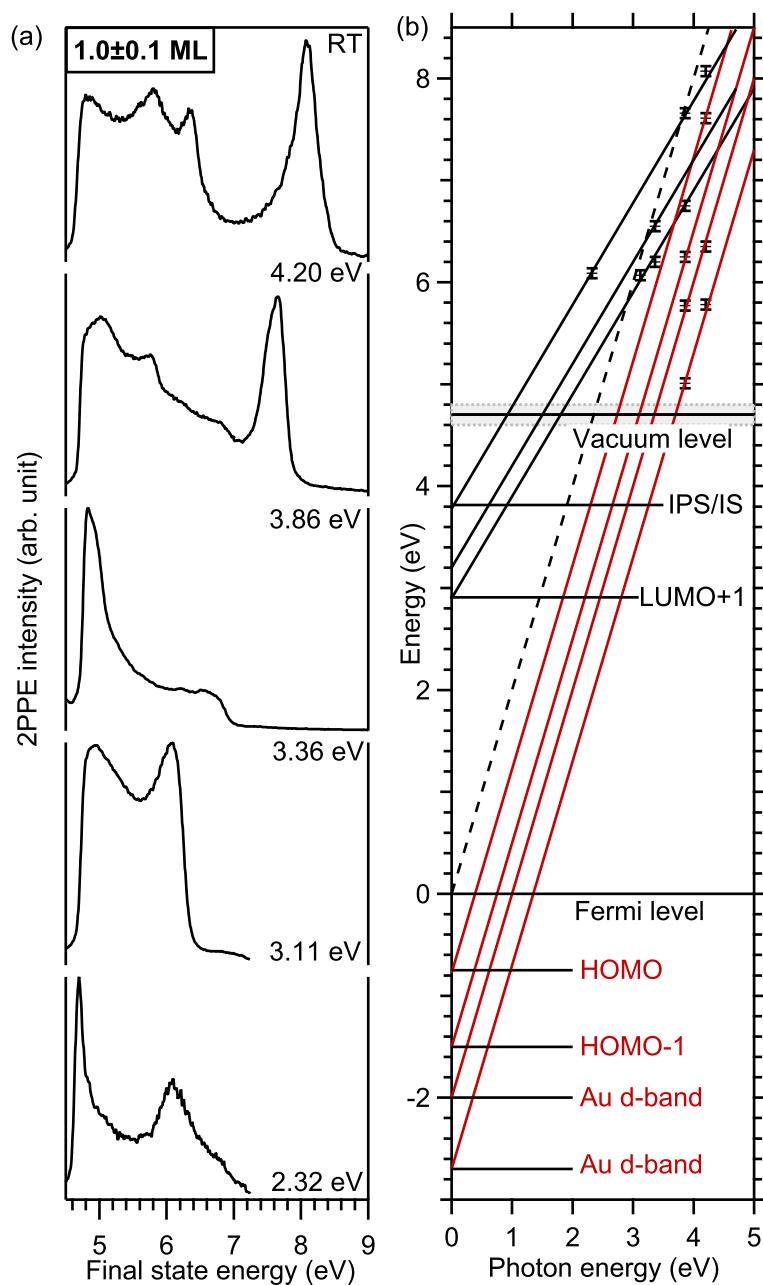


Fig. 4.5: (a) Series of single color 2PPE spectra for different photon energies. The spectra are measured at room temperature with the following parameters: $E_{ph}=2.32$ eV and $E_{ph}=3.11$ eV: $E_{kin}=5.0$ V, $E_{pass}=25$ V, $V_B=0.200$ V, 100 s exposure; $E_{ph}=3.36$ eV: $E_{kin}=5.6$ V, $E_{pass}=35$ V, $V_B=0$ V, 160 s exposure; $E_{ph}=3.86$ eV and $E_{ph}=4.20$ eV: assembled spectra measured with $V_B=0.200$ V, 100 s exposure, which means that below 7 eV the spectra are measured with $E_{kin}=5.5$ V, $E_{pass}=25$ V and the higher energetic part is measured with $E_{kin}=6$ V, $E_{pass}=35$ V. In order to assemble the two spectra with the different settings, the offset determined in the energy range below 3 eV was subtracted and afterwards the spectra were scaled to each other at 7 eV. In all spectra the applied bias voltages V_B are already subtracted in the given final state energies. (b) Final state energies (markers in the top part) read-off from the spectra shown in (a) plotted as a function of the photon energy used for excitation. Linear curves with a slope of 1 (black) connect states resulting from the same intermediate state while linear curves with a slope of 2 (red) connect those belonging to the same initial state. The intercepts of the linear curves with the y energy-axis give the energetic position of two intermediate states (IPS/IS and LUMO+1) and four initial states (HOMO, HOMO-1 and 2 Au d-band states) with respect to the Fermi level ($E=0$).

To be able to assign the peaks in the spectra to the corresponding states of the sample, their energetic positions are read-off and displayed as a function of photon energy in Fig. 4.5b. According to the procedure for assigning initial and intermediate states given in Sec. 3.1.2, linear curves with a slope of 2 (red lines) are used to connect final state energies resulting

from initial states and linear curves with a slope of 1 (black lines) connect intermediate states. The y-axis intercept marks the energetic position of the identified state with respect to the Fermi level ($E=0$). In total, 6 well distinguishable states appear across the different spectra. Their assignment is summarized in Fig. 4.5b. The lowest lying states, which are only detected for the two highest photon energies of 3.86 eV and 4.20 eV are assigned to Au d-band states in agreement with measurements of the clean surface (cf. Sec. A.2). As a starting point for further assignments the 2PPE study of 6T/Au(111) presented by Varene *et al.* was used. They determined two initial states at -0.8 eV and -1.5 eV, which they assigned to the HOMO and HOMO-1 of the 6T molecule respectively. The same values have been found by Jäckel *et al.* [119] performing scanning tunneling spectroscopy at single 6T molecules adsorbed on a Au(111) surface. Here, only in the spectrum obtained for excitation with 3.86 eV the peak obtained at $E - E_F = 6.2$ eV could be assigned to an initial state at -1.5 eV. In contrast, three detected peaks could be assigned to an initial state at -0.75 ± 0.05 eV, but two of them also fit to an intermediate state at 2.9 ± 0.1 eV. Varene *et al.* suggested the LUMO+1 to be found at $E - E_F = 3$ eV. The strongest indication for an unoccupied state in this energy range is the high 2PPE intensity measured close to the Fermi edge in the 3.11 eV excitation spectrum. Such high amplitudes are only expected for resonant excitation, especially since the spectrum observed for an only 150 meV higher photon energy does not show such a high intensity. This could be an indication for the presence of an interface state just below the Fermi level. An intermediate state at 2.1 eV, as suggested by Varene *et al.*, is not observed in the present work.

The 3PPE signal in the 2.32 eV can be assigned to the same intermediate state as the prominent peaks close to the Fermi edge in the spectra observed for 3.86 and 4.20 eV excitation. The intermediate state energy with respect to E_F corresponding to this state, which is labeled IPS/IS in Fig. 4.5b is 3.8 eV. Varene *et al.* [120] evaluated the dispersion of this state and identified it as an image-potential state. An analysis of the energetic distance of the state to the vacuum level for a series of one monolayer samples (cf. Sec. A.3.2, Fig. A.4) supports this interpretation since the energetic position of the peak changes with the work function. The binding energy with respect to the vacuum level is determined as $E_{vac} - E = 0.76 \pm 0.02$ eV, which is rather close to the binding energy of the image-potential state $E_{vac} - E = 0.8$ eV in front of the clean Au(111) surface [121]. However, as it will be discussed below, the coverage dependence of the peak questions the assignment to an image-potential state.

In the monochromatic experiments no exciton was observed. In the following bichromatic 2PPE experiments are performed in order to make the pump and probe energies independent from each other. In this way the energy of the pump photons can be varied in order to look for a resonant intramolecular excitation, whereas the energy of the probe photons stays the same. Furthermore, in time-resolved 2PPE experiments, initial and intermediate states can be distinguished by their dependence on the pump-probe delay. Figure 4.6a shows a false color plot mapping the 2PPE intensity as a function of pump-probe delay (x-axis) and final state energy (y-axis) for photon energies of $h\nu_1 = 2.32$ eV and $h\nu_2 = 4.20$ eV. Vertical line profiles through this 2D map show the 2PPE spectra at given pump-probe delays. Figure 4.6b shows a series

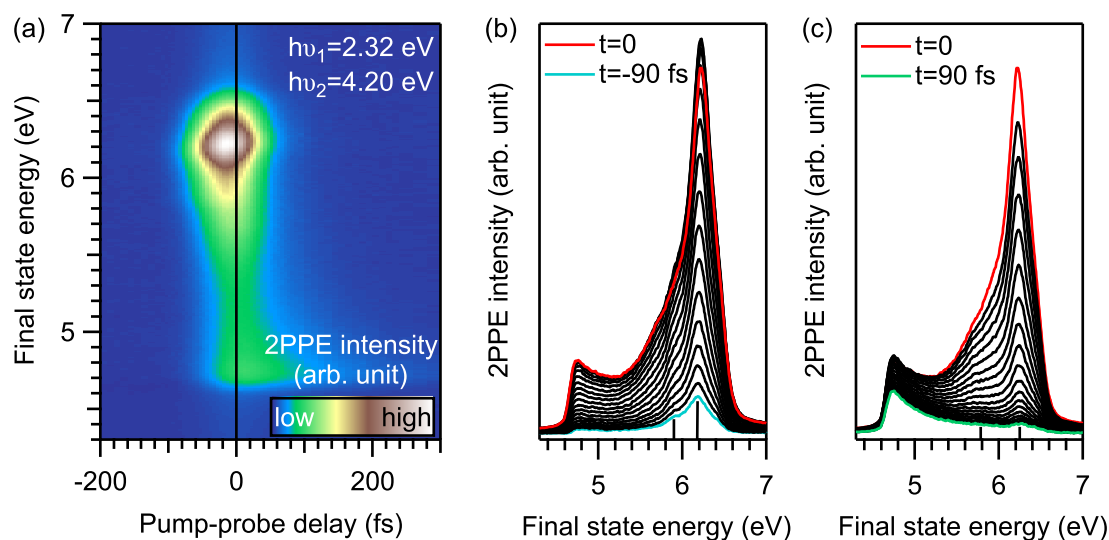


Fig. 4.6: (a) 2PPE intensity as a function of pump-probe delay and final state energy measured with photon energies $h\nu_1=2.32$ eV and $h\nu_2=4.20$ eV. (b) Series of 2PPE spectra at time delays from 0 (red curve) to -90 fs (blue curve) in 5 fs steps. (c) Series of 2PPE spectra at time delays from 0 (red curve) to 90 fs (green curve) in 5 fs steps.

of 2PPE spectra at negative delays (i.e., 4.20 eV is the pump and 2.32 eV the probe photon energy). The spectrum observed when both pulses arrive at the sample at the same time (red curve) shows a shoulder below the IPS/IS detected at a final state energy of 6.2 eV for this combination of photon energies.¹ Tracing the evolution of the 2PPE intensity with increasing pump-probe delay, it can be seen that the shoulder has two components. 300 meV below the image-potential state or interface state a state arises that is not visible for positive time delays where the sample is pumped with 2.32 eV and probed with 4.20 eV (cf. Fig. 4.6c). This state is hence assigned to an intermediate state at 3.6 eV. Since the energy of the UV pulse is not enough to perform an intramolecular excitation from the HOMO into an intermediate state at 3.6 eV, it is concluded that the population of this state arises from charge transfer of excited, hot electrons in the gold substrate. The rather short lived state is hence interpreted as a higher lying unoccupied state (LUMO+n). The second component of the lower energetic shoulder accompanying the IPS or IS, observed at 5.8 eV, vanishes quite symmetric around t_0 and fits energetically to the initial state energy of the HOMO.

Increasing the pump photon energy from 2.32 eV to 3.11 eV, another state appears at a final state energy of 5.60 ± 0.03 eV (cf. Fig. 4.7a,b).² The maximum of this peak is clearly shifted to positive time delay, meaning that it corresponds to an intermediate state at 1.38 eV excited

¹The slight shift of ≈ 60 meV in energy of the image-potential or interface state when comparing negative and positive time delays results from a chirp of the 2.32 eV laser pulse and not from an additional state pumped and probed with the two pulses in the opposite order.

²It has to be noted that the obtained spectra significantly differ from those shown by Varene *et al.* [120], even though the photon energies are close to the ones used in their work. As it will be shown later in Fig. 4.9, the monolayer spectrum found by Varene *et al.* resembles spectra corresponding to film thicknesses of at least 3 ML. It is hence concluded that they underestimated their film thicknesses by a factor of 3, which has to be multiplied with the given coverages in Ref. [120] to compare the data to those presented in this work.

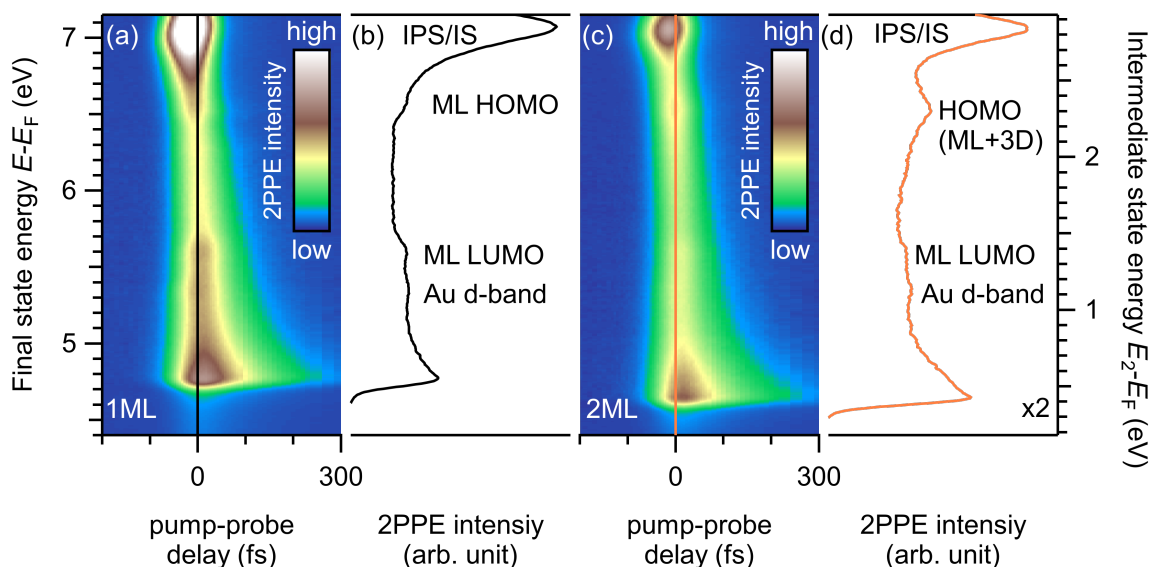


Fig. 4.7: 2PPE data of 6T/Au(111) films measured with $h\nu_1=3.11$ eV and $h\nu_2=4.22$ eV. (a) 2PPE intensity map for a 1 ML thick film. (b) Spectrum at zero pump-probe delay taken from the map shown in (a). (c) 2PPE intensity map for a 2 ML thick film. (d) Spectrum at zero pump-probe delay taken from the map shown in (c).

with 3.11 eV photons. Two possible origins of the peak can be discussed; it may either result from an intramolecular excitation leading to an excitonic state or from the population of an unoccupied molecular states with electrons from the substrate. In the case of an excitonic state, it is disputable which optical transition is driven. The DRS measurements showed that the S_1 absorption band is centered at 2.4 eV with a FWHM of almost 0.5 eV. Photon energies of 2.3 eV and 2.5 eV should hence be sufficient for this excitation, but do not show a clear signature in the tr-2PPE data since a series of other peaks is observed in the same final state range (for 2.5 eV pump photons cf. Sec. A.3.2 or Ref. [104]). On the other hand, the pump pulse photon energy of 3.11 eV is already at the onset of the next absorption band, but this transition is much less intense in the DRS measurements than the S_1 band (cf. Fig. 2.13). I would hence exclude that the peak is originating from an excitonic state and assign it to the lowest unoccupied molecular state of molecules in the first, chemisorbed layer populated by charge transfer from the Au substrate. The short lifetime of the state supports this assignment as well. In accordance with the coverage dependence which will be discussed in the following the state will be denominated ML LUMO.

The wetting layer observed in the PEEM experiments consists of two layers. It can be assumed that the second layer grows in a similar fashion as the first layer. However, the second layer is less bound to the surface than the first layer, as it was observed in TPD experiments [52, 104]. The difference in bonding as well as the different screening of the charged states in the first and second layer by the substrate electrons could lead to shifts in the energetic positions of the molecular states with respect to the Fermi level. Figure 4.7c shows time-resolved 2PPE data with photon energies $h\nu_1=3.11$ eV and $h\nu_2=4.22$ eV recorded for a two-monolayer thick film.

4.2. THE INTERPLAY OF MORPHOLOGY AND ELECTRONIC STRUCTURE IN THIN SEXITHIOPHENE FILMS ON Au(111)

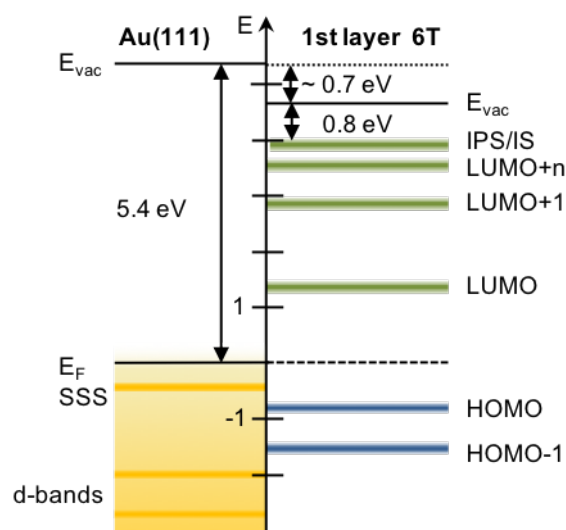


Fig. 4.8: Energy diagram of a monolayer thick 6T film on Au(111). The energies are given with respect to the Fermi level of the gold substrate.

For comparison, the intensity map is scaled to the same color scale as the monolayer map in (a). The 2PPE spectrum extracted from the map at zero pump-probe delay, shown in Fig. 4.7d, is multiplied by a factor of 2 for better visibility of the features. The low-energy cut-off shifts to lower energies for the 2 ML sample with respect to the 1 ML film, which means that the work function decreases. This observation is in agreement with Varene *et al.* and the PEEM experiments shown in the previous section. The number of states and their energetic position is identical for the monolayer and the bilayer samples. The Au d-band at -2 eV, the ML LUMO, the ML HOMO and the IPS or IS are detected. It is evident that the amplitude of the 2PPE signal is reduced over the whole spectrum of the 2 ML film in comparison to the ML coverage. This has to be interpreted as a damping of the 2PPE signal of the ML due to the second layer of molecules on top. The second layer seems to add no contribution besides a broad peak in the energy range of the ML HOMO, which causes a slight gain in the 2PPE signal starting from 6 eV final state energy. As suggested by the 2PPE spectra observed for higher coverages presented in the following, this feature can be interpreted as the HOMO of molecules in the second layer, which shifts to lower initial state energies in comparison to the ML HOMO, due to the lower interaction with the substrate. The coverage dependence of the peak assigned to the ML LUMO supports the assignment to a characteristic of the monolayer. The shift of the LUMO in the monolayer towards lower energies compared to the LUMO in the crystallites [20] is explained by screening of the excess charge by the charge carriers of the substrate [122]. Considering the intermediate state at 3.8 eV (IPS/IS), it is striking that it is observed at the same final state energy for a coverage of one and two layers of 6T and that its amplitude is reduced when the second layer is added. This observation questions if it is an image-potential state or rather an interface state that is confined to the molecule-metal interface. Bronner *et al.* proposed such interface states delocalized parallel to the surface for azobenzene derivatives on Au(111) [123]. Alternatively, staying with the interpretation of an image-potential state one has to conclude that after deposition of the second layer still areas of the bare monolayer exist. These areas would have to be small enough that they cannot be observed in PEEM, but

sufficiently large to support the formation of an image-potential state delocalized parallel to the surface. Nevertheless confinement should shift the IPS to higher binding energies [124].

The electronic structure detected on sample areas covered with the two layers thick wetting layer resembles the electronic structure of the 6T monolayer, which is summarized in Fig. 4.8.

3D Crystallites

Along with the change in morphology, films with an average film thickness of 3 ML or higher show a significantly different electronic structure and dynamics compared with the wetting layer. Figure 4.9 shows the 2PPE intensity map for photon energies $h\nu_1=3.11$ eV and $h\nu_2=4.22$ eV and pump-probe delays ranging from -200 to 300 fs of a 6T film with an average coverage of 3 ML (a) and 10 ML (c). Figures 4.9b and d show the respective 2PPE spectra without delay between pump and probe pulses. At both coverages the IPS or IS and the ML HOMO are still probed, which indicates the presence of sample areas covered only by the wetting layer. The amplitude of the IPS/IS and the ML HOMO signals in the 2PPE spectra are only slightly lower for an average film thickness of 10 ML than for an average film thickness of 3 ML. In disagreement to Varene *et al.* [7, 120], even at a coverage of 30 ML the IPS/IS is observed when the film is prepared at room temperature (cf. Sec. A.3.2, Figure A.6), indicating that the crystallites grow rather in height than in diameter.

In contrast to the electronic structure of the wetting layer, an average film thickness of 3 ML shows an intermediate state with considerable lifetime at an intermediate state energy of 1.2 eV.

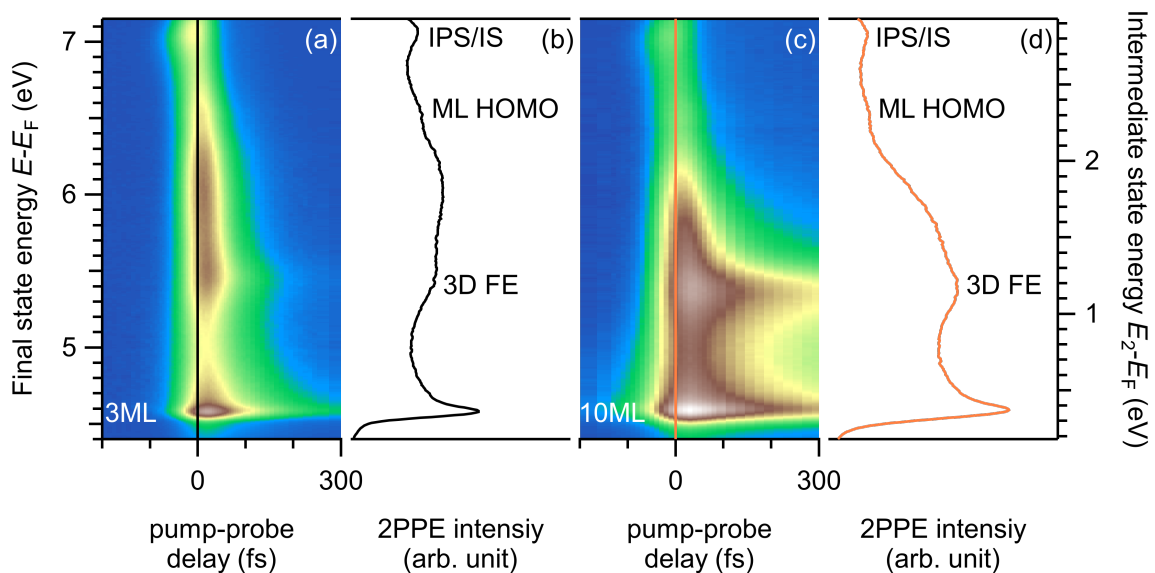
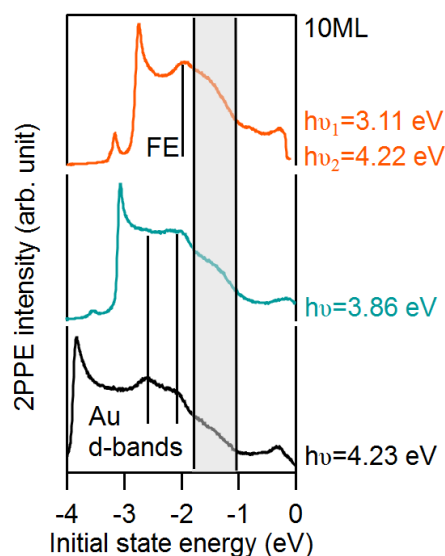


Fig. 4.9: 2PPE data of 6T/Au(111) films measured with $h\nu_1=3.11$ eV and $h\nu_2=4.22$ eV. (a) 2PPE intensity map for a film with an average thickness of 3 ML. (b) Spectrum at zero pump-probe delay taken from the map shown in (a). (c) 2PPE intensity map for a film with an average thickness of 10 ML. (d) Spectrum at zero pump-probe delay taken from the map shown in (d).

Fig. 4.10: 2PPE spectra of a 6T film with an average coverage of 10 ML as a function of initial state energy for excitation with 4.23 eV (black curve), 3.86 eV (turquoise curve) and the correlated signal of 3.11 eV and 4.22 eV (orange curve) photons. The gray shadowed area marks the range of the 3D HOMO.



This state is attributed to the S_1 Frenkel exciton (FE) in agreement with Varene *et al.* [120]. Two important conclusions can be drawn: 1) FEs with a considerable long lifetime can be created only in the crystallites and 2) the wetting layer can be interpreted as a buffer layer that decouples the 6T molecules in the crystallites from the substrate, thus delaying the transfer of the excitation energy into the substrate. Furthermore, the energetic position of the FE depends on the 6T coverage. In case of a film with an average thickness of 10 ML, the FE is detected at ≈ 100 meV lower intermediate state energy and shows significantly longer lifetimes than in the 3 ML film. This observation is in disagreement with the data presented by Varene *et al.* [120], which is attributed to a differing coverage calibration.³ A detailed analysis of the coverage dependent population and relaxation dynamics will be given in Sec. 4.3.

In a broad range of final state energies around 6 eV, essentially covering the whole range between the signatures of the Frenkel exciton and the ML HOMO, a pronounced 2PPE intensity is observed for the 3 ML and the 10 ML coverage. The maximum of the intensity distribution in the discussed energy range is shifted towards positive time delays, which leads to the conclusion that it corresponds to an intermediate state pumped with 3.11 eV photons and hence being energetically located in the range from 1.3 to 2.2 eV above the Fermi level.

Considering the single color 2PPE spectra for excitation with 4.23 eV (black curve in Fig. 4.10) or 3.86 eV (turquoise curve in Fig. 4.10) for the sample with an average coverage of 10 ML, a broad initial state is observed in the range of -1 eV to -1.8 eV, which is here interpreted as the HOMO of the 6T molecules within the crystallites (3D HOMO). If the correlated 2PPE signal of 3.11 eV and 4.22 eV photons shown in Fig. 4.9d is plotted as a function of initial state energies (orange curve in Fig. 4.10), it becomes evident that the broad feature observed above the FE is populated from the 3D HOMO. The 3D HOMO is the initial state for excitations into

³A detailed comparison of the data shown in the publication of Varene *et al.* and the present work suggest that the coverages given by Varene *et al.* are a factor of 3 higher than reported, when following the coverage calibration suggested in this work and by Zielke [104].

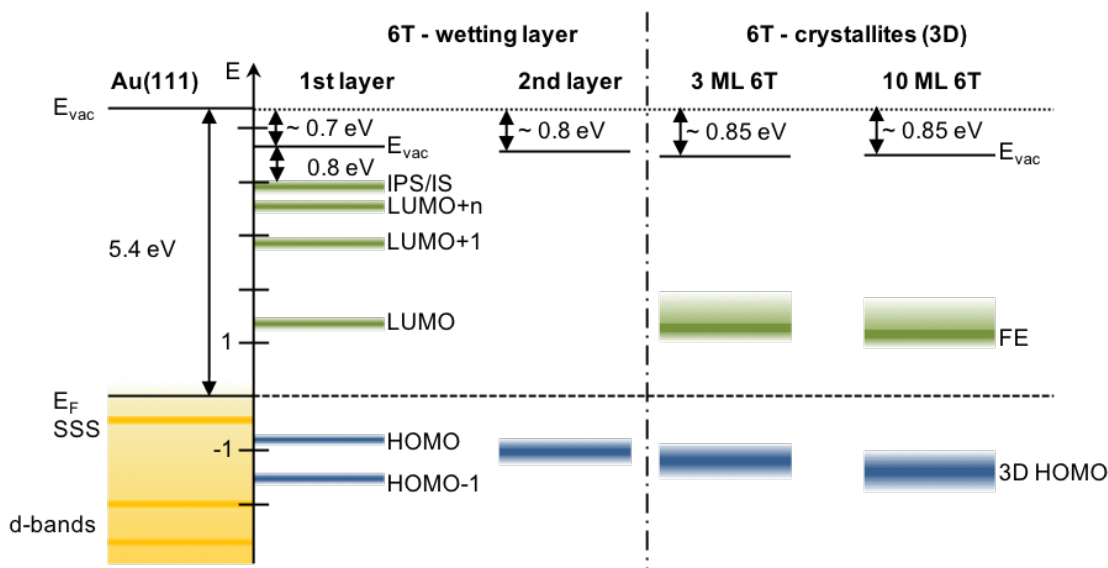


Fig. 4.11: Layer resolved energy diagram of the electronic structure observed for 6T molecules adsorbed on Au(111) including occupied and unoccupied molecular states as well as excitonic states. At the left part of the figure the electronic structure of a clean Au(111) surface is given for comparison.

the FE state. As it is shown in the DRS measurements, 3.11 eV photons have excess energy with respect to the purely electronic excitation of the FE, which results in vibronic excitations as it will be discussed in detail in Sec. 4.3.2. This interpretation is in disagreement with the work of Varene *et al.*, who assigned this state to the LUMO+1 at an intermediate state energy of 3 eV, which would mean that the state is pumped by the 4.22 eV photons and probed by 3.11 eV photons. The data shown in Figures 4.9a,c clearly contradict this assignment. As a summary, Fig. 4.11 shows the electronic structure of 6T on Au(111) observed for different film thicknesses, which is an extended version of the energy diagram sketched for the monolayer in Fig. 4.8. Besides the characteristics of the ML, samples with 6T coverages higher than 3 ML, including crystallites on top of the wetting layer, show a signature of the S_1 Frenkel exciton and a 3D HOMO in the 2PPE data. The assignments given here extend the picture of the electronic structure of 6T/Au(111) drawn by Varene *et al.* [120] by including the coexistence of two different morphologies on the surface (wetting layer and crystallites). These results question the exciton formation process given by the same authors [7]. A new interpretation of the exciton population and relaxation dynamics will be given in the following section of the present chapter.

4.3 Exciton Dynamics in Thin Sexithiophene Films

On the basis of the electronic structure discussed in the previous section, the present section focusses on the analysis of the population and relaxation dynamics of thin 6T films on Au(111). In 2012 Varene *et al.* [7] published the first time-resolved 2PPE data for a 30 ML thick 6T film on Au(111) taken with photon energies of 3.0 and 4.3 eV. Considering the DRS measurements presented in this work (cf. Sec. 4.2.1) and in the PhD thesis of Zielke [104], the pump photon energy of 3.0 eV is at the higher energetic edge of the S_1 absorption band. Varene *et al.* suggested a population process of the S_1 Frenkel exciton where first an electron is excited from the HOMO into the LUMO and the exciton is formed subsequently within 100 fs. They assigned the delayed population of the excitonic state to the decay of the polarization before the population of the state can take place. They hence concluded that photon energies at least as high as the transport gap are needed to induce exciton formation. In the PhD thesis of Kristof Zielke [104] we were able to show that an instantaneous excitation of the S_1 Frenkel exciton is possible when exciting a 10 ML 6T/Au(111) sample with 2.47 eV photons.

Based on the DRS results in the present thesis, time-resolved 2PPE experiments were performed for a series of different pump photon energies in the range of 2.3 to 3.1 eV, to clarify the fundamental processes in 6T exciton dynamics.

4.3.1 Exciton Relaxation Dynamics in α -Sexithiophene Crystallites

To analyze the exciton dynamics in 6T crystallites in dependence of the excitation energy, I will start with the case of a resonant excitation of the S_1 band bottom with a photon energy of 2.3 eV. Figures 4.12a and b show 2PPE intensity maps for average 6T coverages of 1 and 10 ML on Au(111) using photon energies of $h\nu_1=2.32$ eV and $h\nu_2=4.19$ eV. To immobilize the molecules and reduce the secondary electron background, the measurements shown here are performed under liquid nitrogen cooling of the sample after film preparation at room temperature. As described in Sec. 4.2, the population of the S_1 Frenkel exciton (appearing with its maximum at a final state energy of 5.3 eV) is observed only for molecules within crystallites on top of the wetting layer. To determine the population dynamics of the state, the 2PPE intensity is analyzed as a function of pump-probe delay. In order to capture the whole peak, the 2PPE intensity is summed over the final state energies from 4.9 to 5.6 eV. The corresponding cross-correlation curves for 1 and 10 ML films and pump-probe delays up to 1 ps are shown in Fig. 4.12c. Figure 4.12d shows the population decay up to pump-probe delays of 120 ps for the case of a 10 ML film. The 2PPE intensity on the y-axis is plotted on a logarithmic scale, so that it becomes clear that the decay behavior is multi-exponential. A coverage dependent analysis of the cross-correlation curves as performed by Varene *et al.* [7] and K. Zielke in his PhD thesis [104] shows that the longest decay constant increases with increasing 6T coverage. We attribute this behavior to distance dependent transfer rates of the exciton energy from the molecules to the gold substrate. Since the pump and probe pulses in 2PPE excite and

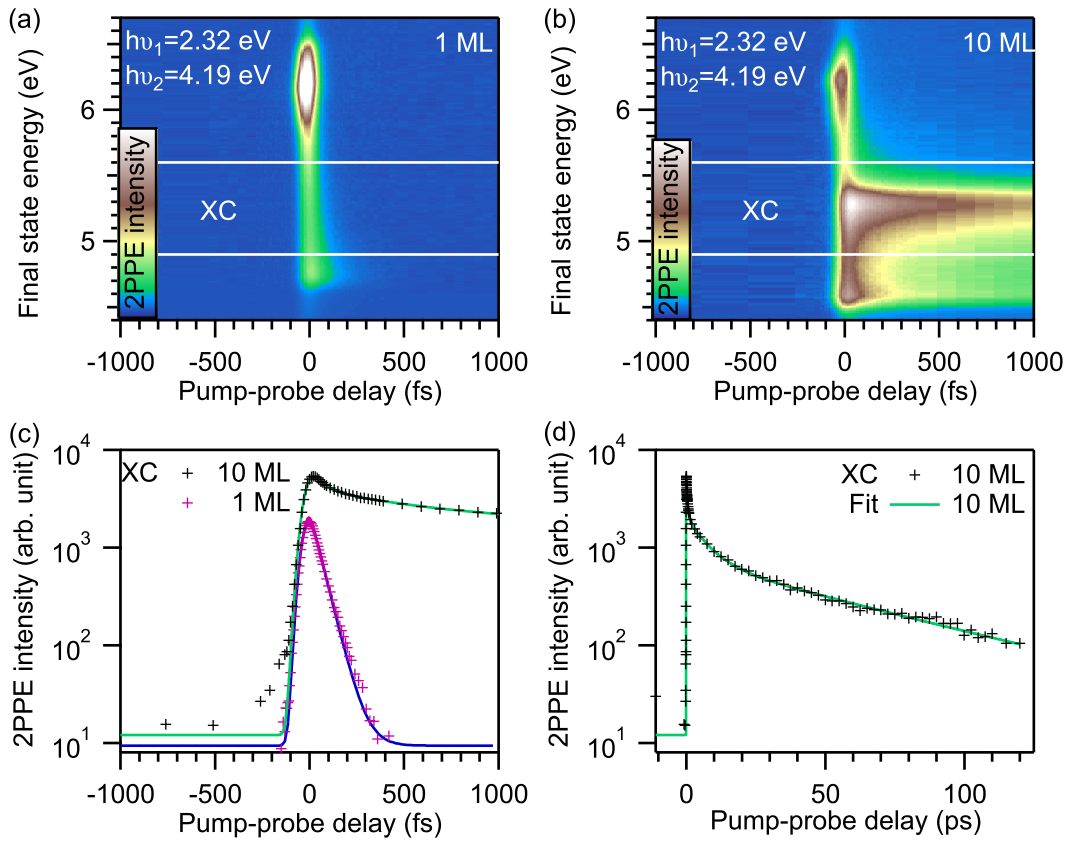


Fig. 4.12: **(a)** 2PPE intensity map as a function of final state energy and pump-probe delay observed for a 1 ML thick 6T film on Au(111) cooled to 120 K after preparation at room temperature. The data were recorded with photon energies of $h\nu_1=2.32$ eV and $h\nu_2=4.19$ eV. **(b)** 2PPE intensity map observed for a 6T film on Au(111) with an average thickness of 10 ML. The data were recorded under similar measurement conditions as in (a). **(c)** Cross-correlation (XC) curves extracted from the maps shown in (a) and (b) summed over the final state energy interval from 4.9 to 5.6 eV are shown by magenta and black markers for the 1 and 10 ML film, respectively. The solid blue curve corresponds to a fit with a single-exponential decay, whereas the green curve displays a fit with a fourfold exponential decay. **(d)** Cross-correlation curve for delays up to 120 ps for the 10 ML film summed over the same energy range as in (c).

probe excitons throughout the film, the measured signal contains information about the decay time in each layer. To describe the depopulation dynamics of the exciton ensemble four exponential functions with decay coefficients distributed over four orders of magnitude are used as representatives for the continuous distribution of decay times. The shortest lifetime is mainly influenced by the dynamics of hot electrons excited in the gold substrate. Therefore the cross-correlation of a 1 ML thick film is evaluated in the same energy range where the FE is found in thicker layers. The corresponding data are shown by the magenta markers in Fig. 4.12c. The cross-correlation curve is fitted according to Eq. 3.11 with a single exponential decay with a decay constant $\tau = (55 \pm 1)$ fs. The corresponding fit is shown by the solid blue curve. The cross-correlation of the 10 ML film is shown in Fig. 4.12c and d by black markers and the fourfold exponential fit of the data is shown by the green solid line. Assuming the fastest decay constant τ_1 to be determined by the dynamics of the hot electrons and therefore fixing it to 55 fs, the other three decay constants are fitted to be $\tau_2 = (580 \pm 30)$ fs, $\tau_3 = (6.9 \pm 0.6)$ ps and

4.3. EXCITON DYNAMICS IN THIN SEXITHIOPHENE FILMS

$\tau_4 = (58 \pm 4)$ ps and the amplitude ratios $A_2/A_1 = 0.53$, $A_3/A_1 = 0.33$ and $A_4/A_1 = 0.18$.

In order to compare the results obtained in the present work with those obtained in a former study by using an excitation energy of 2.47 eV [104], Fig. 4.13 shows the cross-correlation curves observed on a film with an average thickness of 10 ML integrated over final state energies in the range from 4.9 eV to 5.6 eV for both excitation energies, 2.32 eV (black curve) and 2.47 eV (red curve). Both curves run parallel with respect to each other over the whole range of measured pump-probe delays, which indicates that the results are identical within the measurement accuracy.

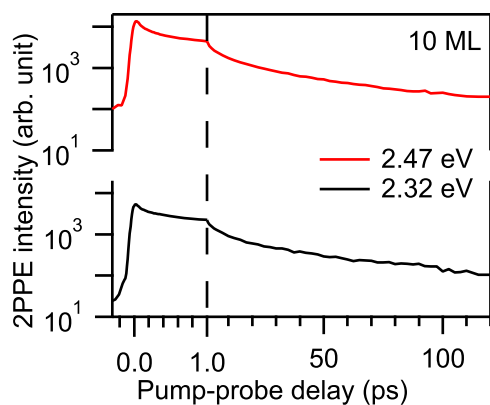


Fig. 4.13: Comparison of the population decay dynamics of a 6T film with an average thickness of 10 ML for excitation with 2.47 eV (red curve) and 2.32 eV (black curve). Both curves show the same multi-exponential decay, indicated by their parallel run over the whole range of pump-probe delays. The dashed vertical line marks a change in the scaling of the x-axis.

4.3.2 Vibrational Hot Exciton Relaxation

The black curve in Fig. 4.14a shows an example spectrum of a 6T coverage of 10 ML observed at 1.2 ps after excitation with 2.3 eV photons. The spectrum is dominated by the Frenkel exciton peak which has an asymmetric shape. As suggested by Zielke [104], the asymmetry of the exciton peak to lower final state energies can be explained by the excitation of vibrations in the photoemission process, leading to a lower kinetic energy of the emitted electron. The process is sketched in Fig. 4.14b. Starting from non-vibrating 6T molecules, the excitation of the 6T molecules with a photon energy of 2.3 eV only allows for the population of the vibrational ground state of the exciton state. After excitation the molecule is therefore in the intermediate state $|x\rangle$ in the ν_0 level. The probe photon, which induces photoemission then leaves the system in a final state $|f\rangle$, where the molecule is singly ionized and in a particular vibrational mode. The probability to leave the molecule in a particular vibrational level is given by the Frank-Condon factors for a transition from the vibrational ground state of the intermediate state into the respective final state level. In a collaboration with Dr. Ralph Püttner we performed model calculations on the basis of a single-molecule picture, so far excluding environmental effects as the influence of the aggregate formation. We assumed a harmonic potential for the intermediate state and allowed the final state to be anharmonic. It was possible to determine Frank-Condon factors, which would lead to the observed peak asymmetry. The blue curve in Fig. 4.14a shows a fit to the spectrum according to the model, in

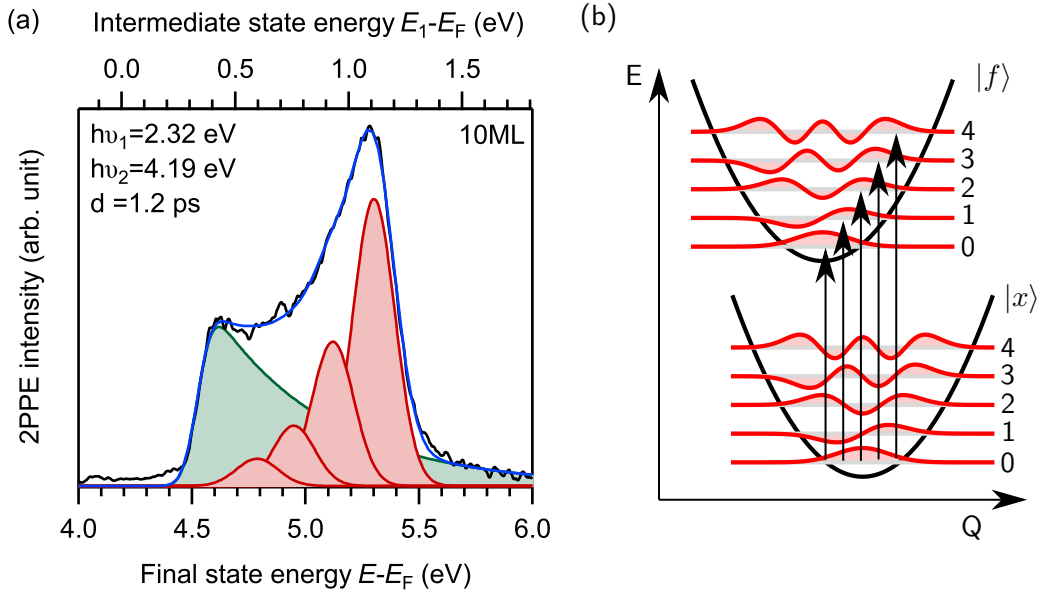


Fig. 4.14: **(a)** 2PPE spectrum (black curve) of a 6T film with an average thickness of 10 ML measured at a time delay of 1.2 ps between pulses with photon energies $h\nu_1=2.32$ eV and $h\nu_2=4.19$ eV. The 6T film was prepared at room temperature and afterwards cooled down to 120 K to perform the measurement. The blue curve presents a fit to the data, which considers a secondary electron background (green shadowed area) and losses in the kinetic energy of the emitted electrons due to the excitation of the breathing mode of the 6T molecule by the probing photon. **(b)** Schematic illustration of the probe process, considering the possibility of the excitation of molecular vibrations.

which we assumed that in the intermediate state only the vibrational ground state is occupied. The green curve describes the secondary electron background. The fit gives an anharmonicity for the final state leading to a reduction of the spacing between the vibronic sublevels with increasing level: $\Delta\nu_{01} = 181$ meV, $\Delta\nu_{12} = 172$ meV, $\Delta\nu_{23} = 161 \pm$ meV and $\Delta\nu_{34} = 153$ meV. The contributions of the four transitions to the fit are shown by the red curves in Fig. 4.14a. Furthermore, the fit gives a shift between the potential energy curves of intermediate and final state so that the Franck-Condon factors $P_{\nu\nu'}$ corresponding to a transition from $\nu = 0$ in the intermediate state to the four lowest vibronic sublevels of the final state ν' are found to be: $P_{01} = 0.52$, $P_{02} = 0.26$, $P_{03} = 0.11$ and $P_{04} = 0.05$.

In the present work, I investigate the influence of vibrational excitations in the intermediate excitonic state on the photoemission spectrum. If the excitation energy is changed from resonant excitation of the band bottom as discussed in Sec. 4.3.1 to off-resonant excitation with excess energy, the 2PPE spectrum changes for short pump-probe delays. Figure 4.15a shows the 2PPE map for an average 6T coverage of 10 ML as a function of intermediate state energy and pump-probe delay for a resonant excitation with 2.32 eV (left) in comparison to an off-resonant excitation with 3.11 eV (right). In both cases the exciton state at an intermediate state energy of ≈ 1.1 eV is observed with a decay constant of several ps. For short pump-probe delays, the excess energy leads to a higher energetic shoulder of the exciton peak, as it becomes obvious in the zoom-in shown in Fig. 4.15b and in the series of spectra taken for different pump-probe

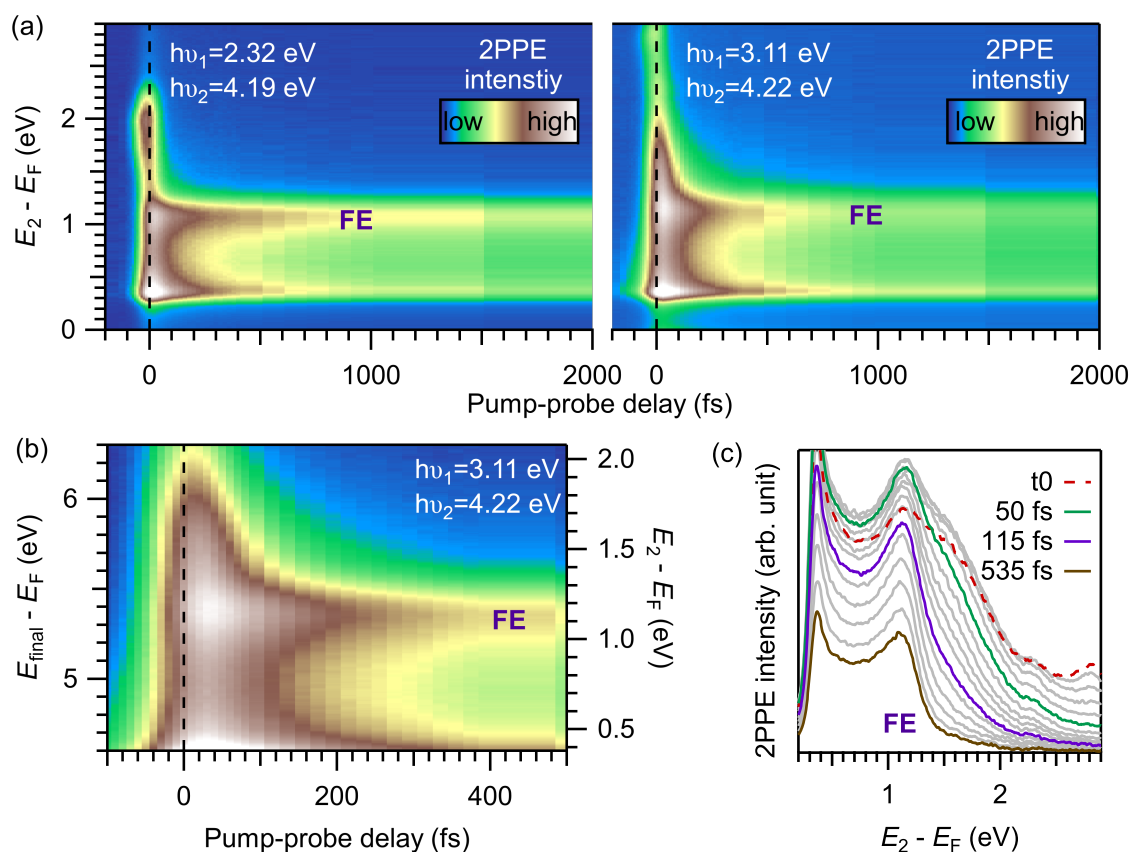


Fig. 4.15: (a) 2PPE intensity maps of 6T films with an average thickness of 10 ML. The map at the left side was measured with photon energies of $h\nu_1=2.32$ eV and $h\nu_2=4.19$ eV and the map at the right side with photon energies of $h\nu_1=3.10$ eV and $h\nu_2=4.22$ eV. Both samples are prepared and measured at room temperature. The exciton peak at the intermediate state energy of 1.1 eV shows a short-lived higher energetic shoulder when exciting with $h\nu_1=3.10$ eV instead of 2.32 eV. (b) Zoom-in of the 2PPE intensity map measured with $h\nu_1=3.10$ eV and $h\nu_2=4.22$ eV. (c) Series of 2PPE spectra for different pump-probe delays taken from the map at the right side of part (a). Within the first 0.5 ps, the higher energetic shoulder of the exciton peak has completely disappeared.

delays presented in Fig. 4.15c. The shoulder of the exciton peak spreads up to 6.2 eV final state energy, which corresponds to an intermediate state energy of 2 eV. The presence of this shoulder was already shortly discussed when discussing the coverage dependent electronic structure of 6T/Au(111) in Sec. 4.2.2. It was pointed out that the extension of the shoulder of the exciton peak energetically overlaps with a projection of the 3D HOMO. However, as it is seen in the series of spectra in Fig. 4.15c, the shoulder decays with a finite lifetime and completely vanishes within the first 500 fs after excitation with 3.11 eV pulses. This behavior suggests a resonant excitation from the 3D HOMO into an intermediate state. In the following I will discuss the possibility of a vibronic excitation, which means that absorption of the 3.11 eV photons induce an electronic excitation of the S_1 Frenkel exciton accompanied by a vibrational excitation of the excited molecule.

A photon energy of 3.11 eV contains an excess energy of 0.8 eV with respect to the resonant excitation of the exciton band bottom. Since the spacing between the vibronic sublevels is 180 meV, the excess energy is sufficient to excite electrons from the HOMO of a non-vibrating

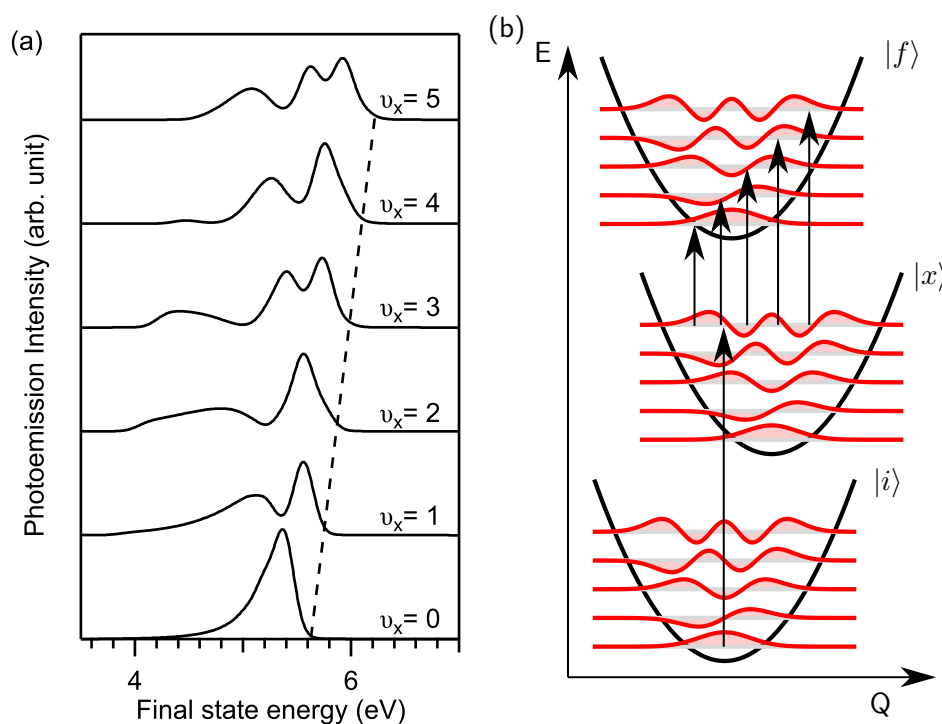


Fig. 4.16: **(a)** Simulated photoemission spectra corresponding to a vibronic transition from an intermediate state with occupied vibrational level ν_x to all available vibrational levels of the final state corresponding to a vibrating single ionized molecule. **(b)** Schematic illustration of the vibronic transitions from a non-vibrating molecule in the ground state (initial state $|i\rangle$) into an electronically and vibrational excited intermediate state $|x\rangle$ (here exemplarily a resonant excitation of the $\nu_x = 4$ level is sketched) followed by a second vibronic transition into a final state, where a singly ionized molecule is left in a certain vibrational state and a photoelectron is emitted, which takes away the difference in energy.

molecule into the fourth or fifth vibrational level of the intermediate, excitonic state. Figure 4.16 shows a simulation of the photoemission spectrum in the case of a vibronic transition from a specific vibrational level ν_x in the intermediate state into all available vibrational levels ν' of the final state taking relative shift and anharmonicity from the fit of the photoemission spectrum from the $\nu_x = 0$ intermediate state. Following the evolution of the simulated photoemission spectrum, one can see that the high energy end of the distribution shifts to higher energies. Starting from $\nu_x = 4$, final state energies up to 6.1 eV can be reached. This qualitatively fits to the observation that an excitation energy of 3.11 eV leads to a high energetic shoulder of the exciton peak for short pump-probe delays.

As it is shown in the data presented in Fig. 4.15b and c, the higher energetic shoulder of the exciton peak vanishes completely within the first 500 fs after excitation. To investigate whether the shoulder of the exciton peak arises due to the excitation of vibrations in the pumping step, a model based on rate equations is applied that describes the dynamics of the electronic and vibrational relaxation processes. Assuming that relaxation of the excited vibrations is a stepwise process with equal decay constants τ_ν from one vibrational level to another, the following set of differential equations describes the vibrational relaxation process starting from the fifth

vibrational level:

$$\begin{aligned}
 \frac{dN_5(t)}{dt} &= -\tau_\nu^{-1} N_5(t) \\
 \frac{dN_4(t)}{dt} &= \tau_\nu^{-1} (N_5(t) - N_4(t)) \\
 \frac{dN_3(t)}{dt} &= \tau_\nu^{-1} (N_4(t) - N_3(t)) \\
 \frac{dN_2(t)}{dt} &= \tau_\nu^{-1} (N_3(t) - N_2(t)) \\
 \frac{dN_1(t)}{dt} &= \tau_\nu^{-1} (N_2(t) - N_1(t)) \\
 \frac{dN_0(t)}{dt} &= \tau_\nu^{-1} N_1(t).
 \end{aligned} \tag{4.1}$$

$N_i(t)$ is the number of excited molecules with electrons occupying the vibrational sub-level ν_i of the S_1 exciton state. As the simplest approach the relaxation time of all sub-levels besides the ground state are assumed to be equal.

The general solutions of the differential equations 4.1 are:

$$\begin{aligned}
 N_5(t) &= N_5(0) \cdot e^{-\tau_\nu^{-1} \cdot t} \\
 N_4(t) &= \left(N_5(0) \cdot \tau_\nu^{-1} \cdot t + N_4(0) \right) \cdot e^{-\tau_\nu^{-1} \cdot t} \\
 N_3(t) &= \left(\frac{N_5(0)}{2} \cdot \tau_\nu^{-2} \cdot t^2 + N_4(0) \cdot \tau_\nu^{-1} \cdot t + N_3(0) \right) \cdot e^{-\tau_\nu^{-1} \cdot t} \\
 N_2(t) &= \left(\frac{N_5(0)}{6} \cdot \tau_\nu^{-3} \cdot t^3 + \frac{N_4(0)}{2} \cdot \tau_\nu^{-2} \cdot t^2 + N_3(0) \cdot \tau_\nu^{-1} \cdot t + N_2(0) \right) \cdot e^{-\tau_\nu^{-1} \cdot t} \\
 N_1(t) &= \left(\frac{N_5(0)}{24} \cdot \tau_\nu^{-4} \cdot t^4 + \frac{N_4(0)}{6} \cdot \tau_\nu^{-3} \cdot t^3 \right. \\
 &\quad \left. + \frac{N_3(0)}{2} \cdot \tau_\nu^{-2} \cdot t^2 + N_2(0) \cdot \tau_\nu^{-1} \cdot t + N_1(0) \right) \cdot e^{-\tau_\nu^{-1} \cdot t} \\
 N_0(t) &= - \left[N_5(0) \cdot \left(1 + \tau_\nu^{-1} \cdot t + \frac{1}{2} \cdot \tau_\nu^{-2} \cdot t^2 + \frac{1}{6} \cdot \tau_\nu^{-3} \cdot t^3 + \frac{1}{24} \cdot \tau_\nu^{-4} \cdot t^4 \right) \right. \\
 &\quad + N_4(0) \cdot \left(1 + \tau_\nu^{-1} \cdot t + \frac{1}{2} \cdot \tau_\nu^{-2} \cdot t^2 + \frac{1}{6} \cdot \tau_\nu^{-3} \cdot t^3 \right) \\
 &\quad + N_3(0) \cdot \left(1 + \tau_\nu^{-1} \cdot t + \frac{1}{2} \cdot \tau_\nu^{-2} \cdot t^2 \right) \\
 &\quad \left. + N_2(0) \cdot \left(1 + \tau_\nu^{-1} \cdot t \right) + N_1(0) \right] \cdot e^{-\tau_\nu^{-1} \cdot t} + \sum_{i=0}^5 N_i(0).
 \end{aligned} \tag{4.2}$$

Besides the decay into lower vibrational levels of the exciton state, the exciton state itself can decay, as shown before for the case of the excitation with 2.3 eV. Therefore, to describe the population dynamics of the exciton peak, the equations for each vibrational level i given in 4.2

are multiplied with a multi-exponential decay to obtain the relaxation dynamics in dependence of the populated vibrational sub-level in the intermediate state:

$$N_i^*(t) = N_i(t) \cdot \sum_j A_j \cdot e^{-t/\tau_j}. \quad (4.3)$$

As previously done, four exponential decays with different orders of magnitude of the decay constant are used to approximate the continuum of decay constants.

In a simple picture starting from the single molecule approach, the pump pulse should only populate those vibrational sub-levels which are resonantly excitable from the initial state (an electronically non-excited, non-vibrating molecule). In the case of an excitation energy of 3.11 eV one can assume that the 4th and 5th vibrational level are equally occupied and all others are unoccupied: $N_5(0) = N_4(0) = A$; $N_3(0) = N_2(0) = N_1(0) = N_0(0) = 0$.

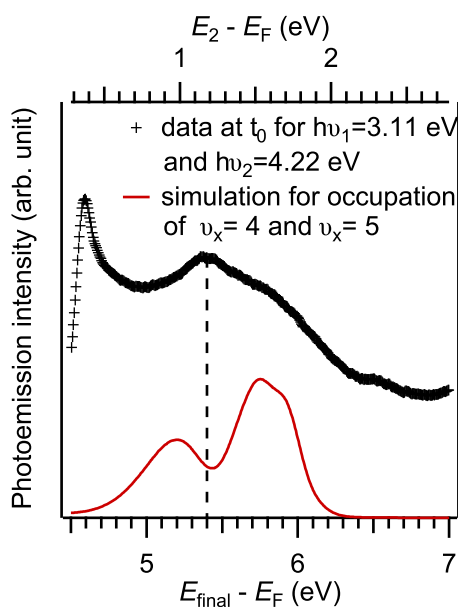


Fig. 4.17: Comparison of the 2PPE spectrum measured with photon energies of $h\nu_1=3.10$ eV and $h\nu_2=4.22$ eV at zero time delay between the two pulses (black markers) and the sum of the calculated photoemission signals for photoemission from the $\nu_x = 4$ and $\nu_x = 5$ levels of S_1 Frenkel exciton peak (red curve).

Comparing the resulting spectrum when adding the spectra calculated for $\nu_x = 4$ and $\nu_x = 5$ with the measured data at zero time delay between the two pulses (cf. Fig. 4.17), the simulated spectrum shows a minimum where the data show a maximum (indicated in Fig. 4.17 by the dashed line). The intensity in this energy range would be filled up by occupation of the $\nu_x = 0$ level. Assuming that there is no initial occupation of this level, one has to assume a decay constant of the vibrational relaxation shorter than the temporal duration of the pulses. A qualitative agreement with the measured spectrum at zero pump-probe delay would be reached assuming τ_ν in the order of 10 fs, as shown by the simulation presented in the following.

Using the photoemission intensity curves calculated for photoemission from the different vibrational sub-levels of the intermediate state, depicted in Fig. 4.16a, and the derived population dynamics (Eq. 4.3), it is possible to simulate the photoemission data in dependence of the vibrational decay constant τ_ν . Vibrational relaxation time constants of less than 100 fs have been suggested by Kersting *et al.* [125] when studying a π -conjugated polymer and its oligomers.

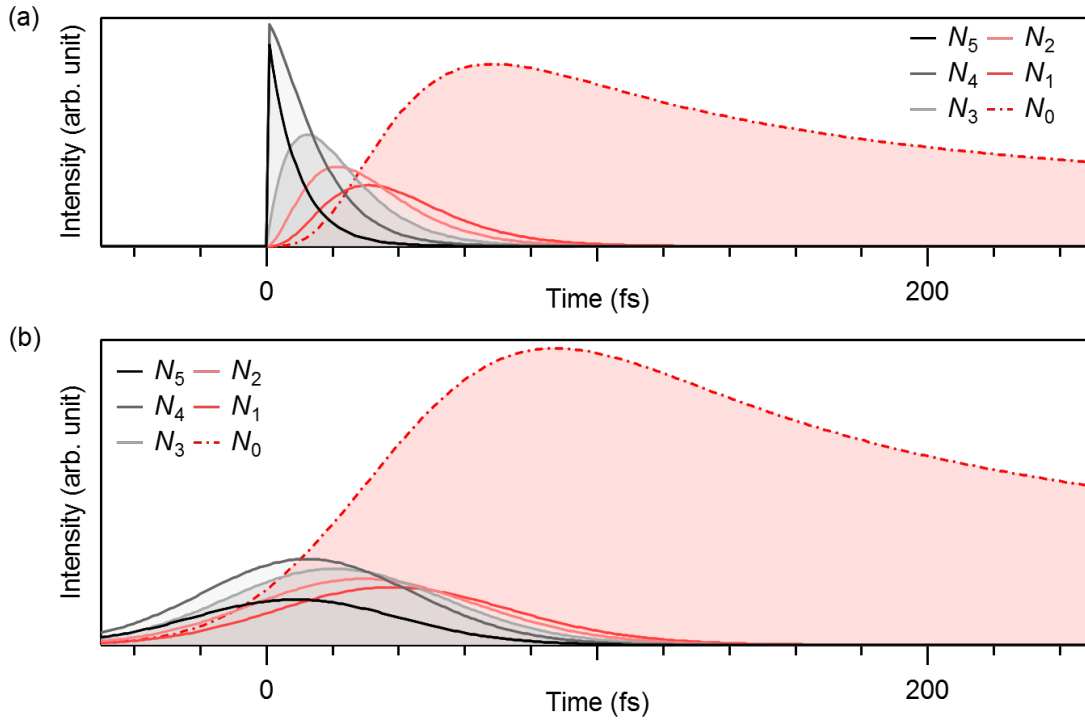


Fig. 4.18: **(a)** Temporal evolution of the population of the i th vibrational sub-level of the S_1 Frenkel exciton state according to Eq.4.3 assuming $\tau_\nu = 10$ fs and a multi-exponential decay of the exciton state with a fastest time constant of 50 fs. **(b)** Resulting cross-correlation curves for the convolution of the population curves shown in (a) and the cross-correlation intensity curve of the laser pulses.

Figure 4.18a shows the population and relaxation dynamics within the first 250 fs after excitation according to Eq. 4.3 assuming $\tau_\nu = 10$ fs and exponential decay constants of the exciton derived from the data in Fig. 4.15 measured with photon energies of $h\nu_1=3.10$ eV and $h\nu_2=4.22$ eV .

In order to simulate a real experiment, the cross-correlation intensity of the laser pulses has to be taken into account as well. Accordingly, Fig. 4.18b shows the convolution of the cross-correlation intensity curves of the laser pulses I_{XC} and the population dynamics according to Eq. 4.3. The higher vibrationally excited states are significantly broadened, which strongly reduces their maximal amplitudes. Multiplying the temporal evolution of the population of the different vibrational levels with the corresponding photoemission spectra, the contribution of the single levels to the time-resolved photoemission data can be simulated. The resulting intensity maps as a function of final state energy and pump-probe delay are shown in Fig. 4.19a. The sum of these maps, which is shown in Fig. 4.19b, has to be compared to the measured 2PPE data. Figure 4.19c shows a series of spectra extracted from the map shown in part (b) of the figure. The spectra at $t=0$ (red dashed dotted), 50 fs (green), 100 fs (purple) and 500 fs (black) are highlighted. Note, that the simulation does not include secondary electron backgrounds or photoemission signals from the substrate which cause an increase in the photoemission signal of the experimental data at final state energies below the exciton peak.

When comparing the simulation to the experimental data, two characteristics of the time-resolved 2PPE spectra are considered: the spectrum at zero time delay and the population

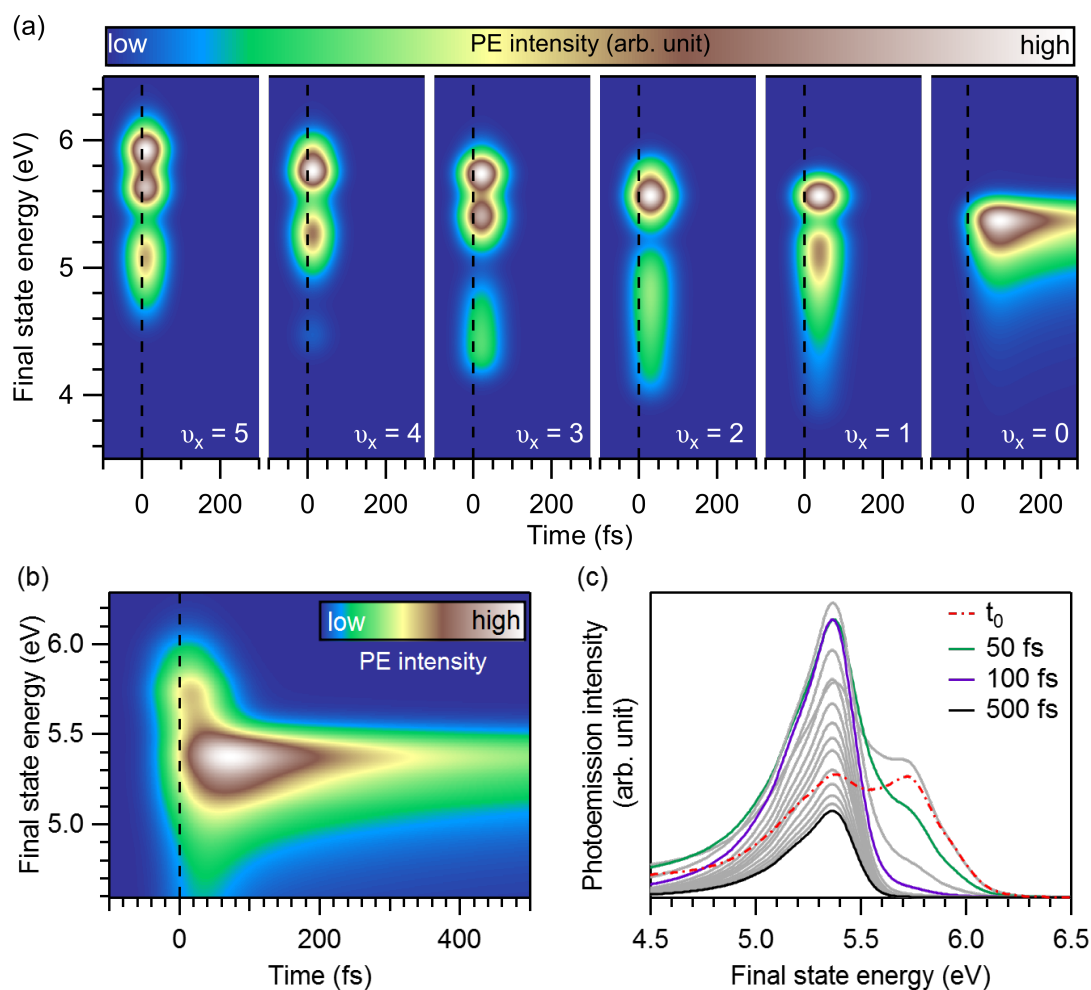


Fig. 4.19: Simulation of time-resolved photoemission including vibrational excitations in the pumping step. **(a)** Simulation of the 2D maps corresponding to photoemission from the vibrational sub-levels ν_x of the S_1 exciton state considering the population curves $N_i(t)$ shown in Fig. 4.18b. **(b)** Sum of the maps shown in (a). **(c)** Series of spectra for different time delays taken from (b).

dynamics taken as a cross-correlation integrated over the energy range of the exciton peak. Whereas the spectrum at $t = 0$ qualitatively agrees with the data (cf. Fig. 4.15c) since it shows the FE band bottom corresponding to the $\nu_x = 0$ contribution as well as a higher energetic shoulder, the dynamics is not described in a sufficiently proper way. The intensity in the higher energetic shoulder, which corresponds to higher vibrational sub-levels, already vanishes within the first 100 fs. This means that the vibrational decay constant of $\tau_\nu = 10$ fs is too fast to reproduce properly the experimental data. However, if a longer time for the decay constant is used, the spectrum at $t = 0$ cannot be reproduced anymore, since this reduces the intensity of the $\nu_x = 0$ branch. An example for a simulation with $\tau_\nu = 70$ fs is shown in Fig. A.7 in Sec. A.3.3 of the appendix. Here, the decay of the intensity of the higher vibrational levels fits quite well to the data, but the initial spectra includes no contribution from photoemission from the $\nu_x = 0$ branch.

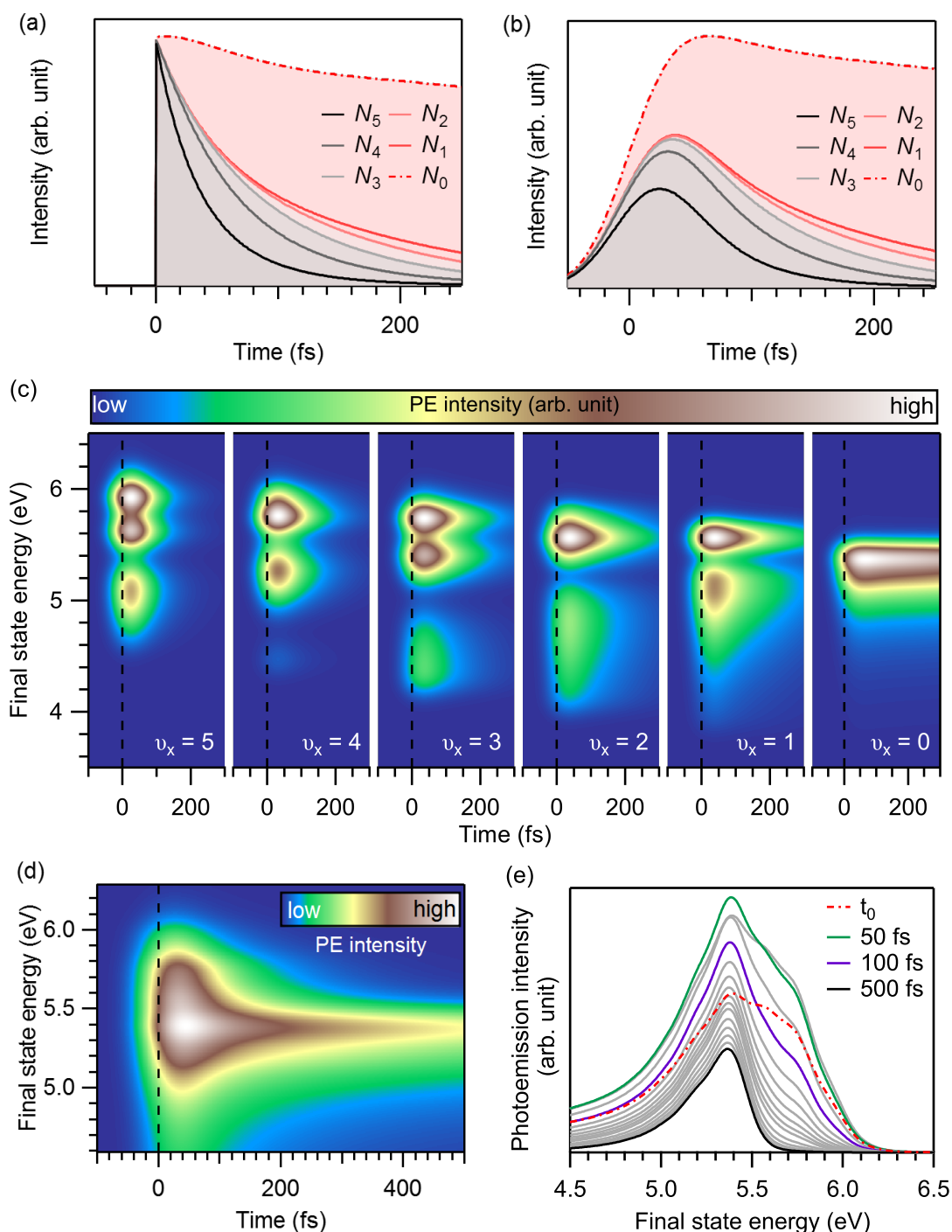


Fig. 4.20: Simulation of time-resolved photoemission including vibrational excitations in the pumping step. **(a)** Temporal evolution of the population of the i th vibrational sub-level of the S_1 Frenkel exciton state according to Eq.4.3 assuming all vibrational levels being equally occupied in the beginning, $\tau_\nu = 70$ fs and a multi-exponential decay of the exciton state with a fastest time constant of 50 fs. **(b)** Resulting cross-correlation curves for the convolution of the population curves shown in (a) and the cross-correlation intensity curve of the laser pulses. **(c)** Simulation of the 2D maps corresponding to photoemission from the vibrational sub-levels ν_x of the S_1 exciton state considering the population curves $N_i(t)$ shown in (b). **(d)** Sum of the maps shown in (c). **(e)** Series of spectra for different time delays taken from (d).

Consequently, it is not possible to describe both, the spectrum at zero time delay and the

population dynamics observed for the higher energetic shoulder of the exciton peak with the approach of populating only $\nu_x = 4$ and $\nu_x = 5$ with the pump pulse.

The so far discussed approach is based on a single molecule picture. However, in an aggregate, the molecules are embedded in a molecular matrix. As Spano [117, 126] suggested, besides the transfer of the whole energy to one molecule within the matrix, there is also a finite probability to vibrationally excite molecules in the surrounding of the electronically excited molecule due to their interaction. In this way, the electronically excited molecule ends up in a lower vibrationally excited state than it would reach when all the energy of the exciting photon is transferred to it. Spano described this collective excitation of a vibronic excitation of one molecule and a purely vibrational excitation of another molecule vibronic/vibrational pair.

Allowing for vibronic/vibrational pair excitations as well, in a first approach all initial populations of the vibrational levels ν_x up to the levels corresponding to the direct excitation are estimated to be equal: $N_i(0) = A$. Using this assumption for the initial population, a vibrational decay constant of $\tau_\nu = 70$ fs and the multi-exponential exciton decay parameters as before, the simulation has a much better qualitative agreement with the data, as it is shown in Fig. 4.20. At zero pump-probe delay the simulated spectrum shows a reasonable contribution of photoemission from the $\nu_x = 0$ level as well as a pronounced higher energetic shoulder, as it is the case in the measured data (cf. Fig. 4.15c). Furthermore, the shoulder vanishes on a time scale comparable with the measured one.

A quasi instantaneous equal population of all sub-levels requires on one hand that vibronic/vibrational pair excitations represent the dominant excitation channel and on the other hand that the dephasing of these pair excitations occurs on the few fs time-scale to convert the polarization into a population [91]. Further input from theory would be needed to elucidate the role of vibronic/vibrational pair excitations. The discussion so far based on potential energy curves deduced from the single molecule picture. However, the formation of an aggregate can also distort the potential energy curves. This would change the Franck-Condon factors of the transitions.

4.3.3 Morphology Induced Changes in the Exciton Dynamics

The time-resolved data for excitation with 3.11 eV presented in Sec. 4.3.2 differ from time-resolved 2PPE experiments performed by Varene *et al.* for pump photons at an energy of 3 eV [7]. They observed an approximately gaussian shaped intensity distribution which sharpens and shifts to lower energies with increasing pump-probe delay and shows a double-exponential behavior. This observation lead them to the conclusion that the fast energy shift of the intensity distribution corresponds to the time-scale of the exciton formation process, which they determined to be in the order of 100 fs. The data shown in Sec. 4.3.1 and 4.3.2 of this work clearly show that the population of the exciton state happens within the pulse-width of the laser pulses and is hence much faster than suggested by Varene *et al.* Furthermore, no shift in

4.3. EXCITON DYNAMICS IN THIN SEXITHIOPHENE FILMS

energy of the exciton band bottom was observed. The difference between the data presented by Varene *et al.* and in this work, which were measured with comparable photon energies, is attributed to differing film morphologies, as it will be explained in the following.

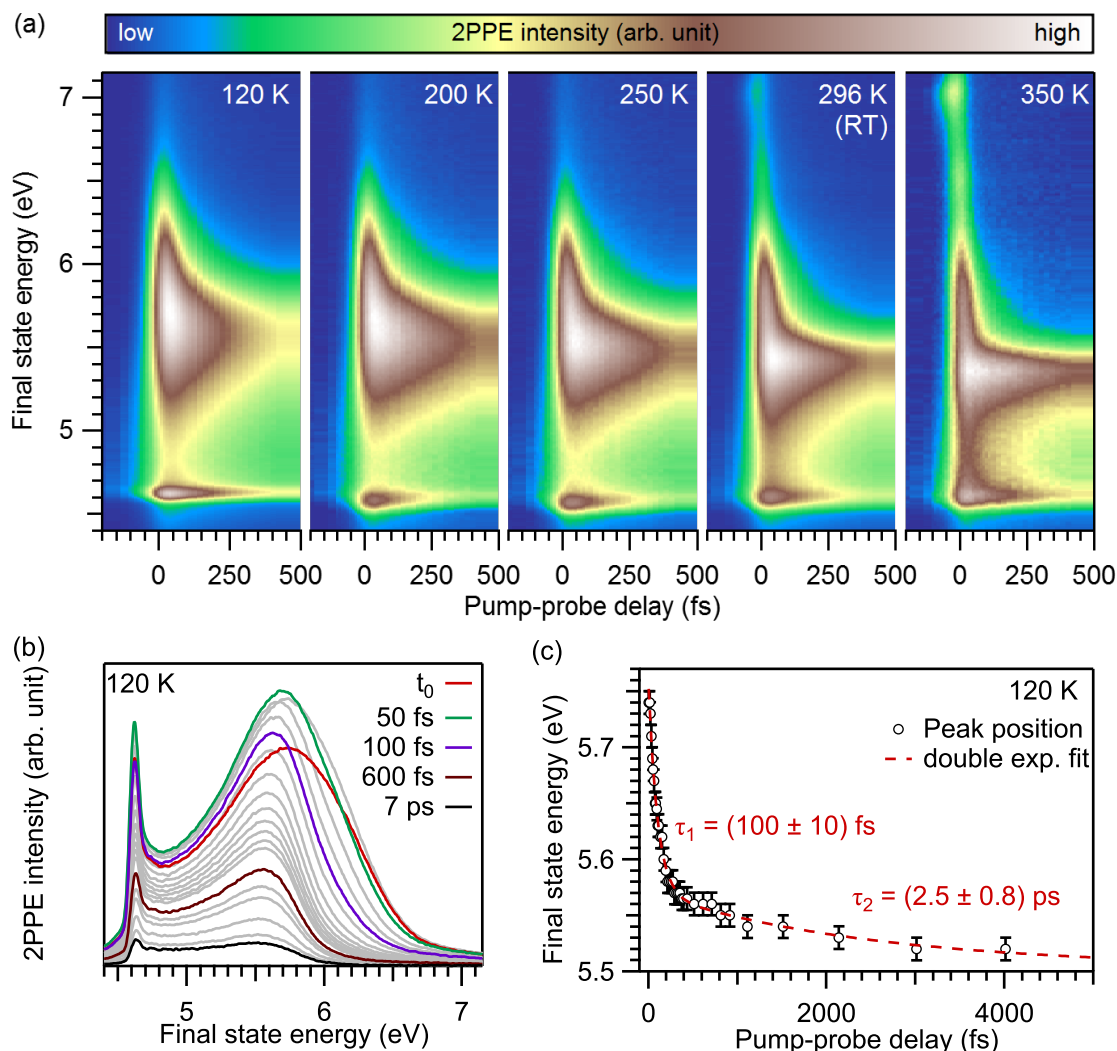


Fig. 4.21: **(a)** Film morphology dependent 2PPE intensity as a function of final state energy and pump-probe delay for excitation of a 6T film with an average thickness of 10 ML with $h\nu_1=3.10$ eV and $h\nu_2=4.22$ eV. The film was deposited on the Au(111) single crystal surface at 120 K and then stepwise heated up to a maximal temperature of 350 K. After each heating step the sample was cooled down again to record data. **(b)** Series of spectra taken for different pump-probe delays from the leftmost map in part (a), where the 6T film was directly measured after deposition onto the sample held at a temperature of 120 K. Spectra for selected pump-probe delays are highlighted in color. **(c)** Position of the peak maximum of the intensity distribution shown in the spectra in part (b) as a function of pump-probe delay. The peak shift follows a double exponential curve with time constants $\tau_1 = (100 \pm 10)$ fs and $\tau_2 = (2.5 \pm 0.8)$ ps, as demonstrated by the fit (red dashed curve).

To investigate the role of the film morphology on the exciton dynamics, the results discussed so far for films grown at room temperature are compared with non-ordered films grown on a substrate at a temperature of 120 K. The 6T molecules are expected to freeze at the sample surface at 120 K and hence do not form the well ordered structure of wetting layer and crystallites

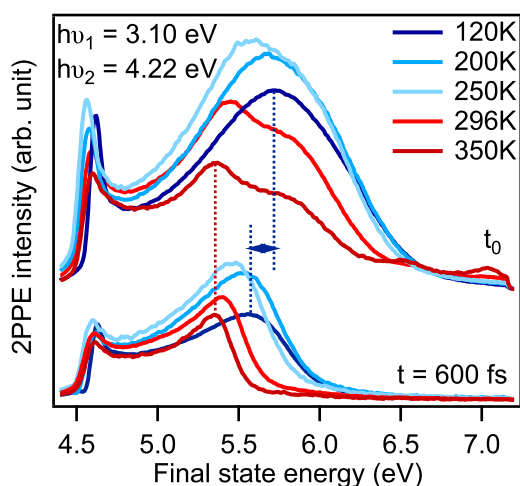


Fig. 4.22: 2PPE spectra for different heating steps when both pulses arrive simultaneously (t_0) and for a pump-probe delay of 600 fs.

that is observed at room temperature. Subsequent heating of the non-ordered film should then induce order by thermal activation of the molecules. Figure 4.21a shows the time-resolved data for a 10 ML film prepared at 120 K and then stepwise heated to 200 K, 250 K, 296 K (which corresponds to the room temperature in the laboratory) and 350 K.⁴ After heating, the sample was again cooled down to 120 K to perform the measurement, in order to prevent further changes in the sample structure during the measurement. The non-ordered molecular film measured before sample heating shows the same characteristics as observed by Varene *et al.* [7]. At zero time delay a broad intensity distribution is observed. The maximum shifts to lower energies with increasing pump-probe delay, as shown by the series of spectra in Fig. 4.21b and the read-off positions of the peak maxima plotted in Fig. 4.21c. An energetic shift of almost 200 meV is observed within the first 5 ps after excitation. The position of the peak maximum can be fitted with a double exponential function, as it was described by Varene *et al.* The faster decay constant is found to be (100 ± 10) fs, which is exactly the time constant Varene *et al.* interpreted as the exciton stabilization time. The second, slower decay was interpreted by Varene *et al.* as a polaron formation process, which leads to an additional shift in energy.

Stepwise heating of the sample results in a lowering of the energy of the excited state towards which the initially broad distribution relaxes. Furthermore, the shift in the maximum of the distribution becomes smaller with every heating step, as demonstrated in Fig. 4.22 where the 2PPE spectra observed at zero pump-probe delay and at a delay of 600 fs are compared for every heating step. When reaching room temperature by heating, no energetic shift is observed anymore. Furthermore, the image-potential or interface state and the monolayer HOMO are visible as in the case of films prepared and measured at room temperature, which leads to the conclusion that the morphology of the films changed back to the wetting layer with 3D crystallites on top as described in Sec. 4.2. By heating to 350 K, these states become even

⁴The maximal target temperature in the series was set to 350 K, which is far below the heat induced polymerization threshold of 450 K detected by Sander *et al.* for Au(001). Since the Au(111) surface is even less reactive than the (001) surface, it is expected that the threshold temperature for polymerization is even higher at the investigated surface.

4.3. EXCITON DYNAMICS IN THIN SEXITHIOPHENE FILMS

more pronounced, which gives a hint that the crystallites become bigger and hence larger areas of the surface are covered with only the wetting layer, when more thermal energy is transferred to the system.

The energy shift observed in the less-ordered films is attributed to exciton migration towards energetically more favorable sites, a process also known as down-hill migration [127, 128]. This means that the exciton is hopping to energetically more favorable sites. Different local environments of the molecules are supposed to result in different electronic structures. The broadness of the distribution at 600 fs after excitation as well as the size of the energy shift are interpreted to be a measure of the ordering of the film. The sharper the peak and the smaller the energy shift, the more uniform is the film structure in terms of variety in differing local environments of the molecules. I attribute the fast component of the shift (100 fs) to a change in the peak asymmetry due to the vibrational relaxation into the exciton ground state, which was found in the simulations performed in Sec. 4.3.2 to be in the same order of magnitude. The slower time constant (2.5 ps) is interpreted as the time scale of the downhill migration.

4.4 Summary

In the present chapter the interplay between film morphology and detected two-photon photoemission signal was elucidated on the example of thin 6T films on Au(111) surfaces. The room temperature growth of 6T/Au(111) was studied by means of photoelectron emission microscopy. The detected contrast in the PEEM images and the measured distributions of the local electron yields suggested the formation of a two-layer thick wetting layer and statistically distributed crystallites with diameters in the order of 1 μm . In case of an average surface coverage with 9 ML, it was observed that the crystallites have an average height of 12 ML above the wetting layer and cover 60% of the surface. It was discussed that the coexistence of sample areas with two different types of morphology - wetting layer and crystallites - has to be taken into account in the interpretation of data measured with techniques that probe sample areas larger than the size of the mono-morphologic areas. 2PPE measurements on films with average thickness higher than the wetting layer showed unperturbed signatures of the wetting layer as well as of other states, characterizing the electronic structure of 6T molecules within the crystallites. Coverage-dependent measurements of the electronic structure of the 6T films revealed that the formation of long-lived exciton states is observed for excitation of 6T molecules in the crystallites.

Furthermore, I discussed different aspects of the exciton dynamics in dependence of the excitation energy and film morphology. The multi-exponential decay behavior of the exciton state with an increasing longest decay time for increasing 6T coverage is explained by the film morphology. Due to crystalline growth on top of the wetting layer, the laser pulses can excite and probe excitons in molecules being at different distances to the gold substrate. The closer the excited molecule to the gold surface, the more probable is the energy transfer of the exciton energy to the substrate, and hence, the shorter is the exciton lifetime.

If the exciton is excited with excess energy with respect to the exciton band bottom, a higher energetic shoulder of the exciton peak appears, which has a much shorter lifetime than the exciton peak itself. This shoulder and its dynamics were simulated using the approach of vibronic excitations in the pumping step. A qualitative agreement of the simulations with the experimental data was found for a vibrational relaxation constant of 70 fs and a significant contribution of vibronic/vibrational pair states in the excitation process.

Finally, a morphology dependent investigation of the exciton relaxation dynamics allowed to explain the discrepancy between the photoemission data presented by Varene *et al.* and those shown in the present work and led to a novel interpretation. The observed double exponential time-dependent energy shift was interpreted as a downhill migration process appearing in non-ordered films, which adds on the energy shift caused by vibrational relaxation towards the exciton band bottom.

5

Azobenzene–Functionalized Alkanethiolate Self–Assembled Monolayers on Au(111)

Besides pure surface modification with organic layers, surface manipulation with external stimuli is one of the crucial goals in modern device fabrication. The functionalization of surfaces with photochromic molecular switches gives the opportunity to create photoresponsive surfaces. Azobenzene is one of the most studied examples of such a photoreactive switch [11]. A variety of potential applications, e.g. in the field of light-driven motion [129–131], the control of cell adhesion [132], gating of organic field-effect transistors [14] or even the increase of the efficiency in light-emitting diodes due to anode functionalization [133] have been discussed. The functionalized gold surfaces presented in this work are produced by the method of self-assembly of azobenzene-functionalized alkanethiolates in a wet-chemical process. Details are given in Sec. 5.1.

As described in the introductory chapter (cf. Sec. 2.3.2), the azobenzene molecule consists of two phenyl rings, which are either on the opposite sides of the connecting dinitrogen group (*trans* isomer) or on the same side (*cis* isomer). These two configurations have different static dipole moments. In Sec. 5.2 this is used to optically tune the work function of an azobenzene-functionalized surface. In contrast to a solution, the orientation of the azobenzene molecules in a SAM is restricted, which leads to excitonic coupling among the *trans* chromophores [57]. One of the unsolved questions is the role of the excitonic coupling in the switching process of the molecular ensemble. Using the sensitivity of the sample work-function to the photostationary state of the SAM, this question is answered in Sec. 5.3.

Parts of the physical contents presented in this chapter are published in W. Bronsch *et al.*, *Fast optical work-function tuning at an organic/metal interface*, Applied Physics Letters **111**, 081601 (2017) and in W. Bronsch *et al.*, *Delocalized vs localized excitations in the photoisomerization of azobenzene-functionalized alkanethiolate SAMs*, Journal of Physics: Condensed Matter **29**, 484002 (2017).

5.1 Wet-Chemical Preparation of Alkanethiol-Based SAMs

To perform the experiments presented in this chapter, pure and mixed SAMs containing 1-dodecanethiol (C12) and/or 11-(4-(phenyldiazenyl)phenoxy)undecane-1-thiol (Az11) have been prepared on Au(111) surfaces in a wet-chemical process following the method described by Moldt *et al.* (cf. part 2.1 of the supplementary information of Ref. [57] and Ref. [134]).

2PPE experiments were performed on Au(111) single crystals. These crystals were initially prepared by several cycles of sputtering and annealing cycles. In the ion bombardment treatment, argon ions were accelerated with 800 V in normal incidence with an ion current of 5–8 μA for 10 min. Afterwards the sample was ramped to final temperatures in the range of 770–870 K with a rate of 1 K/s. The target temperature was hold for 10 minutes before the sample was cooled down with a cooling rate of maximal 1 K/s. The whole heating process was controlled automatically. When the surface was already covered with a SAM, this was removed by chemical cleaning with peroxomonosulfuric acid [$\text{H}_2\text{O}_2(30\%):\text{H}_2\text{SO}_4(>95\%)=1:7 \text{ v/v}$] for 10 min at room temperature and 20 min while heating to 60 °C.

PEEM experiments were performed on 300 nm thick Au(111) films epitaxially grown on mica. The substrates were fabricated and supplied by Georg Albert PVD-Beschichtungen and rinsed with HPLC methanol before SAM preparation.

The Az11 molecules were synthesized in the group of Rafal Klajn at the Weizmann Institute of Science (Rehovot, Israel); the C12 molecules were purchased from Alfa-Aesar (Thermo Fisher Scientific). Both chemicals were delivered in the solid phase, which required the preparation of stock solutions as a first step. The solvent chosen to prepare the stock solutions is methanol (HPLC grade). Since the solubility of Az11 in methanol is low, the suspension was filtered till its absorbance no longer changed after a filtering iteration. The concentrations of Az11 and C12 in the stock solution were determined with a PerkinElmer Lambda 850 Spectrophotometer. These stock solutions were then used to produce the immersion solutions, which had a total thiol concentration $c = 0.1 \text{ mM}$.

Since on the surface there is a preferential adsorption of Az11 molecules compared to C12, the fraction of Az11 molecules at the surface does not scale linearly with its fraction in solution [57]. To get a 20 % surface coverage, a solution with a 20 % fraction of Az11 is used, whereas a solution with a 30 % fraction of Az11 molecules is used to get a 50 % surface coverage. The gold samples were placed for 20 h in the immersion solution and afterwards rinsed with HPLC methanol to remove molecules not bound to the gold surface before they were dried under argon flow. The dried crystals were then mounted on molybdenum sample plates and transferred into the vacuum chamber.

During the whole preparation procedure as well as during the sample transfer and the experiments, the chemical laboratory and the experimental hall were enlightened only with yellow ($\lambda > 500 \text{ nm}$) light in order to prevent premature switching.

5.2 Manipulation of the Sample Work-Function by Light

A crucial part in the field of optoelectronic device fabrication is the level alignment of electronic states at inorganic/organic or organic/organic interfaces in a layered system [14, 135–137]. In this context, the functionalization of inorganic surfaces with organic materials allows for work-function modification e.g. due to the formation of interface dipoles [135, 136, 138–142]. These modifications are mainly static and a special chemical design of the organic adsorbate has to be chosen to reach specific work-function changes. To further develop the idea from a static modification to an externally controllable one, the organic layers can be functionalized with molecular switches like the photochromic azobenzene [143–150]. In the following, the effect of work-function manipulation by azobenzene-functionalized SAMs is used to establish a method to freely tune the work function between two extrema via the interplay of two simultaneously applied external optical stimuli.

5.2.1 Dipole-Induced Shifts of the Work Function

Besides a charge transfer between adsorbate and surface, a step in the potential in front of the surface can be present due to a static dipole moment of the adsorbate and additionally influence the sample work-function. The basic principle behind this effect is the Coulomb interaction. Depending on its orientation, the dipole in front of the surface may either lower or raise the energetic barrier to be overcome by the electrons to leave the sample. A dipole induced work-function shift $\Delta\Phi$ can be described by the solution of the Helmholtz equation [151]:

$$\Delta\Phi = -\frac{e}{\epsilon_0} \frac{\mu_z}{A}, \quad (5.1)$$

including the elementary charge e , the vacuum permittivity ϵ_0 and the surface dipole density μ_z/A , considering that only the component of the dipole moment perpendicular to the surface μ_z contributes to a change in the work function. In the present case, an array of additional dipoles is formed by the azobenzene head groups in the SAM. Since the interest is not drawn to the static modification due to the presence of the chromophores, but to additional shifts in the sample work-function due to the *trans* – *cis* switching of the molecules [152], in Eq. 5.1 μ_z is replaced by the number of *cis* molecules times the change in dipole moment perpendicular to the surface $N_c \cdot \Delta p_\perp$. Furthermore, the relative permittivity of the organic material ϵ has to be considered. This leads to

$$\Delta\Phi = \frac{e}{\epsilon_0\epsilon} \frac{N_c}{A} \Delta p_\perp. \quad (5.2)$$

Whereas non-modified *trans* isomers of azobenzene have no static dipole moment due to their inversion symmetry, the net dipole moments change in Az11, since the azobenzene is at one side connected to an alkyl chain via an oxygen atom. The response of the surface in terms of the work function to switching strongly depends on the orientations of the two isomers. Near edge X-ray absorption fine structure spectroscopy (NEXAFS) has been used for determination of tilt

5.2. MANIPULATION OF THE SAMPLE WORK-FUNCTION BY LIGHT

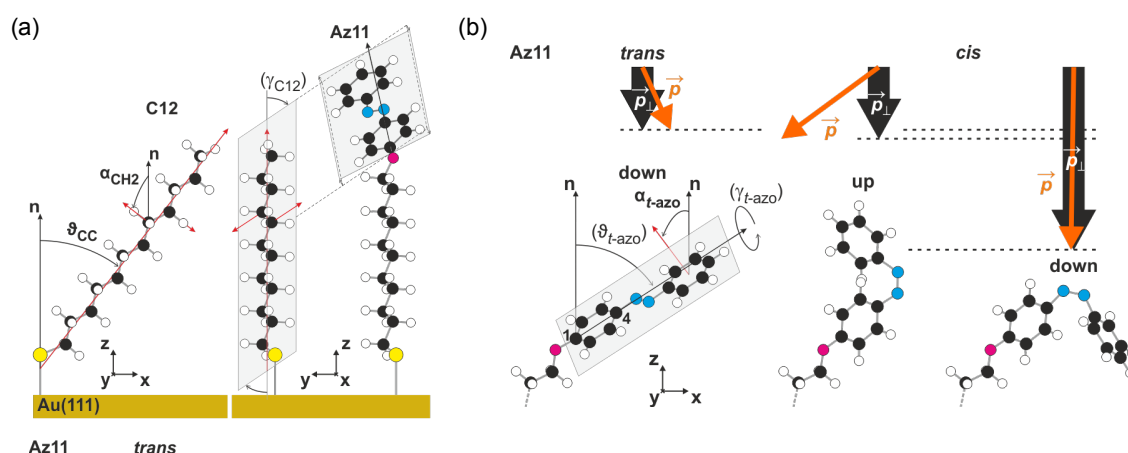


Fig. 5.1: [Figure adapted from Bronsch *et al.* [153]] (a) Schematic of the NEXAFS-compatible, DFT-optimized orientations of tilt ϑ , twist α and roll γ angles of the C12 spacers and *trans*-Az11 with respect to the surface normal \mathbf{n} . (b) Schematic of the *trans* down and *cis* up and down isomer orientations. Orange and black arrows above the ball-and-stick models of the isomers represent the projections of their respective dipole-moment vectors \mathbf{p} in the x - z plane and the dipole-moment component parallel to the surface normal \mathbf{p}_\perp . The respective mirror images (*) of the *cis* isomers obtained by reflection through the alkyl linker chain plane are not shown.

and twist angles of *trans* Az6 in a closed-packed Az6 SAM [64] as mentioned in Sec. 2.3.2, as well as tilt angles for *trans* Az11 in closed packed and mixed SAMs with 100%, 80% and 15% Az11 coverage [57].

Figure 5.1 shows the angles needed to describe the orientation of the molecules. As indicated in Fig. 5.1a, in the pure C12 SAM the alkyl chains are canted away from the surface with an average angle $\vartheta_{CC} \approx 38^\circ$. Considering the *trans* azobenzene head group (Fig. 5.1b, left), its phenyl-ring planes are tilted with respect to the surface normal by $\alpha_{t-azo} \approx (45 \pm 5)^\circ$ in the case of a reduced Az11 coverage of 15% (which leads to $\vartheta_{t-azo} \leq 45^\circ$), while the N=N double bond is rather parallel to the surface [57]. Very little is known from experiments about the orientation of the *cis* isomers in a SAM, but minor polarization dependence in NEXAFS measurements point towards various orientations of the chromophore [154]. In general the N=N double bond may either stay parallel to the surface upon switching (*cis* down) or change to perpendicular orientation (*cis* up), as illustrated in the middle and right part of Fig. 5.1b. For both orientations, also their respective mirror images (marked with *), obtained by reflection at the plane of the alkyl-chain linker, have to be considered as possible orientations.

On the basis of the geometrical restrictions given by NEXAFS and assuming that all molecules adopt an orientation with the deduced average angles, Daniel Przyrembel performed *ab-initio* calculations with perturbation theory (MP2) and density functional theory (DFT) to determine the total dipole moments as well as their components perpendicular to the surface in the case of a 20% Az11-SAM for both isomers. All values are given in Tab. 5.1. DFT results are given in parentheses. The relative orientations of the dipole moments are indicated by the arrows above the schematic illustrations of the isomer orientations. A more detailed description of the calculations can be found in Ref. [153] and in the PhD thesis of Daniel Przyrembel [155]. Using

dipole moments in D	<i>trans</i>		<i>cis</i>			
	down	up	down	down*	up	up*
\vec{p}	2.30 (2.33)	2.39 (2.53)	4.75 (4.74)		3.34 (3.44)	
\vec{p}_\perp	1.61 (1.79)	1.70 (1.94)	4.69 (4.67)	3.56 (3.64)	1.84 (2.06)	3.05 (3.17)

Tab. 5.1: List of calculated total dipole moments and their component perpendicular to the surface from *ab-initio* perturbation theory using MP2/6-311++G(d,p)//B3LYP/6-311++G(d,p) determined for the chromophore orientations shown in the Fig.5.1b and their respective mirror images (*) obtained by reflection through the alkyl linker chain plane. In parentheses the results from DFT calculations using B3LYP/6-311++G(d,p) are given for reference.

the results for p_\perp for the possible *trans* and *cis* orientations, Δp_\perp ranges between 0.14 D and 3.08 D. Considering Eq. 5.2, the determination of the work-function shift between the all-*trans* SAM and the PSS under 365 nm illumination which will be discussed in the following, will allow for estimating the relative orientations of the isomers with respect to the surface normal.

5.2.2 Work-Function Tuning in Bichromatic Experiments

As described in Sec. 3.1.2, the sample work-function Φ is given by the low-energy cut-off in a 2PPE spectrum. To determine the work function for a PSS containing mainly *cis* isomers, 2PPE was performed at a $24 \pm 5\%$ Az11 SAM with a pulsed laser at 368 nm. The low-energy parts of the resulting spectra are shown in Fig. 5.2 (magenta and black markers). Fitting the low-energy cut-off of these spectra with Eq. 3.3 gives $\Phi_{\text{PSS}}(368 \text{ nm}) = (4.465 \pm 0.003) \text{ eV}$. To probe the work function for different *cis* fractions in the PSS, diluted SAMs were irradiated simultaneously with a power-tunable continuous-wave (cw) laser in the blue regime (450 nm). Photoelectrons are still only produced by the pulsed laser. The continuous wave laser only shifts the PSS of the azobenzene ensemble. Figure 5.2 shows an example series of 2PPE-spectra with varying flux ratio $J_{450/368} = j(450\text{nm})/j(368\text{nm})$ of the cw and pulsed laser. In comparison to the measurement with 368 nm only, additional illumination with 450 nm leads to a lowering of the work function (cf. decreasing final state energy of the low-energy cut-off with increasing J in the series of violet to blue curves).

In order to explain the lowering of the work function with increasing J , the local dipole fields created by the azobenzene unit in its two different configurations, as described in the previous subsection Sec. 5.2.1, have to be considered. Photoelectrons excited in the gold substrate have to pass the dipole field at the interface of the organic layer and vacuum. Since the perpendicular component of the dipole moment of an Az11 molecule is pointing towards the sample surface and its absolute value is smaller in the *trans* form than in the *cis* form of the molecule, the work function is locally higher in the case of a *cis*-azobenzene than in the *trans* case [146, 147]. The influence of local work-function variations on the value measured far away from the

5.2. MANIPULATION OF THE SAMPLE WORK-FUNCTION BY LIGHT

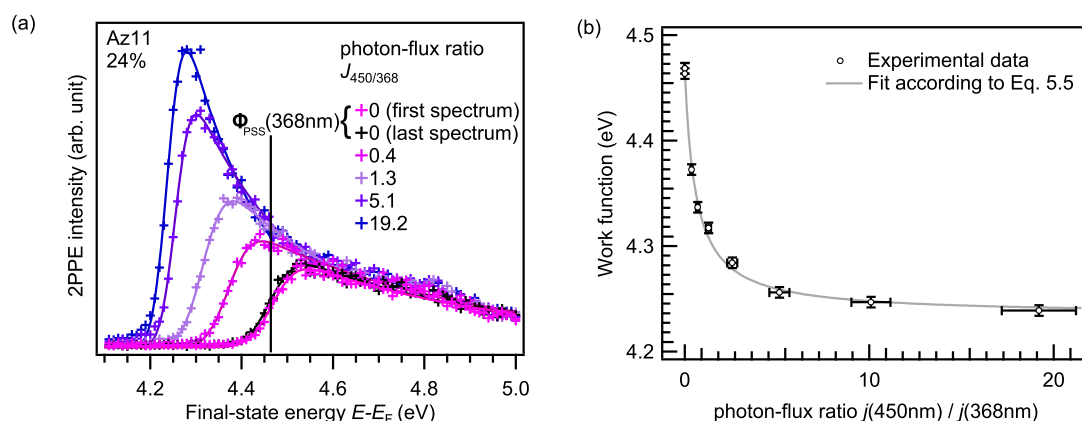


Fig. 5.2: [Figure as published in Bronsch *et al.* [153]] (a) Spectra of a 20% Az11 SAM under 368 nm illumination (magenta and black curve) and under simultaneous illumination with 368 and 450 nm with different photon flux ratios. A higher photon flux at 450 nm, $j(450\text{ nm})$, results in a shift of the low-energy cut-off to lower energies. The photon flux of 368 nm was kept constant at $j(368\text{ nm}) = (5.4 \pm 0.5) \cdot 10^{17} \text{ s}^{-1} \text{ cm}^{-2}$. (b) Sample work-function as a function of the ratio of the photon fluxes at 450 nm and 368 nm and fit according to first order switching kinetics (cf. Eq. 5.5).

surface was recently studied by Schultz *et al.* [156]. They reported that non-uniform work functions across the sample result in a split low-energy cut-off. The work function corresponds to the maximum of the potential barrier on the emission pathway. In the case of a locally high work function the maximum of the potential barrier is close to the surface meaning that the measured work-function value is only a local average. In contrast, if the local work function is low, the maximum of the potential barrier is further away from the surface and thereby stronger influenced by the surrounding. This results in a weighted average value of the work function that will be measured in a certain distance to the sample surface. If both regions are probed at the same time the locally high work function and average work function will be measured in parallel resulting in a double structure of the cut-off. Considering the samples investigated in the present thesis, all parts of the sample that are not illuminated are decorated with *trans* molecules leading to a lower work function than in those areas where some molecules are optically switched into the *cis* configuration. Since in 2PPE only the illuminated areas are probed, only the higher work-function value will be measured. This maximal work-function value will be an average value resulting from the local potential distribution, since the local work-function variations within the illuminated spot are much smaller than the distance of the potential maximum to the surface. Therefore a continuous change in the work function measured by 2PPE is expected when tuning the *trans* to *cis* ratio of the chromophores. An evaluation of the work function for different photon flux ratios $J = j(450\text{ nm})/j(368\text{ nm}) \equiv x$ leads to the dependence shown in Fig. 5.2b. To learn more about the nanoscopic structure of the SAMs, we aim to relate the induced work-function shift to the average change in dipole moment per illuminated molecule. As mentioned previously, the Helmholtz equation (Eq. 5.2) allows to calculate the shift of the work function due to a certain change in dipole moment. To calculate the contribution of a single chromophore to this shift, the total amount of molecules within the illuminated area and the portion of *cis* molecules have to be known. The molecular

density of a 100% SAM on a Au(111) surface has been studied by Jaschke *et al.* [157] by means of atomic force microscopy. They found 2 molecules in a rectangular unit cell with sides $a = (6.23 \pm 0.28) \text{ \AA}$ and $b = (7.77 \pm 0.35) \text{ \AA}$. Independently, Mannsfeld *et al.* [158] determined a 10% larger unit cell by means of STM. In the given example we worked with a chromophore density of $24 \pm 5\%$ of the density of a pure Az11-SAM. Hence, we consider only this fraction in the following calculations. The isomerization yield $\chi_c = \frac{N_c}{N} = \frac{r_{tc}}{r_{tc} + r_{ct}}$ (Eq. 2.8) in a bichromatic experiment depends on the flux ratio $x = j_{\lambda 2}/j_{\lambda 1}$. In a first order approximation the rate constants can be defined as $r_{tc} = j_{\lambda 1} \sigma_{tc}^{\lambda 1} + j_{\lambda 2} \sigma_{tc}^{\lambda 2}$ and $r_{ct} = j_{\lambda 1} \sigma_{ct}^{\lambda 1} + j_{\lambda 2} \sigma_{ct}^{\lambda 2} + r_{ct}^{\text{th}}$ under illumination at two wavelengths $\lambda 1$ and $\lambda 2$ including the respective isomerization cross-sections for the two different switching directions σ_{ct} and σ_{tc} . Thermal back switching into the *trans* state r_{ct}^{th} can be neglected in the present experiments, because it occurs on a time-scale more than 100 times longer than the time needed to reach the PSS [154]. We can hence define the fraction of *cis* molecules as follows:

$$\frac{N_c}{N} = \frac{j_{\lambda 1} \sigma_{tc}^{\lambda 1} + j_{\lambda 2} \sigma_{tc}^{\lambda 2}}{j_{\lambda 1} \sigma_{tc}^{\lambda 1} + j_{\lambda 2} \sigma_{tc}^{\lambda 2} + j_{\lambda 1} \sigma_{ct}^{\lambda 1} + j_{\lambda 2} \sigma_{ct}^{\lambda 2}}, \quad (5.3)$$

which can be simplified to

$$\frac{N_c}{N} = \frac{\frac{\sigma_{tc}^{\lambda 1}}{\sigma_{tc}^{\lambda 2}} + x}{\frac{\sigma_{tc}^{\lambda 1} + \sigma_{ct}^{\lambda 1}}{\sigma_{tc}^{\lambda 2}} + x \left(\frac{\sigma_{tc}^{\lambda 2} + \sigma_{ct}^{\lambda 2}}{\sigma_{tc}^{\lambda 2}} \right)}, \quad (5.4)$$

and entered in Eq. 5.2 to define a fitting model for the data shown in Fig. 5.2b:

$$\Phi_{\text{PSS}}(x) = \Phi_t + \Delta\Phi(x), \quad (5.5)$$

with

$$\Delta\Phi(x) = \underbrace{\frac{e}{\epsilon_0 \epsilon} \frac{N}{A} \Delta p_{\perp}}_{\Delta\Phi_{\text{max}}} \left(\frac{\frac{\sigma_{tc}^{\lambda 1}}{\sigma_{tc}^{\lambda 2}} + x}{\frac{\sigma_{tc}^{\lambda 1} + \sigma_{ct}^{\lambda 1}}{\sigma_{tc}^{\lambda 2}} + x \left(\frac{\sigma_{tc}^{\lambda 2} + \sigma_{ct}^{\lambda 2}}{\sigma_{tc}^{\lambda 2}} \right)} \right), \quad (5.6)$$

where $\Delta\Phi_{\text{max}} = \Phi_c - \Phi_t$ gives the work-function shift between an all-*cis* and an all-*trans* SAM. Considering that it is not possible to optically prepare an all-*cis* SAM, in the fit function $\Delta\Phi_{\text{max}}$ has to be expressed including the measurable PSS for illumination with light at wavelength λ

$$\Delta\Phi_{\text{max}} = (\Phi_{\text{PSS}}(\lambda) - \Phi_t) / \chi_c(\lambda) \quad (5.7)$$

to reduce the number of free parameters. If we apply this model to our data with the restriction that $\chi_c^{450\text{nm}} \leq 0.05$ and $\chi_c^{368\text{nm}} \geq 0.67$ [154], the evolution of Φ in dependence of x is described very well, as can be seen in Fig. 5.2b. Second order effects seem to play no crucial role in the switching process in a 24% Az11 SAM. The fit delivers the limiting value $\Phi_t = (4.22 \pm 0.01) \text{ eV}$ leading to $\Delta\Phi_{\text{PSS}}(368 \text{ nm}, t) = (240 \pm 10) \text{ meV}$. As expressed in Eq. 5.5, $\Delta\Phi_{\text{PSS}}(368 \text{ nm}, t)$ can be used to find the average change in dipole moment Δp_{\perp} per illuminated molecule.

According to results from Nagahiro *et al.* [147], the relative permittivity of the SAM is assumed to be $\epsilon = 2.5 \pm 0.2$. Considering the molecular density measured by Jaschke *et al.* [157] (Mannsfield *et al.* [158]), the average change in dipole moment perpendicular to the sample surface ranges from $\Delta p_{\perp} = 1.6 \pm 0.4$ D (1.8 ± 0.5 D) to 2.4 ± 0.6 D (2.6 ± 0.7 D), assuming $\chi_c(368\text{nm})$ ranging from 1 to 0.67. Comparing these results with the calculations performed by Daniel Przyrembel, it can be concluded that neither all isomers switch in the *cis* up, nor in the *cis* down configuration, but there must be a mixture of different orientations with a preference to the *cis* down orientations. This result is in agreement with the low polarization contrast observed in NEXAFS measurements under 365 nm illumination [154].

For potential applications of the investigated system it is necessary to take the fatigue into account. For this purpose, a model to calculate the actual number of switching cycles of a single molecule as soon as the PSS is reached was developed. This number depends on the portion of *cis* -molecules χ_c among the switchable molecules on the surface as expressed in Eq. 2.8 in Sec. 2.3.2. The rate constants r_{tc} and r_{ct} are furthermore directly related to the rise time τ needed to reach a PSS, as it follows from the solution of Eq. 2.6, which describes the change of the amount of *cis* -molecules in time (cf. Sec. A.4.1).

$$\tau = \frac{1}{r_{tc} + r_{ct}}. \quad (5.8)$$

Combining Eq. 2.8 and Eq. 5.8, χ_c can be related to τ in the following way:

$$\tau = \frac{\chi_c}{r_{tc}}. \quad (5.9)$$

To determine the number S_{ct} of *cis* to *trans* isomerizations per molecule per second, the number of *cis* – *trans* isomerizations has to be divided by the number of molecules at the surface:

$$S_{ct} = \frac{r_{ct} \cdot N_c}{N} \stackrel{2.8}{=} r_{ct} \cdot \chi_c \stackrel{5.8}{=} \left(\frac{1}{\tau} - r_{tc} \right) \cdot \chi_c \stackrel{5.9}{=} \left(\frac{1}{\tau} - \frac{\chi_c}{\tau} \right) \cdot \chi_c.$$

Since the isomerization rates $r_{ct} \cdot N_c$ and $r_{tc} \cdot N_t$ are equal in the PSS, the number of switching cycles S_{\odot} per molecule equals the number of switching events in one direction. In a multicolor experiment the rate constants in both isomerization directions add up for the different colors, e.g. $r_{tc} = \sum_i r_{tc}^{\lambda_i}$. Hence, the rise time τ can be expressed by the rise times of the single color experiments:

$$\tau = \left(\sum_i r_{tc}^{\lambda_i} + \sum_i r_{ct}^{\lambda_i} \right)^{-1} = \left(\sum_i \left(r_{tc}^{\lambda_i} + r_{ct}^{\lambda_i} \right) \right)^{-1} = \left(\sum_i \frac{1}{\tau_{\lambda_i}} \right)^{-1}.$$

In the following, all calculations regarding the number of switching cycles per molecule in the PSS of an ensemble are calculated by:

$$S_{\odot} = (\chi_c - \chi_c^2) \sum_i \frac{1}{\tau_i}. \quad (5.10)$$

The highest number of switching cycles is hence reached, when both isomers are present with equal amounts, as shown in Fig. 5.3. This number is furthermore limited to $0.25 \tau^{-1}$. This expression is valid as long as the rise time is long compared to the time needed for the elementary switching process, which is in the order of a picosecond [63]. Since τ depends on the photon flux, the actual switching time can be further reduced. Thereby the damage threshold of the SAM is expected to be the limiting factor.

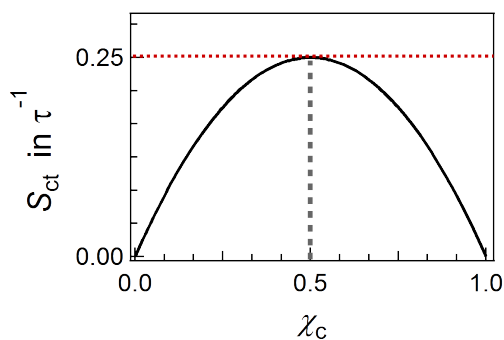


Fig. 5.3: Dependence of the number of switching events per second S_{ct} expressed in orders of τ^{-1} in a PSS on the fraction of *cis*-molecules χ_c at the surface.

Considering the series of data presented in Fig. 5.2, the application of Eq. 5.10 yields at least 400 switching cycles for each molecule.¹ Since the first and last spectrum of the series almost perfect overlay, we can conclude that fatigue does not occur for this number of switching cycles.

¹For this calculation every spectrum was assigned to a specific PSS, considering the limits $\chi_c^{450\text{nm}} \leq 0.05$ and $\chi_c^{368\text{nm}} \geq 0.67$ and assuming a linear scaling of Φ_{PSS} with χ_c according to Eq. 5.5.

5.3 The Role of Aggregation in the Switching Process in Azobenzene-Functionalized SAMs

Tackling an ongoing debate about the role of delocalized excited states in the azobenzene-aggregate [64, 65, 159–161], photostationary states and effective isomerization cross-sections are investigated as a function of the excitation wavelength λ_1 across the S_2 absorption band. As described in Sec. 2.3.2, in the self-assembled monolayers the S_2 transition dipole moments of the *trans*-Az11 molecules may couple and thereby form an H-aggregate. The coupling strength is strongly influenced by the local Az11 density [57]. In a completely ordered system the number of molecules per unit cell defines the number of states among which the oscillator strength of the ensemble is distributed (cf. Sec. 2.1.2). The broad S_2 bands in the SAMs hint to the presence of a variety of states with non-zero oscillator strength due to different relative orientations of the chromophores. In the case of a SAM, the band maximum is shifted to higher energies in comparison to non-coupled *trans* isomers in solution. The stronger the energetic shift with respect to the non-interacting molecules, the more delocalized is the excited state. The question, whether the excitation of the delocalized states does induce significant *trans*–*cis* switching, is investigated by comparing photostationary states and effective isomerization cross-sections across the S_2 band using the method of work-function manipulation described in Sec. 5.2.2.

5.3.1 Wavelength-Dependent Work-Function Shifts

Under optical excitation an ensemble of azobenzene derivatives approaches a wave-length-specific photostationary state. The relative amounts of *cis* isomers in these PSSs is given by Eq. 2.8. In a monochromatic experiment this equation can be transformed into an expression considering only isomerization cross-sections σ_{iso} :

$$\chi_c(\lambda) = \frac{\sigma_{\text{iso},\text{tc}}(\lambda)}{\sigma_{\text{iso},\text{tc}}(\lambda) + \sigma_{\text{iso},\text{ct}}(\lambda)}, \quad (5.11)$$

since $r_{\text{tc}/\text{ct}} = j \cdot \sigma_{\text{iso},\text{tc}/\text{ct}}$ as long as thermal back-switching can be neglected. The isomerization cross-section is defined as the product of the absorption cross-section σ_{abs} and the isomerization quantum yield Q for a specific isomerization direction:

$$\sigma_{\text{iso},\text{tc}/\text{ct}} = \sigma_{\text{abs},\text{t}/\text{c}} \cdot Q_{\text{tc}/\text{ct}}. \quad (5.12)$$

Decisive for the PSS are hence the absorbance of the illuminating light by the two isomers and the isomerization quantum yields.

Whereas the absorbance and quantum yields are well known for the non-interacting Az11 isomers from absorbance measurements in solution, in the SAM only the positions of the *trans* absorption bands are known. However, potential absorption of the light by *cis* isomers has

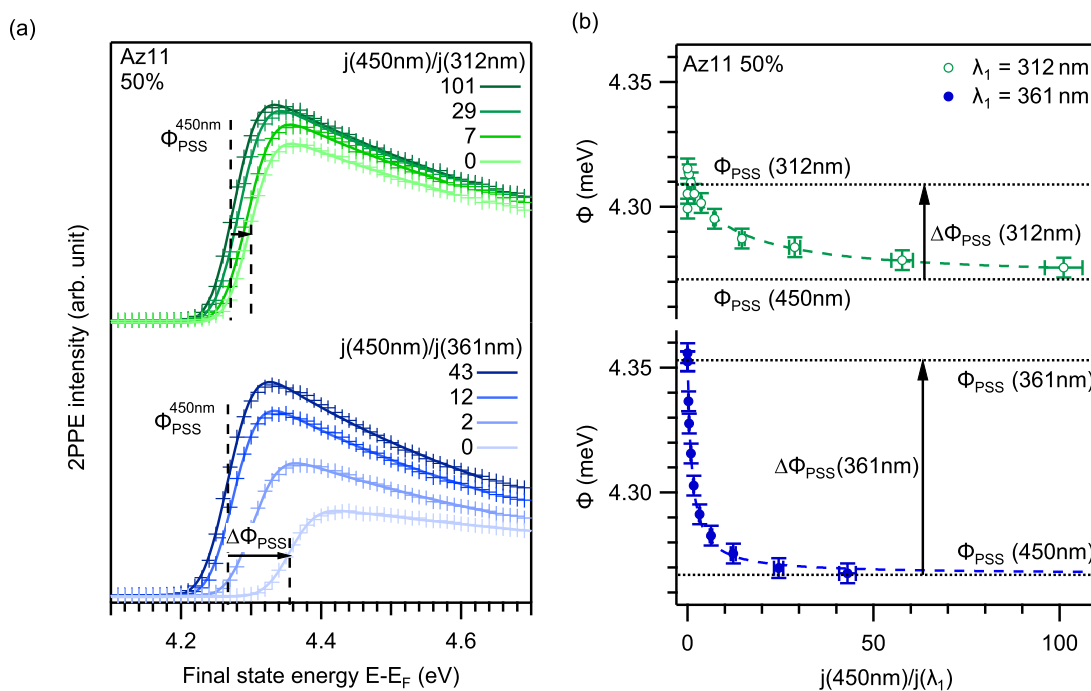


Fig. 5.4: (a) 2PPE spectra of a 50% Az11 SAM under simultaneous illumination with a cw laser at 450 nm and a pulsed laser at $\lambda_1 = 312$ nm (top part, green curves) and 361 nm (bottom part, blue curves) with different photon flux ratios $j(450\text{nm})/j(\lambda_1)$. For comparison the work function, which would be reached under 450 nm illumination only, $\Phi_{\text{PSS}}^{450\text{nm}}$, is marked by a dashed black line. (b) Work function Φ as a function of the photon flux ratio $j(450\text{nm})/j(\lambda_1)$ for $\lambda_1 = 312$ nm and 361 nm (green and blue markers, respectively). The dashed green and blue curves show fits according to Eq. 5.17. Work functions $\Phi_{\text{PSS}}^{450\text{nm}}$, $\Phi_{\text{PSS}}^{312\text{nm}}$ and $\Phi_{\text{PSS}}^{361\text{nm}}$ are marked by horizontal lines to illustrate the size of the work-function changes $\Delta\Phi_{\text{PSS}}$.

to be considered when discussing changes in the switching characteristics for excitations at different wavelengths.

To compare the dependence of PSS on the excitation wavelength λ_1 for non-interacting and excitonically coupled molecules, the work function of a 20% and a 50% Az11 SAM was investigated as a function of λ_1 and compared to the wavelength-dependence derived from absorbance data gained for Az11 in solution. Figure 5.4a shows series of 2PPE spectra analog to the data presented in Sec. 5.2.2, but in this case $\lambda_1 = 312$ nm (top) and $\lambda_1 = 361$ nm (bottom) have been combined with the cw laser at 450 nm. Comparing the low energy cut-off of the spectra taken under illumination with 361 nm and 312 nm to the work function $\Phi_{\text{PSS}}(450\text{nm})$ the sample has in the 450 nm PSS (dashed line), it can be seen that 361 nm illumination shifts the sample work-function stronger than 312 nm illumination. To determine the work-function shifts $\Delta\Phi_{\text{PSS}}(\lambda_1)$, Φ was evaluated as a function of the photon flux ratio $x = j(450\text{nm})/j(\lambda_1)$, as illustrated in Fig. 5.4b.

In Sec. 5.2.2 a model was derived relating the work function of the sample to the PSS created by simultaneous illumination with light of two different wavelengths (cf. Eq. 5.5). Since this equation refers to the all-*trans* and all-*cis* SAMs, which cannot be obtained experimentally, it contains correlated parameters and is only applicable if the PSSs for the monochromatic

5.3. THE ROLE OF AGGREGATION IN THE SWITCHING PROCESS IN AZOBENZENE-FUNCTIONALIZED SAMS

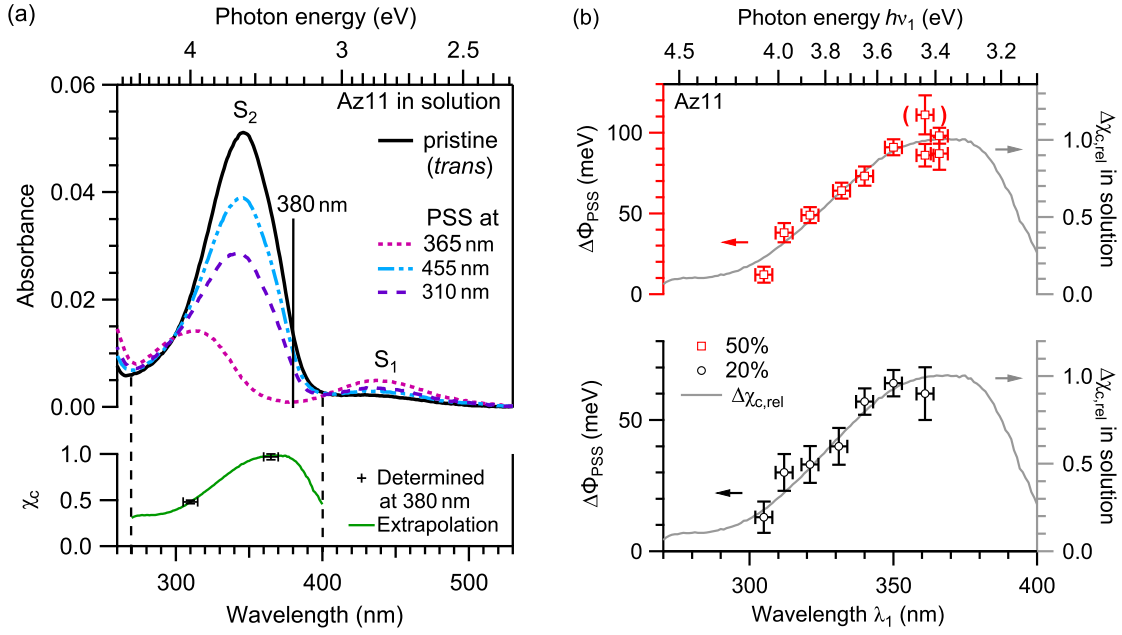


Fig. 5.5: [Figures adapted from Bronsch *et al.* [162]] (a) Absorbance spectra of Az11 solved in methanol under different illumination conditions (top) and extrapolation of the PSS for excitation across the S₂ absorption band (bottom). The extrapolation is calculated according to Eq. 5.19 assuming that the isomerization quantum yield does not change across the S₂ band. (b) Work-function shift in dependence of the excitation wavelength for chromophore densities of 50 and 20% (red rectangles and black circles, respectively) referring to the left axis and expected behavior for non-interacting molecules (gray curves) referring to the right axis. Both chromophore densities show the same trend in the evolution of the PSS, as it is expected for non-interacting molecules. The parenthesized data point stems from a series with unusual high variations, which is indicative of a local sample defect.

illuminations are known. However, these are only available from NEXAFS studies for 365 nm and 455 nm [154]. It is hence necessary to transform Eq. 5.5 to a form with a reduced number of free parameters. Using the boundary conditions

$$\Phi_{\text{PSS}}(\lambda_1) = \Phi(0) = \Phi_t + \Delta\Phi_{\text{max}} \frac{\sigma_{\text{tc}}(\lambda_1)}{\sigma_{\text{tc}}(\lambda_1) + \sigma_{\text{ct}}(\lambda_1)} = \Phi_t + \Delta\Phi_{\text{max}} \chi_c(\lambda_1), \quad (5.13)$$

$$\Phi_{\text{PSS}}(\lambda_2) = \lim_{x \rightarrow \infty} \Phi(x) = \Phi_t + \Delta\Phi_{\text{max}} \chi_c(\lambda_2), \quad (5.14)$$

with $x = j(\lambda_2)/j(\lambda_1)$, Φ_t and $\Delta\Phi_{\text{max}}$ can be related to the measurable PSSs by

$$\Delta\Phi_{\text{PSS}} = \Phi_{\text{PSS}}(\lambda_1) - \Phi_{\text{PSS}}(\lambda_2) = \Delta\Phi_{\text{max}} \cdot (\chi_c(\lambda_1) - \chi_c(\lambda_2)) \quad (5.15)$$

and

$$\Phi_t = \Phi_{\text{PSS}}(\lambda_2) - \Delta\Phi_{\text{max}} \cdot \chi_c(\lambda_2). \quad (5.16)$$

Insertion of Eq. 5.15 and Eq. 5.16 in Eq. 5.5 then yields the new fit function:

$$\Phi(x) = \Phi_{\text{PSS}}(\lambda_2) + \Delta\Phi_{\text{PSS}} \cdot \frac{\tilde{r}}{x + \tilde{r}}, \quad (5.17)$$

with $\tilde{r} = \tilde{\sigma}_{\text{iso}}(\lambda_1)/\tilde{\sigma}_{\text{iso}}(\lambda_2)$ being the ratio of the effective isomerization cross-sections at λ_1

and λ_2 .² In the experiments described below, λ_2 was always chosen to be 450 nm. Whereas $\Delta\Phi_{\text{PSS}}(\lambda_1)$ is a measure of the fraction of *cis* molecules χ_c in the PSS, $\tilde{r}(\lambda_1)$ depends on the effective isomerization cross-section and is hence a measure of the photon dose needed to drive the system into the PSS. The latter will be discussed in the next subsection.

Considering the wavelength-dependence of the PSS, the focus is first drawn to the non-interacting molecules. The upper part of Fig. 5.5a shows again the results for the absorbance of Az11 solved in methanol under different illumination conditions as presented in Sec. 2.3.2. The pristine solution contains only *trans* molecules, whereas under illumination $(97 \pm 3)\%$ of the molecules are in their *cis* configuration.³ The spectral shape of the S_2 absorption bands of the two isomers allows to extract the fraction of *cis* isomers for other illumination conditions, since e.g. at 380 nm only the *trans* isomer absorbs. Hence, it is possible to just read off the absorbance at this wavelength and compare it to the value in the pristine case to determine χ_c . In this way one can find $\chi_c(310 \text{ nm}) = (48 \pm 2)\%$, as marked in the lower part of Fig. 5.5a. Even without measuring the absorbance for illumination at each wavelength separately, the evolution of χ_c across the S_2 band can be estimated from the absorbance measured for the all-*trans* and the all-*cis* case taking into account that in solution the isomerization quantum yields for *trans* – *cis* and *cis* – *trans* isomerization do not change significantly within one absorption band as reported by Zimmerman *et al.* [163]. An expression for χ_c as a function of the absorbance A and the isomerization quantum yields Q can be derived by combining Eq. 5.12 and 5.11 to

$$\chi_c(\lambda) = \left(\frac{Q_{\text{ct}} \sigma_{\text{abs,c}}(\lambda)}{Q_{\text{tc}} \sigma_{\text{abs,t}}(\lambda)} + 1 \right)^{-1} \quad (5.18)$$

and by using the proportionality of σ_{abs} and A according to the Lambert-Beer law:

$$\chi_c(\lambda) = \left(\frac{Q_{\text{ct}} A_c(\lambda)}{Q_{\text{tc}} A_t(\lambda)} + 1 \right)^{-1}. \quad (5.19)$$

The extrapolation of χ_c shown in the lower part of Fig. 5.5a is done by using Eq. 5.19 with the ratio of the isomerization quantum yields fixed to its value at 310 nm:

$$\frac{Q_{\text{ct}}(\lambda)}{Q_{\text{tc}}(\lambda)} \stackrel{!}{=} \frac{Q_{\text{ct}}}{Q_{\text{tc}}} \Big|_{310 \text{ nm}} = \left(\frac{1}{\chi_c(310 \text{ nm})} - 1 \right) \frac{A_t(310 \text{ nm})}{A_c(310 \text{ nm})} = 1.60 \pm 0.13. \quad (5.20)$$

To compare the evolution of the PSS in the excitonically coupled system to the case of the non-interacting molecules, in Fig. 5.5b the extracted wavelength-dependent work-function shifts $\Delta\Phi_{\text{PSS}}$ are plotted as markers against the left axis and the extrapolated change in $\Delta\chi_{c,\text{rel}}$ for non-interacting molecules is plotted as gray curves against the right axis. Since the $\Delta\Phi_{\text{PSS}}$ refers to the PSS at 450 nm, the same is done for the change in the fraction of *cis* molecules, which means that $\Delta\chi_{c,\text{rel}}$ is normalized so that zero corresponds to the PSS under blue light

²A detailed demonstration of the transformation from Eq. 5.5 to Eq. 5.17 is given in Sec. A.4.2.

³This value is estimated from the absorbance at 380 nm of the Az11 SAM under illumination with 365 nm.

illumination and 1 to the maximal achievable fraction of *cis* isomers $\chi_c(365\text{nm})$:

$$\Delta\chi_{c,\text{rel}}(\lambda) = \frac{\chi_c(\lambda) - \chi_c(455\text{nm})}{\chi_c(365\text{nm}) - \chi_c(455\text{nm})}. \quad (5.21)$$

The evolution of the work-function shift follows for both investigated Az11 coverages, 20 and 50 %, the trend of $\Delta\chi_{c,\text{rel}}$ derived from non-interacting molecules.

5.3.2 Wavelength-Dependent Kinetics of the Switching Process

After discussing the evolution of the PSS, the focus is now drawn to the wavelength dependence of the effective isomerization cross-section, which is a measure for the amount of photons needed to reach a PSS. The effective isomerization cross-section is the sum of the isomerization cross-sections of the two isomerization directions. It hence depends on the absorption cross-sections and the isomerization quantum yields for *trans* – *cis* and *cis* – *trans* isomerization. The effective isomerization cross-section can be calculated in an analogue manner as the evolution of χ_c across the S_2 band for the limit of non-interacting molecules, which was determined in the previous section from the absorbance of an Az11 solution, according to:

$$\tilde{\sigma}_{\text{iso}}(\lambda) = \sigma_{\text{abs},t} \cdot Q_{tc} + \sigma_{\text{abs},c} \cdot Q_{ct} \quad (5.22)$$

$$= C \cdot A_t(\lambda) \cdot Q_{tc} + C \cdot A_c(\lambda) \cdot Q_{ct}. \quad (5.23)$$

The proportionality factor $C = 2.0467 \cdot 10^{-15} \text{cm}^2$ between the absorption cross-section σ_{abs} and the absorbance $A(\lambda)$ can be determined from the pristine data.⁴ As before, it is assumed that in solution the isomerization quantum yields are wavelength-independent within one absorption band and the values determined at 310 nm are used for the extrapolation of $\tilde{\sigma}_{\text{iso}}$ shown in the bottom part of Fig. 5.6. The derived development of the effective isomerization cross-section shows a maximum between 330 nm and 340 nm, i.e., at lower wavelength than the maximal absorbance of the *trans* isomer.

Indirect Kinetics Measurements by 2PPE

The second parameter \tilde{r} in Eq. 5.17 is given by the ratio of the effective isomerization cross-sections at wavelengths λ_1 and λ_2 . Since λ_2 was fixed to 450 nm, the wavelength dependence of \tilde{r} represents the one of $\tilde{\sigma}_{\text{iso}}(\lambda_1)$. Figure 5.7a shows fitting results of \tilde{r} for the same data sets for which the wavelengths dependence of $\Delta\Phi_{\text{PSS}}$ was discussed in the previous section. The analysis of the 20 % Az11 SAM is represented by the black open cycles, whereas the red open rectangles mark the values gained for 50 % surface coverage with Az11 molecules. Even though some of the extracted values have quite large error bars, a clear decrease of \tilde{r} is shown

⁴ $C = \frac{\ln(10)}{N_A} \cdot \frac{\epsilon_t(347\text{nm})}{A_t(347\text{nm})}$ with the constant of Avogadro N_A , and $\epsilon_t = 27.3 \cdot 10^6 \text{cm}^2/(\text{mol}\cdot\text{l})$ being the extinction coefficient of the *trans* molecule. For details see the supplementary online material of Ref. [162].

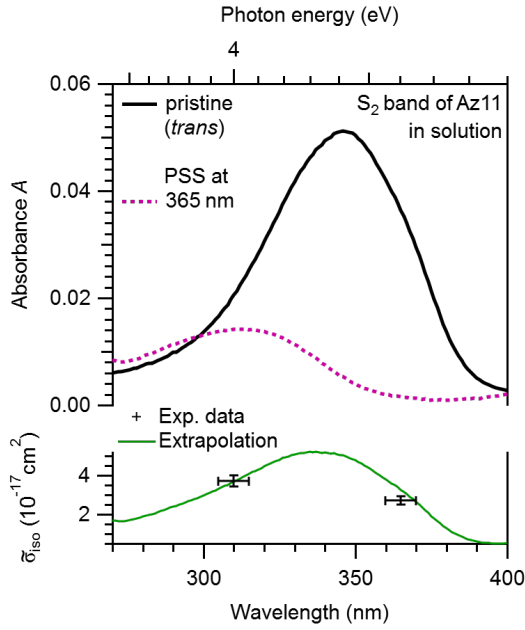


Fig. 5.6: Extrapolation of the wavelength dependence of the effective isomerization cross-section according to Eq. 5.23 (green curve) in the range of the S_2 absorption band in the case of non-interacting Az11 molecules derived from absorbance measurements in solution shown above.

for increasing wavelengths. The largest contribution to the uncertainty is the determination of the spatial overlap of the two laser beams. Whereas this has no influence on the limits of $\Phi(j(\lambda_2)/j(\lambda_1))$, it strongly influences the curvature of the function (see Eqs. 5.17 and Fig. 5.4), which is represented by \tilde{r} . Since the work function is lowest in the center of the cw beam, the spatial overlap of the two laser beams was optimized by maximizing the 2PPE signal and additionally checked by a CCD camera. Exemplary images of the spot profiles of the pulsed and cw beam are given in Fig. 5.7b and c. To account for deviations from 2D gaussian beam profiles, the determination of the mean photon flux ratios included an integration over the two profiles. Furthermore, since only the pulsed beam creates the 2PPE signal, the local photon flux ratios were weighted with the profile of the pulsed beam, leading to the following function to determine the mean photon flux ratio:

$$\frac{j(450\text{nm})}{j(\lambda_1)} = \frac{\int \frac{j(450\text{nm},r)}{j(\lambda_1,r)} j^2(\lambda_1, r) d^2r}{\int j^2(\lambda_1, r) d^2r}. \quad (5.24)$$

Since the CCD chip was placed at the same distance to the focusing mirror as the sample, but outside the chamber, small deviations to the real position of the beams are expected due to the light dispersion caused by the entrance window to the chamber. This is taken into account in the error calculation by adding the difference in the determined photon-flux ratios for perfectly overlapping spots and the geometrical arrangement detected by the camera.

For comparison, the theoretical extrapolation⁵ of the ratios of the effective isomerization cross-sections for the non-interacting Az11 molecules is also shown in Fig. 5.7a by the dashed gray curve. The wavelength dependence of \tilde{r} in the SAMs clearly deviates from the one in

⁵For comparison, the extrapolated curve for $\tilde{\sigma}_{\text{iso}}(\lambda)$ for non-interacting Az11 molecules shown in Fig. 5.6 was divided by $\tilde{\sigma}_{\text{iso}}(450\text{nm}) = 0.7 \cdot 10^{-17} \text{cm}^2$ (cf. Ref. [154]).

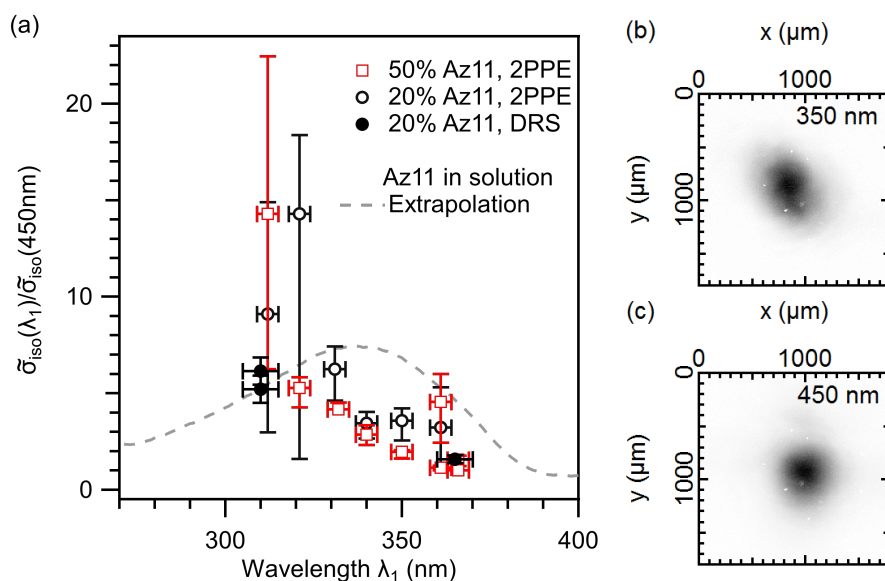


Fig. 5.7: (a) Ratios of the effective isomerization cross-sections at λ_1 and 450 nm as a function of λ_1 for 20 and 50% concentration of Az11 molecules in the SAM (black and red markers respectively). For comparison, the black filled cycles show the data gained by DRS and the dashed gray curve shows the trend expected for non-interacting molecules. (b) and (c) Exemplary camera pictures of the spot profiles of the pulsed laser beam (350 nm) and the continuous-wave laser beam at 450 nm, respectively. The intensity scale ranges from zero (white) to maximal intensity (black).

solution, showing significantly lower cross-section ratios for longer wavelengths within the S_2 band. The significant reduction at longer wavelengths can be explained by the redistribution of oscillator strength in the *trans* aggregate compared to non-interacting *trans* molecules. Only in the range of significant absorbance of the non-interacting *cis* isomers comparable values can be reached in the SAM and in solution. In the latter case $\tilde{\sigma}_{\text{iso}}(\lambda)$ is dominated by $\sigma_{\text{ct}}(\lambda)$.

Direct Kinetics Measurements by 2PPE

Tracking the work function as a function of time allows to determine absolute values of the effective isomerization cross-section. Therefore, the laser setup was adjusted in a way that simultaneously 305 nm pulses and pulses at another wavelength within the S_2 band region were produced by the two OPAs and alternately sent to the sample. Figure 5.8 shows the 2PPE intensity during the kinetics measurements as a function of final state energy and measurement time. Here, 361 nm and 305 nm laser beams were sent alternately to a 20% Az11 SAM. During the first few spectra the sample was not illuminated (dark) before the 361 nm beam was unblocked for a few seconds. Afterwards the 361 nm was blocked and the 305 nm beam unblocked with a short delay. The procedure was repeated several times to monitor the evolution of 2PPE spectra when the sample changes between the PSSs at 361 nm and 305 nm. Due to the high photon flux densities needed to create the 2PPE signal, spectra were recorded every 0.344 s including 0.1 s for signal detection. The work function was evaluated for each spectrum,

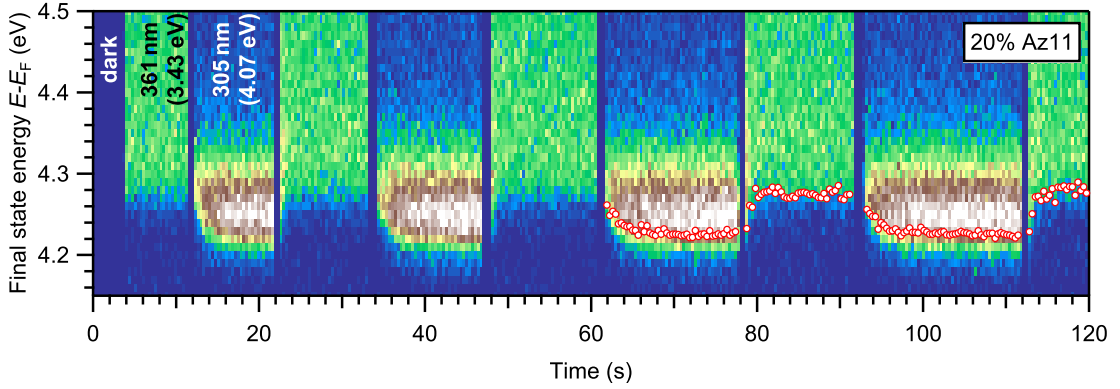


Fig. 5.8: 2PPE intensity as a function of time and final state energy for alternating illumination of a 20 % Az11 SAM with 361 nm and 305 nm. The low-energy cut-off of the spectra changes exponentially as soon as the illumination conditions are changed from one color to the other. The red circles in the right half of the figure mark exemplary the extracted low-energy cut-offs of the single spectra, which are then fitted to determine the isomerization cross-sections.

as indicated with the red markers in the right part of Fig. 5.8.

To theoretically describe the work function as a function of time, the time-dependence of $\chi_c(t)$ has to be considered, which follows from the solution of the differential equation 2.6:

$$\Phi(t) = \Phi(0) + \Delta\Phi_{\max} \cdot (\chi_c(t) - \chi_c(0)) \quad (5.25)$$

$$= \Phi(0) + \Delta\Phi_{\max} \cdot \left(\chi_c(\infty) - \chi_c(0) + (\chi_c(0) - \chi_c(\infty)) \cdot e^{-t \cdot j \cdot \tilde{\sigma}_{\text{iso}}} \right) \quad (5.26)$$

$$= \underbrace{\Phi(0) + \Delta\Phi_{\max} \cdot (\chi_c(\infty) - \chi_c(0))}_{\Phi(\infty)} + \underbrace{\Delta\Phi_{\max} \cdot (\chi_c(0) - \chi_c(\infty))}_{\Delta\Phi_{0,\infty}} \cdot e^{-t \cdot j \cdot \tilde{\sigma}_{\text{iso}}} \quad (5.27)$$

In the 2PPE experiments the light used to switch the molecules is also used to photoemit electrons. Therefore it is necessary to work with focussed beams with a diameter much smaller than the sample size. Due to the gaussian beam profiles, the photon flux j has to be considered as space dependent. Furthermore, since 2PPE is a second order process, the measured electron yield does not scale linearly, but quadratically with the photon flux $j(r)$. To account for this, the change in the work function is weighted with $j^2(r)$ in the fit function $\Phi(t)$ applied to the data:

$$\Phi(t) = \Phi(\infty) + \Delta\Phi_{0,\infty} \cdot \frac{\int_A j^2(r) \cdot e^{-t \cdot j(r) \cdot \tilde{\sigma}_{\text{iso}}} d^2r}{\int_A j^2(r) d^2r}. \quad (5.28)$$

The experiment shown in Fig. 5.8 was repeated with the wavelength combinations 305 nm/350 nm, 305 nm/340 nm and 305 nm/330 nm for the 20 % and a 50 % SAM. The extracted average values for $\tilde{\sigma}_{\text{iso}}(\lambda)$ are shown in Fig. 5.9. The uncertainty values include the range of determined values at each wavelength. The values are again compared to the dependency derived for non-interacting molecules. As already described in the previous paragraph, when comparing the ratios of the effective isomerization cross-sections, lower values are observed in the SAM than in solution, which means that reaching the PSS takes more time in the case of excitonically coupled

5.3. THE ROLE OF AGGREGATION IN THE SWITCHING PROCESS IN AZOBENZENE-FUNCTIONALIZED SAMS

molecules. The reduction of the effective isomerization cross-sections is interpreted as a result of the redistribution of the oscillator strength towards shorter wavelengths. However, these shifted states do not contribute to switching, as it can be concluded from the low cross-sections observed around 310 nm, where the maximum of the excitonically shifted absorption band appears. Hence, only the excitation of weakly coupled states leads to switching.

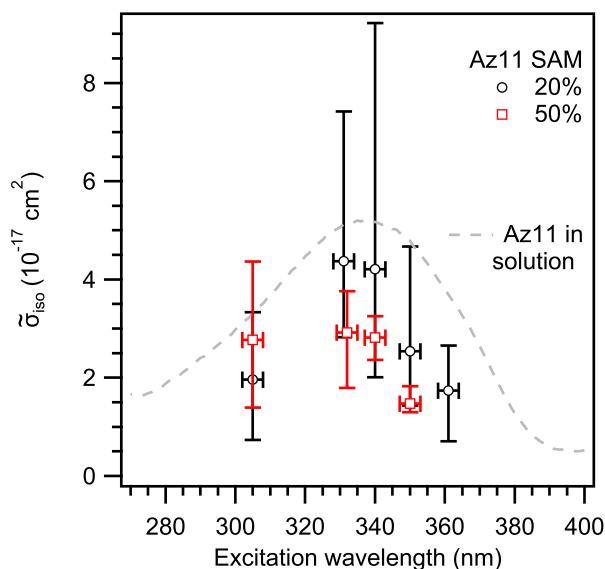


Fig. 5.9: Effective isomerization cross-sections as a function of the excitation wavelength extracted from the temporal evolution of the work-function under illumination of a 20 and a 50 % Az11 SAM (black circles and red rectangles respectively). The dashed gray curve shows the extrapolated evolution for non-interacting molecules.

So far from other experiments only a few values for effective isomerization cross-sections of Az11 SAMs are available, only for 20 % Az11 surface coverage and for two different wavelengths within the S_2 absorption band, namely 310 nm and 365 nm. Changes in the DR signal at 320 nm were recorded to determine $\tilde{\sigma}_{\text{iso}}$. For illumination with 310 nm different values have been found when switching either from the PSS at 455 nm or the PSS at 365 nm towards the PSS at 310 nm. When switching from the PSS at 455 nm to the PSS at 310 nm $\tilde{\sigma}_{\text{iso}}(310\text{nm}) = (0.78 \pm 0.07) \cdot 10^{-17} \text{cm}^2$ was determined, whereas when starting from the PSS at 365 nm, the value was slightly lower, $\tilde{\sigma}_{\text{iso}}(310\text{nm}) = (0.66 \pm 0.07) \cdot 10^{-17} \text{cm}^2$. When switching from the PSS at 455 nm directly to the one at 365 nm, $\tilde{\sigma}_{\text{iso}}(365\text{nm}) = (0.20 \pm 0.01) \cdot 10^{-17} \text{cm}^2$ was observed [162]. Furthermore, NEXAFS spectroscopy results are available, where high-resolution N 1s spectra of the LUMO resonance were used to track changes in the spectral shape during illumination. In NEXAFS $\tilde{\sigma}_{\text{iso}}(365\text{nm}) = (0.14 \pm 0.02) \cdot 10^{-17} \text{cm}^2$ was determined [154]. In the 2PPE experiments cross-sections up to one order of magnitude higher than expected from NEXAFS and DRS results have been measured. When comparing these results, it has to be considered that DRS is measured under ambient conditions, whereas NEXAFS and 2PPE are measured in vacuum. Furthermore, all three techniques measure different physical quantities. Currently this discrepancy is still an open question. One possible influencing variable in the 2PPE experiments might be the sensitivity to changes in the average orientation of the molecules. Weakly coupled molecules, which have larger distances to their nearest neighbors, are expected to switch easier than stronger coupled ones. More space for switching could result in a switching to the *cis* down configuration, which leads to larger changes in the local work function than *cis* up

orientations. This effect might influence the 2PPE kinetic evaluation, since larger amounts of *cis* molecules would switch in a shorter time.

Summarizing the results discussed in the present section analyzing the light induced work-function shifts, it was obtained that the wavelength-dependence of the fraction of *cis* molecules in the SAM as well as the relative and absolute isomerization cross-sections follow the one deduced from non-interacting molecules in solution. In other words, even though the excitonic coupling between the *trans* molecules strongly influences the optical properties of the SAM, the delocalized excited states of the aggregate do not contribute significantly to switching. The obtained results furthermore suggest that the S_2 band of the *cis* molecules in the SAM is not shifted with respect to the non-interacting molecules, meaning that excitonic coupling between the *cis* isomers in the SAM can be neglected.

5.4 Outlook:Towards Spatial Mapping of the Work-Function Shift

In the Bachelor thesis of Jan Böhnke, we used photoelectron emission microscopy for spatial mapping of the work-function shift to show its spatial restriction to the laser beam. The photoelectrons were emitted by a mercury lamp illuminating the sample. The emission spectrum of the lamp is given at the bottom of Fig. 5.10. The most important emission lines (314 nm, 366 nm and 438 nm) are marked with solid lines and related to the corresponding positions in the absorptions bands of aggregated (DRS of a 20 % Az11 SAM, middle) and non-interacting molecules (absorbance of Az11 in solution, top). Considering the effective isomerization cross-sections determined in the previous section, the PSS under illumination with the mercury lamp is expected to be closer to the all-*trans* than to the all-*cis* SAM.

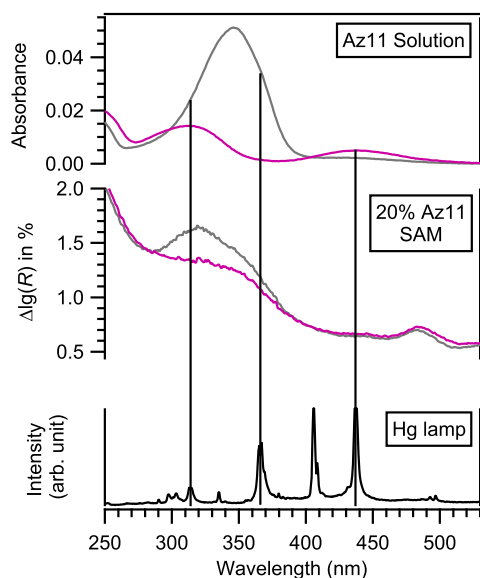


Fig. 5.10: **Top:** Absorbance of non-interacting *trans* (black curve) and *cis* Az11 (magenta curve) molecules. **Middle:** DR signal of a 20 % Az11 SAM in an all-*trans* configuration (black curve) and under 365 nm illumination (magenta curve). **Bottom:** Emission spectrum of the mercury lamp. The solid black lines indicate the most relevant emission lines of the Hg lamp and relate them to the position in the absorption bands of the non-interacting or excitonically coupled Az11 molecules.

To create a significant contrast in the PEEM signal, a continuous-wave laser at 372 nm was focussed onto the probed sample area to shift the PSS towards a higher fraction of *cis* molecules. The laser has in good approximation a 2D gaussian profile with different FWHM values in the two directions. This means that the highest fraction of the measured total photon dose is reached in the center of the laser beam. As discussed above not only the laser, but the Hg lamp as well induced switching of the molecules. The illumination of the sample with the Hg lamp can be assumed to be constant across the whole region of interest. Considering the spatial variation in the relative photon fluxes of both light sources, cw laser and Hg lamp, across the beam profile of the laser pointing on the sample, it is possible to simulate the spatially resolved work-function variations due to the distribution of photostationary states according to Eq.5.17. Whereas the photon flux of the cw laser was varied during the experiments, the photon flux of the Hg lamp was held constant at $j(\text{Hg}) \sim 10^{16}$ photons per second and cm^2 .

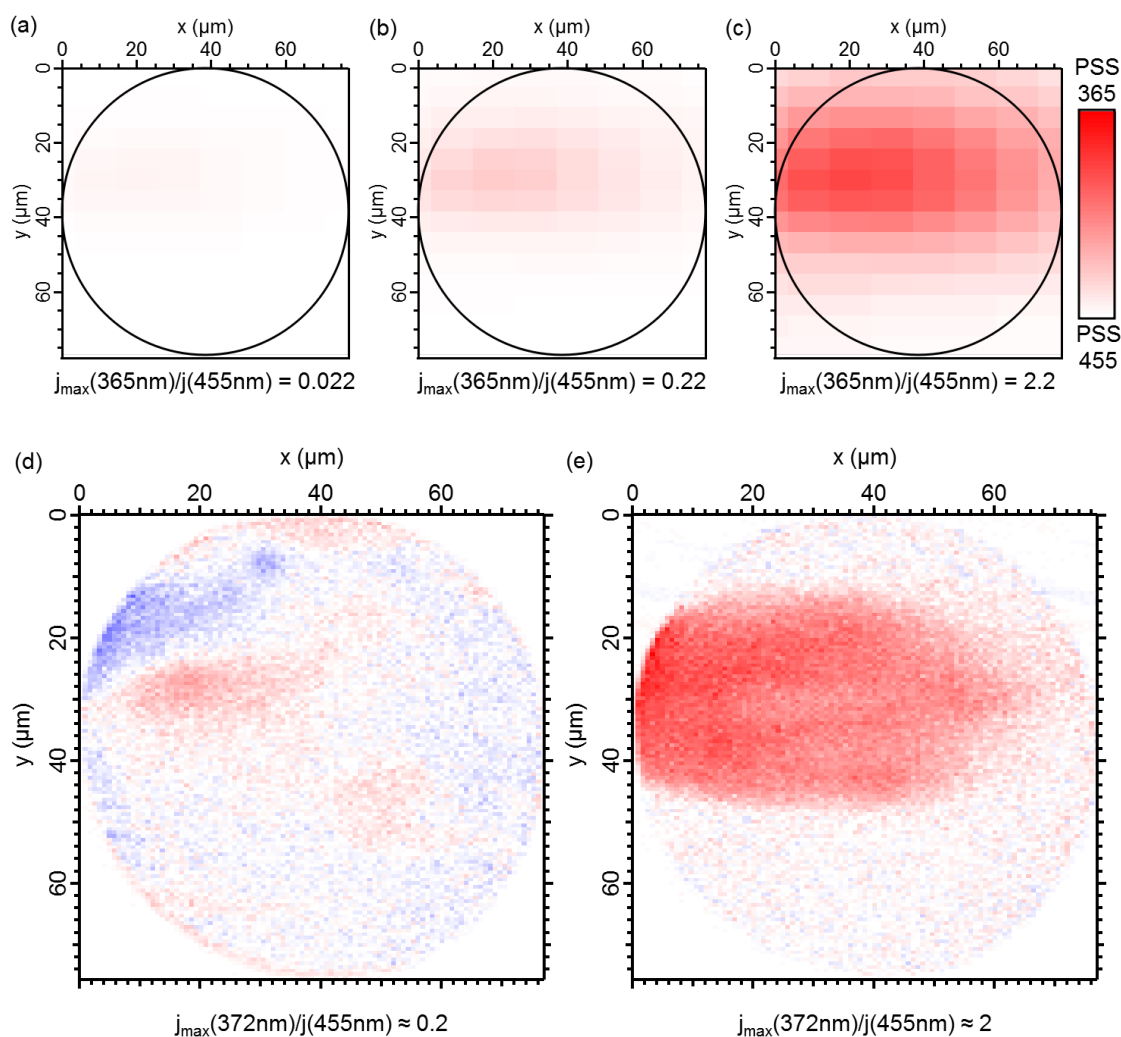


Fig. 5.11: **Top row:** Simulation of the work-function variations according to local photostationary states between the limits of an almost all-*trans* SAM under 455 nm illumination (white) and a predominantly *cis* SAM under 365 nm illumination (red) for a ratio of the photon flux reached in the maximum of the laser beam profile $j_{\max}(365\text{nm})$ and the photon flux of the 455 nm background illumination $j(455\text{nm})$ of (a) $j_{\max}(365\text{nm})/j(455\text{nm}) = 0.022$, (b) $j_{\max}(365\text{nm})/j(455\text{nm}) = 0.22$ and (c) $j_{\max}(365\text{nm})/j(455\text{nm}) = 2.2$. **Bottom row:** Differential PEEM images measured for a ratio (d) $j_{\max}(372\text{nm})/j(\text{Hg}) \approx 0.2$ and (e) $j_{\max}(372\text{nm})/j(\text{Hg}) \approx 2$ of the photon flux reached in the maximum of beam profile of the 372 nm laser and the Hg lamp background illumination. Both figures are set to the same color scale. White areas mark no change in the work function in comparison to the image with Hg lamp illumination only, whereas red areas have lower electron yield (higher work function). Due to statistical fluctuations of the Hg lamp or sample damage some areas show an enhanced signal with respect to the measured background image. Those areas are marked in blue.

To simulate the expected spatial work function variations, I approximate the impact of the Hg lamp by a light source comprising only one wavelength, namely 455 nm since the effective cross-sections $\tilde{\sigma}_{\text{iso}}(455\text{nm}) = 1.2 \cdot 10^{-18} \text{ cm}^2$ is well known from NEXAFS experiments [154]. In addition to a constant 455 nm background, the beam profile of the laser spot measured with a CCD camera was considered assuming a certain photon flux and an effective cross-section of $\tilde{\sigma}_{\text{iso}}(372\text{nm}) \approx \tilde{\sigma}_{\text{iso}}(365 \pm 5\text{nm}) = 1.4 \cdot 10^{-18} \text{ cm}^2$. Figure 5.11a-c show such simulations

for three different ratios of the photon flux reached in the maximum of the beam profile of the laser and the photon flux of the Hg lamp. The color scale is normalized from areas with a work function corresponding to the almost all-*trans* SAM in the PSS of 455 nm (white) to the work-function reached in the case of a predominantly *cis* SAM in the PSS of 365 nm (red). In Figure 5.11a the photon flux in the maximum of the laser beam profile is set to only 0.022 times the value of the photon flux of the 455 nm background illumination, whereas in Figure 5.11b it is set to $0.22 \cdot j(455\text{nm})$ and in Figure 5.11c to $2.2 \cdot j(455\text{nm})$.

For comparison the difference images for PEEM measurements with and without the 372 nm cw laser for a photon flux in the maximum of the laser beam profile of $\approx 0.2 \cdot j(\text{Hg})$ (Fig. 5.11d) and $\approx 2 \cdot j(\text{Hg})$ (Fig. 5.11e) are shown. The areas showing a change in the electron yield nicely fit to the results of the simulation, which assumed first-order kinetics.

The experimental set-up will be equipped with a fs-laser system in near future. This will allow for spatial resolved tracking of the switching kinetics across the beam profile.

5.5 Summary

Studying the work function of mixed Az11 SAMs on Au(111) under different illumination conditions, several aspects of the switching process have been discussed. Since the two Az11 isomers have significantly different static dipole moments, the work function of the SAM/Gold sample is a measure of the photostationary state of the ensemble. Hence, comparing work functions measured under different illumination conditions allows for comparing the fraction of *cis* isomers in the corresponding PSSs. Furthermore, tracking the change in the work function as a function of the photon dose gives insight in the effective isomerization cross-sections under certain illumination conditions. Considering the role of the excitonic coupling of the *trans* isomers in Az11 SAMs, it has been shown that the distribution of oscillator strength among several eigenstates of the ensemble leads to a general lowering of the effective isomerization cross-section. Furthermore, the evolution of the fraction of *cis* isomers for excitation energies across the S_2 absorption band showed similar behavior as for the non-coupled Az11 molecules. This leads to the conclusion that the excitation of delocalized states of the *trans* ensemble does not lead to *trans* – *cis* isomerization. Besides lower fractions of *cis* isomers at lower excitation wavelengths, larger effective isomerization cross-sections have been found. Combined with the evident resemblance of the evolution of the PSS to the behavior of non-interacting molecules, this indicates that the position of the S_2 band of the *cis* isomers in the SAMs has to be in the same energetic region as for the non-coupled molecules. In other words, *cis* molecules do not couple excitonically.

In terms of application the possibility of fast, precise and reliable work-function tuning via simultaneous use of two external optical stimuli with variable relative photon fluxes has been discussed. Here a pulsed laser exciting an S_2 transition was used to measure the work function, while a continuous wave laser excites S_1 transitions and thereby enhances the *cis* – *trans* back-switching rate. Depending on the average orientation of the isomers, work-function shifts up to 240 eV with respect to the all-*trans* SAM have been observed. The experiments showed that reversible work-function tuning is possible on the time scale of a few seconds. Photon fluxes in the order of 10^{17} photons per second and cm^2 can be used to switch every molecule in average more than 800 times within two minutes without measurable fatigue. Furthermore, Photoelectron emission microscopy experiments confirmed that the work function can be changed locally at the position of the focussed beam. Hence, patterns of locally varying work functions can be written onto the sample surface via external optical stimuli.

6

Chapter 6 Summary

Exciton formation and excitonic coupling are important fundamental processes in molecular thin films. Such films are used in modern device technologies such as organic light emitting diodes or organic solar cells. Likewise organic films are used to functionalize photoresponsive surfaces. In the present work two model systems were chosen to investigate the influence of excitonic band formation on the coupling of an electronic excitaton to nuclear degrees of freedom. The fundamental time-scales of the exciton population dynamics are studied at the example of the S_1 Frenkel exciton in α -sexithiophene. Whereas the impact of excitonic coupling on an ensemble property is investigated for the light-induced switching of azobenzene-based self-assembled monolayers. Studies regarding the electronic structure of the samples under investigation and exciton population dynamics were performed by means of time-resolved two-photon photoemission spectroscopy. Furthermore photoelectron emission microscopy and differential reflectance spectroscopy were applied to gain information on film morphologies and optical properties.

In Chapter 4 the focus was drawn to the population dynamics of the S_1 Frenkel exciton (FE) in epitaxially grown thin films of α -sexithiophene on Au(111) surfaces. Three main questions built the basis of the research performed at this model system of an organic semiconductor/metal interface: (1.) What is the population pathway of a singlet Frenkel exciton in an organic semiconductor? Is it necessary to provide excess energy with respect to the optical band gap? (2.) What is the time-scale of dephasing after the initial excitation in order to populate the excitonic state? (3.) How does the interaction with the substrate influence the exciton population and relaxation dynamics?

The electronic and excitonic structure of the molecular film strongly depends on the film morphology. Therefore, the focus was first drawn on the investigation of the coverage-dependent 6T film structure. Photoelectron emission microscopy experiments performed in collaboration with Thorsten Wagner from the Johannes Kepler university in Linz reveal two different phases of the film morphology when growing multilayer films of 6T/Au(111). While the first and second layer close completely, in higher layers μm -sized crystallites form and cover about 60 % of the surface. Time-resolved 2PPE-experiments clearly showed that the two-layer thick wetting layer is needed as a decoupling layer in order to observe a population of the S_1 exciton state and get a significantly long exciton lifetime. When the energy transfer into the substrate takes long enough to observe the exciton state, this state is populated within the pulse duration of the laser pulses. In order to be able to tune the excitation energy through the FE band, differential reflectance spectroscopy data were recorded during the growth process to determine

the coverage dependent energetic position of the exciton band. I showed with 2PPE experiments that the FE can be populated using excitation photon energies in the range from 2.3 eV to at least 3.1 eV, which is the full range observed for the S_1 absorption band. The observation of the population of the exciton state through excitation with 2.3 eV at the exciton band bottom shows that it is not necessary to provide excess energy. In order to create not just a polarization, but a population of the excitonic state it is enough to just overcome the optical bandgap. Excess energy is observed to be mainly transformed in additional vibrational excitations of the 6T molecules. In a collaboration with Ralph Püttner, the impact of vibronic transitions in the pump and probe steps on the photoemission spectra was analyzed. The photoemission spectra were calculated starting from different vibrational levels in the excited state under the assumption of single molecule potential energy curves and only one active vibrational mode, namely the C=C stretching mode with an energy of 180 meV. Combining these calculated spectra with a rate equation model, I modelled time-resolved photoemission data. The simulations performed in this framework demonstrate that the higher energetic shoulder of the exciton band bottom peak can be explained by vibronic excitons in the pumping step when exciting with excess energy. The best agreement was found for a vibrational relaxation time constant of 70 fs, which is a reasonable value for an oligomer [125]. Furthermore, it was elucidated that in amorphous 6T films samples the exciton dynamics are superimposed by downhill migration processes occurring on the picosecond time-scale, which cause a time-dependent energetic shift of the intensity distribution. By comparing the exciton population dynamics of ordered and non-ordered samples, it was possible to link the data presented in the present work to those observed in tr-2PPE experiments on 6T/Au(111) performed by Varene *et al.* [7] and to give a new interpretation on the exciton population pathway and the exciton relaxation mechanisms from their data.

In Chapter 5 the role of the excitonic coupling in the photoisomerization of azobenzene units in diluted azobenzene-functionalized alkanethiolate self-assembled monolayers was discussed. Using the fact that the different static dipole moments of the *trans* and *cis* chromophores induce a shift of the sample work-function [146, 147], it was shown that the photoisomerization process of the excitonically coupled azobenzenes in the SAM follows the behavior of non-interacting chromophores. Excitonic coupling does not promote cooperative switching but reduces the effective cross section for photoisomerization. This observation is independent of the chromophore density. Furthermore, it was demonstrated that the work function of a SAM/Au(111) sample can be tuned over a range of up to 200 meV by adjusting a photostationary state through variation of the relative intensities of two light sources which are simultaneously exciting the sample. Using PEEM it was possible to image the area of a SAM switched by a laser beam due to the work-function contrast to the environment. The experiments revealed that the work function of a SAM/Au(111) sample can be tuned locally in a fast, precise and reliable way by external optical stimuli.

Bibliography

- [1] S. Reineke, F. Lindner, G. Schwartz, N. Seidler, K. Walzer, B. Lüssem, and K. Leo. "White organic light-emitting diodes with fluorescent tube efficiency." *Nature* 459 (2009), pp. 234–238. DOI: [10.1038/nature08003](https://doi.org/10.1038/nature08003) (cit. on p. 1).
- [2] H. Nakanotani, T. Higuchi, T. Furukawa, K. Masui, K. Morimoto, M. Numata, H. Tanaka, Y. Sagara, T. Yasuda, and C. Adachi. "High-efficiency organic light-emitting diodes with fluorescent emitters." *Nature Communications* 5 (2014), p. 4016. DOI: [10.1038/ncomms5016](https://doi.org/10.1038/ncomms5016) (cit. on p. 1).
- [3] R. Capelli, S. Toffanin, G. Generali, H. Usta, A. Facchetti, and M. Muccini. "Organic light-emitting transistors with an efficiency that outperforms the equivalent light-emitting diodes." *Nature Materials* 9 (2010), pp. 496–503. DOI: [10.1038/nmat2751](https://doi.org/10.1038/nmat2751) (cit. on p. 1).
- [4] M. Scharber and N. Sariciftci. "Efficiency of bulk-heterojunction organic solar cells." *Progress in Polymer Science* 38 (2013), pp. 1929–1940. DOI: <https://doi.org/10.1016/j.progpolymsci.2013.05.001> (cit. on p. 1).
- [5] A. Rao, M. W. B. Wilson, J. M. Hodgkiss, S. Albert-Seifried, H. Bässler, and R. H. Friend. "Exciton fission and charge generation via triplet excitons in pentacene/C60 bilayers." *Journal of the American Chemical Society* 132 (2010), pp. 12698–12703. DOI: [10.1021/ja1042462](https://doi.org/10.1021/ja1042462) (cit. on p. 1).
- [6] W.-L. Chan, M. Ligges, A. Jailaubekov, L. Kaake, L. Miaja-Avila, and X.-Y. Zhu. "Observing the multiexciton state in singlet fission and ensuing ultrafast multielectron transfer." *Science* 334 (2011), pp. 1541–1545. DOI: [10.1126/science.1213986](https://doi.org/10.1126/science.1213986) (cit. on p. 1).
- [7] E. Varene, L. Bogner, C. Bronner, and P. Tegeder. "Ultrafast exciton population, relaxation, and decay dynamics in thin oligothiophene films." *Physical Review Letters* 109 (2012), p. 207601. DOI: [10.1103/PhysRevLett.109.207601](https://doi.org/10.1103/PhysRevLett.109.207601) (cit. on pp. 1, 29, 47, 61, 63–64, 75, 77, 106, 127).
- [8] J. R. Tritsch, W.-L. Chan, X. Wu, N. R. Monahan, and X.-Y. Zhu. "Harvesting singlet fission for solar energy conversion via triplet energy transfer." *Nature Communications* 4 (2013), p. 2679. DOI: [10.1038/ncomms3679](https://doi.org/10.1038/ncomms3679) (cit. on p. 1).

- [9] K. Kolata, T. Breuer, G. Witte, and S. Chatterjee. "Molecular packing determines singlet exciton fission in organic semiconductors." *ACS Nano* 8 (2014), pp. 7377–7383. DOI: [10.1021/nn502544d](https://doi.org/10.1021/nn502544d) (cit. on p. 1).
- [10] N. Katsonis, M. Lubomska, M. M. Pollard, B. L. Feringa, and P. Rudolf. "Synthetic light-activated molecular switches and motors on surfaces." *Progress in Surface Science* 82 (2007), pp. 407–434. DOI: [10.1016/j.progsurf.2007.03.011](https://doi.org/10.1016/j.progsurf.2007.03.011) (cit. on p. 1).
- [11] B. K. Pathem, S. A. Claridge, Y. B. Zheng, and P. S. Weiss. "Molecular switches and motors on surfaces." *Annual Review of Physical Chemistry* 64 (2013), pp. 605–630. DOI: [10.1146/annurev-physchem-040412-110045](https://doi.org/10.1146/annurev-physchem-040412-110045) (cit. on pp. 1, 81).
- [12] H. Li and D.-H. Qu. "Recent advances in new-type molecular switches." *Science China Chemistry* 58 (2015), pp. 916–921. DOI: [10.1007/s11426-015-5417-7](https://doi.org/10.1007/s11426-015-5417-7) (cit. on p. 1).
- [13] X. Pei, A. Fernandes, B. Mathy, X. Laloyaux, B. Nysten, O. Riant, and A. M. Jonas. "Correlation between the structure and wettability of photoswitchable hydrophilic azobenzene monolayers on silicon." *Langmuir* 27 (2011), pp. 9403–9412. DOI: [10.1021/la201526u](https://doi.org/10.1021/la201526u) (cit. on p. 2).
- [14] N. Crivillers, E. Orgiu, F. Reinders, M. Mayor, and P. Samorì. "Optical modulation of the charge injection in an organic field-effect transistor based on photochromic self-assembled-monolayer-functionalized electrodes." *Advanced Materials* 23 (2011), pp. 1447–1452. DOI: [10.1002/adma.201003736](https://doi.org/10.1002/adma.201003736) (cit. on pp. 2, 81, 83).
- [15] X.-Y. Zhu. "How to draw energy level diagrams in excitonic solar cells." *The Journal of Physical Chemistry Letters* 5 (2014), pp. 2283–2288. DOI: [10.1021/jz5008438](https://doi.org/10.1021/jz5008438) (cit. on pp. 4, 30).
- [16] M. Kasha. "Classification of excitons." In: *Physical Processes in Radiation Biology*. Ed. by L. Augstein, R. Mason, and B. Rosenberg. 1964, pp. 17–19. DOI: [10.1016/B978-1-4831-9824-8.50006-2](https://doi.org/10.1016/B978-1-4831-9824-8.50006-2) (cit. on p. 3).
- [17] G. H. Wannier. "The structure of electronic excitation levels in insulating crystals." *Physical Review* 52 (1937), pp. 191–197. DOI: <https://doi.org/10.1103/PhysRev.52.191> (cit. on p. 4).
- [18] A. S. Davydov. "The theory of molecular excitons." *Soviet Physics Uspekhi* 7 (1964), pp. 145–178. DOI: [10.1070/PU1964v007n02ABEH003659](https://doi.org/10.1070/PU1964v007n02ABEH003659) (cit. on p. 4).
- [19] J. Frenkel. "On the transformation of light into heat in solids. I." *Physical Review* 37 (1931), pp. 17–44. DOI: [10.1103/PhysRev.37.17](https://doi.org/10.1103/PhysRev.37.17) (cit. on p. 4).
- [20] I. Hill, A. Kahn, Z. Soos, and R. P. Jr. "Charge-separation energy in films of π -conjugated organic molecules." *Chemical Physics Letters* 327 (2000), pp. 181–188. DOI: [10.1016/S0009-2614\(00\)00882-4](https://doi.org/10.1016/S0009-2614(00)00882-4) (cit. on pp. 5, 7, 60).
- [21] M. Knupfer. "Exciton binding energies in organic semiconductors." *Applied Physics A* 77 (2003), pp. 623–626. DOI: [10.1007/s00339-003-2182-9](https://doi.org/10.1007/s00339-003-2182-9) (cit. on pp. 6–7).

- [22] S. Berkebile, G. Koller, P. Puschnig, C. Ambrosch-Draxl, F. Netzer, and M. Ramsey. "Angle-resolved photoemission of chain-like molecules: the electronic band structure of sexithiophene and sexiphenyl." *Applied Physics A* 95 (2009), pp. 101–105. DOI: [10.1007/s00339-008-5034-9](https://doi.org/10.1007/s00339-008-5034-9) (cit. on p. 7).
- [23] L. Blinov, S. Palto, G. Ruani, C. Taliani, A. Tevosov, S. Yudin, and R. Zamboni. "Location of charge transfer states in α -sexithienyl determined by the electroabsorption technique." *Chemical Physics Letters* 232 (1995), pp. 401–406. DOI: [10.1016/0009-2614\(94\)01368-6](https://doi.org/10.1016/0009-2614(94)01368-6) (cit. on p. 7).
- [24] F. C. Spano, J. Clark, C. Silva, and R. H. Friend. "Determining exciton coherence from the photoluminescence spectral line shape in poly(3-hexylthiophene) thin films." *The Journal of Chemical Physics* 130 (2009), p. 074904. DOI: [10.1063/1.3076079](https://doi.org/10.1063/1.3076079) (cit. on p. 7).
- [25] A. S. Davydov. "Theory of absorption spectra of molecular crystals." *Zh. Eksp. Teor. Fiz.* 18 (1948), pp. 210–218 (cit. on p. 7).
- [26] A. S. Davydov. *Theory of molecular excitons*. Plenum Press, 1971 (cit. on p. 7).
- [27] E. E. Jelley. "Spectral absorption and fluorescence of dyes in the molecular state." *Nature* (1936), pp. 1009–1010. DOI: [10.1038/1381009a0](https://doi.org/10.1038/1381009a0) (cit. on p. 8).
- [28] M. Kasha. "Energy transfer mechanisms and the molecular exciton model for molecular aggregates." *Radiation Research* 20 (1963), pp. 55–70. DOI: [10.2307/3571331](https://doi.org/10.2307/3571331) (cit. on pp. 8–10, 12).
- [29] E. G. McRae and M. Kasha. "Enhancement of phosphorescence ability upon aggregation of dye molecules." *The Journal of Chemical Physics* 28 (1958), pp. 721–722. DOI: [10.1063/1.1744225](https://doi.org/10.1063/1.1744225) (cit. on pp. 9–10).
- [30] W. T. Simpson and D. L. Peterson. "Coupling strength for resonance force transfer of electronic energy in Van der Waals solids." *The Journal of Chemical Physics* 26 (1957), pp. 588–593. DOI: [10.1063/1.1743351](https://doi.org/10.1063/1.1743351) (cit. on pp. 10–11, 54).
- [31] F. Fennel and S. Lochbrunner. "Exciton-exciton annihilation in a disordered molecular system by direct and multistep Förster transfer." *Physical Review B* 92 (2015), 140301(R). DOI: [10.1103/PhysRevB.92.140301](https://doi.org/10.1103/PhysRevB.92.140301) (cit. on p. 13).
- [32] M. Muntwiler and X. Zhu. "Exciton formation and decay at surfaces and interfaces." In: *Dynamics at Solid State Surfaces and Interfaces*. Wiley-VCH, 2010, pp. 325–358. DOI: [10.1002/9783527633418.ch15](https://doi.org/10.1002/9783527633418.ch15) (cit. on p. 13).
- [33] X.-Y. Zhu, Q. Yang, and M. Muntwiler. "Charge-transfer excitons at organic semiconductor surfaces and interfaces." *Accounts of Chemical Research* 42 (2009), pp. 1779–1787. DOI: [10.1021/ar800269u](https://doi.org/10.1021/ar800269u) (cit. on p. 13).
- [34] S. Günes, H. Neugebauer, and N. S. Sariciftci. "Conjugated polymer-based organic solar cells." *Chemical Reviews* 107 (2007), pp. 1324–1338. DOI: [10.1021/cr050149z](https://doi.org/10.1021/cr050149z) (cit. on pp. 14, 47).

- [35] N. Koch. "Organic electronic devices and their functional interfaces." *ChemPhysChem* 8 (2007), pp. 1438–1455. DOI: [10.1002/cphc.200700177](https://doi.org/10.1002/cphc.200700177) (cit. on pp. 14, 47).
- [36] K. Walzer, B. Maennig, M. Pfeiffer, and K. Leo. "Highly efficient organic devices based on electrically doped transport layers." *Chemical Reviews* 107 (2007), pp. 1233–1271. DOI: [10.1021/cr050156n](https://doi.org/10.1021/cr050156n) (cit. on pp. 14, 47).
- [37] H. E. Katz and J. Huang. "Thin-film organic electronic devices." *Annual Review of Materials Research* 39 (2009), pp. 71–92. DOI: [10.1146/annurev-matsci-082908-145433](https://doi.org/10.1146/annurev-matsci-082908-145433) (cit. on pp. 14, 47).
- [38] M. Váry, M. Perný, M. Kusko, and E. Firický. "Organic semiconductors for solar cells – an overview." *Elektroenergetika* 4 (2011), pp. 14–16 (cit. on p. 14).
- [39] B. P. Rand, J. Genoe, P. Heremans, and J. Poortmans. "Solar cells utilizing small molecular weight organic semiconductors." *Progress in Photovoltaics: Research and Applications* 15 (2007), pp. 659–676. DOI: [10.1002/pip.788](https://doi.org/10.1002/pip.788) (cit. on p. 14).
- [40] G. Horowitz, B. Bachet, A. Yassar, P. Lang, F. Demanze, J.-L. Fave, and F. Garnier. "Growth and characterization of sexithiophene single crystals." *Chemistry of Materials* 7 (1995), pp. 1337–1341. DOI: [10.1021/cm00055a010](https://doi.org/10.1021/cm00055a010) (cit. on p. 14).
- [41] R. Lazzoroni, A. Pal, S. Rossini, G. Ruani, R. Zamboni, and C. Taliani. "Electronic and infrared properties of the α -sexithienyl single crystal." *Synthetic Metals* 42 (1991), pp. 2359–2362. DOI: [https://doi.org/10.1016/0379-6779\(91\)91381-J](https://doi.org/10.1016/0379-6779(91)91381-J) (cit. on p. 14).
- [42] H.-J. Egelhaaf, P. Bäuerle, K. Rauer, V. Hoffmann, and D. Oelkrug. "Orientation and mobility in ultrathin oligothiophene films: UV-Vis, IR and fluorescence studies." *Synthetic Metals* 61 (1993), pp. 143–146. DOI: [10.1016/0379-6779\(93\)91212-K](https://doi.org/10.1016/0379-6779(93)91212-K) (cit. on pp. 14, 17).
- [43] H.-J. Egelhaaf, P. Bäuerle, K. Rauer, V. Hoffmann, and D. Oelkrug. "UV/Vis and IR spectroscopic studies on molecular orientation in ultrathin films of polythiophene model compounds." *Journal of Molecular Structure* 293 (1993), pp. 249–252. DOI: [10.1016/0022-2860\(93\)80060-9](https://doi.org/10.1016/0022-2860(93)80060-9) (cit. on p. 14).
- [44] M. Muccini, E. Lunedei, A. Bree, G. Horowitz, F. Garnier, and C. Taliani. "Polarized fluorescence in α -sexithienyl single crystal at 4.2 K." *The Journal of Chemical Physics* 108 (1998), pp. 7327–7333. DOI: [10.1063/1.476151](https://doi.org/10.1063/1.476151) (cit. on pp. 14–15).
- [45] F. Garnier, G. Horowitz, P. Valat, F. Kouki, and V. Wintgens. "The four-level stimulated emission in sexithiophene single crystals." *Applied Physics Letters* 72 (1998), pp. 2087–2089. DOI: [10.1063/1.121284](https://doi.org/10.1063/1.121284) (cit. on p. 14).
- [46] M. Muccini, E. Lunedei, C. Taliani, F. Garnier, and H. Baessler. "Ordering of low energy electronic excitations in α -sexithiophene single crystal." *Synthetic Metals* 84 (1997), pp. 863–864. DOI: [10.1016/S0379-6779\(96\)04184-7](https://doi.org/10.1016/S0379-6779(96)04184-7) (cit. on p. 15).

- [47] S. Tavazzi, M. Campione, M. Laicini, L. Raimondo, A. Borghesi, and P. Spearman. "Measured Davydov splitting in oligothiophene crystals." *The Journal of Chemical Physics* 124 (2006), p. 194710. DOI: [10.1063/1.2196037](https://doi.org/10.1063/1.2196037) (cit. on p. 15).
- [48] F. C. Spano. "Excitons in conjugated oligomer aggregates, films, and crystals." *Annual Review of Physical Chemistry* 57 (2006), pp. 217–243. DOI: [10.1146/annurev.physchem.57.032905.104557](https://doi.org/10.1146/annurev.physchem.57.032905.104557) (cit. on p. 15).
- [49] L. Sun, S. Berkebile, G. Weidlinger, M. Denk, R. Denk, M. Hohage, G. Koller, F. P. Netzer, M. G. Ramsey, and P. Zeppenfeld. "Layer resolved evolution of the optical properties of α -sexithiophene thin films." *Physical Chemistry Chemical Physics* 14 (2012), pp. 13651–13655. DOI: [10.1039/C2CP42270K](https://doi.org/10.1039/C2CP42270K) (cit. on pp. 15, 17, 53).
- [50] G. Horowitz, P. Valat, F. Garnier, F. Kouki, and V. Wintgens. "Photoinduced spontaneous and stimulated emission in sexithiophene single crystals." *Optical Materials* 9 (1998), pp. 46–52. DOI: [10.1016/S0925-3467\(97\)00068-2](https://doi.org/10.1016/S0925-3467(97)00068-2) (cit. on pp. 15–16).
- [51] M. Kiel, K. Duncker, C. Hagedorf, and W. Widdra. "Molecular structure and chiral separation in α -sexithiophene ultrathin films on Au(111): Low-energy electron diffraction and scanning tunneling microscopy." *Physical Review B* 75 (May 2007), p. 195439. DOI: [10.1103/PhysRevB.75.195439](https://doi.org/10.1103/PhysRevB.75.195439) (cit. on pp. 15–16, 49, 55).
- [52] M. L. Wansleben. "Electron and exciton dynamics in α -sexithiophene on Au(111)." MA thesis. Freie Universität Berlin, 2015 (cit. on pp. 15, 17, 59).
- [53] H. Chosrovian, S. Rentsch, D. Grebner, D. Dahm, E. Birckner, and H. Naarmann. "Time-resolved fluorescence studies on thiophene oligomers in solution." *Synthetic Metals* 60 (1993), pp. 23–26. DOI: [10.1016/0379-6779\(93\)91178-5](https://doi.org/10.1016/0379-6779(93)91178-5) (cit. on pp. 16–17).
- [54] J.-M. Nunzi, N. Pfeffer, F. Charra, and D. Fichou. "Picosecond photoinduced dichroism in sexithiophene thin films." *Chemical Physics Letters* 215 (1993), pp. 114–119. DOI: [10.1016/0009-2614\(93\)89272-J](https://doi.org/10.1016/0009-2614(93)89272-J) (cit. on p. 16).
- [55] T. Wagner, D. R. Fritz, and P. Zeppenfeld. " α -6T on Ag(110): The formation of the wetting layer." *Synthetic Metals* 161 (2011), pp. 2006–2010. DOI: [10.1016/j.synthmet.2011.07.014](https://doi.org/10.1016/j.synthmet.2011.07.014) (cit. on pp. 18, 45, 49).
- [56] T. Wagner, D. R. Fritz, and P. Zeppenfeld. "Standing and flat lying α -6T molecules probed by imaging photoelectron spectroscopy." *Organic Electronics* 12 (2011), pp. 442–446. DOI: [10.1016/j.orgel.2010.12.011](https://doi.org/10.1016/j.orgel.2010.12.011) (cit. on pp. 18, 46, 49, 52).
- [57] T. Moldt, D. Brete, D. Przyrembel, S. Das, J. R. Goldman, P. K. Kundu, C. Gahl, R. Klajn, and M. Weinelt. "Tailoring the properties of surface-immobilized azobenzenes by monolayer dilution and surface curvature." *Langmuir* 31 (2015), pp. 1048–1057. DOI: [10.1021/la504291n](https://doi.org/10.1021/la504291n) (cit. on pp. 18–19, 22, 81–82, 84, 90).

- [58] R. Wang, T. Iyoda, L. Jiang, D. A. Tryk, K. Hashimoto, and A. Fujishima. "Structural investigation of azobenzene-containing self-assembled monolayer films." *Journal of Electroanalytical Chemistry* 438 (1997), pp. 213–219. DOI: [10.1016/S0022-0728\(96\)05031-0](https://doi.org/10.1016/S0022-0728(96)05031-0) (cit. on p. 18).
- [59] M. Han, T. Honda, D. Ishikawa, E. Ito, M. Hara, and Y. Norikane. "Realization of highly photoresponsive azobenzene-functionalized monolayers." *Journal of Materials Chemistry* 21 (2011), pp. 4696–4702. DOI: [10.1039/C0JM03697H](https://doi.org/10.1039/C0JM03697H) (cit. on p. 18).
- [60] E. Mitscherlich. "Ueber das Stickstoffbenzid." *Annalen der Physik und Chemie* 108 (1834), pp. 225–227. DOI: [10.1002/andp.18341081502](https://doi.org/10.1002/andp.18341081502) (cit. on p. 18).
- [61] G. S. Hartley. "The cis-form of azobenzene." *Nature* 140 (1937), p. 281. DOI: [10.1038/140281a0](https://doi.org/10.1038/140281a0) (cit. on p. 18).
- [62] W. Freyer, D. Brete, R. Schmidt, C. Gahl, R. Carley, and M. Weinelt. "Switching behavior and optical absorbance of azobenzene-functionalized alkanethiols in different environments." *Journal of Photochemistry and Photobiology A* 204 (2009), pp. 102–109. DOI: [10.1016/j.jphotochem.2009.02.018](https://doi.org/10.1016/j.jphotochem.2009.02.018) (cit. on p. 19).
- [63] I. Conti, M. Garavelli, and G. Orlandi. "The different photoisomerization efficiency of azobenzene in the lowest $n\pi^*$ and $\pi\pi^*$ singlets: The role of a phantom state." *Journal of the American Chemical Society* 130 (2008), pp. 5216–5230. DOI: [10.1021/ja710275e](https://doi.org/10.1021/ja710275e) (cit. on pp. 20–21, 89).
- [64] C. Gahl, R. Schmidt, D. Brete, E. R. McNellis, W. Freyer, R. Carley, K. Reuter, and M. Weinelt. "Structure and excitonic coupling in self-assembled monolayers of azobenzene-functionalized alkanethiols." *Journal of the American Chemical Society* 132 (2010), pp. 1831–1838. DOI: [10.1021/ja903636q](https://doi.org/10.1021/ja903636q) (cit. on pp. 21–22, 84, 90).
- [65] M. Utecht, T. Klamroth, and P. Saalfrank. "Optical absorption and excitonic coupling in azobenzenes forming self-assembled monolayers: a study based on density functional theory." *Physical Chemistry Chemical Physics* 13 (2011), pp. 21608–21614. DOI: [10.1039/c1cp22793a](https://doi.org/10.1039/c1cp22793a) (cit. on pp. 22, 90).
- [66] N. Heinemann, J. Grunau, T. Leißner, O. Andreyev, S. Kuhn, U. Jung, D. Zargarani, R. Herges, O. Magnussen, and M. Bauer. "Reversible switching in self-assembled monolayers of azobenzene thiolates on Au (111) probed by threshold photoemission." *Chemical Physics* 402 (2012), pp. 22–28. DOI: [10.1016/j.chemphys.2012.03.025](https://doi.org/10.1016/j.chemphys.2012.03.025) (cit. on p. 22).
- [67] A. Einstein. "Über einen die Erzeugung und Verwandlung des Lichtes betreffenden heuristischen Gesichtspunkt." *Annalen der Physik* 17 (1905), pp. 132–148. DOI: <https://doi.org/10.1002/andp.19053220607> (cit. on p. 23).
- [68] T. Hertel, E. Knoesel, M. Wolf, and G. Ertl. "Ultrafast electron dynamics at Cu(111): response of an electron gas to optical excitation." *Physical Review Letters* 76 (3 1996), pp. 535–538. DOI: [10.1103/PhysRevLett.76.535](https://doi.org/10.1103/PhysRevLett.76.535) (cit. on pp. 28–29).

-
- [69] K. Boger, M. Roth, M. Weinelt, T. Fauster, and P.-G. Reinhard. "Linewidths in energy-resolved two-photon photoemission spectroscopy." *Physical Review B* 65 (2002), p. 075104. DOI: [10.1103/PhysRevB.65.075104](https://doi.org/10.1103/PhysRevB.65.075104) (cit. on p. 28).
- [70] M. Weinelt. "Time-resolved two-photon photoemission from metal surfaces." *Journal of Physics: Condensed Matter* 14 (2002), R1099–R1141. DOI: <https://doi.org/10.1088/0953-8984/14/43/202> (cit. on p. 28).
- [71] K. Blum. "Quantum theory of relaxation." In: *Density Matrix Theory and Applications*. Springer Berlin Heidelberg, 2012, pp. 275–312. DOI: [10.1007/978-3-642-20561-3_8](https://doi.org/10.1007/978-3-642-20561-3_8) (cit. on p. 28).
- [72] C. Gahl. "Elektronentransfer- und Solvatisierungsdynamik in Eis adsorbiert auf Metalloberflächen." PhD thesis. Freie Universität Berlin, 2004 (cit. on p. 29).
- [73] P. Heimann, H. Neddermeyer, and H. F. Roloff. "Ultraviolet photoemission for intrinsic surface states of the noble metals." *Journal of Physics C: Solid State Physics* 10 (1977), pp. L17–L22. DOI: <https://doi.org/10.1088/0022-3719/10/1/004> (cit. on p. 29).
- [74] E. Varene and P. Tegeder. "Polaron dynamics in thin polythiophene films studied with time-resolved photoemission." *Applied Physics A* 107 (Apr. 2012), pp. 13–16. DOI: [10.1007/s00339-012-6819-4](https://doi.org/10.1007/s00339-012-6819-4) (cit. on p. 29).
- [75] M. Marks, S. Sachs, C. H. Schwalb, A. Schöll, and U. Höfer. "Electronic structure and excited state dynamics in optically excited PTCDA films investigated with two-photon photoemission." *The Journal of Chemical Physics* 139 (2013), p. 124701. DOI: [10.1063/1.4818541](https://doi.org/10.1063/1.4818541) (cit. on p. 29).
- [76] L. Bogner, Z. Yang, M. Corso, R. Fitzner, P. Bauerle, K. J. Franke, J. I. Pascual, and P. Tegeder. "Electronic structure and excited state dynamics in a dicyanovinyl-substituted oligothiophene on Au(111)." *Physical Chemistry Chemical Physics* 17 (2015), pp. 27118–27126. DOI: [10.1039/C5CP04084A](https://doi.org/10.1039/C5CP04084A) (cit. on p. 29).
- [77] M. P. Seah and W. A. Dench. "Quantitative electron spectroscopy of surfaces: a standard data base for electron inelastic mean free paths in solids." *Surface and Interface Analysis* 1 (1979), pp. 2–11. DOI: <https://doi.org/10.1002/sia.740010103> (cit. on p. 30).
- [78] S. Tanuma, C. J. Powell, and D. R. Penn. "Calculations of electron inelastic mean free paths." *Surface and Interface Analysis* 21 (1993), pp. 165–176. DOI: [10.1002/sia.3522](https://doi.org/10.1002/sia.3522) (cit. on p. 30).
- [79] M. K. Reed, M. K. Steiner-Shepard, and D. K. Negus. "Widely tunable femtosecond optical parametric amplifier at 250 kHz with a Ti:sapphire regenerative amplifier." *Optics Letters* 19 (1994), pp. 1855–1857. DOI: <https://doi.org/10.1364/OL.19.001855> (cit. on p. 33).

- [80] M. K. Reed, M. K. Steiner-Shepard, M. K. Armas, and D. K. Negus. "Microjoule-energy ultrafast optical parametric amplifiers." *Journal of the Optical Society of America B* 12 (1995), pp. 2229–2236. DOI: <https://doi.org/10.1364/JOSAB.12.002229> (cit. on p. 33).
- [81] M. K. Reed, M. K. Armas, M. K. Steiner-Shepard, and D. K. Negus. "30-fs pulses tunable across the visible with a 100-kHz Ti:sapphire regenerative amplifier." *Optics Letters* 20 (1995), pp. 605–607. DOI: <https://doi.org/10.1364/OL.20.000605> (cit. on p. 33).
- [82] P. M. W. French. "The generation of ultrashort laser pulses." *Reports on Progress in Physics* 58 (1995), pp. 169–267. DOI: <https://doi.org/10.1088/0034-4885/58/2/001> (cit. on p. 33).
- [83] J. Eichler and H. J. Eichler. *Laser - Bauformen, Strahlführung, Anwendungen*. 7., aktualisierte Auflage. Springer, 2010. DOI: [10.1007/978-3-642-10462-6](https://doi.org/10.1007/978-3-642-10462-6) (cit. on pp. 33–34).
- [84] D. E. Spence, P. N. Kean, and W. Sibbett. "60-fs pulse generation from a self-mode-locked Ti:sapphire laser." *Optics Letters* 16 (1991), pp. 42–44. DOI: <https://doi.org/10.1364/OL.16.000042> (cit. on p. 33).
- [85] C. Hirlimann. In: *Femtosecond laser pulses - principles and experiments*. Ed. by C. Rullière. Second Edition. Springer, 2005. Chap. Pulsed optics. DOI: [10.1007/b137908](https://doi.org/10.1007/b137908) (cit. on p. 33).
- [86] T. Norris. "Femtosecond pulse amplification at 250 kHz with a Ti:sapphire regenerative amplifier and application to continuum generation." *Optics Letters* 17 (1992), pp. 1009–1011. DOI: <https://doi.org/10.1364/OL.17.001009> (cit. on p. 34).
- [87] F. L. Pedrotti, L. S. Pedrotti, W. Basic, and H. Schmidt. "Akustooptische Effekte." In: *Optik fuer Ingenieure*. Springer Berlin Heidelberg, 2005, pp. 788–793. DOI: [10.1007/b139018](https://doi.org/10.1007/b139018) (cit. on p. 34).
- [88] F. Salin. In: *Femtosecond Laser Pulses - Principles and Experiments*. Ed. by C. Rullière. Second Edition. Springer, 2005. Chap. How to Manipulate and Change the Characteristics of Laser Pulses. DOI: [10.1007/b137908](https://doi.org/10.1007/b137908) (cit. on p. 34).
- [89] W. Demtröder. *Experimentalphysik 2 – Elektrizität und Optik*. Springer, 2006. DOI: [10.1007/978-3-642-29944-5](https://doi.org/10.1007/978-3-642-29944-5) (cit. on p. 34).
- [90] B. Couillaud and V. Fossati-Bellani. "Modelocked lasers and ultrashort pulses I and II." *Lasers and applications* 4 (1985), 79–83 (January 1985) and 91–94 (February 1985) (cit. on p. 36).
- [91] C. Eickhoff. "Zeitaufgelöste Zweiphotonen-Photoemission an der Si(001)-Oberfläche." PhD thesis. Fachbereich Physik der Freien Universität Berlin, 2010 (cit. on pp. 38, 75).

- [92] D. Brete. "Azobenzenes and imines as molecular switches on gold(111): Structure, excitonic coupling, and photoisomerization." PhD Thesis. Fachbereich Physik der Freien Universität Berlin, 2016 (cit. on pp. 38, 48, 123).
- [93] T. Kunze. "Impulsabhängige, ultraschnelle Elektronendynamik an gestuften Oberflächen und typologischen Isolatoren untersucht mit winkelauflösender Flugzeitspektroskopie." PhD thesis. Fachbereich Physik der Freien Universität Berlin, 2014 (cit. on p. 41).
- [94] R. Forker, M. Gruenewald, and T. Fritz. "Optical differential reflectance spectroscopy on thin molecular films." *Annual Reports in Chemistry, Section C: Physical Chemistry* 108 (2012), pp. 34–68. DOI: [10.1039/C2PC90002E](https://doi.org/10.1039/C2PC90002E) (cit. on p. 43).
- [95] J. D. E. McIntyre and D. E. Aspnes. "Differential reflection spectroscopy of very thin surface films." *Surface Science* 24 (1971), pp. 417–434. DOI: [10.1016/0039-6028\(71\)90272-X](https://doi.org/10.1016/0039-6028(71)90272-X) (cit. on p. 43).
- [96] R. Forker and T. Fritz. "Optical differential reflectance spectroscopy of ultrathin epitaxial organic films." *Physical Chemistry Chemical Physics* 11 (2009), pp. 2142–2155. DOI: [10.1039/B814628D](https://doi.org/10.1039/B814628D) (cit. on p. 43).
- [97] F. Nickel, M. Bernien, U. Lipowski, and W. Kuch. "Optical differential reflectance spectroscopy for photochromic molecules on solid surfaces." *Review of Scientific Instruments* 89 (2018), p. 033113. DOI: [10.1063/1.5019415](https://doi.org/10.1063/1.5019415) (cit. on p. 43).
- [98] R. Nitsche and T. Fritz. "Determination of model-free Kramers-Kronig consistent optical constants of thin absorbing films from just one spectral measurement: Application to organic semiconductors." *Physical Review B* 70 (2004), p. 195432. DOI: [10.1103/PhysRevB.70.195432](https://doi.org/10.1103/PhysRevB.70.195432) (cit. on p. 43).
- [99] A. Navarro-Quezada, M. Aiglinger, E. Ghanbari, T. Wagner, and P. Zeppenfeld. "Polarization-dependent differential reflectance spectroscopy for real-time monitoring of organic thin film growth." *Review of Scientific Instruments* 86 (2015), p. 113108. DOI: [10.1063/1.4936352](https://doi.org/10.1063/1.4936352) (cit. on p. 44).
- [100] M. Mundschau. In: *Handbook of microscopy*. Ed. by S. Amelinckx, D. van Dyck, J. van Landuyt, and G. van Tendeloo. Weinheim: Germany: Wiley-VCH, 2008. Chap. Photoelectron emission microscopy, pp. 763–773. DOI: [10.1002/9783527620524.ch10](https://doi.org/10.1002/9783527620524.ch10) (cit. on p. 45).
- [101] E. Bauer. *Surface microscopy with low energy electrons*. Springer, 2014. DOI: [10.1007/978-1-4939-0935-3](https://doi.org/10.1007/978-1-4939-0935-3) (cit. on p. 45).
- [102] G. Schoenhense, A. Oelsner, O. Schmidt, G. Fecher, V. Mergel, O. Jagutzki, and H. Schmidt-Boecking. "Time-of-flight photoemission electron microscopy – a new way to chemical surface analysis." *Surface Science* 480 (2001), pp. 180–187. DOI: [https://doi.org/10.1016/S0039-6028\(01\)00833-0](https://doi.org/10.1016/S0039-6028(01)00833-0) (cit. on p. 46).

- [103] A. Oelsner, O. Schmidt, M. Schicketanz, M. Klais, G. Schoenhense, V. Mergel, O. Jagutzki, and H. Schmidt-Boecking. "Microspectroscopy and imaging using a delay line detector in time-of-flight photoemission microscopy." *Review of Scientific Instruments* 72 (2001), pp. 3968–3974. DOI: [10.1063/1.1405781](https://doi.org/10.1063/1.1405781) (cit. on p. 46).
- [104] K. Zielke. PhD thesis. Freie Universität Berlin, to be published (cit. on pp. 48, 55, 59, 62, 64, 66, 125).
- [105] S. Prato, L. Floreano, D. Cvetko, V. D. Renzi, A. Morgante, S. Modesti, F. Biscarini, R. Zamboni, and C. Taliani. "Anisotropic ordered planar growth of α -sexithienyl thin films." *The Journal of Physical Chemistry B* 103 (1999), pp. 7788–7795. DOI: [10.1021/jp9905878](https://doi.org/10.1021/jp9905878) (cit. on p. 49).
- [106] M. Kiguchi, G. Yoshikawa, and K. Saiki. "Temperature and thickness dependence of molecular orientation of α -sexithienyl on Cu(111)." *Journal of Applied Physics* 94 (2003), pp. 4866–4870. DOI: [10.1063/1.1609637](https://doi.org/10.1063/1.1609637) (cit. on p. 49).
- [107] H. Inoue, G. Yoshikawa, and K. Saiki. "Molecular chain structure of α -sexithienyl on Ag(110) observed by scanning tunneling microscopy." *Japanese Journal of Applied Physics* 45 (2006), pp. 1794–1796. DOI: <https://doi.org/10.1143/JJAP.45.1794> (cit. on p. 49).
- [108] H. Glowatzki, S. Duhm, K.-F. Braun, J. P. Rabe, and N. Koch. "Molecular chains and carpets of sexithiophenes on Au(111)." *Physical Review B* 76 (2007), p. 125425. DOI: [10.1103/PhysRevB.76.125425](https://doi.org/10.1103/PhysRevB.76.125425) (cit. on p. 49).
- [109] K. Duncker, M. Kiel, A. Höfer, and W. Widdra. "Commensurate surface structures and concerted *cis-trans*-isomerization within ordered monolayers of α -sexithiophene on Ag(001)." *Physical Review B* 77 (2008), p. 155423. DOI: [10.1103/PhysRevB.77.155423](https://doi.org/10.1103/PhysRevB.77.155423) (cit. on p. 49).
- [110] A. Höfer, K. Duncker, M. Kiel, S. Wedekind, and W. Widdra. "Adsorption of α -sexithiophene on Au(001): Molecule-induced partial lifting of the substrate reconstruction." *Physical Review B* 83 (2011), p. 075414. DOI: [10.1103/PhysRevB.83.075414](https://doi.org/10.1103/PhysRevB.83.075414) (cit. on p. 49).
- [111] A. Sander, R. Hammer, K. Duncker, S. Förster, and W. Widdra. "Thermally and photoinduced polymerization of ultrathin sexithiophene films." *The Journal of Chemical Physics* 141 (2014), p. 104704. DOI: [10.1063/1.4894437](https://doi.org/10.1063/1.4894437) (cit. on pp. 49, 54).
- [112] T. Wagner, D. R. Fritz, and P. Zeppenfeld. "Probing organic nanostructures by photoelectron-emission microscopy." *Applied Surface Science* 267 (2013), pp. 26–29. DOI: [10.1016/j.apsusc.2012.04.157](https://doi.org/10.1016/j.apsusc.2012.04.157) (cit. on pp. 49, 52).
- [113] E. Ghanbari, T. Wagner, and P. Zeppenfeld. "Layer-resolved evolution of organic thin films monitored by photoelectron emission microscopy and optical reflectance spectroscopy." *The Journal of Physical Chemistry C* 119 (2015), pp. 24174–24181. DOI: [10.1021/acs.jpcc.5b08083](https://doi.org/10.1021/acs.jpcc.5b08083) (cit. on pp. 49, 52).

- [114] T. Wagner, E. Ghanbari, D. Huber, and P. Zeppenfeld. "The growth of α -sexithiophene films on Ag(111) studied by means of PEEM with linearly polarized light." *Ultramicroscopy* 159 (2015), pp. 464–469. DOI: [10.1016/j.ultramicro.2015.06.013](https://doi.org/10.1016/j.ultramicro.2015.06.013) (cit. on pp. 49, 52).
- [115] T. Wagner, D. R. Fritz, Z. Rudolfová, and P. Zeppenfeld. "Role of step edges on the structure formation of α -6T on Ag(441)." *Surface Science* 667 (2018), pp. 17–24. DOI: <https://doi.org/10.1016/j.susc.2017.09.008> (cit. on p. 49).
- [116] T. Wakamatsu, S. Toyoshima, and K. Saito. "Optical reflection response of dye-aggregate films in the absorption bands." *Journal of the Optical Society of America B* 23 (2006), pp. 1859–1866. DOI: [10.1364/JOSAB.23.001859](https://doi.org/10.1364/JOSAB.23.001859) (cit. on p. 52).
- [117] F. C. Spano. "The spectral signatures of Frenkel polarons in H- and J-aggregates." *Accounts of Chemical Research* 43 (2010), pp. 429–439. DOI: [10.1021/ar900233v](https://doi.org/10.1021/ar900233v) (cit. on pp. 54, 75).
- [118] W. Bronsch, T. Wagner, S. Baum, M. Wansleben, K. Zielke, E. Ghanbari, M. Györök, A. Navarro-Quezada, P. Zeppenfeld, M. Weinelt, and C. Gahl. "Interplay between Morphology and Electronic Structure in α -Sexithiophene Films on Au(111)." *The Journal of Physical Chemistry C* 123 (2019), pp. 7931–7939. DOI: [10.1021/acs.jpcc.8b07280](https://doi.org/10.1021/acs.jpcc.8b07280) (cit. on pp. 55, 124, 129).
- [119] F. Jäckel, U. G. E. Perera, V. Iancu, K.-F. Braun, N. Koch, J. P. Rabe, and S.-W. Hla. "Investigating molecular charge transfer complexes with a low temperature scanning tunneling microscope." *Physical Review Letters* 100 (2008), p. 126102. DOI: [10.1103/PhysRevLett.100.126102](https://doi.org/10.1103/PhysRevLett.100.126102) (cit. on p. 57).
- [120] E. Varene, I. Martin, and P. Tegeder. "Optically induced inter- and intrafacial electron transfer probed by two-photon photoemission: Electronic states of sexithiophene on Au(111)." *Journal of Chemical Physics Letters* 2 (2011), pp. 252–256. DOI: [10.1021/jz1016203](https://doi.org/10.1021/jz1016203) (cit. on pp. 57–58, 61–63, 124).
- [121] T. Fauster and W. Steinmann. "Electromagnetic waves: Recent developments in research." In: ed. by P. Halevi. Vol. 2: Photonic Probes of surfaces. Elsevier, 1995. Chap. Two-photon photoemission spectroscopy of image states, pp. 347–411. DOI: <https://doi.org/10.1016/B978-0-444-82198-0.50015-1> (cit. on p. 57).
- [122] G. Dutton and X.-Y. Zhu. "Unoccupied states in C60 thin films probed by two-photon photoemission." *The Journal of Physical Chemistry B* 106 (2002), pp. 5975–5981. DOI: [10.1021/jp0256589](https://doi.org/10.1021/jp0256589) (cit. on p. 60).
- [123] C. Bronner, M. Schulze, S. Hagen, and P. Tegeder. "The influence of the electronic structure of adsorbate-substrate complexes on photoisomerization ability." *New Journal of Physics* 14 (2012), p. 043023. DOI: [doi : 10.1088/1367-2630/14/4/043023](https://doi.org/10.1088/1367-2630/14/4/043023) (cit. on p. 60).

- [124] T. Fauster. "Quantization of electronic states on metal surfaces." *Applied Physics A Solids and Surfaces* 59 (1994), pp. 479–486. DOI: [10.1007/BF00348266](https://doi.org/10.1007/BF00348266) (cit. on p. 61).
- [125] R. Kersting, U. Lemmer, R. F. Mahrt, K. Leo, H. Kurz, H. Bässler, and E. O. Göbel. "Femtosecond energy relaxation in π -conjugated polymers." *Physical Review Letters* 70 (1993), pp. 3820–3823. DOI: [10.1103/PhysRevLett.70.3820](https://doi.org/10.1103/PhysRevLett.70.3820) (cit. on pp. 71, 106).
- [126] F. Spano. "Analysis of the UV/Vis and CD spectral line shapes of carotenoid assemblies: Spectral signatures of chiral H-aggregates." *Journal of the American Chemical Society* 131 (2009), pp. 4267–4278. DOI: [10.1021/ja806853v](https://doi.org/10.1021/ja806853v) (cit. on p. 75).
- [127] O. V. Mikhnenko, F. Cordella, A. B. Sieval, J. C. Hummelen, P. W. M. Blom, and M. A. Loi. "Temperature dependence of exciton diffusion in conjugated polymers." *The Journal of Physical Chemistry B* 112 (2008), pp. 11601–11604. DOI: [10.1021/jp8042363](https://doi.org/10.1021/jp8042363) (cit. on p. 78).
- [128] O. V. Mikhnenko, P. W. M. Blom, and T.-Q. Nguyen. "Exciton diffusion in organic semiconductors." *Energy and Environmental Science* 8 (2015), pp. 1867–1888. DOI: [10.1039/C5EE00925A](https://doi.org/10.1039/C5EE00925A) (cit. on p. 78).
- [129] K. Ichimura, S.-K. Oh, and M. Nakagawa. "Light-driven motion of liquids on a photosensitive surface." *Science* 288 (2000), pp. 1624–1626. DOI: [10.1126/science.288.5471.1624](https://doi.org/10.1126/science.288.5471.1624) (cit. on p. 81).
- [130] T. Kudernac, N. Ruangsapapichat, M. Parschau, B. Maciá, N. Katsonis, S. R. Harutyunyan, K.-H. Ernst, and B. L. Feringa. "Electrically driven directional motion of a four-wheeled molecule on a metal surface." *Nature* 479 (2011), pp. 208–211. DOI: [10.1038/nature10587](https://doi.org/10.1038/nature10587) (cit. on p. 81).
- [131] J. M. Abendroth, O. S. Bushuyev, P. S. Weiss, and C. J. Barrett. "Controlling motion at the nanoscale: Rise of the molecular machines." *ACS Nano* 9 (2015), pp. 7746–7768. DOI: [10.1021/acsnano.5b03367](https://doi.org/10.1021/acsnano.5b03367) (cit. on p. 81).
- [132] D. Liu, Y. Xie, H. Shao, and X. Jiang. "Using azobenzene-embedded self-assembled monolayers to photochemically control cell adhesion reversibly." *Angewandte Chemie, Internationale Edition* 48 (2009), pp. 4406–4408. DOI: [10.1002/anie.200901130](https://doi.org/10.1002/anie.200901130) (cit. on p. 81).
- [133] G. M. Lazzerini, S. Mian, F. D. Stasio, A. M. Masillamani, N. Crivillers, F. Reinders, M. Mayor, P. Samorì, and F. Cacialli. "Increased efficiency of light-emitting diodes incorporating anodes functionalized with fluorinated azobenzene monolayers and a green-emitting polyfluorene derivative." *Applied Physics Letters* 101 (2012), p. 153306. DOI: [10.1063/1.4758682](https://doi.org/10.1063/1.4758682) (cit. on p. 81).
- [134] L. Boie. "Ultrafast electron dynamics in molecular switches at metal surfaces." MA thesis. Freie Universität Berlin, 2016 (cit. on p. 82).

-
- [135] M. Oehzelt, K. Akaike, N. Koch, and G. Heimel. "Energy-level alignment at organic heterointerfaces." *Science Advances* 1 (2015), pp. 1–8. DOI: [10.1126/sciadv.1501127](https://doi.org/10.1126/sciadv.1501127) (cit. on p. 83).
- [136] T. Schultz, R. Schlesinger, J. Niederhausen, F. Henneberger, S. Sadofev, S. Blumstengel, A. Vollmer, F. Bussolotti, J.-P. Yang, S. Kera, K. Parvez, N. Ueno, K. Müllen, and N. Koch. "Tuning the work function of GaN with organic molecular acceptors." *Physical Review B* 93 (2016), p. 125309. DOI: [10.1103/PhysRevB.93.125309](https://doi.org/10.1103/PhysRevB.93.125309) (cit. on p. 83).
- [137] S. Braun, M. P. de Jong, W. Osikowicz, and W. R. Salaneck. "Influence of the electrode work function on the energy level alignment at organicorganic interfaces." *Applied Physics Letters* 91 (2007), p. 202108. DOI: <https://doi.org/10.1063/1.2806938> (cit. on p. 83).
- [138] R. W. Zehner, B. F. Parsons, R. P. Hsung, and L. R. Sita. "Tuning the work function of gold with self-assembled monolayers derived from X-[C₆H₄-C-C-]_nC₆H₄-SH (n = 0, 1, 2; X = H, F, CH₃, CF₃, and OCH₃)." *Langmuir* 15 (1999), pp. 1121–1127. DOI: [10.1021/la981114f](https://doi.org/10.1021/la981114f) (cit. on p. 83).
- [139] D. M. Alloway, M. Hofmann, D. L. Smith, N. E. Gruhn, A. L. Graham, R. J. Colorado, V. H. Wysocki, T. R. Lee, P. A. Lee, and N. R. Armstrong. "Interface dipoles arising from self-assembled monolayers on Gold: UV-photoemission studies of alkanethiols and partially fluorinated alkanethiols." *The Journal of Physical Chemistry B* 107 (2003), pp. 11690–11699. DOI: [10.1021/jp034665+](https://doi.org/10.1021/jp034665+) (cit. on p. 83).
- [140] B. de Boer, A. Hadipour, M. M. Mandoc, T. van Woudenberg, and P. W. M. Blom. "Tuning of metal work functions with self-assembled monolayers." *Advanced Materials* 17 (2005), pp. 621–625. DOI: [10.1002/adma.200401216](https://doi.org/10.1002/adma.200401216) (cit. on p. 83).
- [141] V. De Renzi, R. Rousseau, D. Marchetto, R. Biagi, S. Scandolo, and U. del Pennino. "Metal work-function changes induced by organic adsorbates: A combined experimental and theoretical study." *Physical Review Letters* 95 (2005), p. 046804. DOI: [10.1103/PhysRevLett.95.046804](https://doi.org/10.1103/PhysRevLett.95.046804) (cit. on p. 83).
- [142] F. Piersimoni, R. Schlesinger, J. Benduhn, D. Spoltore, S. Reiter, I. Lange, N. Koch, K. Vandewal, and D. Neher. "Charge transfer absorption and emission at ZnO/organic interfaces." *Journal of Chemical Physics Letters* 6 (2015), pp. 500–504. DOI: [10.1021/jz502657z](https://doi.org/10.1021/jz502657z) (cit. on p. 83).
- [143] D. Gustina, E. Markava, I. Muzikante, B. Stiller, and L. Brehmer. "Photoisomerisation process of self-assembled monolayers of some novel azobenzenes." *Advanced Materials for Optics and Electronics* 9 (1999), pp. 245–251. DOI: [10.1002/1099-0712\(199911/12\)9:6<245::AID-AM0388>3.0.CO;2-M](https://doi.org/10.1002/1099-0712(199911/12)9:6<245::AID-AM0388>3.0.CO;2-M) (cit. on p. 83).

- [144] B. Stiller, G. Knochenhauer, E. Markava, D. Gustina, I. Muzikante, P. Karageorgiev, and L. Brehmer. "Self-assembled monolayers of novel azobenzenes for optically induced switching." *Materials Science and Engineering: C* 8 (1999), pp. 385–389. DOI: [https://doi.org/10.1016/S0928-4931\(99\)00050-8](https://doi.org/10.1016/S0928-4931(99)00050-8) (cit. on p. 83).
- [145] B. Stiller, P. Karageorgiev, T. Jüngling, D. Prescher, T. Zetzsche, R. Dietel, G. Knochenhauer, and L. Brehmer. "Optically induced switching of azobenzene containing self assembling monolayers investigated by Kelvin Probe and Scanning Force Microscopy." *Molecular Crystals and Liquid Crystal Science and Technology* 355 (2001), pp. 401–411. DOI: [10.1080/10587250108023673](https://doi.org/10.1080/10587250108023673) (cit. on p. 83).
- [146] L. F. N. Ah Qune, H. Akiyama, T. Nagahiro, K. Tamada, and A. T. S. Wee. "Reversible work function changes induced by photoisomerization of asymmetric azobenzene dithiol self-assembled monolayers on gold." *Applied Physics Letters* 93 (2008), p. 083109. DOI: [10.1063/1.2969468](https://doi.org/10.1063/1.2969468) (cit. on pp. 83, 85, 106).
- [147] T. Nagahiro, H. Akiyama, M. Hara, and K. Tamada. "Photoisomerization of azobenzene containing self-assembled monolayers investigated by Kelvin probe work function measurements." *Journal of Electron Spectroscopy and Related Phenomena* 172 (2009), pp. 128–133. DOI: [10.1016/j.elspec.2009.02.009](https://doi.org/10.1016/j.elspec.2009.02.009) (cit. on pp. 83, 85, 88, 106).
- [148] N. Crivillers, A. Liscio, F. Di Stasio, C. Van Dyck, S. Osella, D. Cornil, S. Mian, G. M. Lazzerini, O. Fenwick, E. Orgiu, F. Reinders, S. Braun, M. Fahlman, M. Mayor, J. Cornil, V. Palermo, F. Cacialli, and P. Samorì. "Photoinduced work function changes by isomerization of a densely packed azobenzene-based SAM on Au: a joint experimental and theoretical study." *Physical Chemistry Chemical Physics* 13 (2011), pp. 14302–14310. DOI: [10.1039/C1CP20851A](https://doi.org/10.1039/C1CP20851A) (cit. on p. 83).
- [149] E. Orgiu, N. Crivillers, M. Herder, L. Grubert, M. Pätzelt, J. Frisch, E. Pavlica, D. T. Duong, G. Bratina, A. Salleo, N. Koch, S. Hecht, and P. Samorì. "Optically switchable transistor via energy-level phototuning in a bicomponent organic semiconductor." *Nature Chemistry* 4 (2012), pp. 675–679. DOI: [10.1038/nchem.1384](https://doi.org/10.1038/nchem.1384) (cit. on p. 83).
- [150] N. Crivillers, S. Osella, C. Van Dyck, G. M. Lazzerini, D. Cornil, A. Liscio, F. Di Stasio, S. Mian, O. Fenwick, F. Reinders, M. Neuburger, E. Treossi, M. Mayor, V. Palermo, F. Cacialli, J. Cornil, and P. Samorì. "Large work function shift of gold induced by a novel perfluorinated azobenzene-based self-assembled monolayer." *Advanced Materials* 25 (2013), pp. 432–436. DOI: [10.1002/adma.201201737](https://doi.org/10.1002/adma.201201737) (cit. on p. 83).
- [151] O. T. Hofmann, J.-C. Deinert, Y. Xu, P. Rinke, J. Stähler, M. Wolf, and M. Scheffler. "Large work function reduction by adsorption of a molecule with a negative electron affinity: Pyridine on ZnO(10 $\bar{1}$ 0)." *Journal of Chemical Physics* 139 (2013), p. 174701. DOI: <https://doi.org/10.1063/1.4827017> (cit. on p. 83).
- [152] G. S. Hartley and R. J. W. Le Fevre. "The dipole moments of cis- and trans-azobenzenes and of some related compounds." *Journal of the Chemical Society* (1939), pp. 531–535. DOI: [10.1039/JR9390000531](https://doi.org/10.1039/JR9390000531) (cit. on p. 83).

- [153] W. Bronsch, D. Przyrembel, L. Boie, C. Gahl, and M. Weinelt. "Fast optical work-function tuning at an organic/metal interface." *Applied Physics Letters* 111 (2017), p. 081601. DOI: [10.1063/1.4999436](https://doi.org/10.1063/1.4999436) (cit. on pp. 84, 86).
- [154] T. Moldt, D. Przyrembel, M. Schulze, W. Bronsch, L. Boie, D. Brete, C. Gahl, R. Klajn, P. Tegeder, and M. Weinelt. "Differing isomerization kinetics of azobenzene-functionalized self-assembled monolayers in ambient air and in vacuum." *Langmuir* 32 (2016), pp. 10795–10801. DOI: [10.1021/acs.langmuir.6b01690](https://doi.org/10.1021/acs.langmuir.6b01690) (cit. on pp. 84, 87–88, 92, 95, 98, 101).
- [155] D. Przyrembel. PhD thesis. Freie Universität Berlin, to be published (cit. on p. 84).
- [156] T. Schultz, T. Lenz, N. Kotadiya, G. Heimel, G. Glasser, R. Berger, P. W. M. Blom, P. Amsalem, D. M. de Leeuw, and N. Koch. "Reliable work function determination of multicomponent surfaces and interfaces: The role of electrostatic potentials in ultraviolet photoelectron spectroscopy." *Advanced Materials Interfaces* 4 (2017), p. 1700324. DOI: [10.1002/admi.201700324](https://doi.org/10.1002/admi.201700324) (cit. on p. 86).
- [157] M. Jaschke, H. Schönherr, H. Wolf, H.-J. Butt, E. Bamberg, M. K. Besocke, and H. Ringsdorf. "Structure of alkyl and perfluoroalkyl disulfide and azobenzenethiol monolayers on gold(111) revealed by atomic force microscopy." *the Journal of Physical Chemistry* 100 (1996), pp. 2290–2301. DOI: [10.1021/jp952355o](https://doi.org/10.1021/jp952355o) (cit. on pp. 87–88).
- [158] S. C. B. Mannsfeld, T. W. Canzler, T. Fritz, H. Proehl, K. Leo, S. Stumpf, G. Goretzki, and K. Gloe. "The structure of [4-(phenylazo)phenoxy]hexane-1-thiol self-assembled monolayers on Au(111)." *The Journal of Physical Chemistry B* 106 (2002), pp. 2255–2260. DOI: [10.1021/jp012771a](https://doi.org/10.1021/jp012771a) (cit. on pp. 87–88).
- [159] E. Benassi and S. Corni. "Exciton transfer of azobenzene derivatives in self-assembled monolayers." *The Journal of Physical Chemistry C* 117 (2013), pp. 25026–25041. DOI: [10.1021/jp405077w](https://doi.org/10.1021/jp405077w) (cit. on p. 90).
- [160] N. R. Krekieh, M. Müller, U. Jung, S. Ulrich, R. Herges, and O. M. Magnussen. "UV/Vis spectroscopy studies of the photoisomerization kinetics in self-assembled azobenzene-containing adlayers." *Langmuir* 31 (2015), pp. 8362–8370. DOI: [10.1021/acs.langmuir.5b01645](https://doi.org/10.1021/acs.langmuir.5b01645) (cit. on p. 90).
- [161] C. Cocchi, T. Moldt, C. Gahl, M. Weinelt, and C. Draxl. "Optical properties of azobenzene-functionalized self-assembled monolayers: Intermolecular coupling and many-body interactions." *The Journal of Chemical Physics* 145 (2016), p. 234701. DOI: [10.1063/1.4971436](https://doi.org/10.1063/1.4971436) (cit. on p. 90).
- [162] W. Bronsch, T. Moldt, L. Boie, C. Gahl, and M. Weinelt. "Delocalized versus localized excitations in the photoisomerization of azobenzene-functionalized alkanethiolate SAMs." *Journal of Physics: Condensed Matter* 29 (2017), p. 484002. DOI: <https://doi.org/10.1088/1361-648X/aa9309> (cit. on pp. 92, 94, 98).

- [163] G. Zimmerman, L.-Y. Chow, and U.-J. Paik. "The photochemical isomerization of azobenzene." *Journal of the American Chemical Society* 80 (1958), pp. 3528–3531. DOI: [10.1021/ja01547a010](https://doi.org/10.1021/ja01547a010) (cit. on p. 93).
- [164] P. Nilsson and L. Ilver. "Angular dependences in u.v.-photoemission from single crystals of Au." *Solid State Communications* 17 (1975), pp. 667–671. DOI: [https://doi.org/10.1016/0038-1098\(75\)90381-6](https://doi.org/10.1016/0038-1098(75)90381-6) (cit. on p. 124).
- [165] F. Roth, T. Arion, H. Kaser, A. Gottwald, and W. Eberhardt. "Angle resolved Photoemission from Ag and Au single crystals: Final state lifetimes in the attosecond range." *Journal of Electron Spectroscopy and Related Phenomena* 224 (2017), pp. 84–92. DOI: <https://doi.org/10.1016/j.elspec.2017.05.008> (cit. on p. 124).
- [166] G. V. Hansson and S. A. Flodström. "Photoemission study of the bulk and surface electronic structure of single crystals of gold." *Physical Review B* 18 (1978), pp. 1572–1585. DOI: [10.1103/PhysRevB.18.1572](https://doi.org/10.1103/PhysRevB.18.1572) (cit. on p. 124).
- [167] D. P. Woodruff, W. A. Royer, and N. V. Smith. "Empty surface states, image states, and band edge on Au(111)." *Physical Review B* 34 (1986), pp. 764–767. DOI: [10.1103/PhysRevB.34.764](https://doi.org/10.1103/PhysRevB.34.764) (cit. on p. 124).
- [168] N. Hirata, M. Schibuta, R. Matsui, and A. Nakajima. "Electronic states of alkanethiolate self-assembled monolayers on Au(111) studied by two-photon photoemission spectroscopy." *The Journal of Physical Chemistry C* 116 (2012), pp. 13623–13628. DOI: [10.1021/jp302545r](https://doi.org/10.1021/jp302545r) (cit. on p. 124).
- [169] C. D. Lindstrom, D. Quinn, and X.-Y. Zhu. "Using image resonances to probe molecular conduction at the n-heptane/Au(111) interface." *The Journal of Chemical Physics* 122 (2005), p. 124714. DOI: [10.1063/1.1873632](https://doi.org/10.1063/1.1873632) (cit. on p. 124).

A

Supplementary Material

A.1 Evaporator Design Modification

As discussed in Sec. 3.1.4, the evaporator for organic molecules originally designed by Daniel Brete [92] was used in a slightly modified version. The original design of the evaporator contains a base plate for upright mounting of two crucibles. The glass crucibles are surrounded by copper shieldings. To reach a satisfactory thermal connection between the copper and the glass crucible, a crinkled aluminum foil has to be added between them. The copper cylinders are heated independently of each other via filaments surrounding them. To electrical isolate the filament wires from the copper, a thin glass cylinder encases the copper cylinders. The electrical isolation from the base plate is achieved through quartz cylinders and ceramic disks at all necessary positions.

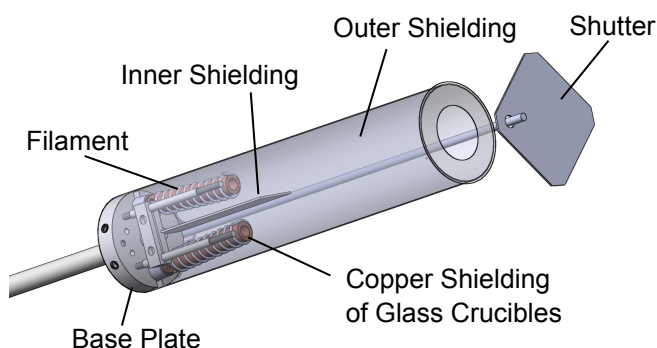


Fig. A.1: Modified evaporator design containing canted crucibles and an inner and outer shielding to prevent condensation of molecules at unwanted places within and outside the evaporator.

In the present work a new base plate was designed, which tilts the two crucibles by 7° to make them point to the same spot at a distance of 10 cm with respect to the opening of the crucibles. The structure of the evaporator in the new design is shown in Fig. A.1. This design allows for simultaneously evaporation from both crucibles, if co-adsorption of two different molecules is desired for network formation. To prevent molecules from condensing at the neighboring crucible, a shield was added in between the crucibles (cf. inner shielding in Fig. A.1). Furthermore, an outer shield surrounding both crucibles was added to prevent unnecessary contamination of the UHV chamber with organic molecules.

A.2 Electronic Structure of Au(111)

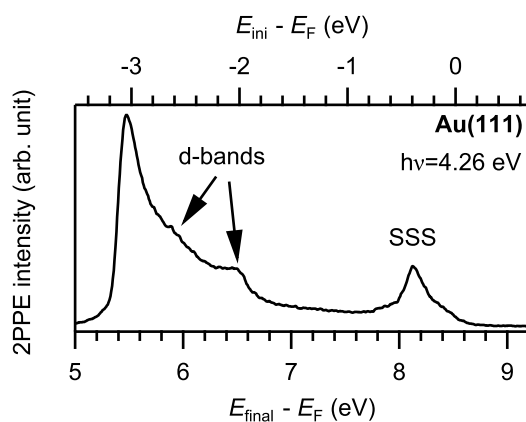


Fig. A.2: 2PPE spectrum of Au(111) for excitation with $h\nu = 4.26$ eV photons.

In order to discriminate the electronic structure of the organic film and the organic/inorganic interface from the one of the Au(111) substrate, an exemplary 2PPE spectrum of the clean gold substrate excited with photons of energy $h\nu = 4.26$ eV is presented in Fig. A.2. The spectrum shows initial states at binding energies of -2.6 and -2 eV with respect to the Fermi level, which is the expected range of Au d-bands according to theory and experiments presented in literature [164, 165] as well as the Shockley surface state (SSS) at 0.4 eV below E_F , as expected for a clean Au(111) surface (cf. Ref. [165–167]). The kink observed below the surface state is assigned to the gold sp-bands [168]. In agreement to literature, the work function of the clean surface, which is read off from the low-energy cut-off, amounts to 5.4 eV [120, 169].

This section is also published in the supplementary material of Bronsch *et al.* [118].

A.3 α -Sexithiophene/Au(111)

A.3.1 Intensity Loss and Background Correction

A decrease in intensity upon light exposure was observed in the 2PPE experiments of the present study, as it was observed also by Zielke [104]. To prevent distortions in the analysis of the life times of the excited states due to this effect, an intensity loss correction was applied to the raw data before performing further data evaluation. This correction accounts for 2PPE intensity losses due to small changes in the sample structure as well as decreases of the laser power. The correction scheme is valid under the assumption that the relative signal loss is the same over the whole spectrum. This assumption is fulfilled in good approximation for most 2PPE measurements. Otherwise the data have been neglected, since significant changes in the electronic structure with illumination time are an indication for considerable changes in the sample structure and therefore exclude the use of the data. Usually the time-resolved measurements were repeated 10 times to improve the statistics. Figure A.3a shows the raw data of 10 repetitions of a time-resolved measurement with non-equidistant pump-probe delay steps as a function of the measuring time. To proof the trustability of the data, the angle-integrated, non-correlated background spectrum and the spectrum of temporal overlap were compared for each repetition, as shown in Fig. A.3b. Afterwards, the intensity decrease was fitted as a function of the measurement time. This is important especially for time-resolved measurements with non-equidistant pump-probe delays, since in this case the intensity loss with measuring time influences the fast contributions to the relaxation times stronger than the slower ones due to the higher density of data points for short pump-probe delays. For this purpose, the series of angle-integrated spectra were plotted as a function of measuring time and integrated in the energy range of 5.18 to 5.75 eV (cf. Fig. A.3c). The integration window was chosen so that it is well above the low-energy cut-off and well below the image-potential state, since these two characteristics could show changes due to redistributions of the 6T molecules on the surface (e.g. due to Oswald ripening), without implying changes in the chemical structure and hence in the electronic structure of the molecules. To fit the intensity loss, the temporal evolution of the non-correlated background spectrum was fitted with a single exponential function (cf. Fig. A.3c). The inverse of the resulting fit was then used as a scaling function. Each row of the intensity map was multiplied with the scaling function before the individual repetitions were summed up and the averaged 2PPE intensity was plotted as a function of final state energy and pump-probe delay (cf. Fig. A.3d).

To distinguish the correlated 2PPE signal of the two pulses from the non-correlated background signal, the time-resolved measurements included a few data points at large negative delays, where no correlated signal is expected. The average of these spectra was used to determine the non-correlated background and subtract it from each spectrum. The background corrected version of the data shown in Fig. A.3d is displayed in part (e) of the same figure.

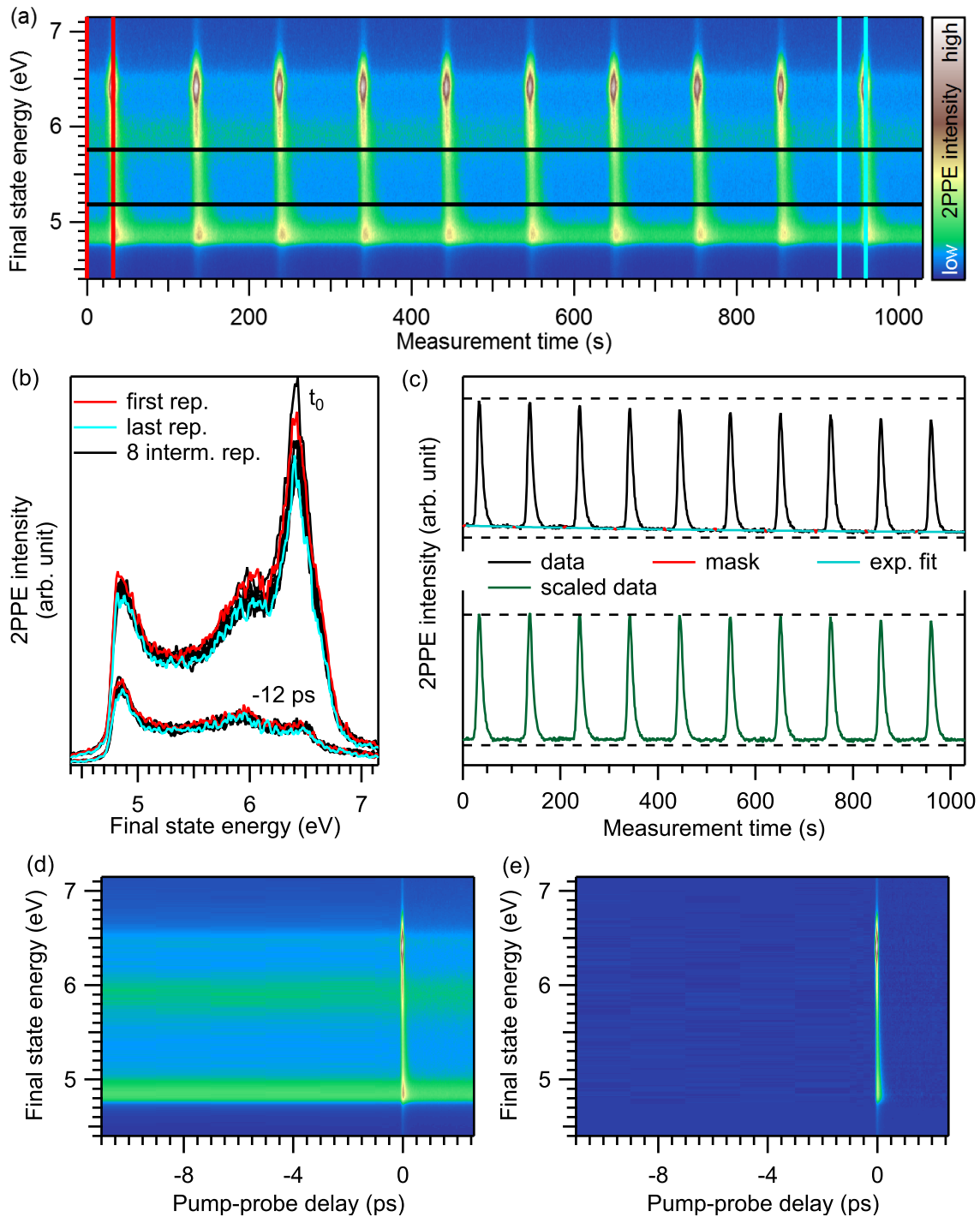


Fig. A.3: (a) 2PPE intensity as a function of final state energy and measuring time for ten repetitions with non-equidistant pump-probe delays. (b) 2PPE spectra for pump-probe delays of $t=0$ (larger amplitude) and $t=-12$ ps (smaller amplitude) of each repetition. The first repetitions is marked in red, the last one in blue as marked in the map in (a). The spectra taken from the remaining repetitions are colored in black. (c) 2PPE intensity summed in the energy range between the black horizontal lines drawn in (a) (black curve). The first five data points in each repetition (red markers) are used to fit the loss in intensity over time with an exponential function. To scale the data, they are multiplied with the inverse of the fit result (blue curve), so that each repetition is scaled to the first one (cf. olive curve). (d) Summed 2PPE intensity of the scaled repetitions as a function of final state energy and pump-probe delay including the non-correlated background and the correlated signal of the two pulses. (e) Correlated 2PPE intensity. The non-correlated background signal (average of the first 5 spectra for large negative delays) is subtracted from the map shown in (d).

A.3.2 Electronic Structure

Image-potential state in front of the 6T monolayer: In Sec. 4.2.2 it was discussed whether the intermediate state at 3.8 eV above the Fermi level may result from an image-potential state as proposed by Varene *et al.* [7] In this case the state should pin to the vacuum level of the sample. In order to proof this pinning, the work function and the intermediate state energy of the observed feature have been evaluated for a number of different film preparations with a thickness of 1 ML. As shown in Fig. A.4, the energy of the state (red markers) with respect to the Fermi level changes according to the work function (black markers), which is in agreement with the assignment to an image-potential state. The binding energy of the state is then given by the distance of its intermediate state energy to the vacuum level. The extracted values for the binding energy are given by the blue markers in Fig. A.4. The average value determined from these data amounts to 0.76 ± 0.02 eV. Work-function variations are observed from 4.6 to 4.8 eV. In the low coverage range small variations in the film thickness are expected to cause rather large changes in the sample work-function. The accuracy of the film thickness preparation is estimated to 10 %.

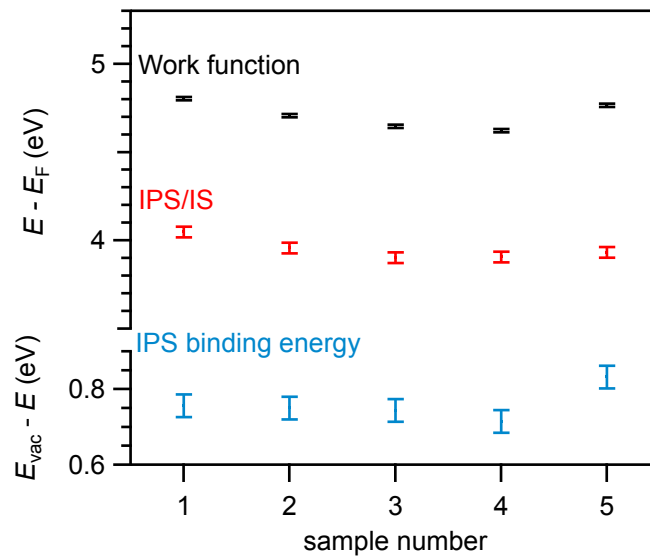


Fig. A.4: Work functions (black) and intermediate state energies of the IPS/IS (red) for five 1 ML thick 6T films and the corresponding IPS binding energies for the specific samples (blue).

Additional tr-2PPE data for 1 ML 6T/Au(111): Additionally to the data presented in Sec. 4.2.2, tr-2PPE experiments on monolayers were also performed with the photon energy combinations $h\nu_1=2.47$ eV / $h\nu_2=4.26$ eV and $h\nu_1=3.11$ eV / $h\nu_2=3.86$ eV. The corresponding data are shown in Fig. A.5. The data sets corroborate the presence of the intermediate state at 3.6 eV (final state energy of 6.07 eV), as indicated in the spectra for negative time delays. Furthermore, the change of the UV photon energy from 4.26 eV (cf. Fig. 4.7a,b in Sec. 4.2.2) to 3.86 eV in combination with 3.11 eV photons shows the expected separation of the HOMO from the IPS and the intermediate state at 3.6 eV (final state energy of 6.71 eV).

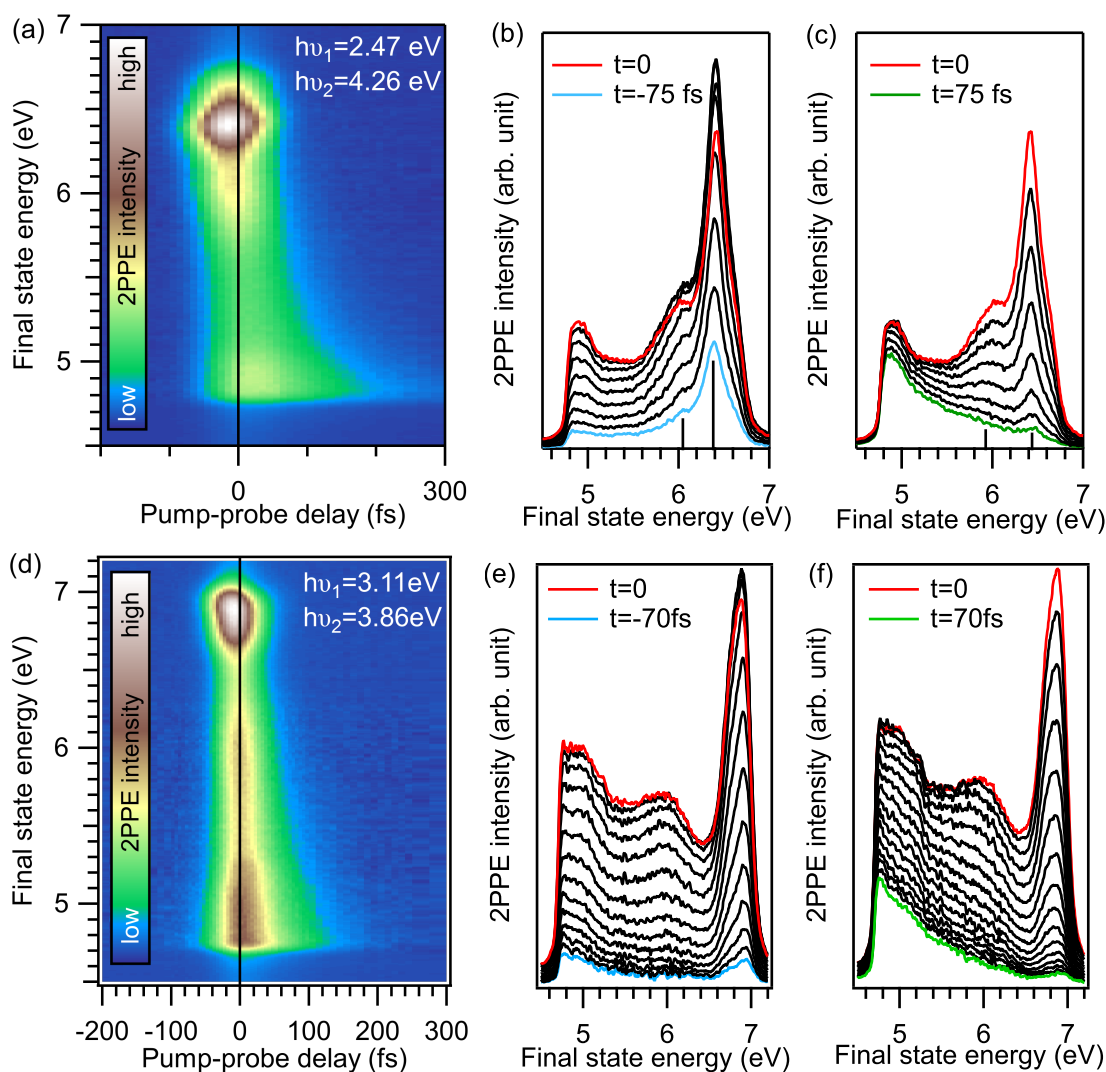


Fig. A.5: (a) 2PPE intensity as a function of pump-probe delay and final state energy measured with photon energies $h\nu_1=2.47$ eV and $h\nu_2=4.26$ eV. (b) Series of 2PPE spectra taken from the map shown in (a) at time delays from 0 (red curve) to -90 fs (blue curve) in 5 fs steps. (c) Series of 2PPE spectra taken from the map shown in (a) at time delays from 0 (red curve) to 90 fs (green curve) in 5 fs steps. (d) 2PPE intensity as a function of pump-probe delay and final state energy measured with photon energies $h\nu_1=3.11$ eV and $h\nu_2=3.86$ eV. (e) Series of 2PPE spectra taken from the map shown in (d) at time delays from 0 (red curve) to -70 fs (blue curve) in 5 fs steps. (f) Series of 2PPE spectra taken from the map shown in (d) at time delays from 0 (red curve) to 70 fs (green curve) in 5 fs steps.

Tr-2PPE Data of a 30 ML 6T/Au(111) Film To proof the continuity of the film growth for coverages higher than an average film thickness of 10 ML, a film with an average thickness of 30 ML was prepared and measured at room temperature. Figure A.6 shows a time-resolved dataset measured with photon energies $h\nu_1=2.69$ eV and $h\nu_2=4.38$ eV. The 3D Frenkel exciton observed in the 6T crystallites appears at a final state energy of 5.44 ± 0.05 eV, which corresponds to an intermediate state energy of 1.06 eV, which is 50 meV lower than observed for an average film thickness of 10 ML. The 2PPE spectrum at -20 fs displayed in the right panel of Fig. A.6 clearly shows the presence of the IPS/IS, which points out that some parts of the sample area are still covered only by the wetting layer.

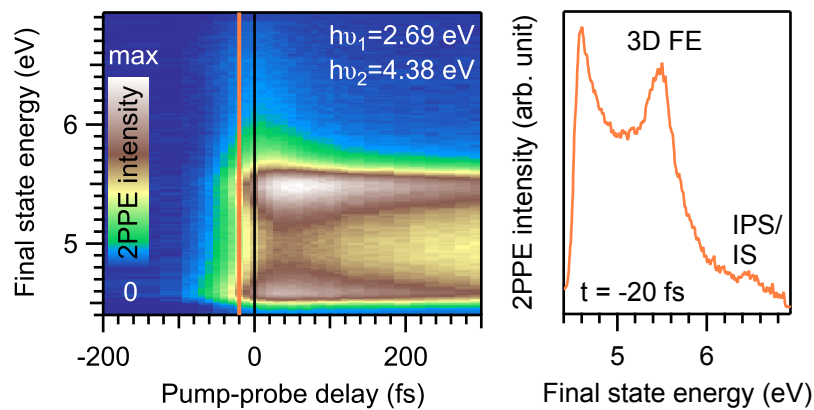


Fig. A.6: **Left:** 2PPE intensity map of a 6T/Au(111) film with an average thickness of 30 ML measured with photon energies $h\nu_1=2.69$ eV and $h\nu_2=4.38$ eV. **Right:** Spectrum at a pump-probe delay of -20 fs.

This paragraph is also published in the supplementary material of Bronsch *et al.* [118].

A.3.3 Vibrational Relaxation Dynamics

Additional Simulation for 10 ML 6T/Au(111): In Sec. 4.3.2 a vibronic excitation model was used to develop simulations of the 2PPE spectra of 10 ML 6T/Au(111) for excitation at 3.1 eV. Figure A.7 shows a simulation of exciton dynamics according to Eq. 4.3 and the calculated photoemission spectra for photoemission from the 5th lowest vibrational sub-levels of the S_1 Frenkel exciton band shown in Fig. 4.16a.

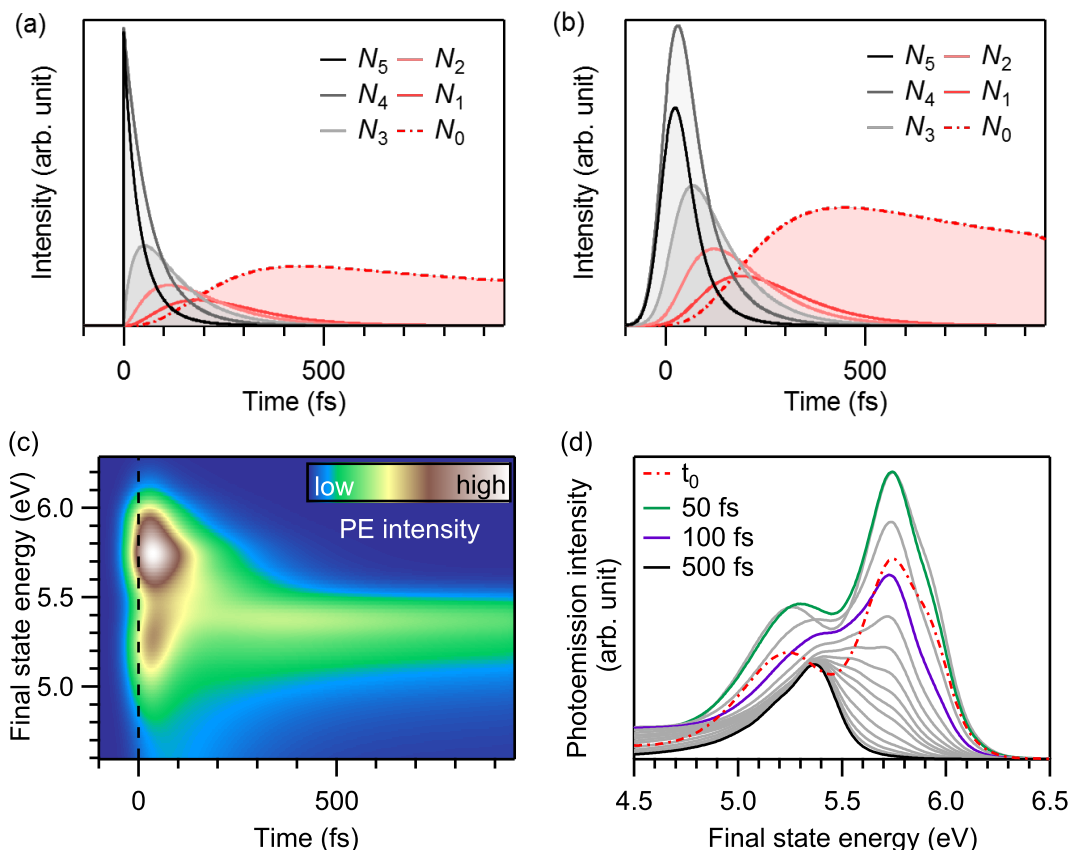


Fig. A.7: Simulation of time-resolved photoemission including vibrational excitations in the pumping step. **(a)** Temporal evolution of the population of the i th vibrational sub-level of the S_1 Frenkel exciton state according to Eq.4.3 assuming that only the 4th and 5th vibrational levels are occupied at the beginning, $\tau_\nu = 70$ fs and a multi-exponential decay of the exciton state with a fastest time constant of 50 fs. **(b)** Resulting cross-correlation curves for the convolution of the population curves shown in (a) and the cross-correlation intensity curve of the laser pulses. **(c)** Simulation of the sum of the 2D maps corresponding to photoemission from the vibrational sub-levels ν_x of the S_1 exciton state considering the population curves $N_i(t)$ shown in (b). **(d)** Series of spectra for different time delays taken from (c).

As in to the simulations shown in Sec. 4.3.2, here an equal initial population of the 4th and 5th vibrational level is assumed, whereas all other levels are initially unoccupied. The vibrational relaxation constant is assumed to be 70 fs, in order to describe the time-dependence of the intensity observed in the higher energetic shoulder of the Frenkel exciton peak. The decay constants of the electronic state are fixed to the same values as for the other simulations shown in the main text. Figure A.7a and b show the population dynamics for each vibrational sub-level

independently. In contrast to part (a), part (b) of the figure includes the convolution of the population curves with the cross-correlation intensity of the laser pulses. Figure A.7c shows the intensity map that results from the sum of the 2D maps of each vibrational sub-level and Fig. A.7d a selection of spectra extracted from the map at different times after excitation. As it can be seen, initially the intensity in the range of the $\nu_x = 0$ level is much lower with respect to the intensity in the higher vibrational levels. This behavior is not observed in the measured data, shown in Fig. 4.15. Hence, the assumption of occupying only the 4th and 5th vibrational level instantaneously is not in agreement with the measurements.

A.4 Azobenzene-Based Self-Assembled Monolayers/Au(111)

A.4.1 First Order Kinetics

Assuming the switching probability of an azobenzene unit being independent of its environment, rate constants k_{tc} and k_{ct} can be defined for *trans* – *cis* and *cis* – *trans* isomerization acting on the present amount of *trans* or *cis* molecules, N_t and N_c , within the amount of switchable molecules N . Since the *trans* form is the thermodynamically stable form, k_{tc} is purely photon-induced, whereas k_{ct} has a photon-induced k_{ct}^{ph} and a thermal induced k_{ct}^{th} component. The temporal change of the number of *cis* molecules during illumination can hence be described by:

$$\frac{dN_c(t)}{dt} = k_{tc} \cdot N_t(t) - k_{ct} \cdot N_c(t) \quad (\text{A.1})$$

$$= k_{tc} \cdot (N - N_c(t)) - k_{ct} \cdot N_c(t) \quad (\text{A.2})$$

$$= N \cdot k_{tc} - N_c(t) \cdot (k_{tc} + k_{ct}). \quad (\text{A.3})$$

The solution of this differential equation gives an exponential dependence on the illumination time t :

$$N_c(t) = \frac{1}{k_{tc} + k_{ct}} \cdot \left(N \cdot k_{tc} + (N_c(0) \cdot (k_{tc} + k_{ct}) - N \cdot k_{tc}) \cdot e^{-(k_{tc} + k_{ct}) \cdot t} \right) \quad (\text{A.4})$$

$$= N \cdot \frac{k_{tc}}{k_{tc} + k_{ct}} + \left(N_c(0) - N \cdot \frac{k_{tc}}{k_{tc} + k_{ct}} \right) \cdot e^{-(k_{tc} + k_{ct}) \cdot t}. \quad (\text{A.5})$$

Considering that $\dot{N}_c = 0$ within the PSS, Eq. A.3 gives:

$$\frac{N_{c,\text{PSS}}}{N} = \frac{k_{tc}}{k_{tc} + k_{ct}} := \chi_{c,\text{PSS}}. \quad (\text{A.6})$$

Dividing Eq. A.5 by N gives:

$$\frac{N_c(t)}{N} := \chi_c(t) = \chi_{c,\text{PSS}} + (\chi_c(0) - \chi_{c,\text{PSS}}) \cdot e^{-(k_{tc} + k_{ct}) \cdot t}. \quad (\text{A.7})$$

The rise time τ of the fraction of *cis* molecules χ_c under illumination is hence given by the inverse of the sum of all rate constants.

A.4.2 Derivation of the Fit Function for Work-Function Changes in Bichromatic Experiments

Starting from the Helmholtz equation for work-function changes due to a dipole layer in front of the surface, in Sec. 5.2.2 the expression:

$$\Phi(x) = \Phi_t + \Delta\Phi(x) = \Phi_t + \underbrace{\frac{e N_0}{\epsilon_0 \epsilon A} \Delta p_{\perp}}_{\Delta\Phi_{\max}} \left(\frac{\frac{\sigma_{tc}(\lambda_1)}{\sigma_{tc}(\lambda_2)} + x}{\frac{\sigma_{tc}(\lambda_1) + \sigma_{ct}(\lambda_1)}{\sigma_{tc}(\lambda_2)} + x \cdot \frac{\sigma_{tc}(\lambda_2) + \sigma_{ct}(\lambda_2)}{\sigma_{tc}(\lambda_2)}} \right) \quad (\text{A.8})$$

was derived to relate the change in the work function $\Phi(x)$ under simultaneous illumination with two colors to the number of molecules changing from the *trans* to the *cis* form with respect to the all-*trans* SAM. Here, Φ_t is the work function of the *trans* SAM and $\Delta\Phi_{\max}$ is the maximal work-function shift which would be achieved if all switchable molecules N_0 are switched to the *cis* configuration. According to the Helmholtz equation, $\Delta\Phi_{\max}$ includes the dielectric constant of the organic material $\epsilon_0 \cdot \epsilon$, the elementary charge e , the density of switchable molecules N_0/A and the change in dipole moment per switchable isomer Δp_{\perp} . The portion of molecules switching for a given photon-flux ratio $x = j(\lambda_2)/j(\lambda_1)$ of the contributing wavelengths λ_1 and λ_2 , depends on the isomerization cross-sections $\sigma_{tc}(\lambda)$ and $\sigma_{ct}(\lambda)$ for *trans-cis* and *cis-trans* isomerization of the two wavelengths.

Since it is not possible to measure the work function of the all-*trans* or the all-*cis* SAM and the isomerization cross-sections are not known for the different wavelengths in the range of the S_2 band, it is necessary to transform Eq. A.8 into a form with only two unknown parameters, accounting for the limiting value for infinite x , which is $\Phi_{\text{PSS}}(450 \text{ nm})$, and the curvature, which should depend on the different isomerization cross-sections. Hence, the dependence of Φ on the photon-flux ratio should be described by a function in the form:

$$\Phi(x) = \Phi_{\text{PSS}}(\lambda_2) + \Delta\Phi_{\text{PSS}} \cdot \frac{\tilde{r}}{\tilde{r} + x}, \quad (\text{A.9})$$

where $\Delta\Phi_{\text{PSS}} = \Phi_{\text{PSS}}(\lambda_1) - \Phi_{\text{PSS}}(\lambda_2)$ is the difference in work function for the two photostationary states reached with monochromatic illumination for the two involved wavelengths and \tilde{r} a parameter which determines the curvature of the fit function and will be derived in the following. The photostationary states of monochromatic illumination with λ_1 or λ_2 , respectively, correspond to

$$\begin{aligned} \Phi_{\text{PSS}}(\lambda_1) &= \Phi(0) = \Phi_t + \Delta\Phi_{\max} \frac{\sigma_{tc}(\lambda_1)}{\sigma_{tc}(\lambda_1) + \sigma_{ct}(\lambda_1)} = \Phi_t + \Delta\Phi_{\max} \chi_c(\lambda_1), \\ \Phi_{\text{PSS}}(\lambda_2) &= \lim_{x \rightarrow \infty} \Phi(x) = \Phi_t + \Delta\Phi_{\max} \chi_c(\lambda_2). \end{aligned}$$

$\chi_c = \frac{\sigma_{tc}(\lambda_1)}{\sigma_{tc}(\lambda_1) + \sigma_{ct}(\lambda_1)}$ is the fraction of *cis* molecules among the switchable molecules in the PSS.

Accordingly, the work-function difference can be written as:

$$\Delta\Phi_{\text{PSS}} = \Phi_{\text{PSS}}(\lambda_1) - \Phi_{\text{PSS}}(\lambda_2) = \Delta\Phi_{\text{max}} \cdot (\chi_c(\lambda_1) - \chi_c(\lambda_2)). \quad (\text{A.10})$$

This expression can be rearranged for $\Delta\Phi_{\text{max}}$ and inserted into Eq. A.8, which leads to

$$\Phi(x) = \Phi_t + \Delta\Phi_{\text{PSS}} \cdot \frac{1}{\chi_c(\lambda_1) - \chi_c(\lambda_2)} \cdot \left(\frac{\frac{\sigma_{\text{tc}}(\lambda_1)}{\sigma_{\text{tc}}(\lambda_2)} + x}{\frac{\sigma_{\text{tc}}(\lambda_1) + \sigma_{\text{ct}}(\lambda_1)}{\sigma_{\text{tc}}(\lambda_2)} + x \cdot \frac{\sigma_{\text{tc}}(\lambda_2) + \sigma_{\text{ct}}(\lambda_2)}{\sigma_{\text{tc}}(\lambda_2)}}} \right). \quad (\text{A.11})$$

Furthermore, the variable Φ_t can be replaced by

$$\begin{aligned} \Phi_t &= \Phi_{\text{PSS}}(\lambda_2) - \Delta\Phi_{\text{max}} \cdot \chi_c(\lambda_2) \\ &= \Phi_{\text{PSS}}(\lambda_2) - \Delta\Phi_{\text{PSS}} \cdot \frac{\chi_c(\lambda_2)}{\chi_c(\lambda_1) - \chi_c(\lambda_2)}. \end{aligned}$$

Hence, Eq. A.11 can be written as:

$$\begin{aligned} \Phi(x) &= \Phi_{\text{PSS}}(\lambda_2) + \\ &\Delta\Phi_{\text{PSS}} \cdot \frac{1}{\chi_c(\lambda_1) - \chi_c(\lambda_2)} \cdot \left(\frac{\frac{\sigma_{\text{tc}}(\lambda_1)}{\sigma_{\text{tc}}(\lambda_2)} + x}{\frac{\sigma_{\text{tc}}(\lambda_1) + \sigma_{\text{ct}}(\lambda_1)}{\sigma_{\text{tc}}(\lambda_2)} + x \cdot \frac{\sigma_{\text{tc}}(\lambda_2) + \sigma_{\text{ct}}(\lambda_2)}{\sigma_{\text{tc}}(\lambda_2)}}} - \chi_c(\lambda_2) \right). \end{aligned} \quad (\text{A.12})$$

Using $\chi_c(\lambda_2) = \sigma_{\text{tc}}(\lambda_2)/(\sigma_{\text{tc}}(\lambda_2) + \sigma_{\text{ct}}(\lambda_2))$ and choosing a common denominator for the two summands in the parenthesis we can write:

$$\begin{aligned} \Phi(x) &= \Phi_{\text{PSS}}(\lambda_2) + \\ &\Delta\Phi_{\text{PSS}} \cdot \frac{1}{\chi_c(\lambda_1) - \chi_c(\lambda_2)} \cdot \left(\frac{\frac{\sigma_{\text{tc}}(\lambda_1)}{\sigma_{\text{tc}}(\lambda_2)} - \frac{\sigma_{\text{tc}}(\lambda_1) + \sigma_{\text{ct}}(\lambda_1)}{\sigma_{\text{tc}}(\lambda_2)} \cdot \frac{\sigma_{\text{tc}}(\lambda_2)}{\sigma_{\text{tc}}(\lambda_2) + \sigma_{\text{ct}}(\lambda_2)}}{\frac{\sigma_{\text{tc}}(\lambda_1) + \sigma_{\text{ct}}(\lambda_1)}{\sigma_{\text{tc}}(\lambda_2)} + x \cdot \frac{\sigma_{\text{tc}}(\lambda_2) + \sigma_{\text{ct}}(\lambda_2)}{\sigma_{\text{tc}}(\lambda_2)}}} \right). \end{aligned} \quad (\text{A.13})$$

To shorten the expressions we define $\tilde{\sigma}(\lambda_i) = \sigma_{\text{tc}}(\lambda_i) + \sigma_{\text{ct}}(\lambda_i)$, $i \in \{1, 2\}$. This simplifies Eq. A.13 to

$$\Phi(x) = \Phi_{\text{PSS}}(\lambda_2) + \Delta\Phi_{\text{PSS}} \cdot \frac{1}{\frac{\sigma_{\text{tc}}(\lambda_1)}{\tilde{\sigma}(\lambda_1)} - \frac{\sigma_{\text{tc}}(\lambda_2)}{\tilde{\sigma}(\lambda_2)}} \cdot \left(\frac{\frac{\sigma_{\text{tc}}(\lambda_1)}{\sigma_{\text{tc}}(\lambda_2)} - \frac{\tilde{\sigma}(\lambda_1)}{\tilde{\sigma}(\lambda_2)}}{\frac{\tilde{\sigma}(\lambda_1)}{\sigma_{\text{tc}}(\lambda_2)} + x \cdot \frac{\tilde{\sigma}(\lambda_2)}{\sigma_{\text{tc}}(\lambda_2)}}} \right) \quad (\text{A.14})$$

$$= \Phi_{\text{PSS}}(\lambda_2) + \Delta\Phi_{\text{PSS}} \cdot \left(\frac{\frac{\sigma_{\text{tc}}(\lambda_1)}{\sigma_{\text{tc}}(\lambda_2)} - \frac{\tilde{\sigma}(\lambda_1)}{\tilde{\sigma}(\lambda_2)}}{\frac{\sigma_{\text{tc}}(\lambda_1)}{\sigma_{\text{tc}}(\lambda_2)} - \frac{\tilde{\sigma}(\lambda_1)}{\tilde{\sigma}(\lambda_2)} + x \cdot \frac{\tilde{\sigma}(\lambda_2)}{\tilde{\sigma}(\lambda_1)} \frac{\sigma_{\text{tc}}(\lambda_1)}{\sigma_{\text{tc}}(\lambda_2)} - x} \right) \quad (\text{A.15})$$

$$= \Phi_{\text{PSS}}(\lambda_2) + \Delta\Phi_{\text{PSS}} \cdot \left(1 + \frac{x \cdot \frac{\tilde{\sigma}(\lambda_2)}{\tilde{\sigma}(\lambda_1)} \frac{\sigma_{\text{tc}}(\lambda_1)}{\sigma_{\text{tc}}(\lambda_2)} - x}{\frac{\sigma_{\text{tc}}(\lambda_1)}{\sigma_{\text{tc}}(\lambda_2)} - \frac{\tilde{\sigma}(\lambda_1)}{\tilde{\sigma}(\lambda_2)}}} \right)^{-1} \quad (\text{A.16})$$

$$= \Phi_{\text{PSS}}(\lambda_2) + \Delta\Phi_{\text{PSS}} \cdot \left(1 + \frac{x \cdot \left(\frac{\tilde{\sigma}(\lambda_2)}{\tilde{\sigma}(\lambda_1)} \frac{\sigma_{\text{tc}}(\lambda_1)}{\sigma_{\text{tc}}(\lambda_2)} - 1 \right)}{\frac{\tilde{\sigma}(\lambda_1)}{\tilde{\sigma}(\lambda_2)} \left(\frac{\tilde{\sigma}(\lambda_2)}{\tilde{\sigma}(\lambda_1)} \frac{\sigma_{\text{tc}}(\lambda_1)}{\sigma_{\text{tc}}(\lambda_2)} - 1 \right)} \right)^{-1} \quad (\text{A.17})$$

$$\Phi(x) = \Phi_{\text{PSS}}(\lambda_2) + \Delta\Phi_{\text{PSS}} \cdot \left(1 + \frac{x}{\frac{\tilde{\sigma}(\lambda_1)}{\tilde{\sigma}(\lambda_2)}}\right)^{-1} \quad (\text{A.18})$$

$$= \Phi_{\text{PSS}}(\lambda_2) + \Delta\Phi_{\text{PSS}} \cdot \left(\frac{\frac{\tilde{\sigma}(\lambda_1)}{\tilde{\sigma}(\lambda_2)}}{\frac{\tilde{\sigma}(\lambda_1)}{\tilde{\sigma}(\lambda_2)} + x}\right). \quad (\text{A.19})$$

This is the form which was aimed for in Eq. A.9 with $\tilde{r} = \tilde{\sigma}(\lambda_1)/\tilde{\sigma}(\lambda_2)$.

B List of Acronyms and Abbreviations

- 2PPE** Two-Photon Photoemission
- 3PPE** Three-Photon Photoemission
- 6T** α -Sexithiophene
- Az11** 11-(4-(phenyldiazenyl)phenoxy)undecane-1-thiol
- BBO** Barium Boron Oxide
- C12** 1-dodecanethiol
- cw** Continuous Wave
- DFG** Difference-Frequency Generations
- DFT** Density Functional Theory
- DR** Differential Reflectance
- DRS** Differential Reflectance Spectroscopy
- FE** Frenkel Exciton
- FWHM** Full Width Half Maximum
- HOMO** Highest Occupied Molecular Orbital
- IMFP** Inelastic Mean Free Path
- IPES** Inverse Photoemission Spectroscopy
- IPS** Image-Potential State
- IR** Infrared
- IS** Interface State
- LAD** Low Angular Dispersion
- LED** Light Emitting Diode
- LEED** Low-Energy Electron Diffraction
- LEY** Local Electron Yield
- LUMO** Lowest Unoccupied Molecular Orbital
- MCP** Multi-Channel Plate

ML Monolayer
NEXAFS Near-Edge X-ray Absorption Fine Structure
NSD Normalized Standard Deviation
OLED Organic Light Emitting Diode
OPA Optical Parametrical Amplifier
OSC Organic Solar Cell
PE Photoemission
PEEM Photoelectron Emission Microscopy
p-pol p-polarized
PSS Photostationary State
RegA Regenerativ Amplifier
RT Room Temperature
SAM Self-Assembled Monolayer
SHG Second Harmonic Generation
s-pol s-polarized
SSS Shockley Surface State
STM Scanning Tunneling Microscopy
TDM Transition Dipole Moment
TPD Temperature Programmed Desorption
tr-2PPE Time-Resolved Two-Photon Photoemission
UHV Ultrahigh Vacuum
UPS Ultraviolet Photoemission Spectroscopy
UV Ultraviolet
Vis Visible
WAM Wide-Angle Mode
WL Wetting Layer

C Appendix C

List of Frequently Used Symbols

a	lattice constant
A	amplitude
a_0	Bohr radius
c	velocity of light
e	elementary charge
E_b	binding energy
E_B	exciton binding energy
E_i	initial state energy
E_{int}	intermediate state energy
E_f	final state energy
E_F	Fermi energy
E_{kin}	kinetic energy
E_{ph}	photon energy
E_{vac}	vacuum level
ϵ	relative dielectric constant
ϵ_0	vacuum dielectric constant
ϕ	work function
ϕ_{isom}	isomerization quantum yield
h	Planck constant
I	Intensity
j	photon flux
k	transfer rate
λ	wavelength
m_e	electron mass
μ	reduced mass

n	refractive index
N_c	number of molecules in <i>cis</i> configuration
N_t	number of molecules in <i>trans</i> configuration
\vec{p}_t	transition dipole moment
R	reflectance
r_{ct}	<i>cis</i> to <i>trans</i> switching rate
r_{tc}	<i>trans</i> to <i>cis</i> switching rate
R_∞	Rydberg energy
S_0	ground state potential energy surface
S_1	potential energy surface of the first excited state
S_n	potential energy surface of a higher excited state
$S_{\nu\nu'}$	Franck-Condon overlap integral
σ_{abs}	absorption cross-section
σ_{isom}	isomerization cross-section
$\sigma_{\text{isom,ct}} = \sigma_{ct}$	isomerization cross-section for <i>cis</i> to <i>trans</i> switching
σ_{tc}	isomerization cross-section for <i>trans</i> to <i>cis</i> switching
T	transmittance
τ	time constant
χ_c	fraction of <i>cis</i> molecules

D List of Publications

Published:

1. Wibke Bronsch, Thorsten Wagner, Sebastian Baum, Malte Wansleben, Kristof Zielke, Ebrahim Ghanbari, Michael Györök, Andrea Navarro-Quezada, Peter Zeppenfeld, Martin Weinelt, and Cornelius Gahl *Interplay between morphology and electronic structure of α -sexithiophene films on Au(111)*, Journal of Physical Chemistry C **123**, 7931-7939 (2019)
2. Wibke Bronsch, Thomas Moldt, Larissa Boie, Cornelius Gahl, and Martin Weinelt, *Delocalized vs localized excitations in the photoisomerization of azobenzene-functionalized alkanethiolate SAMs*, Journal of Physics: Condensed Matter **29**, 484002 (2017)
3. Wibke Bronsch, Daniel Przyrembel, Larissa Boie, Cornelius Gahl, and Martin Weinelt, *Fast optical work-function tuning at an organic/metal interface*, Applied Physics Letters **111**, 081601 (2017)
4. Thomas Moldt, Daniel Przyrembel, Michael Schulze, Wibke Bronsch, Larissa Boie, Daniel Brete, Cornelius Gahl, Rafal Klajn, Petra Tegeder, and Martin Weinelt, *Differing isomerization kinetics of azobenzene-functionalized self-assembled monolayers in ambient air and in vacuum*, Langmuir **42**, 10795 (2016)

In preparation:

5. Wibke Bronsch, Kristof Zielke, Malte Wansleben, Sebastian Baum, Ebrahim Ghanbari, Thorsten Wagner, Martin Weinelt, and Cornelius Gahl *Ultrafast population of Frenkel exciton states through direct excitation*, to be submitted
6. Wibke Bronsch, Jan Böhnke, Larissa Boie, Cornelius Gahl, Beatrice Andres, and Martin Weinelt *Local work-function manipulation by external optical stimulation*, to be submitted
7. Thomas Moldt, Wibke Bronsch, Cornelius Gahl, and Martin Weinelt *Probing the aggregate formation kinetics in azobenzene-functionalized alkanethiolate SAMs by UV/vis spectroscopy*
8. Wibke Bronsch, Ralph Püttner, Sebastian Baum, Martin Weinelt, and Cornelius Gahl *Morphology dependent Frenkel-exciton dynamics including ultrafast vibronic relaxations*

E

Appendix E

Scientific Contributions and Research Stays

Talks

- 05/2018 *Birth and Death of a Molecular Exciton*; UNESCO Day of Light event organized by Nature Research; May 16th; Berlin; Germany
- 03/2017 *Wavelength Sensitivity of the Photostationary State of Azobenzene-Functionalized SAMs*; DPG Spring Meeting of the Condensed Matter Section; March 19th – 24th; Dresden; Germany
- 09/2016 *Electron and Exciton Dynamics in Amorphous and Crystalline Sexithiophene Films on Au(111)*; 32nd European Conference on Surface Science (ECOSS); August 28th – September 2nd; Grenoble; France
- 04/2016 *The Influence of Morphology on the Electron and Exciton Dynamics in Sexithiophene Films on Au(111)*; Seminar talk at the Department of Atomic Physics and Surface Science of the Johannes Kepler Universität; April 26th; Linz; Austria
- 03/2016 *Ultrafast Exciton Dynamics in Thin Sexithiophene Films*; Seminar talk in the group seminar of Prof. Xiaoyang Zhu at the Columbia University; March 31st; New York; USA
- 03/2015 *Probing the Photostationary State of Photochromic SAMs by Two-Photon Photoemission Spectroscopy*; DPG Spring Meeting of the Condensed Matter Section; March 16th – 20th; Berlin; Germany
- 03/2015 *Ultrafast Exciton Dynamics in Thin Sexithiophene Films*; Winter School on Ultrafast Processes in Condensed Matter; March 2nd – 6th; Reit im Winkl; Germany
- 10/2014 *Ultrafast Exciton Dynamics in Thin Sexithiophene Films*; Interdisciplinary Workshop on Elementary Processes in Molecular Switches at Surfaces; October 9th – 10th; Lübbenau; Germany
- 03/2014 *Electron Dynamics in Self-Assembled Monolayers of Azobenzene Functionalized Alkanethiols on Gold*; Young Investigators Workshop on Ultrafast Dynamics; March 9th – 14th; Reit im Winkl; Germany

Poster Presentations

- 09/2018 *Spin-Dependent Magnetization Dynamics in the Tb(0001) Surface State*; European School on Magnetism; September 18th – 28th; Krakow; Poland
- 03/2018 *Photoisomerization Characteristics of Azobenzene-functionalized SAMs/Au(111)*; DPG Spring Meeting of the Condensed Matter Section; March 11th – 16th; Berlin; Germany
- 06/2017 *Exciton Relaxation and Migration Dynamics in α -Sexithiophene/Au(111)*; Ultrafast Surface Dynamics 10; June 11th – 16th; Inzell; Germany
- 04/2017 *Switching Surface Properties by Azobenzene-Functionalized SAMs*; Final Symposium of SFB658 on Elementary Processes in Molecular Switches at Surfaces; April 5th – 6th; Berlin; Germany
- 09/2015 *Ultrafast Exciton Dynamics in Thin Sexithiophene Films*; 31st European Conference on Surface Science (ECOSS); August 31st – September 4th; Barcelona; Spain
- 03/2015 *Ultrafast Exciton Dynamics in Thin Sexithiophene Films*; DPG Spring Meeting of the Condensed Matter Section; March 16th – 20th; Berlin; Germany
- 07/2014 *Ultrafast Exciton Dynamics in Thin Sexithiophene Films*; International Summer School on Semiconductor Interfaces; July 27th – 30th; San Sebastian; Spain
- 04/2014 *Self-Assembly and Electronic Structure of Metallocenes on Pb(111) and Pb(100)*; DPG Spring Meeting of the Condensed Matter Section; March 30th – April 4th; Dresden; Germany
- 09/2013 *Self-Assembling and Electronic Structure of Metallocenes on Pb(111) and Pb(100)*; Workshop on Forces and Photons in Molecular Tunnelling Junctions; September 23rd – 25th; Berlin; Germany

Research Stays

- 2016 Research stay in the group of Prof. Xiaoyang Zhu at the Columbia University in New York; USA; March 7th – April 15th (6 weeks)
- 2016 Research Stay in the group of Dr. Thorsten Wagner at the Johannes Kepler Universität Linz; Austria; April 18th – April 29th (2 weeks)

Danksagung

Meine Dankesworte möchte ich zunächst an meinen Doktorvater, Martin Weinelt, richten, ohne den die vorliegende Dissertationsschrift nicht möglich gewesen wäre. Er hat es mir ermöglicht in die Welt der zeitaufgelösten Photoelektronenspektroskopie einzutauchen und somit meinen Horizont im Bereich der Oberflächenphysik beträchtlich zu erweitern. Neben dem wissenschaftlichen Input, den ich über die Jahre von ihm erhalten habe, möchte ich mich auch für die stete Unterstützung bei Konferenzteilnahmen und der Beantragung eines mehrwöchigen Forschungsaufenthalt in den USA bedanken. Ich bin froh, ihn als Berater an meiner Seite auch für künftige berufliche Pläne zu wissen.

Auch meiner Zweitgutachterin, Katharina Franke, möchte ich für ihr stetes Interesse am Fortschritt meiner Arbeit und ihr jederzeit offenes Ohr danken. Wann immer ich Rat brauche, weiß ich, dass ich einfach an ihrem Büro vorbeikommen kann.

Ohne Cornelius Gahl wäre die Arbeit im Labor und bei den Auswertungen der Daten sicher um einiges zäher gewesen! Herzlichen Dank für die vielen Stunden intensiver Diskussion zu unseren Forschungsprojekten!

Ferner möchte ich Thorsten Wagner und Ebrahim Ghanbari danken, dass ich sie für zwei Wochen in ihren Laboren an der Universität Linz besuchen konnte, um mit ihnen gemeinsam die Struktur meiner Proben zu untersuchen. Ebenfalls richtet sich besonderer Dank an Ralph Püttner, der es mir mit seiner Berechnung von Photoemissionsspektren aus vibronisch angeregten Zuständen ermöglicht hat eine Simulation zum Einfluss vibronischer Anregungen in den von mir durchgeführten Photoemissionsmessungen zu erstellen.

Meinen Dank möchte ich auch an eine Vielzahl von weiteren Kolleginnen und Kollegen richten, mit denen ich in den beiden Projekten zusammengearbeitet haben. Diese waren im Rahmen des 6T-Projekts: Sebastian Baum, Malte Wansleben und Kristof Zielke und im Rahmen des SAM-Projekts: Beatrice Andres, Larissa Boie, Jan Böhnke, Thomas Moldt und Daniel Przyrembel. Neben gemeinsamen Messzeiten haben viele fruchtbare Diskussionen stattgefunden, die sich in den im Rahmen dieser Arbeit entstandenen Veröffentlichungen und einer Reihe von Konferenzbeiträgen niedergeschlagen haben.

Auch den weiteren aktuellen und ehemaligen Mitgliedern der AG Weinelt möchte ich für die schöne Zeit am und abseits des Arbeitsplatzes danken. Gerne verbringe ich zum sportlichen Ausgleich meine Abende mit euch bei diversen Sportkursen, und hoffe, dass wir das auch weiterhin fortsetzen werden!

Besonderer Dank geht ferner an meinen guten Freund Brunero Cappella, der mir geholfen hat meinen Schreibprozess zur Anfertigung dieser Dissertation zu strukturieren und den entstandenen Text auf Verständlichkeit und sprachliche Korrektheit überprüft hat.

Wie die vorausgegangenen Zeilen schon gezeigt haben, ist man im Leben nie allein und neben der

Unterstützung im beruflichen Rahmen, habe ich auch im Privaten viel Unterstützung erfahren, um mein Studium und meine Promotion so durchführen zu können, wie ich es getan habe. Daher möchte ich auch meinen Partner Christoph Resch und meine Familie nicht unerwähnt lassen, die mir stets mit Rat und Tat zur Seite stehen, wenn Probleme gemeistert werden müssen oder Entscheidungen anstehen.

Selbstständigkeitserklärung gemäß §7 Absatz (4) der Promotionsordnung

Hiermit versichere ich, Wibke Bronsch, dass ich die vorliegende Dissertation selbstständig und nur unter Verwendung der aufgeführten Hilfsmittel und Hilfen angefertigt habe. Diese Arbeit wurde weder in dieser, noch in ähnlicher Form schon einmal in einem Promotionsverfahren eingereicht.

Wibke Bronsch

December 19, 2018